Fatigue Life Prediction of Threaded Pipe Connection

Milad Beheshti

A thesis submitted for the degree of Doctor of Philosophy

Mechanical Engineering Department

Brunel University

United Kingdom

March 2017

Acknowledgements

Firstly, I would like to express my sincere gratitude to my supervisors Dr. David Rees and Professor Hamid Bahai for the continuous support of my Ph.D study and related research, for their patience, motivation, and immense knowledge. His guidance helped me in all the time of research and writing of this thesis. I could not have imagined having a better advisor and mentor for my Ph.D study.

I would like to specially thank my friends Sina Roshanaei and Mahmoudreza Mirmohammadsadeghi, for their motivation and encouragement to carry on with my Ph.D; also a thanks to all of my friends who have helped me on this journey.

Last but not the least, I would like to thank my father, mother and my brothers supporting me spiritually throughout writing this thesis and my life in general.

Abstract

In the oil and gas industry, threaded pipe connection is frequently used to connect the casing string, drill pipe strings or production and transportation risers and pipelines. The connection is normally preloaded in order to maintain a sealed and secure connection while in service and avoid leakage. Tapered thread are a common connection and in order to introduce preload to the threaded connection when they are assembled a certain make-up torque is going to be applied. The make-up torque plus external loads result in a multiaxial stress distribution over the connection, where the threaded connections act as stress risers. Environment such as waves and currents cause dynamic loads acting on the pipe line and offshore structures. The weakest point in offshore structure is the pipe connection because of fatigue crack initiated in the connection's threads.

Researchers and engineers developed a variety of patented threaded pipe connection which all claiming to improve a connection's fatigue life. The experimental data for patented designs, available in literature, is limited. Most published studies usually comprise experiments on a single connection type. For detailed fatigue analysis those published studies cannot be used since there is no uniformity in testing setup, loading conditions and damage detection technique exist. Moreover, current design curves in codes and standards lead to overly conservative or inaccurate results.

The aim of this work is to provide a better understanding of the fatigue mechanisms of threaded pipe connections and to study the effect of different design features on a connection's fatigue life. The final goal is to formulate guidelines for new fatigue resistant connection designs.

API connection is used as a reference in this study. Several modifications and design features are applied to the connection type. To simulate the effect of these modifications, a parametric 2D axisymmetric finite element model, ABAQUS is used. 2D finite element result are compared with a 3D model to prove its validity for both make-up. In addition, the results of the 2D axisymmetric simulation are validated by static strain gauge measurements during a make-up test and an axial tension test. The validated model is then used to evaluated the influence of the connection properties and design features on the threaded connection's behaviour.

Test rigs were designed to perform axial fatigue experiment on two scales: the small-scale experiments on 1" (33.4 mm outer diameter) connections are performed in axial fatigue testing, the medium scale tests on 4.5" (114.3 mm) connections are carried out under axial tension for which a setup is developed.

The majority of the performed fatigue tests are small scale experiments. Several modified configurations are tested. The S-N curve is constructed, so that the effect of certain configuration on the connection's fatigue life can be quantified. The local modification of the threaded connection's geometry as well as the connection's contact condition's contact conditions can have an important influence on the fatigue life of the connection.

A beach marking technique is used to visualized the crack fronts at different moments during the tests so that exact crack shape can be seen during post-mortem analysis. The result shown that a crack initiates at the root of the last engaged thread of the male part of the connection, and propagates slowly over a large segment of the circumference, forming a long shallow crack. When the crack penetrates the pipe wall, it rapidly increases in size along two crack fronts. The shape of crack observed in beach mark analysis do not have a semi-elliptical shape as commonly used in fracture mechanics. A fatigue crack growth analysis that considers the crack as an annular flaw, is effective in describing the crack growth behaviour.

The experimentally obtained *S-N* curves and the result from the finite element simulations are combined in multiaxial damage evolution law. The observed trend in fatigue lives of the configuration are explained by using the fatigue analysis. Using a connection's thread load distribution as a measure for its fatigue life is proven to be inaccurate. The main reason for this is that the load distribution is related to axial stresses over the connection. The fatigue life of a threaded connection is determined by the local multiaxial stress distribution and strain range around the root of the last engaged thread.

These local conditions are not only the result of the load distribution, but they are also affected by the hoop stress introduced during make-up, which can additionally be affected by a changed connection stiffness.

The multiaxial damage evolution law is used to analyse the influence of several features on a connection's fatigue life. It is not for all patented modifications that an increased fatigue life is predicted when applied to the API connection.

The final conclusion reached is that, in order to optimize a fatigue resistant connection, several design features must be combined together. The thread shape can be optimized to obtained a low stress concentration factor and reduce the local strains at the thread root. The connection's global geometry and make-up conditions can be optimized to improve the load distribution over the threads and reduce local stresses and strains at the threads.

Table of Contents

Symbols and acronyms

Symbols		Units
a	Crack depth	μm
A	Surface area	m^2
b	Fatigue strength exponent	-
c	Fatigue ductility exponent	-
C	Damping matrix	kg/s
C_i	i^{th} arbitrary constant	-
D	Accumulated damage	-
D_b	Box (Female) outside diameter	mm
D_P	Pin (Male) outside diameter	mm
E	Young's modulus of elasticity	GPa
f_i	i^{th} eigenfrequency	Hz
F	Force matrix	N
F_e	Excitation force	N
I	Area moment of inertia	m^4
J	Mass moment of inertia	$kg.m^2$
K_a	Loading mode correction factor	-
K_b	Size effect correction factor	-
K_c	Surface roughness correction factor	-
K	Stiffness matrix	N/m
K	Stress intensity factor	$MPa.m^{\frac{1}{2}}$
K'	Cyclic strength coefficient	-
K_f	Fatigue notch factor	-
K_t	Stress concentration factor	-
K_{tg}	Gross stress concentration factor	-
K_{tn}	Net stress concentration factor	-
l , L	Lengths	m
L_b	Box length	mm

L_c	Critical distance	m
m	Strain hardening exponent	-
m_b	Beam mass	kg
m_l	Total mass of the left end weight	kg
m_r	Total mass of the right end weight	kg
M	Mass	kg
$\widetilde{\boldsymbol{M}}$	Mass matrix	kg
$M(x)$	Bending moment	Nm
n	Number of stress cycles	-
n'	Cyclic strain hardening exponent	-
N	Cycle or number of cycles to failure	-
N_i	Number of cycle to crack initiation	-
p	Pressure	MPa or bar
P	Thread pitch	-
q	Notch sensitivity factor	-
R	Load ratio	-
R_c	Radius of the contact surface	mm
R_i	Inside radius	mm
R_o	Outside radius	mm
R_V	Triaxiality function	
s	Distance	m
S	Nominal stress	MPa
S_a	Stress amplitude	MPa
S_f	Fatigue stress	MPa
S_m	Mean stress	MPa
S_r	Stress range	MPa
t	Number of make-up turns	-
T	Torque	Nm
TR	Transmissibility function	-
$u(x,t)$	Deflection	m

$U(x)$	Deflection amplitude	m
$U_f(x)$	Deflection amplitude due to forced vibration	
Y	Geometric factor in the Paris law	-
α	Taper angle	°
a	Damage evolution law material parameter	
a_e	Excentre angle[1]	°
β	Damage evolution law material parameter	
γ	Wave number	m^{-1}
δ	Degree of freedom	
ΔK	Difference in stress intensity factor	$MPa.m^{\frac{1}{2}}$
ΔK_{th}	Threshold value of ΔK	$MPa.m^{\frac{1}{2}}$
$\Delta\varepsilon$	Local strain range	-
$\Delta\sigma$	Local stress range	MPa
Δt	Taper difference	°
ε	Strain	-
ε_f'	Fatigue ductility coefficient	-
ε_P	Equivalent plastic strain	-
θ	Skin depth	mm
k	Dang Van material parameter	-
λ	Dang Van material parameter	-
φ	Half thread angle	°
μ	Magnetic permeability	$H.m^{-1}$
v	Poisson's ratio	-
ρ	Density	kg/m^3
σ	(Local) Stress	MPa

[1] An **excenter** is a point at which the line bisecting one interior angle meets the bisectors of the two exterior angles on the opposite side. This is the center of a circle, called an excircle which is tangent to one side of the **triangle** and the extensions of the other two sides.

σ_e	Electrical conductivity	$S.m^{-1}$
σ_{eq}	Von Mises equivalent stress	MPa
σ_f'	Fatigue strength coefficient	MPa
σ_H	Hydrostatic pressure	MPa
$\sigma_i (i = 1 \dots 3)$	Principal stress component	MPa
σ_{UTS}	Ultimate tensile strength	MPa
σ_y	Yield strength	MPa
ζ	Damping ratio	-
τ	Shear stress	MPa
ω	Angular frequency	s^{-1}
ω_1	First/natural angular Eigen Frequency	s^{-1}

Definitions and acronyms

ACFM	Alternating current field measurement
ACPD	Alternating current potential drop
AM	Area method
API	American Petroleum Institute
ASME	American Society of Mechanical Engineers
Box	Female part of a threaded connection
BSPT	British Standard Pipe Thread
Buttress	trapezoidal thread type
CMS	component mode synthesis
COF	coefficient of friction
DCPD	direct current potential drop
DEL	damage evolution law
DIC	digital image correlation
Flush	as in flush connection: integral connection produced in the pipe material without any local increase in inside or outside diameter.

Integral	as in integral connection: connection type where the pipes have a pin and box at either end; no separate coupling part is used for these connections.
ISO	International Organization for Standardization
LET	last engaged thread
Load flank	thread flank that carries the connection's load under axial tension
LVDT	linear variable displacement transducer
Make-up	the process of assembling a threaded connection to its final state
MPI	magnetic particle inspection
NC	numbered connection style drill pipe see API spec.7 (API specification 7, 1997)
NDT	non-destructive testing
NPT	National Pipe Thread Taper
OCTG	oil country tubular goods; general term for pipes for casing tubing, line pipe and transportation pipes for oil and gas
OMA	operational modal analysis
OMAX	operational modal analysis with exogenous inputs
Pin	male part of a threaded connection
REG	regular style drill pipe acc. See API spec.7 (API specification 7, 1997)
SCF	stress concentration factor
SEM	scanning electron microscopy
Stab flank	thread flank opposite to the load flank
TCD	theory of critical distance
Tpi	number of thread per inch
T&C	threaded and coupled; connection type where the pipes have two pin threads at either side and are connected by a separate box.
Upset	as in upset connection: integral connection where the pin and box are produced in a part with a thicker wall than the other part of the pipe

Chapter 1 Introduction

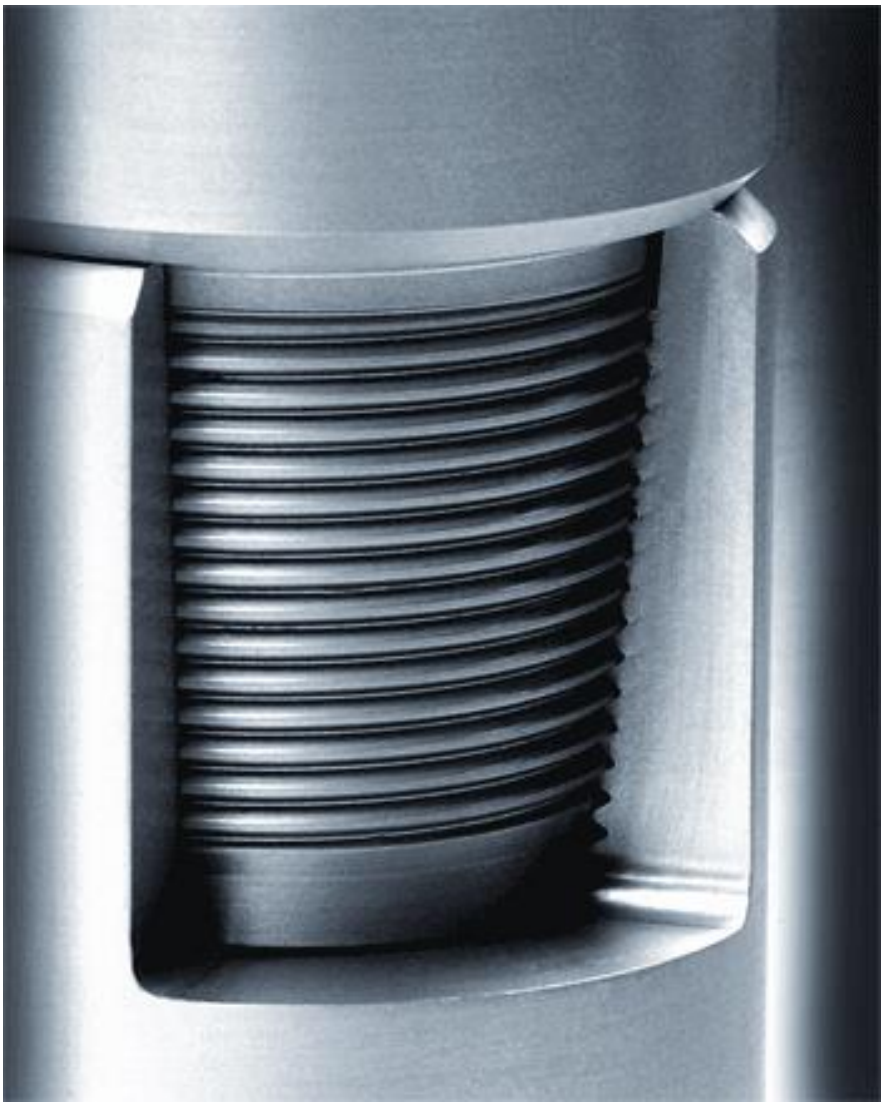

1 An Overview of Threaded Pipe Connections

1.1 Background and History

Fatigue Failure in engineering component is considered to be important as it has led to fatal consequences. For more than a century fatigue failure has been topic of research by engineers. Crack initiation and propagation is a result of repeated cyclic loading below the yield stress of material which can lead to tragic failure. The results of catastrophic failure as a result of fatigue failure over the past fifty years give the researcher the will to understand how and why fatigue failure happens.

For example, tragic accidents from fatigue failure can be pointed to the capsizing of the Alexandera L.Kelland oil platform due to a poor welding, reducing the fatigue strength of the structure, and disintegration of two de Havilland Comet jetliners which claimed so many life see Figure 1.1.

Figure 1.1: Top is (*Alexander L. Kielland (platform)*, 2017)*, Bottom Comet jet* (LIASCH and completo, 2016)*.*

In March 1980 Alexander L. Kielland platform collapsed and it claimed 123 lives. In March 1981, an investigation conducted by the engineers and it reveals that the rig

collapsed due to a fatigue crack in one of its six bracings (bracing D-6), which connected the collapsed D-leg to the rest of the rig. The cause of failure was traced back to a small 6mm fillet weld which joined a non-load-bearing flange to the D-6 bracing. The sonar device was held with this flange plate which was used during drilling operations. The poor profile of the fillet weld led to a reduction in its fatigue strength and caused the rig to collapse.

Due to high stress concentration at window corners of Comet jet, it showed a low fatigue resistance of the cabin and it caused the fuselage to crack, since there is a pressure difference between inside and outside the aircraft it led to a sudden failure in fuselage, as result of this failure there was 13 fatal crashes which resulted in 426 fatalities.

There are three major approaches for analysing and designing against fatigue failure (API, R., 1999. 5C1); the fracture mechanic approach, the stress based approach and strain based approach.

The fracture mechanics approach is further divided into lifetime approach (number of cycle to failure) or a fatigue crack growth approach (damage tolerance). Fatigue crack growth caused by repeated cyclic loading (API, R., 1999. 5C1).

The most common approach is the stress based approach, as it considers the nominal (average) stress in the affected areas for the analysis of the fatigue life.

The strain based approach treats the localized plastic deformation/yielding that may occur in regions with stress raisers such as edges and notches.

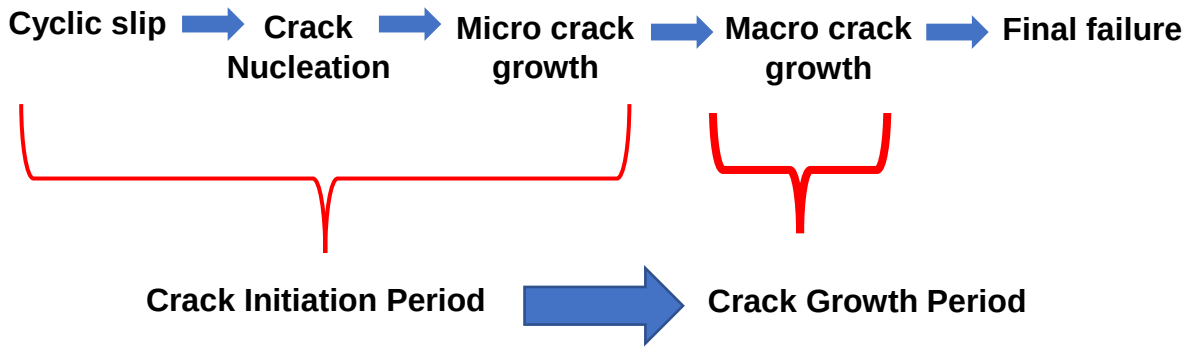

Figure 1.2: Different period of fatigue life (Beden, 2009)

Since the 1950's, many engineers and researchers were focused on investigating how early cracks can be detected in fatigue life. This divided the fatigue life in two period/phases; the crack initiation period and the crack growth (RP579, A.P.I., 2000). The Crack initiation period is the largest period in fatigue life for high cycle fatigue. The Crack growth period is the most important part for low cycle fatigue.

Until today the most difficult and challenging part in fatigue is how to specify the transition between the crack initiation period and crack growth, as shown in figure 1.2. To define the transition between crack initiation period and crack growth period Paris

et al. proposed in 1961 a correlation between crack growth rate, $\frac{da}{dN}$ and the stress intensity factor range, ΔK which in later chapter 5 will be discus in more details.

1.1.1 Application

The oil and gas industry use threaded pipe connection for connecting structures for both on shore and offshore risers. The threaded pipe connection is more practical to use where welding is not an option. A good example of threaded pipe connection is in drill pipe, which has to be coupled and uncoupled frequently, as shown in figure 1.3.

Figure 1.3: Drill pipe threaded connection. (Khiggins, 2012)

The increasing demand for fossil fuels moves the exploration of new sources to greater depths, deeper ocean water and harsher environments.

In offshore drilling and harsher environment in ocean need extreme requirements for the pipe line to use more advance threaded joint connection. First step for construction of a well, a hole is drilled using a drilling tool connected to a long string of drill pipes. In order to prevent well collapse, they place a casing pipe inside the well. After the drilling and construction of the hole is finished, they inserted a tube for oil and gas flow to the surface. A wellhead at the bottom of the sea is connected to the production line using an extra riser pipe. The drill pipes, casing and tubing, regularly called *Oil Country Tubular Goods* (OCTG), and in many cases also the riser pipes, are connected using threaded connections.

As well as using for connecting pipe, it threaded connection is used for structural applications such as connect tendons of tension leg platforms, to connect offshore caissons, in pillars offshore structures and columns of vertical pumps.

The use of threaded pipe connections can be seen in pressure fitting and transport pipeline. However, they are most commonly used in OCTG application.

The manufacturing of different threaded connections is important. One of the major impact of World War I on United State of America (USA) was shortage of equipment which caused delays in drilling operations. The industry attempted to overcome this problem by pooling equipment. Since there was no uniformity in pipe size and threaded coupling the program was a failure. As result of this failure rise a new regulation called American Petroleum Institute (API) took up the challenge of developing industry wide standards (API's History). In 1924 first specification were published and after the first publication an update is published every couple of years (Specification, A.P.I. 1998).

A number of fittings, line pipe, casing, tubing and drill pipe connections have been standardized by other organisations such as the European Committee for Standardizations (European Committee for Standardization, 2004), the American Society of Mechanical Engineering (ASME) (ANSI/ASME) and the International Organization for standardization (ISO) (ISO 3183).

The standard connection is only restricted and applicable to oil wells and onshore gas wells with limited depth and bottom hole pressure.

However, as can be seen from Table 1, for more severe duty, better connection are made using premium or propriety connections.

Table 1.1: Applicability of API and premium connections

Gas Wells	Offshore	Premium Connections
	Onshore	Standard Connections
Oil Wells		
Well Depth		3km 6km
Bottom Hole Pressure (bar)		275 550

Premium connections have better performance and design while still satisfying the standardized minimum requirements and sometimes they remain interchangeable with standard connections. For example, their structural strength, fatigue resistance or leak tightness is improved by changing the connection's geometry or thread shape, adding additional seals or improving the productions process.

These improvements are patented and all the information such as how many test conducted, what test setup was used etc, is kept secret due to competition between the companies therefore little is known on how specific features affect the global connection performance.

The standard OCTG connection is designed for multi propose use such as single or combined static load to the string, including tension or compression, bending and internal or external pressure. The main objectives of design of these connections are leak tightness and resistance against high bottom hole pressure.

Fatigue resistance become important when dynamic load act on the connections. This load can be caused by operational use or environmental effect. Dynamic loads in drill string are typically caused by torque vibrations and by bending of the string during operation.

Fatigue damage due to dynamic bending is the most important cause of failure of drill pipes (API recommended Practice 7G, 1998, Vaisberg, MacDonlad, 1995)

As well as risers in offshore structures, other parts such tendons and columns are also subjected to dynamic environmental load as shown in Figure 1.4. These are mainly caused by wave and currents. The latter can cause *Vortex Induce Vibration* (VIV) on the pipe string. Additionally, wind acting on a floating platform or production vessel can cause the structure to move, creating more fluctuation. These load condition are so severe that fatigue damage is the main failure mode for offshore risers (MacDonald & Deans, 1995).

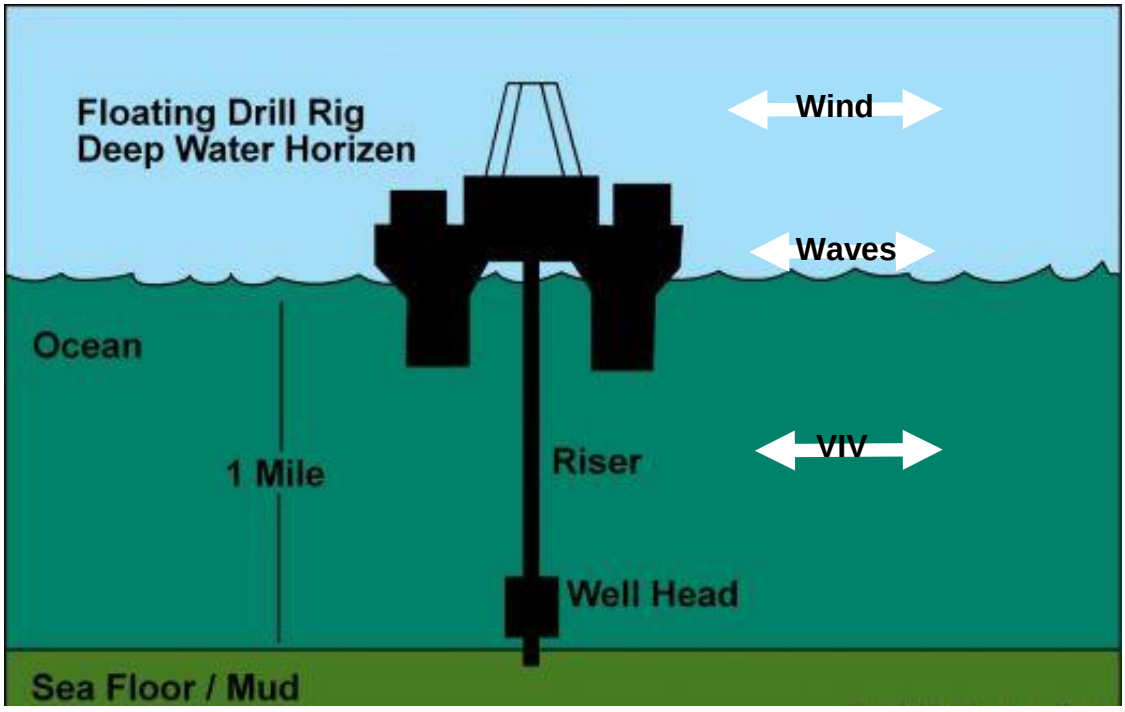

Figure 1.4: Environmental dynamic loads on offshore pipelines. (Articles, 2016)

Since there is a wide range of premium connection available, for the past few years there is a tendency to use casing pipes for drilling particular wells (Santi, 2005). As the casing can stay in the well after drilling and no drill pipe is needed this is more cost effective. This practice requires better fatigue properties for the connections, as they become subjected to additional dynamic loads resulting from the drilling operation.

Since search and exploration for fossil fuel is moving to harsher environment conditions, threaded connections of all kind need continue improvement and fatigue life is one of important feature that need attention.

1.2 Principle

The screw form is a highly significant mechanical principle in that it is a basic relation between rotational and translation motion. Its applications are numerous, ranging from gears to conveyors. With the development of modern manufacturing techniques, the screw form could be utilised as an efficient reversible fasteners. These fasteners or threaded connections are available in many different forms and types to suit their designed operation. Because the number of applications for these is vast, categorisation of the different connection type is difficult. However, connection are usually required to satisfy one or both of the following functions:

1) To make a strong structural joint.
2) To make a pressure sealed joint.

1.2.1 Bolts and Nuts

Different screw thread system have been stablished, such as Whitworth figure 1.7, B.S.F., American National (Sellers) and System international. The form of the thread were simply symmetrical triangular shape thread with modification such as flat or round crest and root and fine coarse pitches.

In 1965 the British standard Institution (BSI) introduced an internationally agreed International Organisation for Standardisation (ISO) metric thread as its standard for structural friction grip bolts. Figure 1.5 shows the basic form of the thread. The threaded connection is categorized in three forms, general, higher-parallel shank and higher waisted shank. The general grade is the basic form. The higher-grade parallel is geometrically similar to general form thread but is made from high strength steel and only to be used in joints exposed to shear loading.

The higher grade waisted shank form is shown in figure 1.6. This form has more advantage to parallel shank bolts due to their low shank ductility, to overcome this limitation the higher grade waisted shank can be used successfully for application that require tensile and shear strength together. The chance of damage increases in lower ductility of parallel shank if the combined stresses from torque and tension reaches the ultimate. The axial ductility of the connection is the main factor especially when it is designed to with stand fatigue failure.

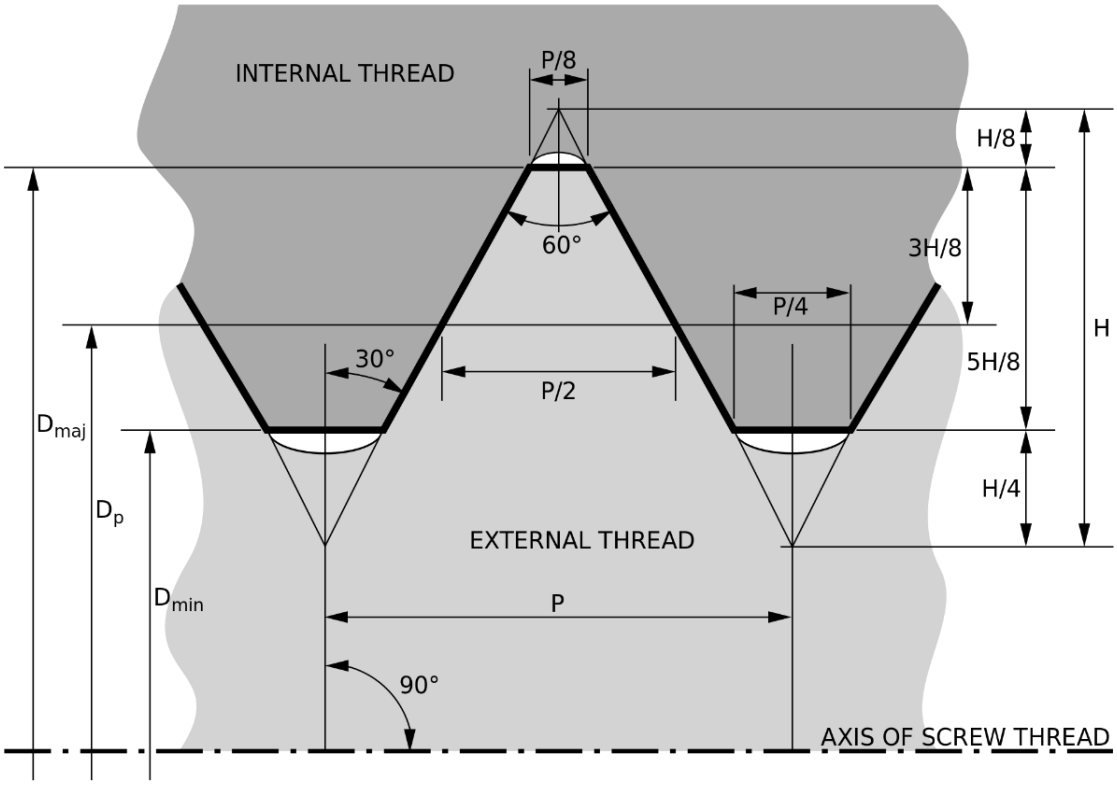

Figure 1.5: ISO Metric Thread Form. (*ISO metric screw thread,* 2016)

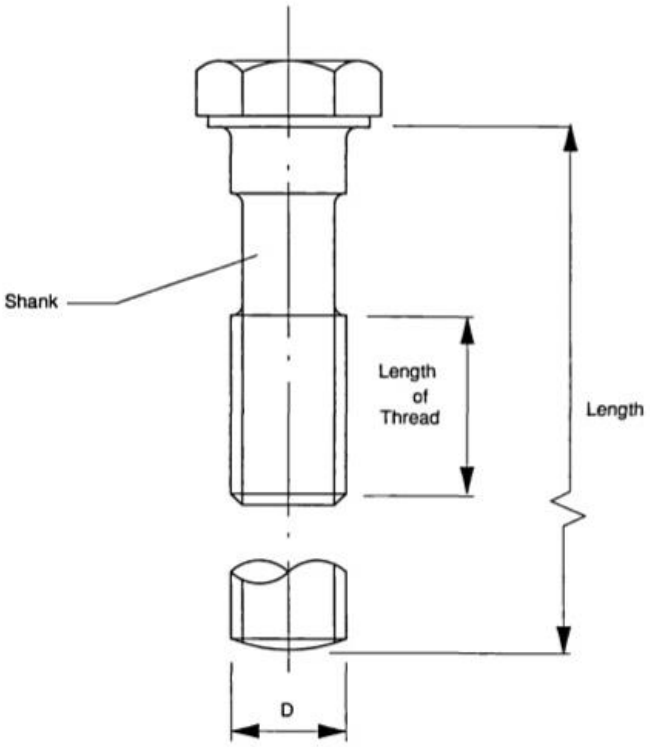

Figure 1.6: ISO Metric Waisted Shank (Brennan, 1992).

Other characteristics may change for different bolts such as length, diameter, pitch and material. The effective thread area increases when the bolt diameter increases and this reduces stress, but this is practical with certain limitations. As it will be

discussing in later chapter 5 there is no advantages on length or number of engaged threads over a critical value as the load is not evenly distributed along its length and between the threads.

Newport (1989) studied the influence of the thread pitch on the critical tooth stress. His research shows stress reduces as the pitch increases, however the friction force plays an important role to hold the male and female section together and prevent sliding on an inclined plane. Increasing the pitch without increasing the diameter influences the helix angle and as a result causes the possibility of un-torqueing the connection under the axial loading.

Despite the modification on the geometrical form mentioned, many other modifications have been used on the thread form. The use of different pitches has shown the reduced on critical tooth but tolerance required in production make an it impractical option for general use. Over time in operation, strains within the connection might reduce the stress lowering modification ineffective. In a taper thread the cross sectional area is limited due to taper angle which the stress lowering effect is significant when dealing with structural bolts having relatively large core cross-sectional areas.

Conical grinding of a frustum on the first threads of the nut improves fatigue life but detrimentally affects static capacity, increasing the possibility of “Jump Out”. Similar effects are seen with truncated and rounded crests and roots (Kawashima, 1990).

It has been tried and is an on-going practice for designed for strength in screw threaded connection and many results have been produced were encouraging (Sparling, 1982). Unfortunately, manufacturing of some of these findings on a large scale for general use is often not possible, since the effect could be so critical that relaxation due to aging strains and thread damage during service can offset their advantages with adverse effects.

1.2.2 Pressure Threaded Joint

The pressure tight joints are made on the thread for pipe thread and fitting by British Standard (BS). These BS standards are a Withworth thread form for internal and external tapered threads. It is identical to the ISO standard for pressure-tight thread joints.

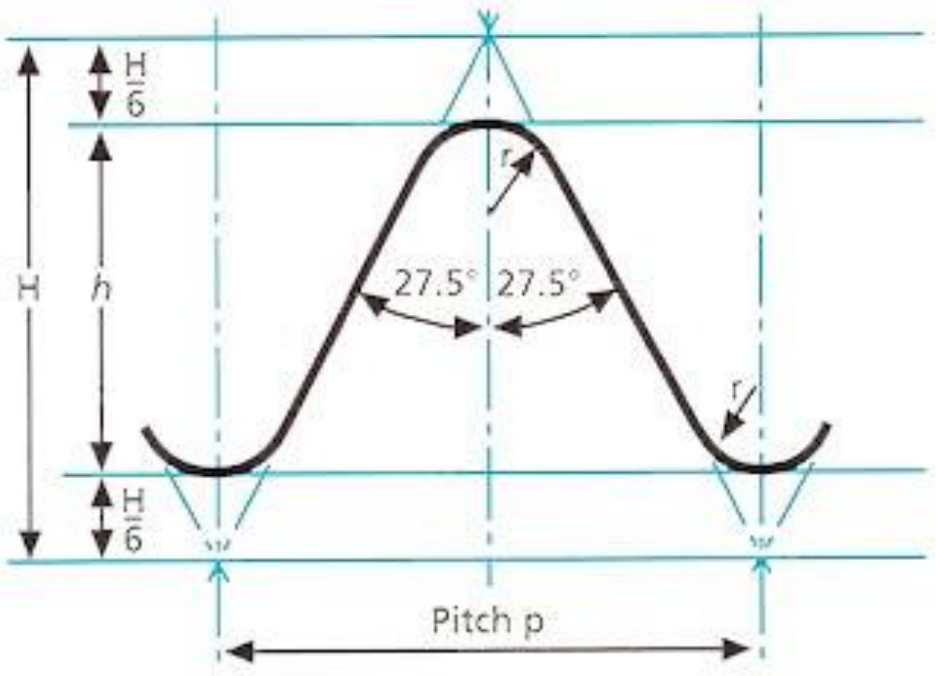

Figure 1.7: Whitworth Thread Form (Original gauge Co Ltd, 2012).

Since there are many types use for pipe connections, many modifications to the basic form exist. For oil well drilling the most common type use is API's round thread coupling, which is used also in casing. With this type of thread in joints there is a clearance between male and female thread, which provides a leak path. In order to avoid leaking between the threaded components a special thread compound is needed to maintain internal pressure.

For pressure sealed thread the most commonly used connection is the long screw thread or a modification to this. These types can be a Buttress or V-form thread. Pressure-tight seals can be made directly between machined faces, with O-rings or by compressing a soft material on to the surface of the external thread by tightening a backnut against a socket.

Using the right thread is sole depend on the viscosity and pressure of the conveyed fluid. For many fluids, it is important to avoid leakage and it is important to use an internal rotatory shoulder so that non-turbulent flow is encouraged by the smooth transition between pin and box. In offshore drilling this is very important as the fluid is multiphase flow, which mean conveying mixtures of fluid together, in this case oil and gas. Gas "slugs" can under turbulent conditions create considerable dynamic bending loads contributing to fatigue damage.

In order to avoid the "Jump Out" effect between the threaded joint connections as a possible static failure, the buttress thread can used, which reduces this effect greatly by the low flank angle. Buttress threads have a higher axial stiffness than V-form threads per unit thread height.

1.3 Classification

Threaded connection pipe is made in two-parts, male and female, called respectively pin and box. Based on the method of manufacture threaded connection can be divided into three main categories. Figure 1.8 show these three types. The first type of connection two male pipe connection connected together using separate coupling part. Figure 1.8a show threaded and coupled connection (T&C), this connection is usually used for casing tubing and riser application. The figure 1.8b connection is called integral type where the pipe has a male and female connection at either end. Hence no separate coupling part is used for these connections.

Flush connection as seen in figure 1.8b is when the pipe material without any local increases in inside or outside diameter is produced. Figure 1.8c shows an upset connection where in the connection is proposed in a part with a thicker wall than the other part of the pipe. For tubing and drill pipe the most common type used in casing pipe is integral flush connection.

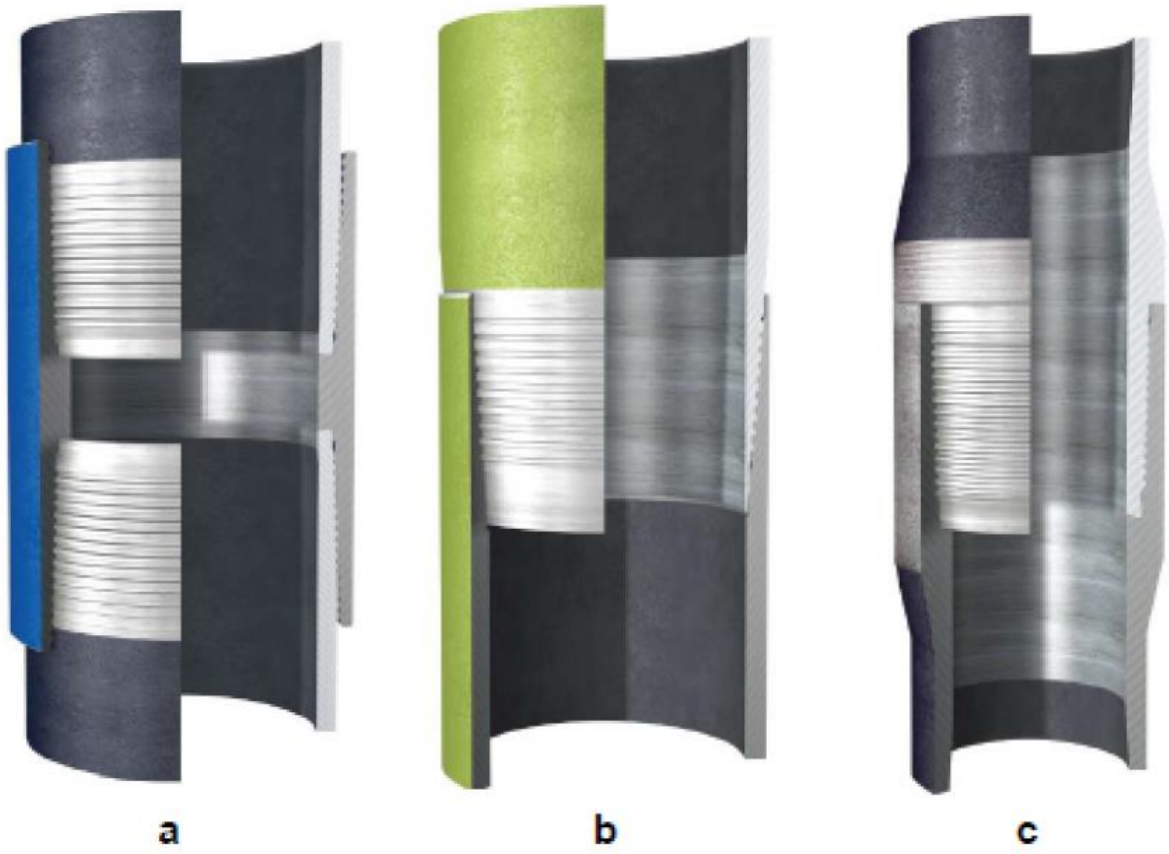

Figure 1.8: a) Threaded and Coupled, b) Integral Flush, c) Integral Upset Connection (TenarisHydril, 2016).

The research and report failure cases and laboratory tests done by researchers (Griffin et al, Ferjani et al, Sches et al), shows that despite the threaded connection type, the fatigue damage for all connection type is the root of the Last Engaged Thread (LET) of the pin as shown in figure 1.9. Although in drill pipes fatigue crack are also commonly found in the LET of the box (MacDonald, 1995).

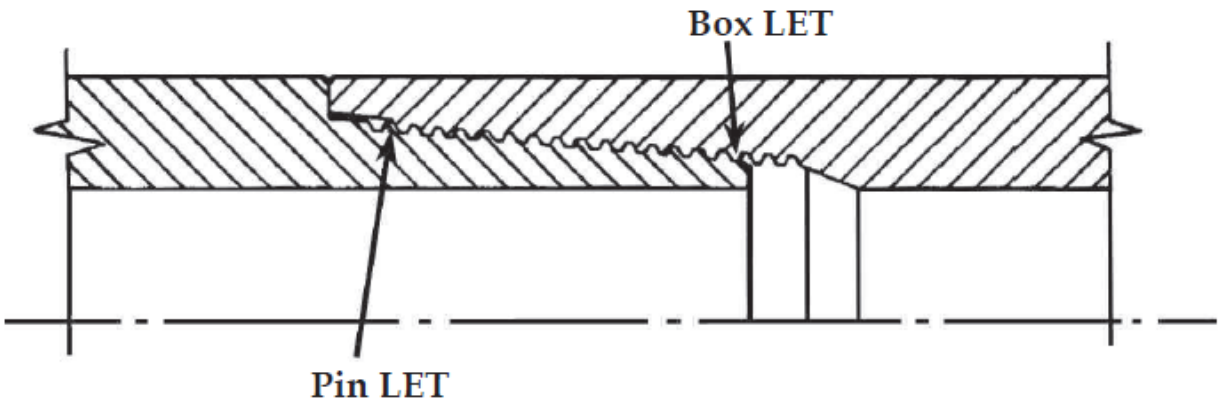

Figure 1.9: Common fatigue crack initiation areas in threaded pipe connections (MacDonald, 1995).

1.3.1 Make-up

Preloading is applied to the threaded joint connection to make sure there is sufficient sealing capacity and to avoid the connections loosening due to vibrations. The connections have a conical shape. The preload is introduced by assembling the connection with a certain torque. Depending on the connection type and size the torque applied varies, this being commonly referred to as the make-up torque.

In some standard and several premium connections, one or more torque shoulders are added. As shown in figure 1.10 there is a part of the connection where the pin and box come in contact beyond the threaded region. The shoulder enables a higher make-up torque to be applied to the connection. This can change the load distribution over the threads. The benefit of the torque shoulder is providing additional sealing. The use of a torque shoulder requires more accurate tolerance on the connection's geometry and accurate torque monitoring during make-up. Once the shoulders are in contact, the resulting torque increases rapidly for given rotation but over torque can cause the connection to fail.

A single and double shoulder configuration can be seen in figure 1.10. Additional metal to metal seals can be provided in the axial direction as can be seen in the double shouldered connection of Figure 1.10b, this design improves sealing that preventing leakage of oil and gas and avoids dirt or sea water to enter into the pipeline.

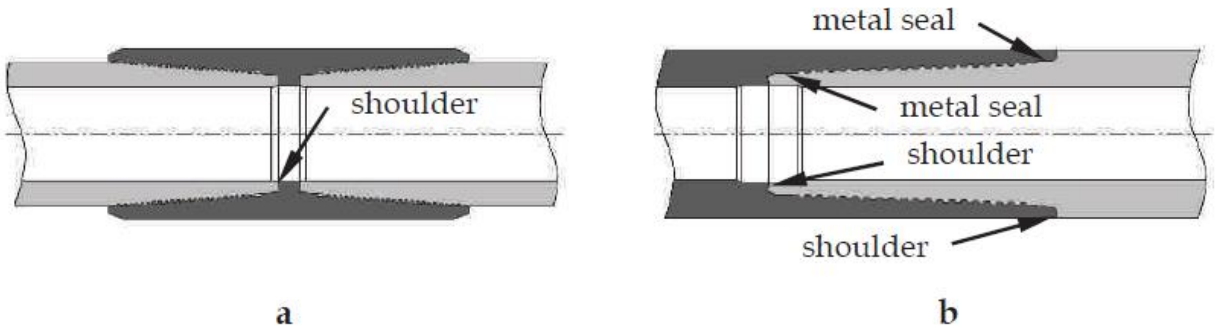

Figure 1.10: a) single shoulder T&C connection; b) double shoulder integral flush connection (Wittenberghe, 2011).

1.3.2 Thread type

There are many thread type used for threaded pipe connections, of which three are standardized by API specification 5B (API specification 5B, 1998) seen figure 1.11 a to c. The triangular thread figure 1.11a is used in the API line pipe connection.

The thread flank of the connection that carries the load under axial tension is referred to as the load flank, while the unloaded flank is called the stab flank. To obtain a reduced stress concentration when the connection is loaded, the thread roots and crest can be rounded (see figure 1.11.b). This kind of thread is standardized for API round casing and tubing connections and for British Standard Pipe Taper Thread (BSPT).

When subjected to an axial load, triangular threads will carry reaction forces with a high radial component. This can cause the pin and box to deform which can cause the connection to leak. Next to this, due to their triangular shape, at the crest the thread is much more narrow than at the root. This means that the thread crests can be easily damaged due to overload. For these reasons, thread types with small flank angles are available. They have a more constant section over the thread height. The most common pipe thread of this kind is the buttress thread which has a rounded trapezoidal shape, as can be seen in figure 1.11.c. This thread type is standardized for the API Buttress connection.

Numerous variations of these three thread types exist to enhance connections. For example, the thread angle, flank angles and root geometry or tolerances are changed to get an improved behaviour. Some of those designs are discussed more in detail in chapter 2. Additionally, completely different thread types can be found such as the wedge type of figure 11.d. this type is capable of carrying high torsion and compression loads together with reliable sealing capabilities. However, wedge threads are more subjected to wear during multiple make-up and break out operations (Mallis, 2010).

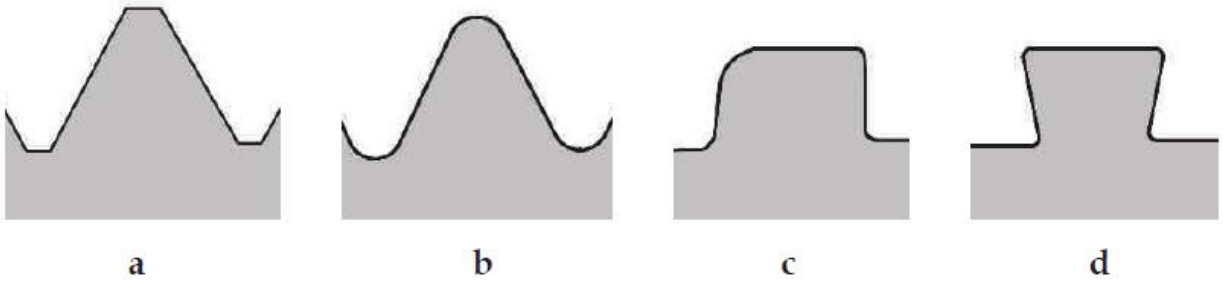

Figure 1.11: Thread type a) triangular; b) round; c) buttress; d) wedge (Wittenberghe, 2011).

1.4 Scope of This Work

The purpose of this research is to provide a better understanding of the fatigue mechanisms of threaded pipe connections. Different features that are expected to improve a connection's fatigue life are studied as until now it remained impossible to quantify their influence. In addition, current design curves in codes and standards lead

to overly conservative results. For this reason, several connection designs are analysed using an approach combining experimental testing with numerical simulations. In the following chapters, the methodology used, the results obtained and conclusions will be presented.

In chapter 2 an overview is given of the current knowledge of the fatigue life of threaded pipe connections based on information from the literature, Codes and Standards. The best connection is selected by comparing existing modelling techniques, fatigue analysis methods and experimental testing facilities.

As there is no general method for online monitoring of fatigue damage in threaded connections, chapter 3 includes an overview of available measuring techniques and focuses on the technique used during the experiments. To be able to perform fatigue experiments on small and medium scale pipe, an experimental test rig had to be developed. In chapter 4 the design and working principles of the axial testing fatigue test setup are presented. Additionally, experimental tests are carried out at two small scales. The test equipment, material and connection type used, the loading conditions applied and results obtained are analysed in chapter 5, where also a detailed analysis is carried out in which the experimental observation are compared with standard design curve and the results from the finite element model. Local data from the model is used for fatigue analysis in order to explain in the observed trends in the connection’s fatigue life.

Chapter 6 is dedicated to the finite element model that is developed to assess the behaviour of the threaded connections. The modelling details concerned, including the assumption used and the boundary conditions, are explained. The model is validated by comparing with previously presented experimental results. Comparison with results from the literature is also provided.

Conclusions related to the fatigue behaviour of threaded pipe connections are presented in chapter 7, together with possibilities for future research related to experimental testing and numerical modelling of threaded pipe connections.

The final goal is to use the scientific findings of this work to formulate guidelines for new fatigue resistant optimum threaded pipe connection designs.

References

- *Alexander L. Kielland (platform)* (2017) in *Wikipedia*. Available at: https://en.wikipedia.org/wiki/Alexander_L._Kielland_ (platform) (Accessed: 30 January 2017).
- ANSI/ASME B1.20.1-1983, Pipe Threads, General Purpose (Inch), 1983.
- API Recommended Practice 7G, Recommended Practice for drill stem design and operating limits, American Petroleum Institute, sixteenth ed., 1998.
- API, A., RP579-Recommended Practice for Fitness-For-Service (2000). *American Petroleum Institute*.
- API, R., 1999. 5C1 "Recommended Practice for Care and Use of Casing and Tubing".
- API's History, http://www.api.org/, retrieved 31/08/2016.
- Articles, 241 F. 23 (2016) *Black gold in the deep blue: Report from ground Zero*. Available at: http://hubpages.com/politics/Black-Gold-in-the-Deep-Blue-Report-from-Ground-Zero (Accessed: 30 January 2017).
- Beden, S.M., Abdullah, S. and Ariffin, A.K., 2009. Review of fatigue crack propagation models for metallic components. *European Journal of Scientific Research*, *28*(3), pp.364-397.
- Brennan, F.P., 1992. *Fatigue and fracture mechanics analysis of threaded connections* (Doctoral dissertation, University of London).
- EN 10226-1:2004: E, Pipe Threads where pressure tight joints are made on the thread –Part 1: Taper external threads and parallel internal threads – Dimensions, tolerance and designation, European Committee for Standardization, 2004.
- Ferjani,M.,Integration des Phenomenes dynamiques dans l'analyse en fatigue des garnitures de forage, PhD Thesis, Ecole Polytechnique, Palaiseau, France, 2006.
- Griffin, R.C., Kamruzzaman, S.,Strickler, R.D., Casing drilling drill collars eliminate downhole failures, Offshore Technology Conference OTC16569, 2004.
- *ISO metric screw thread* (2016) in *Wikipedia*. Available at: https://en.wikipedia.org/wiki/ISO_metric_screw_thread (Accessed: 30 January 2017).
- KAWASHIMA, H., 1990. Effect of incomplete threads on the jump-out tensile failure of premium connections for oil or gas wells. *JSME international journal. Ser. 1, Solid mechanics, strength of materials*, *33*(1), pp.107-112.
- Khiggins (2012) *Technology update*. Available at: http://www.spe.org/jpt/article/351-technology-update-september-2008/ (Accessed: 31 August 2016).
- LIASCH, J. and completo, V. meu perfil (2016) *A trágica carreira dos DeHavilland comet 1*. Available at:

http://culturaaeronautica.blogspot.co.uk/2011/09/tragica-carreira-dos-de-havilland-comet.html (Accessed: 30 January 2017).

- MacDonalds, K.A., Deans, W.F., Stress Analysis of Drillstring Threaded Connections Using The Finite Element Method, Engineering Failure Analysis, 2, 1-30, 1995.
- MacDonlad, K.A., Bjune, J.V., Failure analysis of drillstrings, Engineering Failure Analysis, 14, 1641-1666, 2007.
- Mallis, D.L., Reynolds, H.A., Wedge Thread with Torque Shoulder, United States Patent US7, 690,696 B2, 2010.
- Newport, A., 1989. *Stress and fatigue analysis of threaded tether connections* (Doctoral dissertation, University College London (University of London)).
- *Original gauge Co Ltd* (2012) Available at: http://www.thegauge.co.uk/technical-specifications/bsw-and-bsf-thread-gauges/ (Accessed: 1 February 2017).
- Santi, N.J., Carcagno, G.E., Toscano, R., Premium & Semi-premium Connections Design Optimization for Varied Drilling-with-Casing Applications, Offshore Technology Conference, OTC17221, 2005.
- Sches, C., Desdoit, E., Massaglia, J., Fatigue Resistant Threaded and Coupled connectors for Deepwater Riser Systems: Design and Performance Evaluation by Analysis and Full Scale Test, ASME 27TH International Conference on Offshore Mechanics and Arctic Engineering, OMAE2008-57603,2008.
- Sparling, L.G.M., 1982. Improving the strength of screw fasteners. *Chartered Mechanical Engineer*, *29*, pp.58-9.
- Specification, A.P.I., 1996. 5B, Specification for Threading, Gauging and Thread Inspection of Casing, Tubing and Line Pipe Threads (US Customary Units). *American Petroleum Institute*.
- Specification, A.P.I., 1998. Specification for rotary drill stem elements.
- TenarisHydril, Premium connections catalogue, http://www.tenaris.com/tenarishydril/,Version 01, September 2016.
- Vaisberg, O., Vincke, O., Perrin, G., Sarda, J.P. and Fay, J.B., 2002. Fatigue of drillstring: state of the art. *Oil & Gas Science and Technology*, *57*(1), pp.7-37.
- Van Wittenberghe, J., 2011. *Experimental analysis and modelling of the fatigue behaviour of threaded pipe connections* (Doctoral dissertation, Ghent University).

Chapter 2 Fatigue of Threaded Pipe Connections

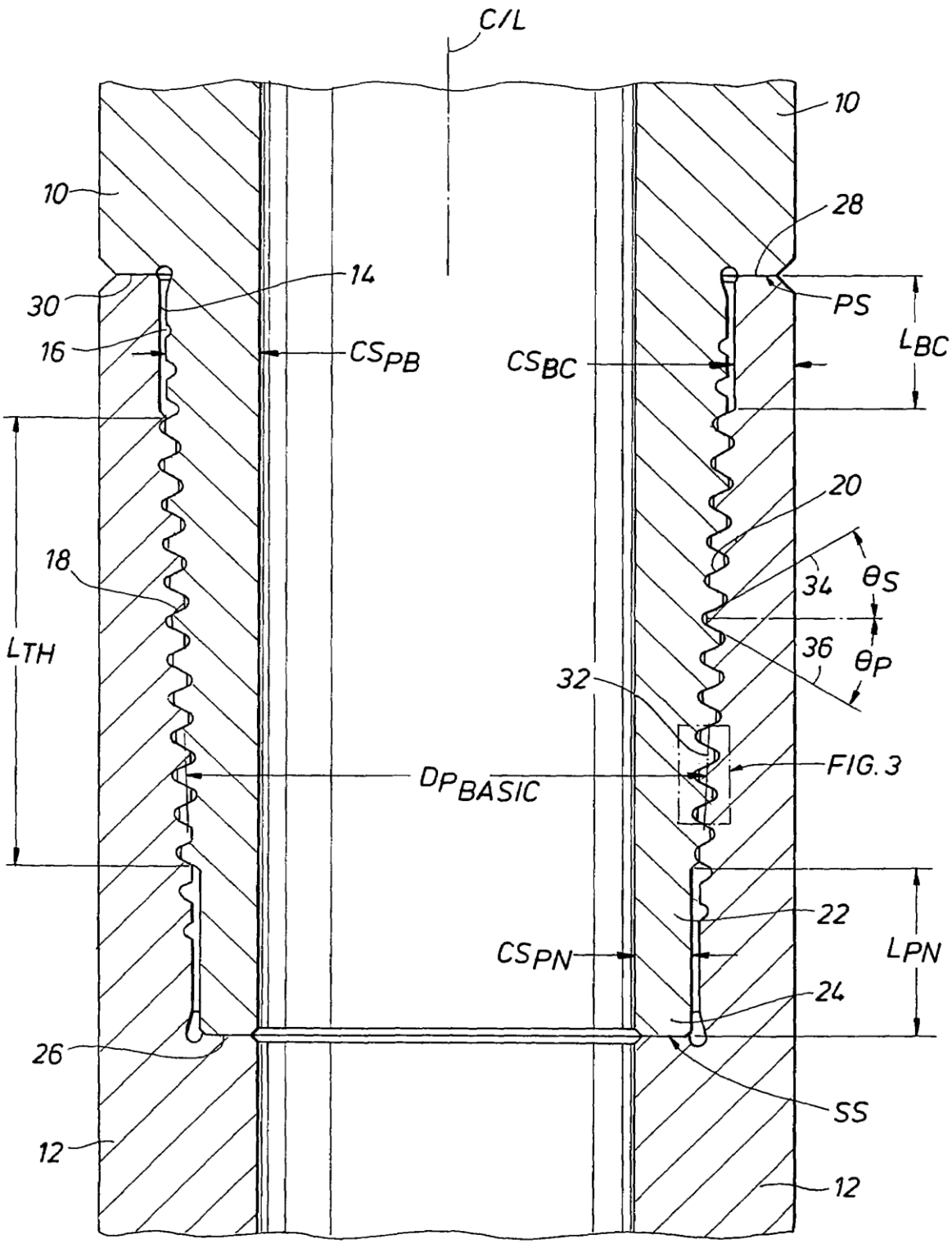

2.0 Summary

The aim of this chapter is to present the current knowledge on fatigue of threaded pipe connection and to determine the focus of this research.

This chapter reviews the current research and the extensive study on fatigue of threaded pipe connections. Different modelling techniques are studied and compared to each other and factors such as stress distribution and load distribution over the different thread types studied. An overview is given for patented premium connections or connection modification that claim to improve the connection's fatigue life. Finally, existing experimental fatigue setups are discussed and available fatigue data of threaded connections is compared to existing standards.

2.1 Basic Concept of Failure Mechanisms

Two main analyses are: a) identification of failure mode and b) failure mechanisms. The way failure is observed can be defined as the failure mode. The way in which the failure happens and its impact on equipment operation can be explained. Failure mode depend on the performance of different components. A failure mode can be caused by several factors. All the probable and independent causes for each failure mode must be identified and described. Depending on the way analysis is done, a failure mode could also cause the failure of another element in the system.

Failure mechanism is the actual physical defect or condition that causes the failure mode to occur. For instance, a physical, chemical, mechanical or other process that lead to failure is called a failure mechanisms. It is essential to distinguish between failure modes and failure mechanisms. For instance, wear and fatigue are not failure modes, they are failure mechanisms. In this study damage and fracture mechanics approaches is used to deal with fatigue crack initiation and propagation, respectively. Therefore, in this section the basic concept of fatigue of material, damage and fracture mechanics are reviewed.

2.2 Fatigue of Material

Fatigue is one of the failure modes of a structural element, subjected to a repetitive load application. As a simple example of life, we are not able to break by hand a simple clip by applying a constant force, but if we apply a repetitive force, sooner or later the clip will break. Repetitive force even smaller than the ultimate load of material can cause material failure by the phenomenon called fatigue. It has been estimated that fatigue contributes to approximately 90% of all mechanical service failure (Campbell, 2008). Any component or load bearing part that moves can be influenced by fatigue, as an example aircraft wing and fuselages, ship at sea, auto-mobile on road, nuclear reactors, jet engines and land based turbines are subjected to fatigue failure. In Europe by 1800s fatigue was initially recognized by engineers where bridge and rail-road components were cracking when subjected to repeated load (Campbell, 2008).

As the century progressed and the use of metals expanded with the increasing use of machines, more and more failures of components subjected to repeated load were recorded. Nowadays, structural fatigue has assumed an even greater importance as a result of the ever-increasing use of high-strength materials and the desire for higher performance from these materials. Fatigue depends on several factors, some industry have more strict rules and regulation for fatigue. For instance an air-plane structural components fatigue life depends of the following points:

- The material properties against fatigue
- Stress concentration factor applied to the structural component
- Amplitude of the load applied to structure
- Frequency of application of the load
- The relation between the minimum and maximum applied cyclic load

Fatigue can be caused by three basic factors: 1) a maximum tensile stress of sufficiently high value, 2) a large enough variation or fluctuation in the applied stress 3) a sufficiently large number of cycles of the applied stress. There are many types of fluctuating stresses. A fully reversed stress cycle, where the maximum and minimum stresses are equal, is commonly used in testing. Another common stress cycle is the repeated stress cycle, in which there is a mean stress σ_m applied in addition to the maximum and minimum stresses i.e. positive stress ratio. The last type of loading cycle is the random or irregular stress cycle, in which the part is subjected to random loads during service. A fluctuating stress is made up of two components: a mean or steady stress, σ_m, and an alternating or variable stress, σ_a. Figure 2.1a show the stress range, σ_{range}, is the difference between the maximum and minimum stress in a cycle:

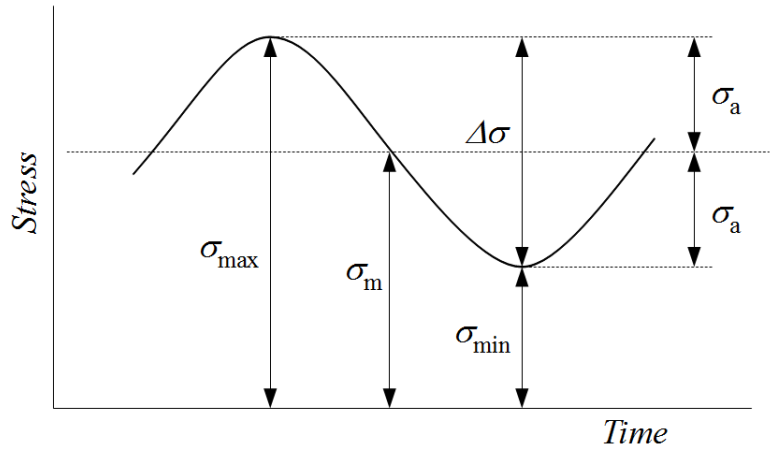

Figure 2.1a shows fatigue stress cycle.

$$\sigma_{range} = \sigma_{max} - \sigma_{min} \quad (2.1)$$

The alternating stress is one-half the stress range:

$$\sigma_a = \frac{\sigma_{range}}{2} = \frac{\sigma_{max} - \sigma_{min}}{2} \quad (2.2)$$

The mean stress is the algebraic average of the maximum and minimum stress in the cycle:

$$\sigma_m = \frac{\sigma_{max}+\sigma_{min}}{2} \quad (2.3)$$

Two ratios frequently used in presenting fatigue data are:

$$R_s = \frac{\sigma_{max}}{\sigma_{min}}, \text{ Stress ratio} \quad (2.4)$$

$$R_A = \frac{\sigma_{max}-\sigma_{min}}{\sigma_{max}+\sigma_{min}} = \frac{R_s-1}{R_s+1} \text{ Amplitude ratio} \quad (2.5)$$

2.2.1 High and Low cycle fatigue

High-cycle fatigue consists a large number of cycles ($N \geq 10^5$ cycle) and an elastically applied stress. Typical high-cycle fatigue tests are usually carried out for at least 10^5 cycles and sometimes 5×10^5 cycles for non-ferrous metals (Campbell, 2008). Although the applied stress is low enough to be elastic, plastic deformation can take place at the crack tip. High-cycle fatigue data usually presented as a plot of stress, S, versus the number of cycles to failure, N (known as S-N curve) figure 2.15. A log scale is used for the number of cycles. The value of stress,S, can be the maximum stress, σ_{max}, the minimum stress, σ_{min}, or the stress amplitude, σ_a. The S-N relationship is usually determined for a specified value of the mean stress, σ_m, or one of the two ratios, R_s or R_A. The fatigue life is the number of cycles to failure at a specified stress level, while the fatigue strength (also known as the endurance limit) is the stress below which failure does not occur. As the applied stress level is declined, the number of cycles to failure rises. Occurrence of crack as a result of fatigue can develop at early stage in the service life of the component by the formation of a small crack, usually at some point on the external surface, it is very difficult to distinguish between crack initiation and propagation period. The crack then propagates slowly through the material in a direction roughly perpendicular to the main tensile axis as depicted in figure 2.1 (Smallman, and Bishop, 1999). Figure 2.2 (Campbell, 2008) illustrates the typical fracture surface of a fatigued high strength steel component.

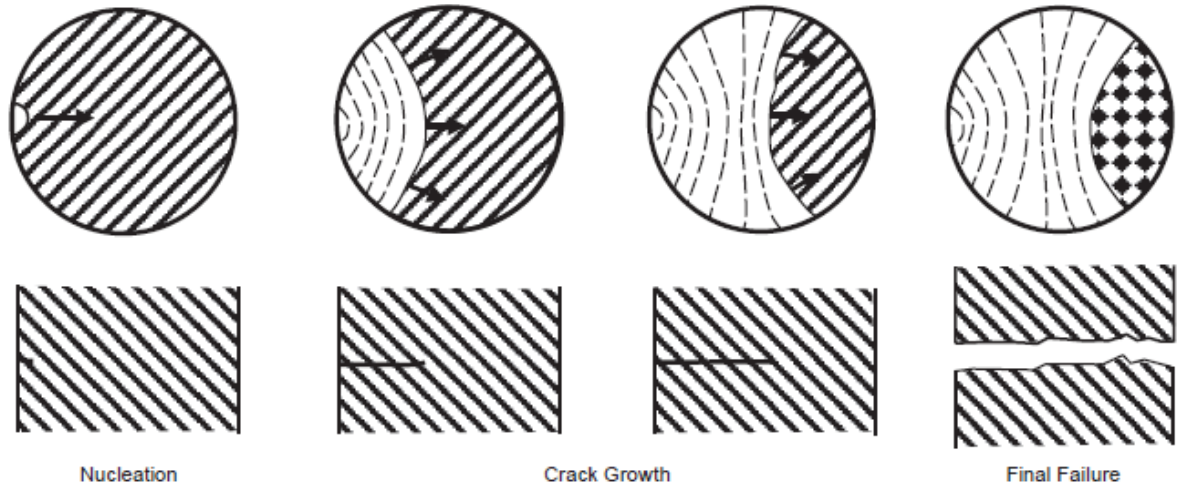

Figure 2.1: Typical fatigue crack propagation (Smallman, and Bishop, 1999).

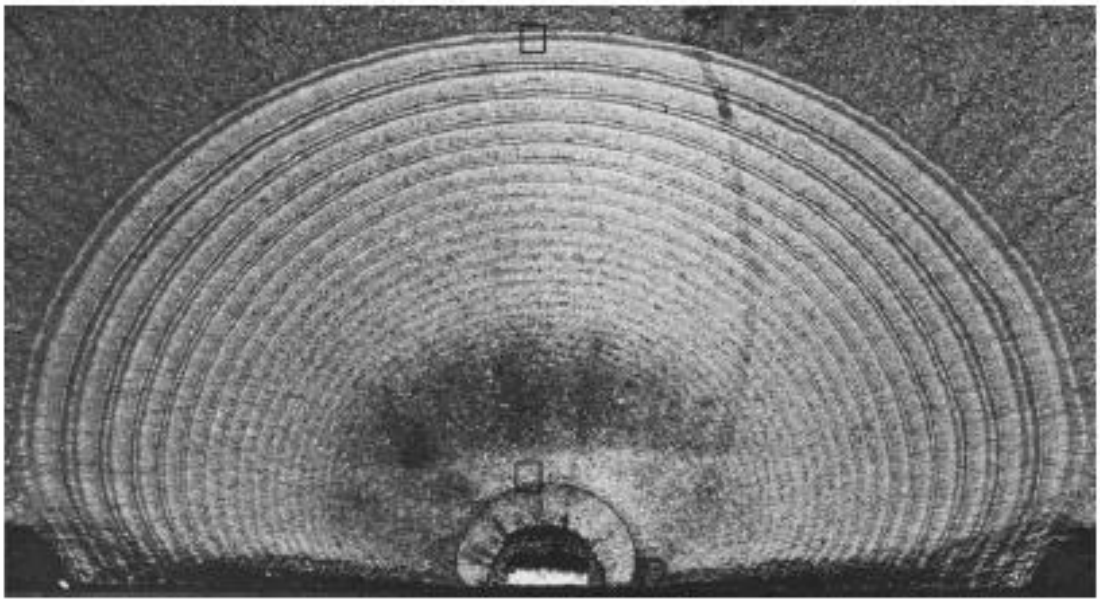

Figure 2.2: Fatigue crack growth in a high-strength steel component (Campbell, 2008).

The first systematic study into the relationship between stress and life was conducted by the German railway engineer August Wöhler (1870), observing that fatigue life was a stronger function of stress range than of peak stress. The ensuing S-N curve approach is still popular. The stress-life approach was developed by Basquin (1910) with the observation of a log-log relationship between stress amplitude and life in high-cycle fatigue.

$$\frac{\Delta\sigma}{2} = \frac{\sigma_f'}{E}\left(2N_f\right)^{b'} \tag{2.6}$$

where $\Delta\sigma$ is the stress range, σ_f' is the fatigue strength coefficient, b' is the fatigue strength exponent and $2N_f$ refers to the number of reversals.

During cyclic loading within the elastic regime, stress and strain are directly related through the elastic modulus. Nonetheless, for cyclic loading that produces plastic strains, the responses are more complex and form a hysteresis loop. The following features are related to low-cycle fatigue: machine or structure exposed to a heavy load. An irreversible strain at a micro-scale or macro-scale level induced by load. The damage accumulated in a structure will reach the point of initiation and propagation of cracks. A cycle is usually defined as interval between two service times. The number of cycle leading to failure (N_f) is relatively small. Lemaitre and Desmorat (2005) have categorized the classification of low cycle fatigue with examples that follows:

- The value of N_f lies between $10 - 10^2$ for aerospace rockets or metal formed by forging.
- The value of N_f lies between $10^2 - 10^3$ for thermal or nuclear power plants or chemical plants.

- The value of N_f lies between $10^3 - 10^4$ for aircraft engines or car engines where stresses induce yield strain ϵ_p magnitudes approaching $\epsilon_p \approx \sigma_{yield}/E$, where σ_{yield} is the yield stress and E is Young's modulus.

The basic characteristic of low cycle fatigue is based on the Coffin-Manson's equation as described in (Radhakrishnan, 1992). Figure 2.3 show a typical Coffin Manson curve. The total strain, $\Delta\epsilon_t$, consists of both elastic and plastic components:

$$\Delta\epsilon_t = \Delta\epsilon_e + \Delta\epsilon_p \tag{2.7}$$

Therefore, based on Coffin-Manson's equation the total strain amplitude can be calculated:

$$\frac{\Delta\epsilon_t}{2} = \frac{\Delta\epsilon_e}{2} + \frac{\Delta\epsilon_p}{2} = \frac{\sigma_f'}{E}(2N_f)^{b'} + \epsilon_f'(2N_f)^{c} \tag{2.8}$$

where $\Delta\epsilon_e/2$ is the elastic amplitude, $\Delta\epsilon_p/2$ is the plastic strain amplitude, σ_f' the fatigue strength coefficient, defined by the stress intercept at one load reversal (see figure 2.3), ϵ_f' is the fatigue ductility coefficient, defined by the strain intercepts at one load reversal, $2N_f$ is the total number of reversals to failure and b' and c are the fatigue ductility exponents (empirical material properties).$\Delta\epsilon_t$

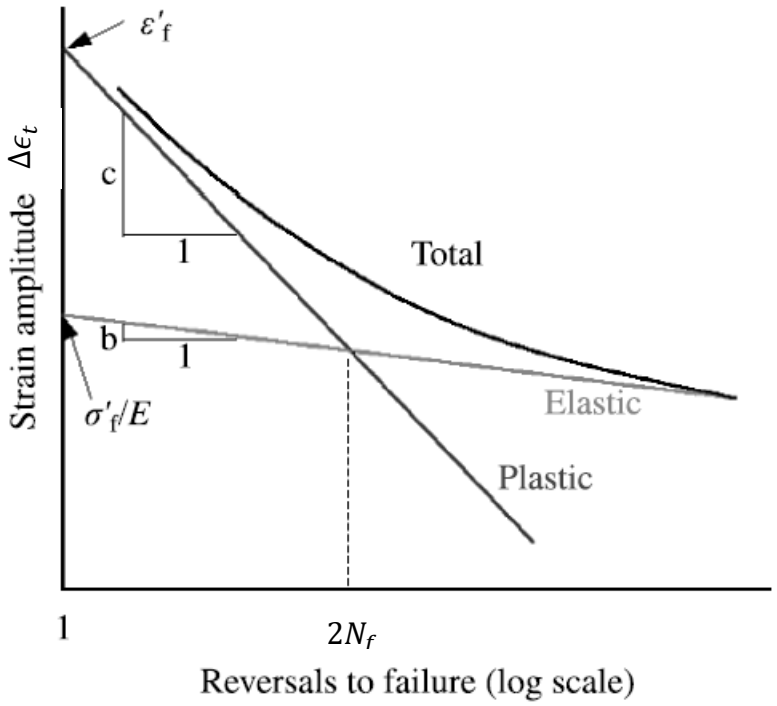

Figure 2.3: Typical joint lifetime according to Coffin-Manson's equation (Lemaitre and Chaboche, 1994)

2.2.2 Fatigue crack initiation and propagation

The fatigue crack in most cases nucleates at a free surface, usually external surfaces, but also can be initiated at sub-surface in presence of defects such as voids and

inclusions. Common surface defects include geometric notches and surface roughness. Fatigue crack nucleation and growth occurs in the following stages (Campbell, 2008):

- $Stage\ I$: Crack initiate usually start at surface discontinuity such as a notch, which acts as a stress risers. In the absence of a surface defect, crack initiation will eventually occur due to the formation of persistent slip bands, a result of the systematic build-up of fine slip movements on the order of approximately one nanometer. Therefore, the relative movement of the slip bands over each other results in the formation of intrusions and extrusions at the surface, which possibly lead to the formation of a crack. The initial crack propagates parallel to the slip bands. The crack propagation during I is very low. The crack initially follows the slip bands at approximately 45° to the principal stress direction as illustrated schematically in figure 2.4.
- $Stage\ II$: When the crack length becomes sufficient for the stress field at the tip to become dominant, the overall crack plane changes and becomes perpendicular to the major principal stress, the crack enters stage II. Fatigue crack growth proceeds by a continual process of crack sharpening followed by blunting by shear, as shown in figure 2.5.
- $Stage\ III$: Eventually, sudden failure occurs when the fatigue crack become long enough that the remaining cross section can no longer support the applied load, which is also called tensile fracture.

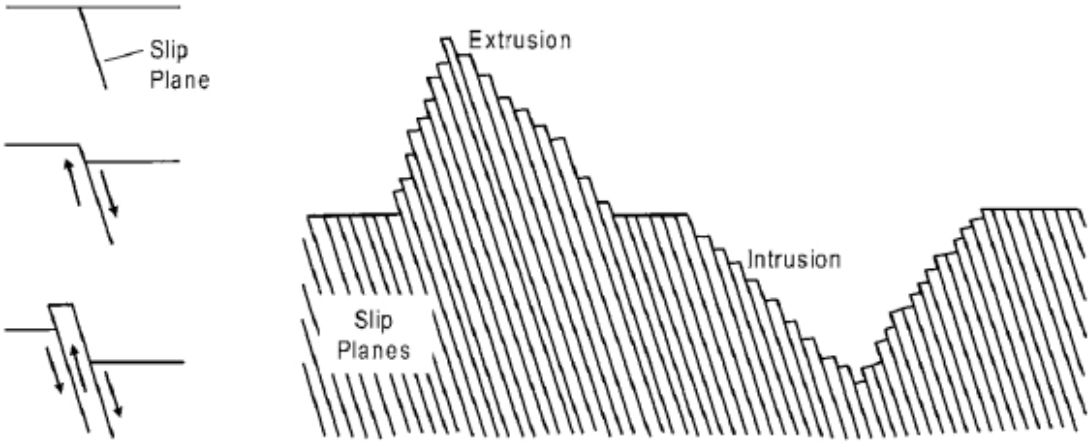

Figure 2.4: Fatigue crack initiation (Smallman and Bishop, 1999)

2.2.3 Fatigue crack growth

The rate of fatigue crack propagation is determined by subjecting fatigue cracked specimens to constant-amplitude cyclic loading. The incremental increase in crack length is recorded along with the corresponding number of elapsed load cycles acquire stress intensity factor (K), crack length (L), and cycle count (N) data during the test. The data is presented in the *L-N* curve. Various L versus N curves can be generated by varying the magnitude of the cycle loading and/or the size of the initial crack. The

data can be reduced to a single curve by presenting the data terms of crack growth rate per cycle of loading ($\frac{dl}{dN}$) versus the fluctuation of the stress Intensity Factor (SIF) at the tip of the crack (ΔK). ΔK is representative of mechanical driving force, and it incorporates the effect of changing crack length and the magnitude of the cyclic loading. The most common form of presenting fatigue crack growth data is a log-log of $\frac{dl}{dN}$ versus ΔK as schematically illustrated in figure 2.6.

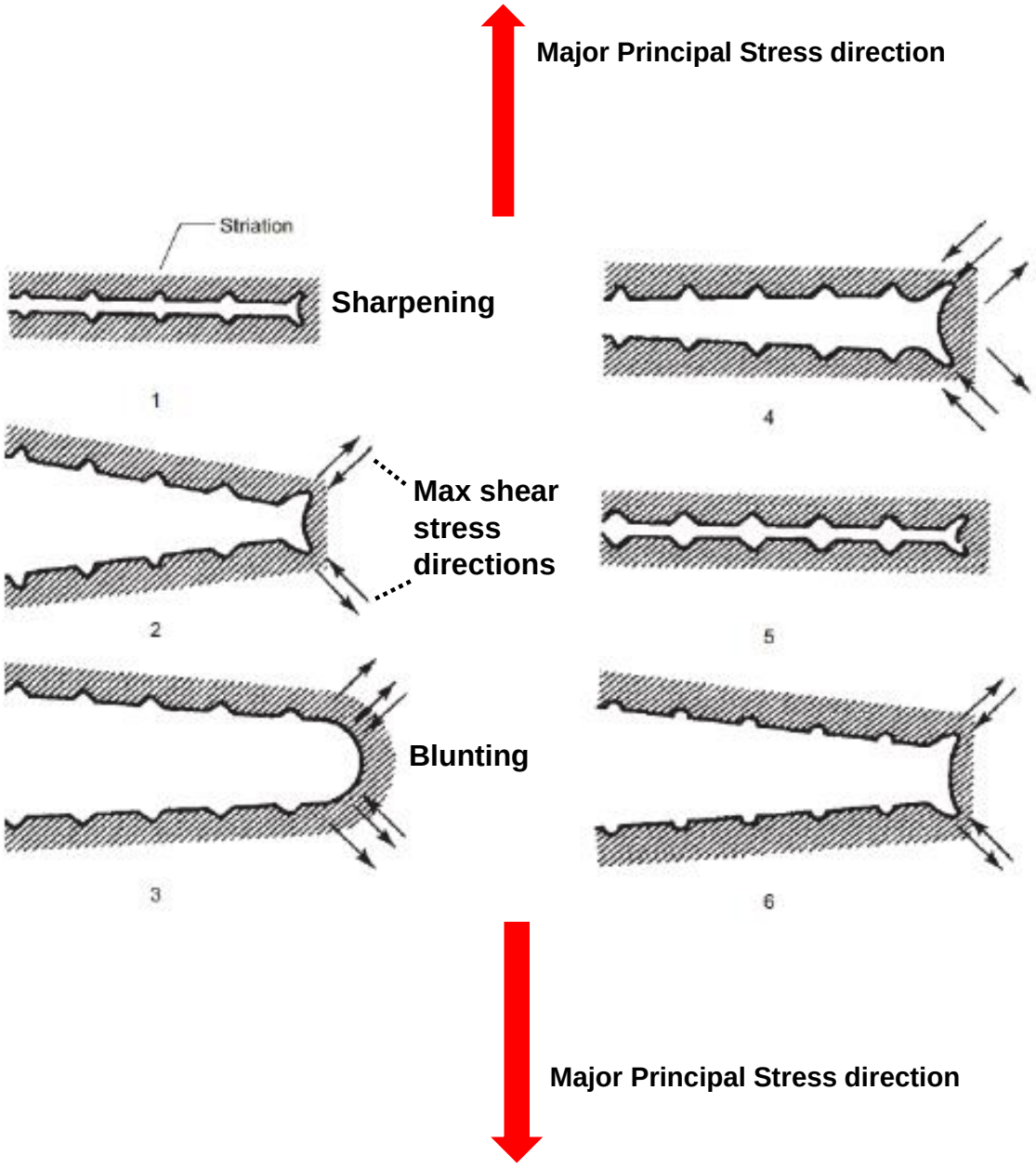

2.5: Fatigue crack growth mechanisms (1) no load (2) loaded (3) maximum load (4) load reduced (5) no load (6) again loaded (Campbell, 2008).

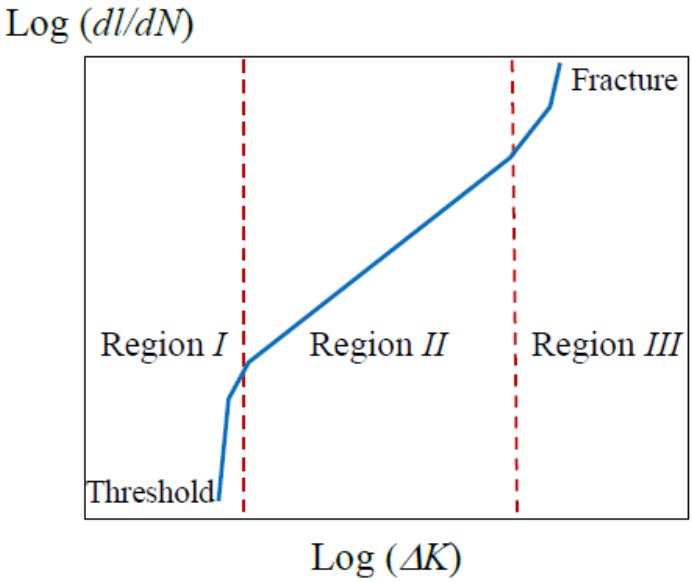

Figure 2.6: Schematic view of fatigue crack growth rate.

The fatigue crack propagation behaviour of many materials can be divided into three regions as shown in figure 2.6. *Region* I, is the fatigue threshold region where ΔK is too low to propagate a crack. $Region\ II$, encompasses data where the rate of crack growth changes roughly linearly with a change in stress intensity fluctuation. In $Region\ III$, small increases in the stress intensity factor amplitude, produce relatively large increases in crack growth rate since the material is nearing the point of unstable fracture.

2.3 Stress Analyses

2.3.1 Introduction

Make-up, preload, axial load, external load with threaded geometry of the connection creates the complicated and complex multiaxial stress and strain distribution which a threaded connection undergoes. Since threaded connections act as stress raisers, cracks can easily be initiated at those locations. Usually the crack initiates in the last engaged thread in the male connection.

The location where highest stresses occur is the region where fatigue failures are found. Accurate knowledge about the stress and strain distributions, the different stress components and multiaxiality of stress is necessary in order to analyse, explain and understand fatigue behaviour fully.

There are two classifications of nonlinearities for analysing the threaded pipe connection: 1) The surface to surface interactions between pin and box cause a small sliding between them and as a result create a nonlinear behaviour. This makes it necessary that the contact properties, in particular the coefficient of friction (COF), are defined accurately. 2) Stress can exceed the material yield strength during make-up stage, which invokes a nonlinear elastic-plastic material response.

Before going into detail about fatigue analysis, an overview is given of stress analysis techniques. These models can be used for evaluating static load cases which in section 5 it will be shown how results from these analyses can be used for fatigue modelling.

2.3.2 Modelling techniques

2.3.2.1 Analytical modelling

The most basic threaded joint connection is bolts and nuts which share similar behaviour to a threaded pipe connection as they have same threaded geometry. The first person who managed to model load distribution between bolts and nuts was by Stromeyer in 1918. His analysis was based on elastic extension of a planar model of riveted joint and ignored the actual threaded geometry. His results show that all the threads do not carry equal load, which mean the load is not distributed equally between them and the last engaged thread of the bolt carries the highest load.

Since it was not possible to measure the appearing stresses accurately at that time, he used a photo-elastic model to confirm his results, it is a strain measurement technique. Stromeyer proposed that the distribution of the load over the thread was dependent on the bending deflections of the threads and relative pitches of nuts and bolt. His proposal was later confirmed by Dragoni (1992). Therefore, it was possible to change the thread geometry in order to optimize the load distribution.

Later research showed that plane models were not sufficiently adequate to describe the behaviour of threaded fasteners. Determination of the behaviour of axial forces as well as circumferential stress induced is very important to this study.

Hetenyi (1997) studied three-dimensional photo elastic models. He found that by changing the global nut shape the load distribution over the thread could be significantly improved; and as a result, the high load concentration on the last engaged thread could be reduced. Additionally, the greatest reduction occurred when tapered thread was used.

As well as the thread bending studies there is a notch effect stress due to the general axial loads in the bolt. Several investigations were performed to study the notch effect of different thread types, root radii, thread angle etc. The results were subsequently catalogued to be used for design purposes. Perhaps the most famous of that work is that of Peterson (1974).

Numerical (FEA) analyses have a number of advantages over experiment techniques. For example, in FEA there is no need of laboratory testing and manufacturing a prototype. Changes and modification can be done easily and numerical and there is no need for remanufacturing of the samples.

The disadvantage of numerical methods is that for complicated geometries the solution might be difficult to find so assumptions are introduced to simplify the problem.

2.3.2.2 Finite Element Analysis

Finite Element Analysis (FEA) is a numerical method for analysing forces within a specimen without carrying out an experiment testing. There has been a lot of research into the FE analysis of threaded connections, mainly two-dimensional modelling and some three-dimensional.

First step in modelling is to start with a 2D model to get an idea of what is happening and to keep the variables to a minimum before modelling 3D. As the bolt is circular it is possible to model it using an axisymmetric model (O'Hara, 1974). Axisymmetric model is a 2D model which is fully rotated around an axis to make it seem like it is 3D. The advantage of this model is that only one slice of it has to be drawn and meshed in 2D. O'Hara corrected the result from the axisymmetric simulation to the Heywood equation which is based on photo elastic data. As a nut and bolt assembly is practically axially symmetric it is possible to just take a slice and model it in 2D. The force transfer between the threads in not straight forward. The easiest way of modelling it is by introducing a layer of elements with orthotropic properties between the nuts and bolt (Bretl and Cook, 1979). The properties of the orthotropic element depend on the geometry and direction of the threads which are in contact with each other. In the work done by Bretl and Cook the finite element analysis results were compared to experimental results presented in the literature and the correlation was good both between tapered and conventional threads. By using contact boundary conditions Assanelli and Dvorkin (1993) analysed the thread.

For this method, nonlinearities must be included in the model to achieve sufficient accuracy. A more popular method introduces interface contact elements (MacDonald and Deans, 1995). The difficulty with contact elements is that a non-linear analysis is required. Interface elements cannot merge and every time they come into contact they try and push each other apart until they come to equilibrium. For this an interpolation method is used. MacDonald increased the mesh density at critical areas to overcome the problem of the non-linear analysis not converging.

The finite element results data demonstrated useful information about thread design, but the accuracy was not perfect due to the lack of contact capability of the finite element software used (NASTRAN). In the case of the nut and bolt scenario an axisymmetric model is not ideal as it does not take the helical thread and the hexagonal nut into account, but can be very useful to calculate individual thread loads (Percy and Sato, 1918). The helix angle in the nut introduces a bending moment which can be accounted for by introducing a bending moment. Hommel analysed two different axisymmetric models to see how different loading affect them (Hommel, 1999). Hommel found that there was only a 4% difference between the two methods and due to the extra time and complications it is better to use the simplified model.

Tanaka et al. researched modelling of threaded connectors. Using an axisymmetric model with contact elements to determine the stress distribution (Tanaka and Hongo, 1981). They extended the studies to look at flange coupling due to transverse loading on the thread (Tanaka, Hongo, 1982). Tanaka used finite element analysis with help of spring models to analyse the loading within a bolt-nut joint with a fastened plate

(Tanaka, Miyazama et al. 1982). The FEA method was used to relate the tensile load within a bolt to the actual service load to assure a good tightening (Tanaka and Yamada, 1986). Zhao also did a lot of work involving FEA and threaded connections. The virtual contact loading method was developed to study the load distribution (Zhao, 1994). Zhao found that the smooth contact method corresponds to the numerical and analytical results but in a frictional sliding contact case it's not so. By increasing computational power efficiency, the accuracy in modelling and analysis is higher. A similar method was used to compare the differences in thread distribution between tapered and straight threads (Zhao, 1998).

Zhao found that with a suitable taper the stress and load distribution in threaded connections can be improved efficiently. Zhao used the same method to find the load distribution in threaded pipes (Zhao, 1996). As mentioned earlier, threaded connections in pipes are very important due to the offshore applications. The traditional thread used in API (American Petroleum Institute) but with the use of FEA a premium threaded connection "FOX" was designed (Yamamoto, Kobayashi et al. 1990).

2D analysis can represent the load distribution in a threaded connection but it was shown that the thread pitch effects on the solution are significant when compared to a 3D model (Rhee, 1990). This can be up to 20% so even though the 3D analysis is more expensive in some cases where accuracy is essential the 3D model should be used. But now these days computation FEA is much cheaper.

3D FEA requires very high computational power which usually involves high costs, and due to this reason only a handful of people have researched this topic further. Bahai (2001), mentioned earlier is one of these people. Using PATRAN, the two-dimensional model was rotated around using a transfer function to give a full three-dimensional model (Bahai, Esat et al. 1992). ABAQUS finite element program was used to analyse the model consisting of isoparametric and interface elements. The results were compared to a so-called hybrid model which consists of bending element that uses spring constants. The stresses from the 3D model showed slight variation around the circumference. This discrepancy however is minimal at the critical site where a failure is likely to take place, hence the cost of the 3D model is may not be justified.

In a pressure vessel, the 3D threaded connection was modelled using MSC/NASTRAN (Grewal and Sabbaghian, 1997). On the connect surface adaptive frictional element (GAP) were used in order to account for the various levels of friction. The model was divided into 45 degree segments as in the full version only four fully engaged threads could be analysed due to lack of computational power. Tafreshi analysed drill string threaded joint using the IDEAS package for modelling and ABAQUS for the finite element analysis (Tafreshi and Dover, 1993). Different scenarios were analysed including bending and torsion. For the torsion scenario, the contact element was changed to a continuous mesh, allowing linear analysis. For bending the 2D model was rotated, corresponding with Bahai and Esat (1992). Tafreshi's results of the finite element analysis have been compared with full-scale fatigue test results on similar joint sizes, and generally showed good agreement. Later

Tafreshi improved these models by introducing SAXA element and Fourier interpolation, but the helix angle was still ignored (Tafreshi, 1999). It was shown that using axisymmetric solid elements with non-linear, asymmetric deformation with Fourier interpolation reduces the computational time and modelling and increases accuracy in comparison to full 3D analysis.

The above listed 3D attempts of modelling threaded connections using finite element analysis have all used some sort of an assumption or simplification. Most recently Zadoke and Kokatam have managed to create a model, which is fully three dimensional and helical. Using contact elements (Zadoke and Kokatam, 1999) the thread was modelled separately from the body of the bolt and nut, and were joined together using fixed contact. This allowed consistent meshing between the thread and body. The contact scenario was modelled in FEM code, and using PROTON3D algorithms it was solved. The connection was then modelled in a dynamic situation. Both analyses require high computational powers are very expensive. They have found that helical threads can be modelled accurately using PROTON3D dynamic analysis and that the result correlate well with empirical values (Zadoks and Yu, 1997). The result was also compared with hand calculations and it was found the good agreement could be achieved using dimensions that were selected based on the FEM results.

2.3.2.3 Numerical methods

In term of threaded connectors, the first real analytical findings were done by Sopwith (1948). Sopwith identified that the loading along the thread is not uniform and that the force on a single thread is concentrated at mid-depth. Sopwith also realised that the maximum load which is at the first thread in a compression scenario is about 4 times as big as the mean loading on the threads. By changing the thread profile, it is possible to make the load distribution more uniform. Using Sopwith and experimental work Miller and Marshek (1983) developed the two-dimensional spring model theorem. The spring model idea is based on the assumption that a thread connector can be divided up into a series of springs that interact with each other. Depending on the material properties and the profile of the thread these spring constants may change (Wang and Marshek 1995).

The spring model was then adapted to different threaded applications. As it was mentioned before tapered threads are used to make the load distribution more uniform. It was shown using analytical methods that there is a significant improvement in the order of 2 to 1 by tapering the thread (Stoeckly and Macke 1952). Analytical studies into threads used in pipes offset the high cost of fatigue testing (Libster and Glinka, 1994). Using numerical methods, it was possible to determine the fatigue life of an offshore pipe. Lulea University research established the load distribution of coupling sleeve type joint (Lunderg, Beccu et al. 1989). This type of joint consists of a cylindrical coupling sleeve with an internal thread which is used to connect two drill rods. The numerical model disregards the wave motion of the sleeve and only accounted for the axial movement in the sleeve. Assumption like this simplify the numerical model but can introduce error and make the model less real. The spring model can be modified in such way that it can be applied to a knuckle shape threaded

joint (Daabin, 1990). These joints are used to transfer high loads in power switchgears. In further studies, sinusoidal and impulse loading was applied to look at the effect of thread loosening (Daabin and Chow, 1991). In these dynamic models the finite difference method was used. Only axial displacement was taken into account. Due to the helix angle and the shape of the thread, there are bending forces acting on a nut and bolt assembly. These tangential forces can be found using numerical methods (Yazawa and Hongo, 1988). These forces contribute to thread loosening. When a nut is under loading, it is subjected to radial deformation (Hosokawa, Sato et al 1989). Hosokawa calculated the radial deformation of the nuts and verified it using experimental methods. In these results, it was shown that the calculated radial displacement of the nuts almost agrees with the measured values, expected in the high nut whose distribution of the load at the mating threads is considered uniform in the bolt-nut unit. The results were also compared to Goodier's report on load distribution (Goodier, 1940). Goodier's measurements showed similar tendencies to the calculated values in Hosokawa's work.

Numerical studies are used to calculate the maximum strength of certain designs. Using the Alexander theory (Elster, J., 1989) it is possible to find the maximum load ability of a bolt and nut assembly (Hagiwara, Itoh et al. 1995). Such calculations are useful when redesigning nuts and trying to keep them safe. The results show that the height of the nut has to be at least 40% of its diameter for it to be effective. The calculations were verified using experimental techniques carried out with accordance to the British standards and it was found that the results were consistent on the whole, with despite some exceptions.

Bahai and Esat spring model is an accurate way of modelling the loading in threads. For the spring model to work the spring constant have to be specified accurately. If the material properties are known, then the spring constant for the nut and the bolt is found by working out the volume and using Young's modulus. To find the spring constant for the actual thread is more difficult as it involves a contact between two surfaces. To overcome this problem Finite Element can be used. By only modelling the thread no model is required for the rest of the assembly, keeping the number of element to a minimum. Bahai and Esat (1991) converted the spring model into a matrix and used FEA to find the spring constant for the thread. The model used for the thread was an axisymmetric model with interface contact elements. The result between the spring model and finite element analysis showed a very good comparison. Bahai then introduce bending element to compensate for the helical thread, and make the model like if it would be three dimensional (Bahai, Esat et al. 1992). Introducing bending element meant a slightly more complicated analysis but improved the accuracy of the result.

2.3.2.4 Semi-analytical models

Threaded pipe connection could be modelled in more detail by finite element analysis since 1980's. Modelling a full nonlinear 3D connection would not be possible at that time due to limited computational performance and power. Hence, threaded pipe

connections were evaluated using hybrid models (Glinka, Newport, Brennan). This technique combined a finite element model with analytical calculations was applied by Glinka et al in 1986. Using a finite element model of three threads subjected to different load cases, a plot of stress concentration factor versus tensile load was obtained and the threads bending stiffness calculated. This bending stiffness was then used as an input in the analytical model to obtain the load distribution in the connection over the different threads. The corresponding stress concentration were calculated using the previously obtained stress concentration plots and load distribution. The calculated stresses were used in a fatigue analysis of buttress threaded connections of tendons for tension leg platforms. By using this technique, Newport (Newport,1989) and Brennan (Brennan,1992) show that shouldered threaded pipe connections with taper threads behave in a similar way as preloaded bolts and nut. The dynamic load on the thread significantly changes by preloading and this can be achieved in two ways; using a torque shoulder or assembling a tapered connection with a certain torque. In the case of a shoulder, the load distribution over the threads closest to the shoulder will receive the preload. Additionally, they found that there is an optimum in the connections number of engaged threads. An optimum number of thread connection between pin and box is very beneficial as a connection without sufficient threads will have a very high load carried by the last engaged thread of the pin, while a connection with more than the optimal number of threads does not get any benefit from the additional threads. Using this technique allowed elastic-plastic material models and introduction of cracks (Zhao, 1994), while limiting the computational requirements. Additionally, the influence of thread parameters could easily be studied because this only required changing the finite element model of the threads without changing the global analytical model. Bahai (2001) generalized the hybrid method by constructing parametric equation based on a large series of simulations. However, this result in empirical equations limited to standard API drill pipe threads.

2.3.2.5 Two-dimensional finite element modelling

2D axisymmetric models became the replacement for the hybrid method because of increasing computing power since 1990. Before then, due to limited computational power and complexity of the contact interaction 3D modelling were not possible. A reasonable calculation time and limited size of the model was one of the advantages of 2D modelling. However, all these advantages were achievable by applying several simplifications. Thread helix were ignored. Since the pitch of the most threaded connections is limited, this simplification was assumed not to have a major effect on the resulting stress distribution. Secondly the thread run-in and run-out region cannot be modelled and hence it is not possible to study these regions in detail. On the other hand, this approach was more versatile then the previous semi-analytical technique and results were in good agreement with observations of photo-elastic models.

A 2D axisymmetric model of API round and buttress connection with an elastic perfectly plastic material model in 1993 by Dvorkin and Assanelli (1993). Additionally, detailed analysis of rotary shouldered connections became possible as was illustrated

by their analysis of a premium connection. Although some basic analysis was carried out using simple linear elastic material behaviour (MacDonald, Bahai), it was pointed out (Hilbert and Kalil, 1992) and Assanelli et al. (1993) that two basic non-linearities had to be incorporated. First elastic-plastic material behaviour should be used instead on linear elastic or elastic perfectly plastic approximations, since the material's yield strength can be exceed even during make-up. Second, surface to surface interactions of the contacting thread surfaces of the pin and box, metal to metal seal surface and torque shoulders result in non-linear contact behaviour. The non-linear aspect of surface interactions are contact sliding and friction. To be able to incorporate all aforementioned aspects in the models, a new element type was created (Dvorkin, 1993). In prior models, contact was modelled by so called gap elements. These elements did not allow for real sliding since the nodes of two contacting elements were tied together by a gap element. When evaluating the failure behaviour of enhanced connections, a third non-linearity arises. To incorporate extreme loads or large displacements, non-linear deformations have to be allowed.

When modelling a connection's make-up, special attention must be paid as it has a huge impact on the accuracy of the result. Rotating the pin and box in simulation is not possible since the model geometry is two dimensional. Make-up is commonly modelled by giving the pin and box a certain radial overlap corresponding to the specified numbers of make-up turns (Abaqus Manual). During the first step of the analysis pin and box are brought into contact and the resulting deformation of pin and box is assumed to be identical to the make-up connection.

The same approach of using 2D axisymmetric finite element models with elastic-plastic material behaviour and elaborate contact interaction of the threads is still used today. A wide range of applications of threaded connections were carried out this way during the last thirty years. Failure of a threaded drilling component were explained by Prinja and Curley (1999) using a non-linear 2D axisymmetric model, although they simplified the exact geometry of the threads. A number of investigations were performed to future understand and behaviour of standard connections. API round casings were studied in 2003 by Dvorkin and Toscano (Dvorkin, 2003) and later by Yuan et al. (Yuan 2004, Yuan 2006). Comparison is given between the simulated strains and strains measured by the strain gauges during experimental tests and found a good correspondence, thereby demonstrating the applicability of 2D axisymmetric models. Standard drill pipes were modelled by Kristensen et al (2005), Bertini et al. (2006) and Santus et al. (2009).

Several studies on enhanced connections have been published. Since those connections are designed to work under extreme loading conditions, the analysis is not only limited to axial tension. Enhanced casing are typically subjected to high internal and external pressure, hence these load case are included in the models (Santus, Takano, Enhanced Joint, Zhong). Strain gauge measurement on enhanced connections have been carried out during male-up by Hillbert and Kalil (1992) and for additional axial loading and internal pressure by Dvorkin et al. (1993) both obtained a good agreement with their corresponding simulations.

The main differences between standard and enhanced designs are that the later designs include features as rotary torque shoulders, metal to metal pressure seals, and elastic ring seals and use non-standard thread types which are in many cases modified buttress threads. Premium connection uses specific required thread where sealing the pressure is not necessary, where as the standard uses thread type as well as sealing the pressure. To minimize relative sliding and separation between the threads buttress thread had been modified to have small or even negative load flank angles. This modification makes the buttress thread a better thread compared to standard triangular or API round thread as it is more resistance to jump out failure. On the other hand, the leak tightness of enhanced designs is generally realized by providing diametral pitch interference between metal to metal seal faces.

Drill string pipe during operation in wells are subjected to high bending loads. During installation the casing is exposed to high bending. This kind of bending load it is not possible to be simulated by axisymmetric models.

MacDonald and Deans (1995) showed that when the wall thickness to diameter ratio is small, it can be represented by a uniform membrane load (see figure. 2.7).

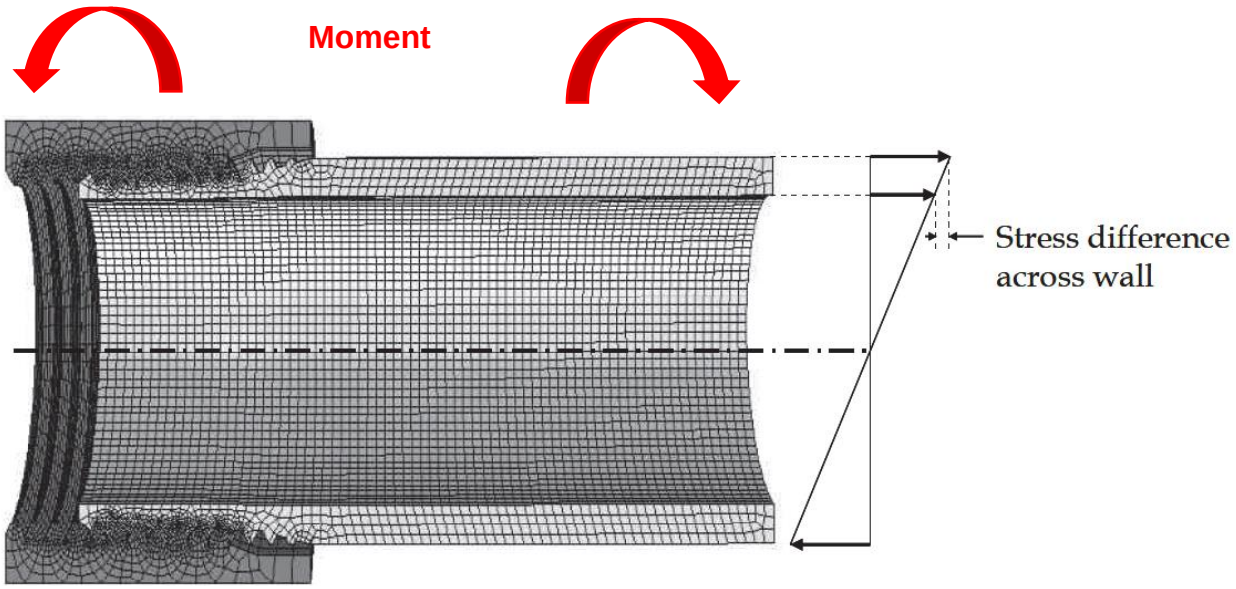

Figure 2.7: Through wall distribution of the stress in a pipe under bending. (MacDonald and Deans, 1995)

On the other hand, modelling bending in a 2D Axisymmetric model, special solid elements can be used that permit non-linear asymmetrical deformation (Takano, 2002, Zhong, 2007, Sugino, 2010, Tafreshi, 1993).

2.3.2.6 Three-Dimensional finite element model

The only way to model bending load on threaded pipe connection is in a full three-dimensional form. Since 1990's the computer performance increases, but a full 3D models of threaded coupling still require very long calculation times due to the high

number of nodes in the contact analysis. In addition to this, due to their complexity and multiple contacting surfaces, full 3D models tend to be less stable and less convergent. 3D simulations are commonly oversimplified by using linear elastic material properties Shahani (2009) or very coarse meshes Placido (2005). This has resulted in inaccurate stress distributions and spurious mesh dependent stress concentration factor without practical use.

A 2D axisymmetric model of threaded pipe connection are in good agreement with a full 3D models but make-up situation was taking to account by Zhong (2007). Further research Chen and Shih (1999) had indicated that for axially loaded bolts 2D axisymmetric models are a very good approximation to calculate the real 3D stress distribution. Therefore, for axisymmetric load situations as make-up and axial tension, a 2D axisymmetric model can be used. A bending load applied on an enhanced threaded and coupled (T&C) connection was modelled in 3D by Sches et al. (2008), but only with elastic material behaviour. The bending of a standard shouldered drill string connection, has been analysed (MacDonald and Deans, 1995) but with simplified modelling of the make-up stage.

Full 3D models are only used in special case where the influence of thread run in and run out or thread helix are studied or when special load cases are examined as due to their high degree of complexity. Calculation times can be more than 30 times higher than those for 2D axisymmetric models and as in most cases only limited additional results are generated. In all other cases, a conventional 2D axisymmetric model is the preferred modelling technique.

2.3.3 Considerations

2.3.3.1 Contact modelling

It is very important to use the right contact in analysis as it has a direct effect on results. Applying the correct contact interaction requires very accurate knowledge about the contact interface properties, e.g. the coefficient of friction (COF). However, there are different COF values which can be used. In ISO 10407-1 (ISO 10407-1) values are specified between 0.06 and 0.14, mentioning a typical value of 0.08 when thread compounds are used. Assanelli & Dvorkin (1997) and Yuan et al. (2004) even use a lower value of about 0.02. In experiment studies friction values between 0.06 and 0.09 were obtained by Ertas et al (1999) for tests on pipeline steel with different thread compounds and Santus et al (2009) measured values of 0.15 during torsion test in full scale threaded connections.

2.3.3.2 Stress concentration factors

The hybrid technique allowed for stress appearing at the thread roots to be calculated. Typically, the highest stress appears at the root of the last engaged thread (LET) of the pin for threaded connections without torque shoulders. In Table 2.1 some typical

values of stress concentration factor (SCF) at the LET of the pin are given for threaded connections as obtained by analyses with elastic-plastic material behaviour.

Table 2.1: Typical values of stress concentration factors.

Connection type	SCF	Source
Premium riser connection	1.8	Sches (Sches 2008)
Metric Bolt	3.7	Shoji et al. (Shoji 2010)
Drill Pipe	5.6	Ferjani (Ferjani 2006)

2.3.4 Discussion

The 2D axisymmetric and 3D FE studied in all consider only one or sometimes two or three distinct connections. In some cases the results of enhanced design are compared to the results of a standard connection, but no qualitative or quantitative comparison between a wide range of design features nor a parametric study has been published in open literature. This is the reason why there are no general design rules available for threaded connections and why the influence of several design features on the overall behaviour of the connections has not yet been documented in detail. This is mainly because commercial enhanced connections are protected by patents. The patent documents, which are freely available in the public domain, only contain claims and the general ideas behind the patented features. No detailed analyses are published as the companies that developed the connection otherwise risk losing their competitive advantage. Nevertheless, even without quantifying the effects, a broad patent overview can identify trends to obtain a certain improvement of the connection's behaviour. This overview is provided in the next section.

2.4 Patent Overview

2.4.1 The early days

Threaded connections have been used to couple pipes for over a century. Before going into detail about patented features that improve a connection's fatigue resistance, it can be useful to look at the history of the threaded pipe connection design (Morse, 1882).

It is difficult to define who invented the first modern threaded pipe connection. Although wrought iron fittings had been used before (Morse, 1882), the first patented connection that could be considered as contemporary threaded and coupled connection dates from 1885 and is shown in figure 2.8.

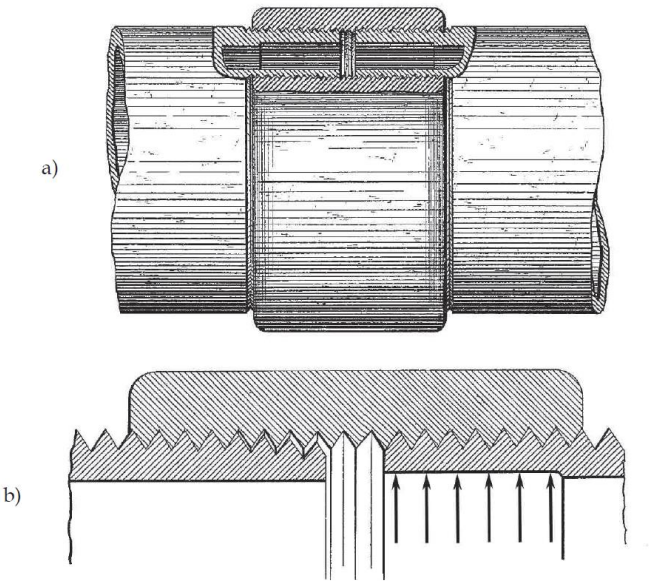

Figure 2.8: Patented connection by W.A. Bole (1885).

This connection and its method of coupling were patented by William A. Bole (Bole, 1885). Unpatented T&C connections existed before. Those connections consisted of a tapered pin and a straight box, since internal taper threads were difficult to produce at that time. The resulting connections consisted of a tapered pin and straight box, since internal connections had only a limited resistance to internal and external pressures. The improvement of Bole's invention consisted of a method to ensure a leak tight connection that would not loosen. To obtain this, the pin should be screwed as tightly as possible into the box, after which the pin's thread surface is radially expanded to take away all clearance between the threads (see figure 2.8b). To apply this plastic deformation a special tube expander was necessary, a device that was patented six month earlier (Bole, 1885). Subsequent patents continued focussing on leak and pressure tightness. Instead of using a pipe expander, Higbee developed a special thread type where material of the threads of the pin would plastically flow in the open space between the threads of the box (Higbee, 1898). Two years later he added special requirements to the thread taper of his developed connection with tapered pin and straight box (Higbee, 1900). Both patented features can nowadays be found in the standard BSPT connections. In following years, more improvements were found to increase pressure tightness. It is notable the most of these patents are based on modifications of the pin of the connection. Several patents propose a special groove to allow for pin plastic deformation (Pistole 1963, Weiner 1970) and new pin designs allow for special shoulder with extra sealing capabilities (Stone,1941).

Although pressure tightness remained to be required, structural strength and resistance against external loads began to gain importance starting from the 1950's. Since oil and gas exploration moved to greater depths and deviated wells, the loads on the pipes and pipe joints increased significantly. Consequently, a joint with the same strength as the pipe, i.e. a joint that is 100% efficient, became desirable. This was obtained by the development of upset connections with increased wall thickness at the threaded portion of the pipe. The first T&C 100% efficient connection was

developed by Webb not earlier than 1956. His connection is shown in figure 2.9a. Its main contribution lays in the fact that the entire thread was engaged, including the last shallow root convolution on the pipe (see detailed thread run out in figure 2.9b). That order the last threads remain efficient, buttress threads were used. It was further stated that the thread should be sufficiently stiff to avoid bending of the threads. Therefore, the width of the threads at the pitch line should be equal to or bigger than the thread height.

Other inventions claimed to improve the resistance to external static loads by enhancing the make-up process of the connection (Ahlstone, 1978) or by improving the load distribution by changing thread profile over the engaged thread length (Van Dar Wissel, 1962).

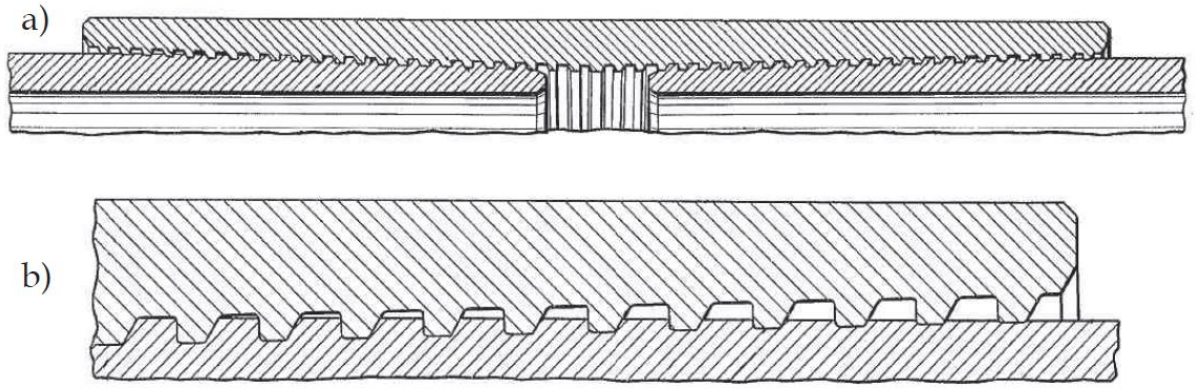

Figure 2.9: First 100% efficient T&C connection by Webb (1956)

2.4.2 Fatigue resistance threaded connections

2.4.2.1 General trends

Starting from the 1960's, threaded connections have been developed which are optimized for the use in dynamic applications. Those fatigues resistant design all try to reduce the maximum stress peaks appearing in the connection. Through all patents two general trends can be identified to achieve this goal. Firstly, the global box geometry is changed to obtain a more uniform load distribution over the threads and hence reducing the high stresses appearing at the LET. It can be noted that to improve the connection's fatigue strength, the box geometry is changed, while in order to improve the pressure tightness of a connection, generally the pin geometry is modified; as explained in section 4.1. The second trend to obtain a fatigue resistant connection is to provide a local modified thread shape. By changing the thread profile, the local stress concentration can be reduced and by altering the thread shape or interference over the engaged thread length, the load distribution can be modified.

2.4.2.2 Global box geometry modifications

In 1961, a new connection was invented (Bodine, 1961) as illustrated by figure 2.10a. This T&C connection was developed to be used in a sonic well pump tubing string. In this application, important fluctuating axial stresses are introduced by the pumping action. Due to the high load carried by the LET of the pin, fatigue cracks would develop at this location in conventional connections. Bodine's connection however, was constructed in such a way that the loads would be distributed more uniformly over the different threads, thereby lowering the concentrated load at the LET of the pin and hence increasing the fatigue life of the entire connection. This improved distribution was obtained by changing the box geometry. In essence, the box of the connection has a bigger wall thickness than the pin and is the most rigid part of the connection.

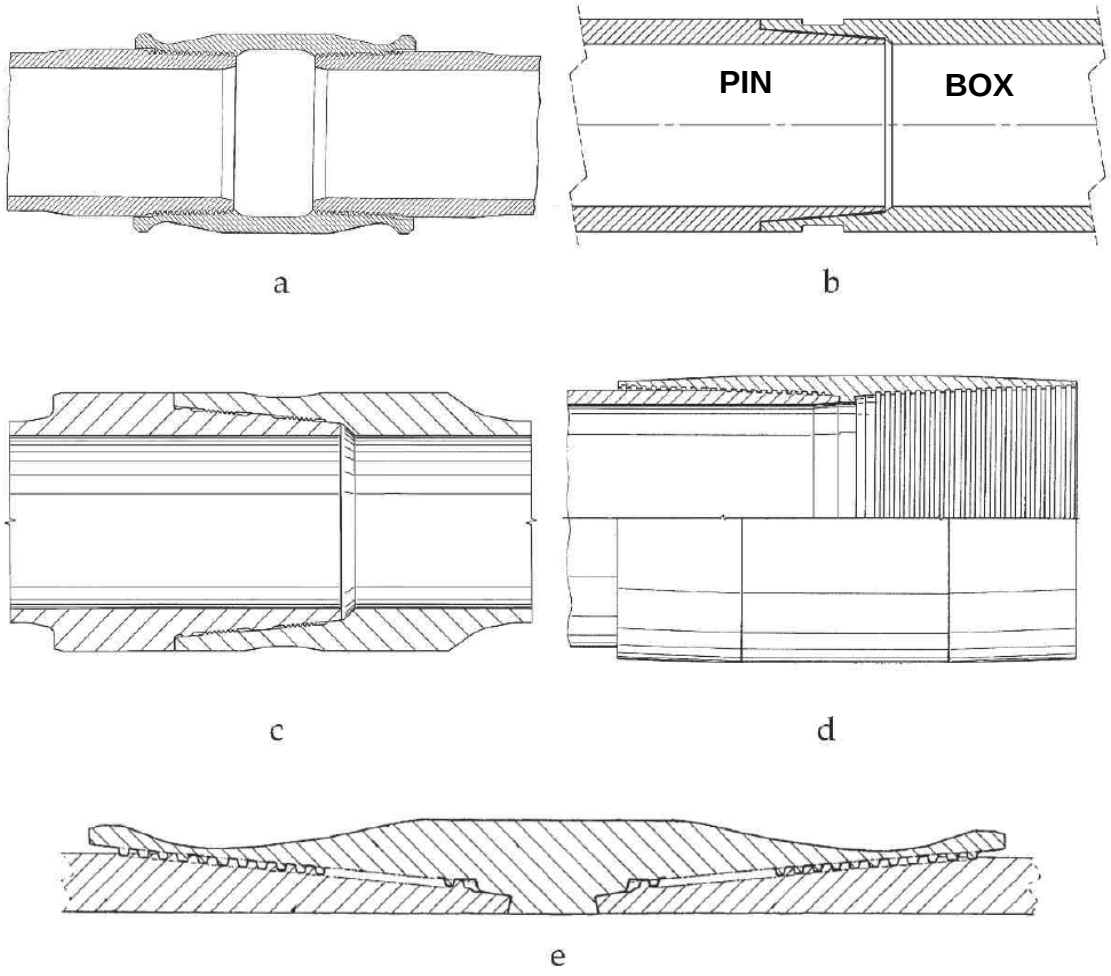

Figure 2.10: Patented box modifications: a) Bodine, (1961), b) Schreier, (1963), c) Galle et al. (2002), d) Delange and Evans, (2003), e) Verdillon, (2004).

However, when reducing the stiffness of the box locally, by applying a grooving in its outer surface located over the last engaged threads of the pin, the box is able to elastically deform and to transfer the load more easily to the adjacent threads.

The same idea of local stiffness reductions to redistribute loads has been used ever since in a variety of other patents. In 1963, an integral drill string connection with a changed box was patented (Schreier, 1963). This connection is shown in figure 2.10.b.

The offshore riser connection of Galle et al. (2002) (figure 2.10.c) used two conical threaded connections. These threaded sections are separated by an intermediate unthreaded region. The central region of the box also carries a recessed groove. Again, this enables a more uniform distribution of the load carried by the two separated threaded sections.

The T&C coupling Delange and Evans (2003) in (figure 2.10.d) claims to provide better fatigue performance by changing the so-called stiffness gradient of the recess region of the box. This modification basically comprises a gradual chamfer of the box that starts over the last fully engaged thread of the pin. Additionally, this design includes a feature previously introduced by Webb (1956). It proposes to apply a long-engaged thread length, including a thread run-out region where the threads are only party engaged. This long-engaged thread region can also be found in the connection of Verdillon (2004) as shown in figure 2.4.e. Which also uses a waisted groove over the highest loaded threads similar to the original design of Bodine (1961). This connection is commercially available and is named the VAM TOP FE connection. Verdillon added the possibility of filling up the machined groove with an elastic filler material, as long as the stiffness of the used filler is sufficiently lower than the stiffness of material of the connection.

2.4.2.3 Local thread modification

To optimize connection threads for fatigue purpose, the thread profiles can be changed to reduce the stress concentration at the thread roots. Additional to this, the thread taper, pitch, interface or tolerance can be changed over the engaged threads to modify the load distribution. Since these modifications generally result in complex thread shapes that require very fine tolerance, local thread modifications can be considered as less robust ways to influence the connection fatigue behaviour. This is because wear or local damage during service can change those tight tolerances and hence eliminate the desired fatigue properties.

Nevertheless, numerous patented thread modifications exist. The so-called Reed-thread developed by Saunders et al. (1985) as shown in figure 2.11.a, is a modified rounded triangular thread. It contains a stress relief groove in the thread root with an increased root radius compared to the standard thread shape to reduce the stress concentration factor. Additionally, the connection contains a pin with a slightly lower taper angle than the box. This results in an artificial change in pitch and radial interference which improves the load distribution, a feature that was also adopted in the sucker rod connection by Ernst and Villasante (2008).

Both Gunderson et al. (1990) and DeLange et al. (1999) proposed a modified buttress thread with enhanced fatigue properties to be used for risers, tendons or drill applications (see figure 2.11.b and c). They both use a zero-degree load flank and increased root radii.

The zero-degree load flank ensure that the axial load on the connection does not produce any significant radial component which would tend to separate the pin and box. An additional modified buttress thread with a positive load flank and optimized root radius (see fig.211e) was patented by Verdillon (2004) (see fig. 2.11.e).

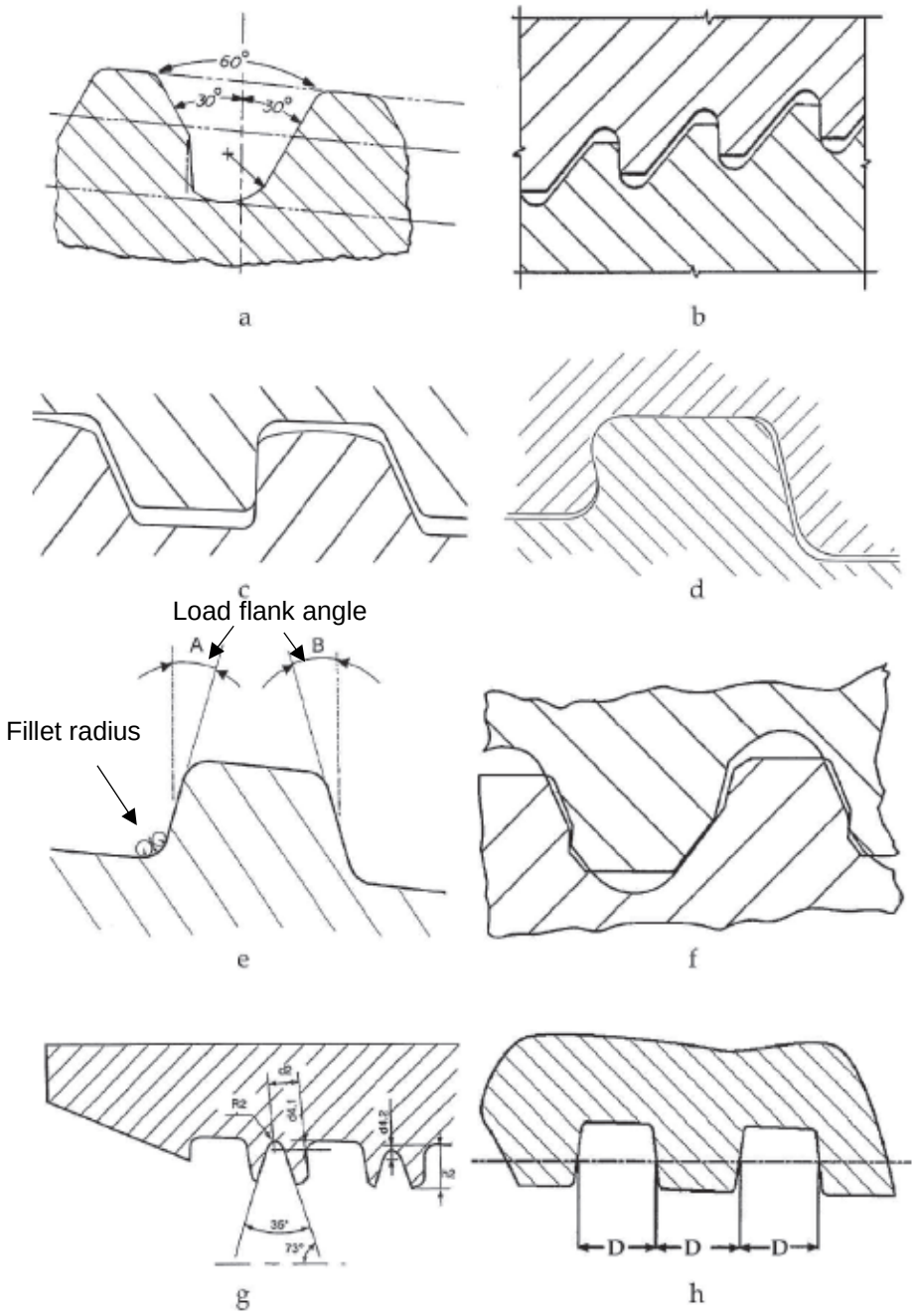

Figure 2.11: Patented Thread types: a) Saunders et al.1985, b) Gunderson et al, 1990, c) DeLange et al., 1999, d) Olivier 2002, e) Verdillon, 2004, f) Pallini et al, 2007, g) Noel and Roussie, 2009, h) Toscano and Di Toro, 2010.

Worth mentioning is that modified buttress threads also exist with a negative load flank. An example of this can be found in the drill string thread by Olivier (2002) as shown in figure 2.11.d. The negative load flank locks the connection together and prevents separation of the threads. Next to reducing fretting fatigue failure, this kind of thread is generally more resistant to yielding and over torque. The Olivier thread type has improved fatigue properties due to the radiused corners of the load flank.

The irregular thread type Pallini et al. (2007) for riser's connections of has an S-shaped load flank that provides a variable load angle depending on the radial position along the contact interface (see fig.2.11f). The thread profile uses a combination of thread cuts that vary in shape and pitch to provide load and stab flanks that vary along the axial length of the engaged threads. Due to the changing interference between the threads, the load distribution becomes more uniform over the engaged length. It is obvious that this kind of threads with varying pitch and profile demands extremely tight tolerance and advanced production tools. This results in high production and maintenance costs since connection repairs can only be carried out be specialized workshops equipped with the required tools. Additionally, the irregular thread shape hinders thread inspection.

Noel and Roussie (2009) developed an additional modification of the buttress thread type. Instead of optimizing the root radii, they provided a portion of the thread with an additional groove in the thread crests as can be seen in figure 2.11.g. The groove is machined only at the first and last engaged threads. The groove reduces the thread stiffness, so the load transfers better to the subsequent threads. The improved load distribution should result in an increased fatigue life of the connection. Nevertheless, the extra groove in the threads makes inspection and repair of the thread more difficult.

The symmetrical trapezoidal thread design of Toscano et al. (2010) for sucker rod connections (figure 2.11.h) provides contact on both the load and stab flank. The diametrical interference created is claimed to reduce thread disengagement and to have improve fatigue properties compared to prior art sucker road connections where only axial interference is applied by using a torque shoulder.

2.4.2.4 Additional fatigue resistant features

Next to the two general trends of improving the fatigue strength of a connection either by changing the global box shape or the local thread shape, some other features are used. The fatigue strength of rounded triangular threads can be improved by cold working in the thread roots, for example by rolling the threads after they have been milled into the connection as was shown by Knight et al. (2003) in their study on drill pipe connections. In that way, compressive residual stresses are introduced at the location where the fatigue cracks tend to initiate, which is beneficial for the fatigue life of the connection. A connection where this introduction of residual stresses is proposed was developed by Benedict et al. (2006).

Stress relief grooves can be used to reduce the stiffness of the connection around the first and last engaged thread locally. This way the load on these locations is partly

transferred to the next threads. Since stress relieved grooves results in a locally decreased wall thickness, they are only used in upset connections which have a bigger wall thickness than the pipe material. An example of a connection with stress relief grooves is shown in figure 2.12.

Metal-to-metal surface are used as seals to prevent leakage, but when the connection is subjected to dynamic bending loads, those seals can have a beneficial effect on the connection's fatigue life. This is because the metal-to-metal seals also provide structural support for the contacting parts and transmit part of the bending load. This decreases the stresses in the threaded region of the connection. In figure 2.13 an example of such a connection is given (Church, 2001). However, as indicated by Santus (2008), metal-to-metal surfaces can also decrease a connection's fatigue life, as fretting phenomena can initiate fatigue cracks in the sealing contact itself.

Another feature that is claimed to provide better fatigue resistance can be found in the patent of Nisida et al. (1980). Although the patent is aimed at bolts, it may be applicable to threaded pipe connections as well. As illustrated in figure 2.14, the last engaged threads of the connection's pin have crest that are cut off. In that way, the last engaged threads of the box will only be partly engaged.

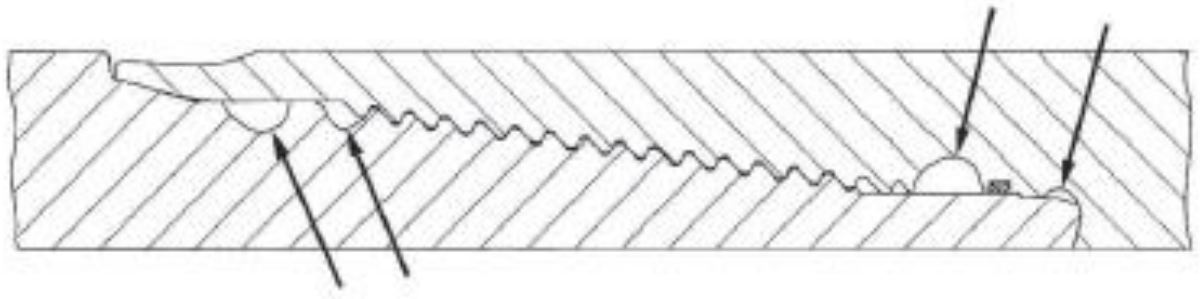

Figure 2.12: Patented connection with stress relief grooves by Pallini 2007, the grooves are indicated by the arrows.

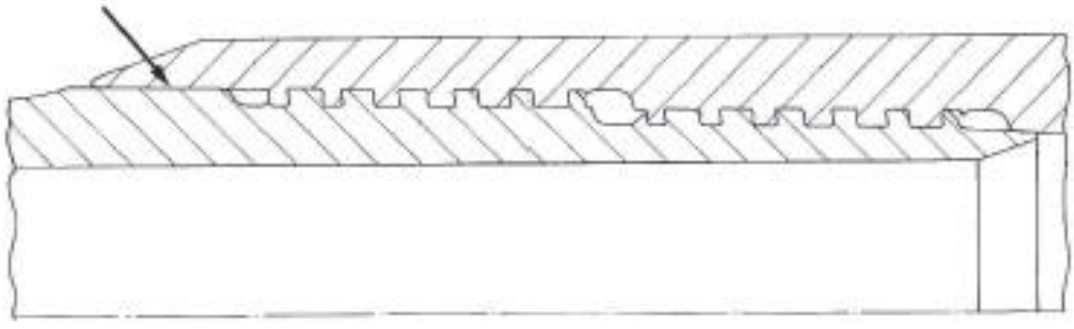

Figure 2.13: Metal to metal sealing surface (indicated by the arrow) can improve the fatigue resistance of a connection subjected to cyclic bending loads (Church, 2001).

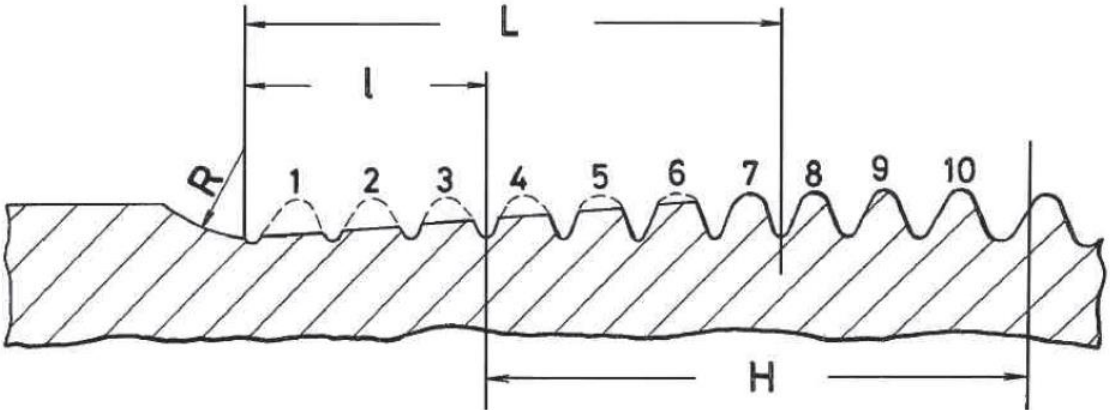

Figure 2.14: Patented thread run out by Nisida (1980).

When subjected to axial loads, the last engaged threads of the box will be bend and the loads will be transmitted to the subsequent threads of the connection. This approach is similar to the threads groove of Noel and Roussie (2009) in figure 2.11.g and the long thread run-out of DeLange and Evans (2003) in figure 2.10.d.

2.4.3 Discussion

From the various designs described above it is clear that fatigue life improvement of threaded pipe connections was studied extensively during the last decades. Numerous patented fatigue resistant connections exist and several are commercially available. However, the information provided in the patent documents concern only general ideas and claims about the resulting performance, but no quantifiable results are published to prove such claims.

Additionally, with this lack of results it is impossible to make an objective comparison between different designs. Moreover, with the lack of parametric studies of threaded connections (see section 3.4), the need for a uniform approach in evaluating and comparing threaded connections has become clear.

2.5 Fatigue Analyses

2.5.1 Introduction

In this section, an overview is given of different fatigue life prediction models. Since it falls beyond the scope of this dissertation to provide a general overview of all existing fatigue modelling techniques, this overview is limited to existing fatigue models relevant for the evaluation of threaded pipe connections. Additionally, the underlying mechanisms of fatigue fracture are considered to be general knowledge.

In the early days, in-service fatigue failure was by ensuring that the stress levels in a component were below the fatigue limit for steel. Generally speaking, for steel no fatigue damage will appear when stresses remain lower than the limit value. This meant that steel components would have an infinite life. Since this results in an

uneconomic design nowadays any metal component or structure is commonly designed for a finite life. This has prompted the development of fatigue models and analysis techniques to predict a component's fatigue life. These techniques can be grouped into the following categories:

- stress life approach
- local strain models
- fracture mechanics
- multiaxial models

The stress life approach was the first fatigue prediction technique to be developed. The technique is generally used to predict the total life of a component. Local strain models, however, only consider the crack initiation life. This approach can be used when crack initiation dominates the total fatigue life. On the other hand, fracture mechanics only deals with the crack propagation stage. When both the crack initiation and propagation stage of a component are important, local strain models can be used in conjunction with fracture mechanics to predict the total fatigue life by simply adding the calculated number of cycles in two stages.

Multiaxial fatigue models take into account the multiaxial stress or strain distribution at notches or crack tips the life predictions have been stress, strain or energy-based. Depending on the criterion, the models predict fatigue crack initiation, propagation or total fatigue life.

2.5.2 Stress life approach

2.5.2.1 S-N curves

The stress-life approach is the oldest among the fatigue analysis techniques. This method was developed by Wohler and is based on experimental observations. The mathematical relations of this approach are derived from the so-called S-N curve or Wohler curve of which an example is shown in figure 2.15. This curve is obtained by subjecting a number of test specimens to fatigue tests at different stress levels. During a single test, the load is fluctuated with a constant amplitude until failure occurs. How failure is defined, depends on the test specimen. For standardized strip or bar-like specimens, failure means commonly total fracture of the specimen, while for tubular specimen's a through-wall crack is generally considered as failure.

The resulting number of load cycles to failure *N* corresponding to the constant stress amplitude S_a applied in each test is then plotted in the *S-N* curve. The number of cycles *N* is plotted on the horizontal axis, with which is conventionally put in logarithmic scale. The normalised stress amplitude on the vertical axis can be either logarithmically or linearly plotted.

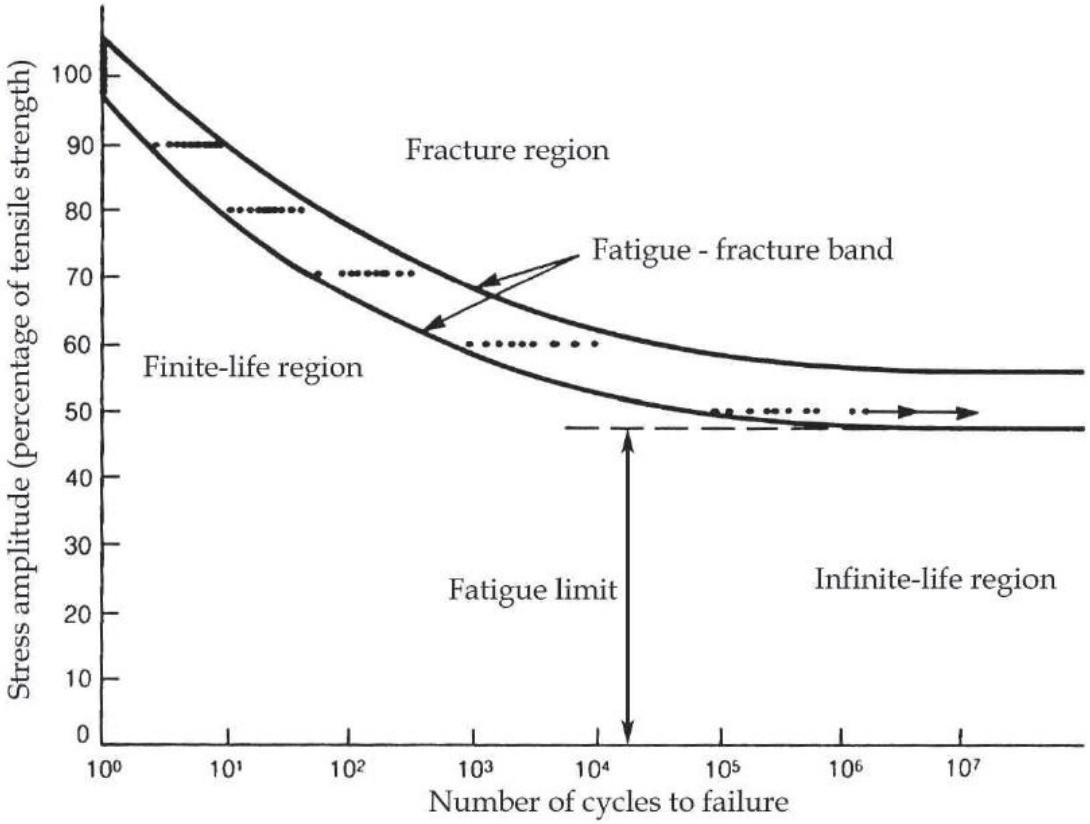

Figure 2.15: Typical S-N curve of a medium strength steel (Boyer 2003).

A typical example of an *S-N* curve for steel is shown in figure 2.15. As can be seen, it starts as a sloping curve changing into a horizontal asymptote with the number of cycles to failure becoming infinite. The stress level corresponding to the asymptote is referred to as the fatigue limit. Since stresses below the fatigue limit would never result in fatigue failure, tests are generally stopped when a certain number of cycles is reached, for example at 2.10^6 cycles.

Fatigue test data are prone to scatter, due to the nature of the fatigue mechanism. Nevertheless, the data can be embedded in a certain fatigue-fracture band where in the probability of failure changes from a low probability next to the finite-life region, to a high probability next to the fracture region. Typically, a mean curve for the finite-life region with a 50% probability of failure is used according to the Basquin relation.

$$S_a^k . N = Constant \tag{2.9}$$

For design purposes a probability of failure of 50% is obviously unacceptable. For this reason, design curve are used which are obtained by subtracting two times the standard deviation from the mean curve which corresponding to a probability of failure of 4.55%.

The stress amplitude to which the fatigue life is related to is generally a nominal stress, since it is derived from the forces applied in the experimental test setup. This has the

advantage that no complex stress analysis is required to evaluate the test specimens. However, this means that results obtained for a specific component cannot easily be extended to a modified component.

Additionally, S-N curves are obtained from constant amplitude test whereas in practice most components are subjected to variable amplitude stresses. To use S-N data for practical load histories, the cumulative fatigue damage model of Miner can be used:

$$D = \sum_i \left(\frac{n_i}{N_i}\right) \tag{2.10}$$

Miner postulated that fatigue damage accumulates linearly. When a component is subjected to n_i stress cycles at a stress which has N_i cycles to failure, then a fraction of n_i/N_i of the total life is consumed. The damage accumulated over the cycles at different stress levels is summed up to give the total damage D. The component would fail if D becomes one. Miner's theory assumes that damage can be superimposed, that the appearing damage is irreversible and that there is no interaction between different stress levels in the sense that it is unimportant in which order the component experience the stress cycles.

2.5.2.2 Probabilistic approach

Different parameters influence the fatigue analysis when it comes to modelling e.g. environment, loading, structural response and fatigue strength. As fatigue strength is generally formulated for constant amplitude stressing, but for more random occurrence of load happening in practice a probabilistic approach is required to define a damage accumulation law. An example of such an approach is that of estimating the fatigue damage of an offshore structure using *S-N* relationship.

2.5.2.3 Cycle counting variable amplitude time histories

Every structure component and mechanical machine experiences its own specific loading sequence. Providing material fatigue behavioural information for every permutation and load sequence is impossible. As a result, most material fatigue properties are obtained at a constant amplitude stress range. Irregular loading sequence therefore need to break down into individual cycles for analysis. The following methods are the most common for this:

1) Range Pair Cycles Methods
2) Rainflow Cycle Counting Methods

Under narrow band variable amplitude loading, the distinction between successive cycles are not possible in the case of broad band loading. The most convenient method is to calculate the root mean square (RMS) and mean stress amplitudes of the time history and treat the loading as its equivalent constant amplitude stress range.

1) Range Pair Cycle Counting

In range pair cycle counting the small cycles are counted first in term of mean stress and stress range. For further analysis, their reversal point which is peaks and valleys are then eliminated. Depending on the diversity of the stress range, this process may repeated a number of times. The result of the count can be expressed in a table of the occurrence of ranges with their corresponding mean values. The range and mean increments can be scaled for more accuracy, however, there will be a compromise between actual accuracy obtained and computational effort required.

2) Rainflow Cycle Counting

A broad band time series is shown in figure 2.16. A series of recorded data is plotted vertically downwards, a water flow is imagined to flow down the record. The beginning of the record is where the flow starts, then at the inside of each peak in the order in which peaks are applied. When it encounters a flow from a higher peak, it stops, a flow from a higher level, or when it reaches the end of the series. Each separate flow is counted as a half cycle, as an example in figure 2.16 there are five and a half cycles. Each cycle will have associated with it a pair of ranges and a mean as before, and can be tabulated similarly. The advantages of rain flow cycles counting is that cycle can be identified as closed stress-strain hysteresis loop.

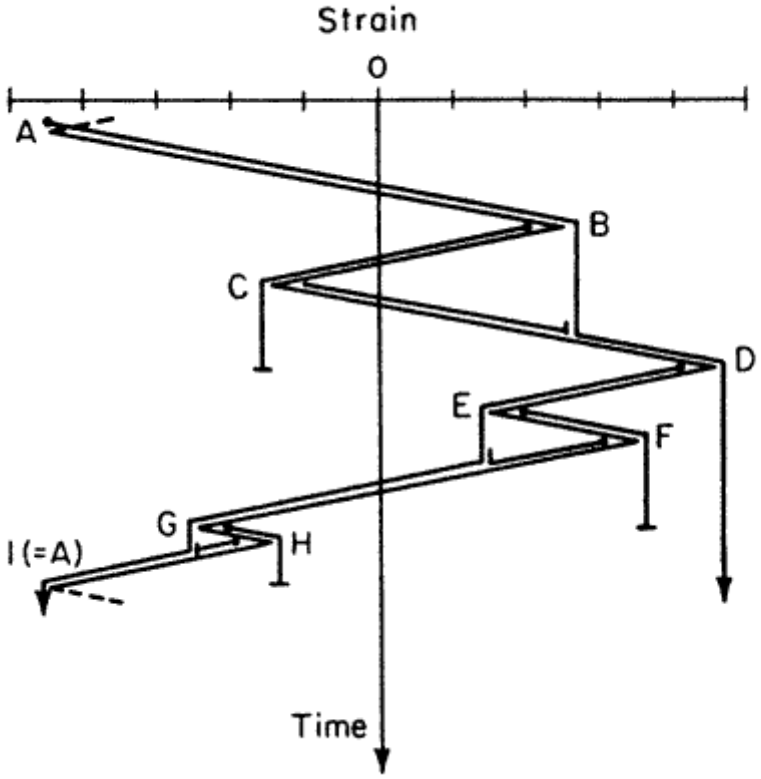

Figure 2.16: Rainflow Cycle Counting (Brennan, 1992).

2.5.2.3 Mean Stress Effect

From the very infancy of fatigue testing it was observed (Wohler, 1871) that the number of cycles to failure depended on the stress range. Furthermore, the stress range require to give failure at any given life decreased as the mean stress increased, more recent work on local behaviour has shown that mean stresses local to a notch tend to relax toward zero in the presence of sufficient cyclic plastic strain (Topper, 1967). Thus, the stress and strain-life approaches detailed above are inappropriate for predicting the effect of mean stress on fatigue life, particularly that of notched components and must therefore be modified.

The earliest representation of mean stress effects was by Gerber equation (2.11) (1874), who proposed a parabolic relationship between the semi-stress range and mean stress based his analysis of Wohler's data:

$$\frac{\Delta\sigma}{2} = \sigma_e \left(1 - \left(\frac{\sigma_m}{\sigma_U}\right)^2\right) \qquad (2.11)$$

where σ_e is the endurance limit, σ_u is the UTS and σ_m is the mean stress.

A schematic parabola is shown in figure 2.17. Goodman noted that experimental data points fell within Gerber's parabola and proposed the following conservative relation for design purposes:

$$\frac{\Delta\sigma}{2} = \sigma_e \left(1 - \left(\frac{\sigma_{mean}}{\sigma_U}\right)\right) \qquad (2.12)$$

The plot of semi-range of stress against mean stress was a direct outcome of Goodman's attempts to analytically express the variation of fatigue strength with mean stress. The result plots as a straight line, figure 2.17, giving a fatigue strength range of zero (when the mean stress equals the *UTS*) to the fatigue limit (when the mean stress is zero). In cases where yielding is undesirable, the mean stress axis limit the *UTS* on the modified Goodman diagram can be replaced with yield stress. In this case the line is referred to as Soderberg line and has the equation (2.13):

$$\frac{\Delta\sigma}{2} = \sigma_e \left(1 - \frac{\sigma_m}{\sigma_Y}\right) \qquad (2.13)$$

In term of local strain, a modification to account for mean stress was proposed (Morrow, 1968) which gives the equivalent zero-mean stress amplitude as a linear relationship similar to the of modified Goodman line but as a function of the fatigue strength coefficient, σ_f':

$$\frac{\Delta\varepsilon}{2} = \frac{\left(\sigma_f' - \sigma_m\right)}{E}(2N_f)^b + \varepsilon_f'(2N_f)^c \qquad (2.14)$$

Equation (2.14) above has been widely accepted as a modification to allow for mean stress effects in assessing fatigue damage at notches.

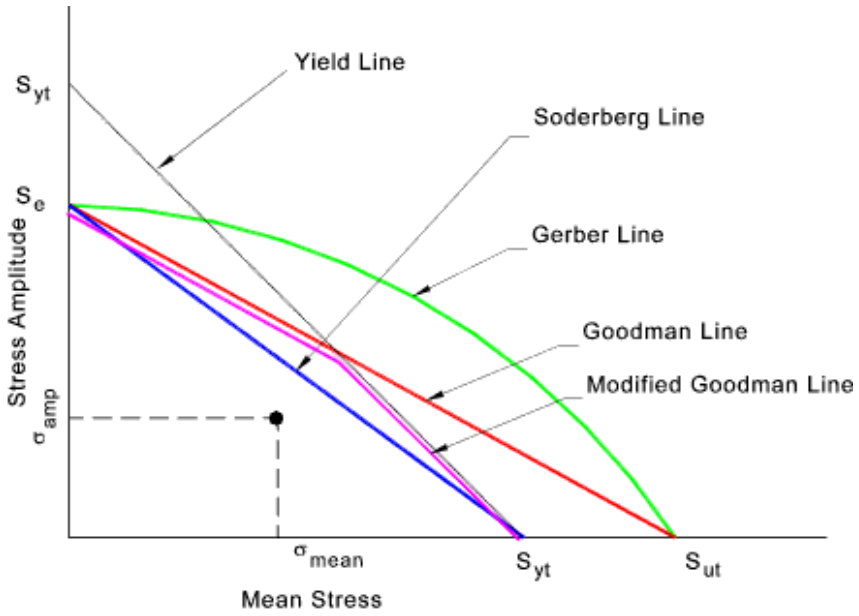

Figure 2.17: Mean stress diagram (Roymech, 2017).

Fatigue tests can be carried out with a fully reversible load with zero mean stress, i.e. a with a fluctuating load with a certain prestress. To make the test conditions clear, a load ratio R as defined by Eq. (2.15) should be mentioned with every *S-N* curve. Where S_{min} and S_{max} are respectively the minimum and maximum applied stress, as shown in figure 2.18. Additionally, S_R is the applied stress range and S_m is the mean stress.

$$\mathrm{R} = \frac{\mathrm{S_{min}}}{\mathrm{S_{max}}} \qquad (2.15)$$

Many *S-N* curves are given for a fully reversible fatigue load with zero mean stress i.e. A load ratio $R = -1$. In order to compare data obtained in tests conducted at a different load ratios, the Goodman Eq. (2.16) can be used to correct the mean stress effect.

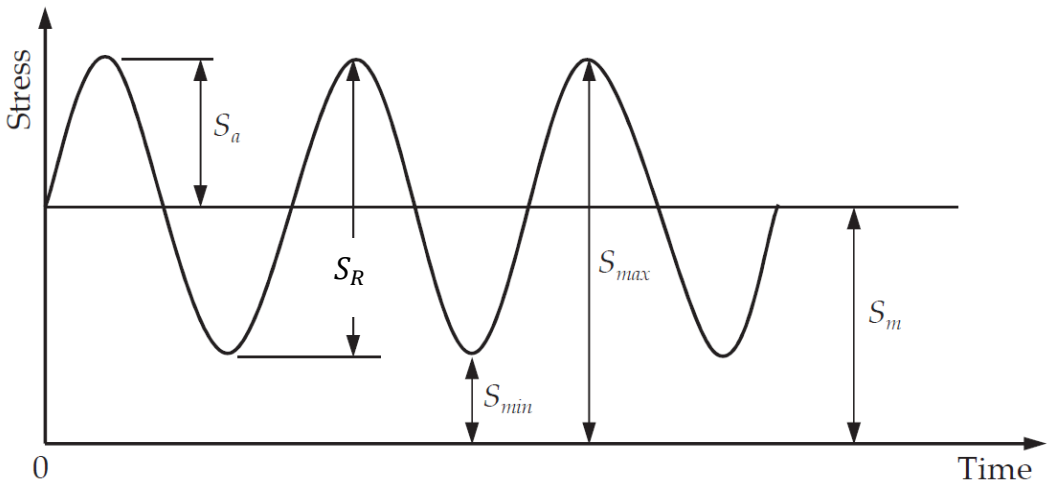

Figure 2.18: Stress definitions.

With this equation, the fatigue stress S_f is the semi-range of stress under a fully reversed cycle $(r_m = 0)$ as fatigue load can be calculated from the applied stress amplitude S_a is calculated from known S_f, σ_{UTS} at given S_m see the graph 2.18a below.

$$\frac{S_a}{S_f} = 1 - \frac{S_m}{\sigma_{UTS}} \tag{2.16}$$

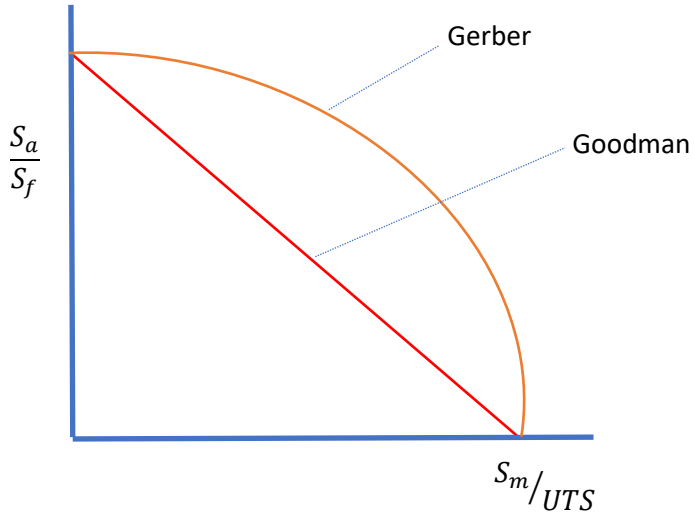

Figure 2.18a: Stress diagram.

2.5.2.4 Stress concentrations

To determine the fatigue life of a machined component, the fatigue data of standard test pieces can be used. However, a real-life component has an arbitrary size with a certain stress concentration, an arbitrary surface finish and an arbitrary loading mode, while standard test specimens have prescribed dimensions and a polished surface. To take all these differences into account, the fatigue stress of the machined component $S_{f,comp}$ can be estimated from the fatigue stress of a standard component S_f by introducing a number of correction factors:

$$S_{f,comp} = k_a . k_b . k_c \frac{S_f}{K_f} \tag{2.17}$$

In this equation K_a is a correction factor for the loading bending mode, since the fatigue behaviour of a component is different when the loads are applied e.g. in tension or bending mode. The factors K_b deals with the size effect, with take into account that the effect of fatigue failure on small standardized specimens can be different from the effect on a bigger structure. K_c is surface roughness factor that relates the results of polished standard specimens to machined parts with higher surface roughness. Finally, K_f is the fatigue notch factor. This can be calculated from the geometrical stress concentration factor K_t by Eq. (2.18) with q the notch sensitivity factor.

$$K_f = 1 + q(K_t - 1) \tag{2.18}$$

when using this technique to evaluate threaded connections based on experimental data of the pipeline steel, one should consider that the factors k_a,k_b, k_c and q are given by empirical relations or charts which means that each single factor is subjected to a certain amount of uncertainty. Additionally, their inputs require measurements of local parameters such as surface roughness and root radii. Next to this, selecting a certain uniaxial loading mode from a complex stress distribution might be an oversimplification. Due to these assumptions and the scatter of every factor, the calculated life might differ significantly from the observed life of the connection.

2.5.3 Local strain models

Local strain models aim to predict the number of load cycles needed for a crack to initiate in a component. Unfortunately, there is no uniform definition of how long a crack must be when initiated. Consequently, the fraction of the total fatigue life taken by initiation depends on the criterion used. In general, this criterion depends on the practical consideration what the minimum crack size is that can be detected with the available measuring technique. Typical size of detectable crack start from smaller than 0.1 mm long using microscope techniques to cracks over 10 mm for example when internal flaws in long welds are sized.

In the local strain approach, it is considered that for a component without initial crack, initiation will most likely take place at the highly stress tip of a notch. Hereby it is assumed that the number of cycles to initiate a crack at the notch tip is equal to the crack initiation in a plane test specimen subjected to the same stress-strain history. Since in notches the local stresses can easily exceed the material's yield strength even if the nominal stresses remain much lower, a distinction is made between elastic and plastic strains. Moreover, the dynamic stress-strain behaviour of a material is different from the quasistatic response.

Hence, a dynamic stress-strain curve is determined using a stable cyclic tensile test. The cyclic stress-strain relation of metallic materials is commonly described by the Ramberg-Osgood equation (2.19). Where $\Delta\varepsilon$ and $\Delta\sigma$ are respectively the local dynamic strain and stress range, E is Young's modulus of elasticity and K' the cyclic strength coefficient and n' the cyclic strain hardening exponent. The first term of the equation is the elastic strain, the second term represent the plastic strain.

$$\frac{\Delta\varepsilon}{2} = \frac{\Delta\sigma}{2E} + \left(\frac{\Delta\sigma}{2K'}\right)^{\frac{1}{n'}} \tag{2.19}$$

Based on the work of Manson and Coffin, the cyclic stress-strain relation can be expressed as a function of fatigue initiation life N_i:

$$\frac{\Delta\varepsilon}{2} = \frac{\sigma_f'}{E}(2N_i)^b + \varepsilon_f'(2N_i)^{c'} \tag{2.20}$$

where σ_f' is the fatigue strength coefficient, b is the fatigue strength exponent, ε_f' is the fatigue ductility coefficient and c is the fatigue ductility exponent. All four terms are

material properties. A typical LCF strain life plot is shown in figure 2.19. The two asymptotes are the different terms for the elastic and plastic strain range.

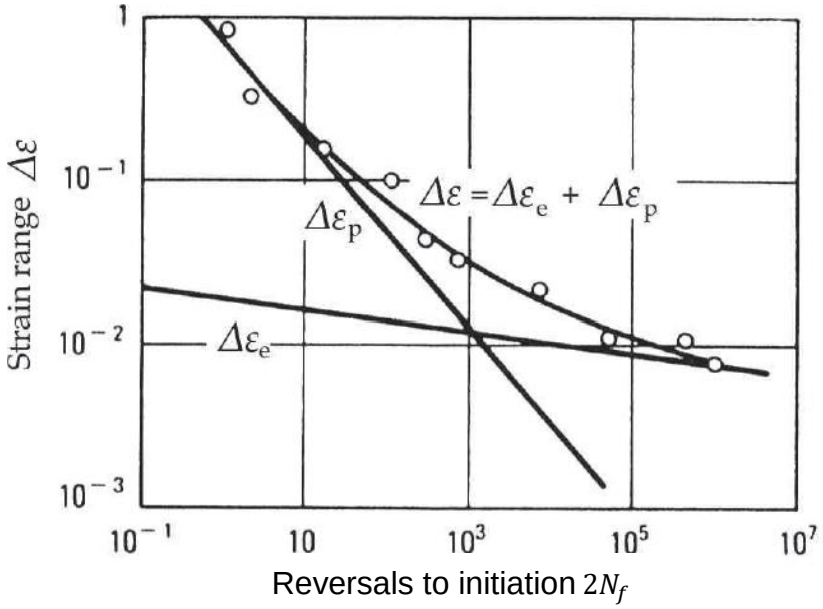

Figure 2.19: Typical Strain range versus cycles to initiation curves (Boyer, 2003).

Equation 2.20 is used to define the material parameters based on experimental fatigue tests of standard test specimens. Once these material parameters are known, a component's fatigue life can be calculated without any additional tests. Allowance for a stress concentration factor K_t appears in the Neuber's rule:

$$\Delta\sigma.\Delta\varepsilon = \frac{K_t^2.S_r^2}{E} \qquad (2.21)$$

Using this rule, it is possible to calculate the local stress range $\Delta\sigma$ and local strain range $\Delta\varepsilon$ based on the nominal stress range S_r. This is done by finding the intersection between the curve described by the equations (2.19) and (2.21). Once the local strain range is found, the fatigue initiation life can be calculated from Eq. (2.20). The difficulty however, in applying Eq.2.21 is to define the appropriate stress concentration factor K_t for practical applications which is not straightforward for the case of preload threaded pipe connections. Next to Neuber's rule, other methodologies exist determine propagation life.

2.5.4 Fracture mechanics

To predict the rate of fatigue crack growth in a component, fracture mechanics can be used. That way a component's crack propagation life can be calculated. When looking at crack propagation under cyclic loading, the parameter ΔK is difference in stress intensity factor which is normally used for evaluation of the crack growth behaviour and is expressed in $MPa.m^{1/2}$. This is the difference in stress intensity factor at maximum and minimum applied load. When experimentally measured crack growth

rate $\frac{da}{dN}$, with a the crack depth, are plotted against ΔK, a typical sigmoidal curve is obtained as shown in figure 2.20. The crack growth rate is generally expressed in μm/cycle.

The curve can be divided into three sections that represent the different regions of fatigue crack growth. The first region exhibits a vertical asymptote at the threshold value ΔK_{th}. ΔK values below this threshold level are too low to cause crack growth. It should be noted that the threshold region is not equal to the crack initiation stage as discussed in section 2.5.3. The crack initiation stage considers the formation of micro cracks only, while fracture mechanics consider pure macroscopic cracks. Even though it is possible that micro cracks initiate at the material surface, it is possible that they are not able to penetrate into the material due to microstructure barriers if ΔK remain below the threshold value. As discussed before, there is no clear size limit to distinguish between micro and macro cracks.

In the region II of figure 2.12 the crack growth rate is described by a power function known as the Paris-Erdogan law:

$$\frac{da}{dN} = C.\Delta K^m \tag{2.22}$$

where C and m are material constants. By rearranging and integrating this equation, the number of cycles can be calculated for a crack to penetrate a given depth.

The third region of figure 2.12 is the stable-tearing crack growth region. In this region, the crack growth rate is high, in the order of 0.01 mm/cycle and above. In this region, a combination of fatigue crack growth and local ductile tearing takes place. Ductile tearing has not yet occurred over the full crack front, but the unstable final failure is imminent. The crack growth life in this region is very limited and hence of less interest for engineering applications. When the maximum crack stress intensity factor appears is exceed the critical value of K_c final fracture take place.

Since $da/dN\ \Delta K$ plots commonly presented with a log-log scale, the power function (2.22) appears as a straight line with a slope m in region II. By fitting the results of an experimental crack growth test on small test specimen, the material parameters C and m can be easily determined, but determining the value of the stress intensity factor K of a crack is often much more complex.

The crack stress intensity factor can be expressed in the general form (2.23).

$$K = Y.S\sqrt{\pi a} \tag{2.23}$$

Where a is the crack depth, S is a chosen nominal stress and Y is a dimensionless parameter which depends on the specimen, crack and loading conditions. A closed form solution exists for many simple geometries. However, when a complex structure is to be analysed, the crack stress intensity factor should be calculated through finite element analysis. Since this requires a very fine mesh around the crack tip and the analysis of different crack depths for a full fatigue crack growth analysis, this technique is both complex and time consuming.

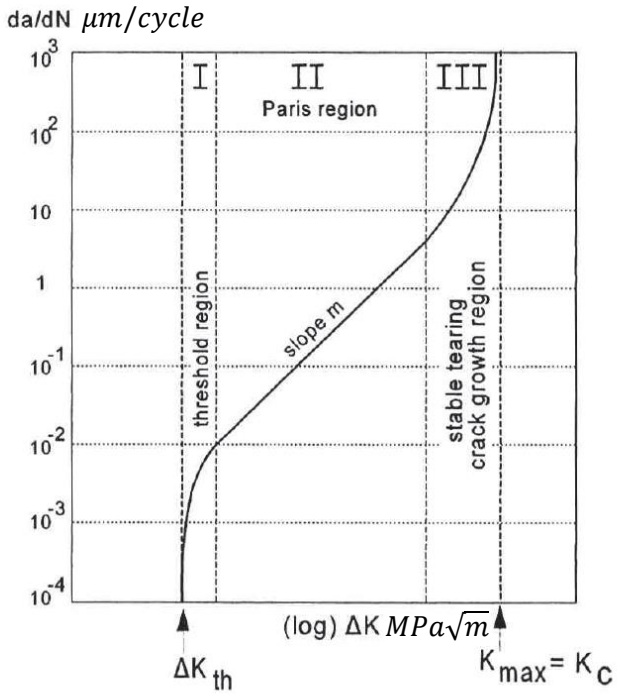

Figure 2.20: Region of crack growth rate as a function of ΔK (Schijve, 2001).

2.5.5 Multiaxial fatigue models

When dealing with a structure subjected to complex loading, the above-mentioned fatigue analysis approaches might not give accurate results since they consider the dynamic loads to be uniaxial. Even in situations where the global acting stress is purely uniaxial, the local stress situation around notches or irregularities can be multiaxial.

To describe such loading more accurately, multiaxial fatigue models were developed. A wide variety of multiaxial fatigue models exist, all with their specific approach and applicability. Nevertheless, they can be classified into two main categories: methods based on an equivalent damage parameter which can be related to stress-strain or energy and methods based on searching for a critical plane. Through the available models, few have been validated against real machine components. Hence this summary is limited to two approaches relevant for fatigue analysis of threaded pipe connections.

2.5.5.1 Dang Van criterion

A method that is widely used for practical applications is the Dang Van criterion (Van, 2013) which is based on a microscopic approach of the critical shearing plane. In this approach, Dang Van postulated that crack initiation may occur in the critical plane of the most unfavorable oriented grains that are subjected to a plastic deformation even if the bulk stress is elastic (Fares, 2006).

Hence the criterion postulates that fatigue damage will appear at a definite time when the combination of local shear stress $\tau\ (t)$ and hydrostatic pressure $\sigma_H(t)$ runs out of the safe region during cyclic loading (as shown in figure 2.21). This criterion can be written as:

$$\max_{A}[\tau(t) + k.\sigma_H(t)] \leq \lambda \tag{2.24}$$

Where A is the studied area, k and λ material parameters that can be obtained by the endurance limits of two fatigue tests, one under reversed bending and the other under reversed torsion. The local shear stress and hydrostatic pressure are calculated according to equations (2.25) and (2.26), with σ_1, σ_2 and σ_3 the principal stresses.

$$\tau(t) = \frac{\sigma_1(t) - \sigma_3(t)}{2} \tag{2.25}$$

$$\sigma_H(t) = \frac{1}{3}[\sigma_1(t) + \sigma_2(t) + \sigma_3(t)] \tag{2.26}$$

Even through the Dang Van criterion Eq. (2.24) does not include predictions for finite fatigue life, using the information from *S-N* curves for loading and torsion the criterion can be extended for this purpose.

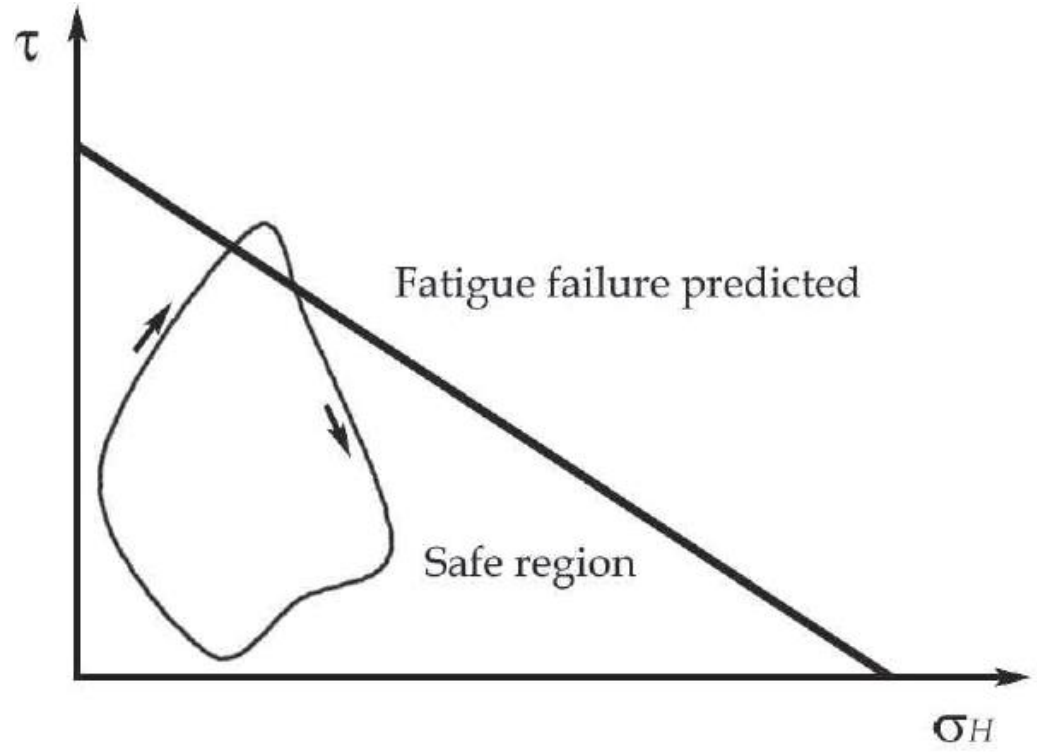

Figure 2.21: Dang Van criterion (2013).

2.5.5.2 Continuum Damage Mechanics (CDM)

Basic concept

The initiation and propagation of micro-cracks and cavities is considered as a damage in materials. At that scale, the damage phenomenon is discontinuous. A continuous variable related to the density of such defects was first studied and introduced by Kachanov (1985). Damage is divided into three categories: fatigue damage, ductile damage and creep damage. A constitutive equation for evolution written in terms of stress and strain by Kachanov may be used in structural calculation in order to predict the initiation of macro-cracks. These constitutive equations have been formulated in the framework of thermodynamics and identified for many phenomena such as dissipation and low cycle fatigue in metals, coupling between damage and creep, high cycle fatigue, creep-fatigue interaction, ductile plastic damage.

The Continuum Damage Mechanics (CDM) theory is based on introducing a damage variable, which is defined as the effective surface area of micro-cracks that intersects with a given plane. The evolution of stress as damage progress describe the damage variable, using the concept of effective stress. The initiation of macro-cracks will take place once the damage accumulated to a critical value. In CDM, failure does not mean fracture, but is a point at which material has sufficiently degraded and continuity of material is lost due to formation of micro-cracks, micro-voids or cavities. From a physical point of view, damage is always related to plastic or irreversible strain and more generally to a strain dissipation either on the meso-scale, the scale of Representative Volume Element (RVE), or on the micro-scale, the scale of the discontinuities. The important element of damage mechanics is described briefly below.

2.5.5.3 Damage variables

Consider a damaged solid in which an element of finite volume has been isolated, of a sufficiently large size with respect to the in-homogeneities of the medium. The element size depicted in figure 2.22a has been grossly enlarged.

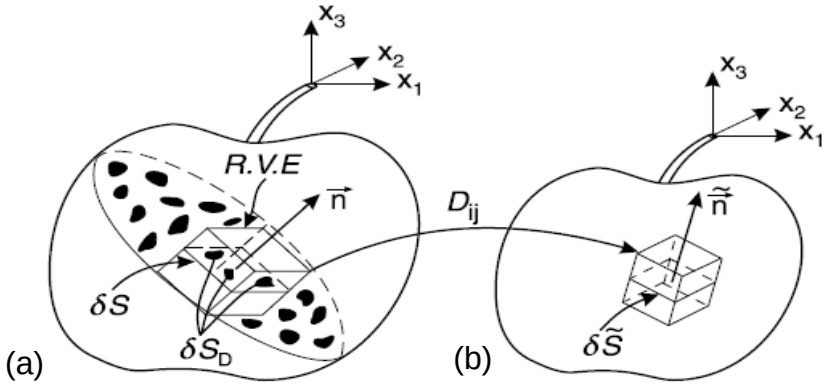

Figure 2.22: Physical damage and mathematical continuous damage (Lemaitre and Desmorat, 2005).

In figure 2.22b, δS is the area of a section of volume element identified by its normal $\vec{n}$. On the section shown in figure 2.22, micro-cracks and cavities, which constitute the damage, leave traces of different forms. By considering $\delta\tilde{S}$ as the effective area of resistance, $\delta\tilde{S} < \delta S$, the stress concentration is in the vicinity of geometric discontinuities between the defects such as micro-cracks and cavities. The effective area can be considered as:

$$\delta S_D = \delta S - \delta\tilde{S} \tag{2.27}$$

Where δS_D, is the total area of defects. Later, it will be explained that using other elements of damage mechanics help to avoid the calculation of total area of defects, which would be extremity difficult to measure due to lack of knowledge of precise geometry of the defects. By definition, the damage variable D associated with direction of normal $\vec{n}$ is:

$$D = \frac{\delta S - \delta\tilde{S}}{\delta S} \tag{2.28}$$

Where $D = 0$ corresponding to the undamaged state, $D = D_C$, where D_c is a critical value, corresponding to the rapture of element in two parts $(0.2 \leq D_c \leq 0.8 \text{ for metals})$ (Lemaitre, 1985). Isotropic damage consists of micro-cracks and cavities with an orientation distributed uniformly in all directions. In this case, the variable does not depend on the orientation of $\vec{n}$ and the damage state is completely characterized by the scalar D.

2.5.5.4 Effective stress

The introduction of a damage variable, which represents a surface density of discontinuities in the material leads directly to the concept of effective stress. The effective stress is the stress calculated over the section area, which resists the forces. Figure 2.23 illustrates the uniaxial case, in which the F is the applied force on a section of the representative volume element, $\sigma = \frac{F}{\delta S}$ in the usual stress satisfying the equilibrium equation. In the presence of isotropic damage, D, the effective area of resistance can be calculated as:

$$\delta S_D = \delta S - \delta\tilde{S} = \delta S(1 - D) \tag{2.29}$$

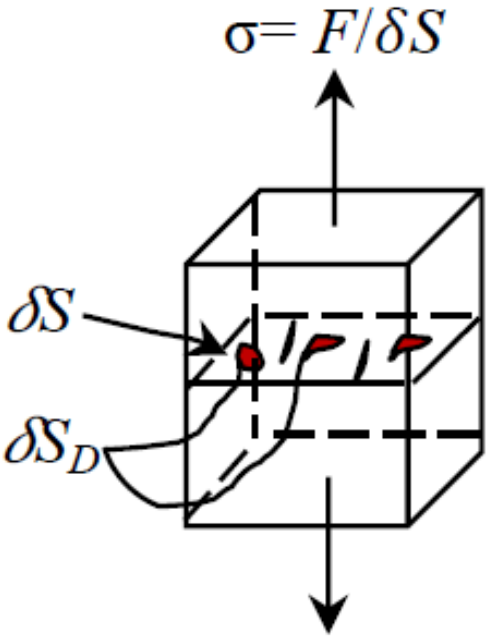

Figure 2.23: Schematic view of concept of effective stress.

According to the definition of the effective stress $\tilde{\sigma}$, it can be calculated as:

$$\tilde{\sigma} = \frac{F}{\delta\tilde{S}} = \frac{F}{\delta S - \delta S_D} = \frac{F}{\delta S(1-D)} \qquad (2.30)$$

Evidently, $\tilde{\sigma} \geq \sigma$, $\tilde{\sigma} = \sigma$ for undamaged material and $\tilde{\sigma} \to \infty$ at the moment of fully damaged material i.e. onset of macro crack initiation.

2.5.5.5 Principle of strain-equivalence

Measuring the effective resisting area is a challenging task. This area can be calculated through mathematical homogenization techniques but the shape and the size of defects must be known, which is somewhat difficult, even with a good electron microscope. To avoid these difficulties, the principle of strain equivalence can be used. It is stated that any strain constitutive for a damage material is derived from the same potential as the undamaged material expect that all the stress variable are replaced by effective stresses (figure 2.24). In one-dimensional linear elasticity:

$$\epsilon_e = \frac{\sigma}{E}\text{, Undamaged material} \qquad (2.31)$$

$$\epsilon_e = \frac{\tilde{\sigma}}{E} = \frac{\sigma}{(1-D)E} = \frac{\sigma}{\tilde{E}}\text{, Damaged material} \qquad (2.32)$$

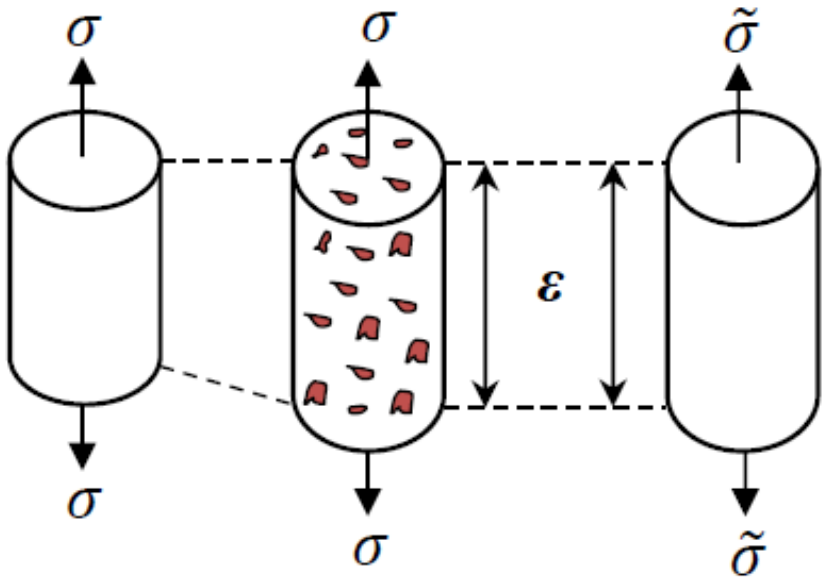

Figure 2.24: Schematic view of equivalence strain concept.

where ϵ_e is the elastic strain and E is Young's modulus. Defining $\tilde{E}$ as the elastic modulus of the damaged material, $\tilde{E} = (1 - D)E,$ the reduction in elastic modulus with the increase in fatigue cycle is shown in figure 2.25. The damage variable is thus given by $D = 1 - \tilde{E}/E$ which can be used to indirectly measure the damage variable D in a process known as the method of variation of elasticity modulus.

2.5.5.6 Thermodynamic approach

In order to model the isotropic phenomena of elasticity, thermal effect, plasticity and damage within the framework of the thermodynamic of irreversible processes, Lemaitre (1985) employed the state variables: total strain ϵ_{total}, elastic strain ϵ_e, and plastic strain $\epsilon_p = \epsilon_{total} - \epsilon_e$. If thermal effects are involved in the damage, the temperature T is introduced as observable state variable with its associated variable, entropy S. The state variable can be defined as observed an internal variable. All these state and associated variables are tabulated in Table 2.1.

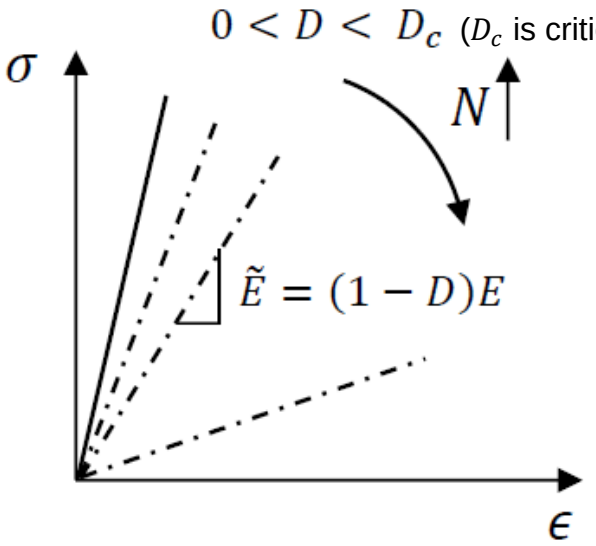

Figure 2.25: Stiffness degradation with increase in fatigue cycles, N.

Table 2.1: Thermodynamics variables.

State variables		
Observable variables	Internal variables	Associated variables
ϵ_e Elastic strain		σ Stress
T Temperature		S Entropy
	P Accumulated plastic strain	R_h Isotropic hardening scalar
	D Damage	$-Y$ Damage strain energy release rate
	V_k	A_k

The state variables, observable and internal, are chosen in accordance with physical mechanisms of deformation and degradation of the material. According to Table 2.1, V_k and A_k can be any internal and associated variables respectively.

2.5.5.7 Damage evolution law

The damage evolution law of Abdel Wahab et al (2001) is a multiaxial fatigue model based on an energy criterion. It is derived using thermodynamic principles, assuming material plasticity at the crack initiation location. Since in the case of threaded connections, plastic deformation can be introduced to the thread roots from the moment the coupling is made up, this methodology can be used for their fatigue life evaluation. The damage evolution law takes into account the multiaxiality of the stress

state at the crack initiation site by introducing a triaxiality function. Accumulated damage is described by the damage parameter *D* given in Eq. (2.33). *D* is 0 for the virgin material and 1 for the completely damaged material. In this equation, a and β are damage parameters and material constant *m* is the strain hardening exponent of the material according to the Ramberg-Osgood relation. $\Delta\sigma_{eq}$ is the difference between the maximum and minimum Von Mises equivalent stress during a load cycle and R_V is the triaxiality function as given in Eq. (2.34) in which σ_H is the hydrostatic pressure.

$$D = 1 - [1 - a(\beta + m + 1)\Delta\sigma_{eq}^{\beta+m} R_V^{\frac{\beta}{2}} N]^{\frac{1}{\beta+m+1}} \quad (2.33)$$

$$R_V = \frac{2}{3}(1 + v) + 3(1 - 2v)[\frac{\sigma_H}{\sigma_{eq}}]^2 \quad (2.34)$$

The number of cycles to crack initiation N, is determine from Eq. (2.33) by assuming a fully damaged situation (*D* = 1). This results in following relation:

$$N = \frac{\Delta\sigma_{eq}^{-(\beta+m)} R_V^{-\beta/2}}{a(\beta+m+1)} \quad (2.35)$$

The damage parameters a and β can be estimated by calculating the correlation between the nominal stress and the local stresses and fitting the results of an *S-N* curve to Eq. (2.35). This makes it possible to apply this method to test results of a real component even if no detailed fatigue properties of the component's material are known.

2.5.6 Practical application and recommended approach

2.5.6.1 Stress-life approach in codes and standard

Due to its simplicity and close relation to experimental testing, the stress life approach is the most widely adopted for the evaluation of threaded pipe connections. Even though the use of a nominal stress to predict fatigue failure precludes an accurate description of local effects at the thread roots, the stress-life approach is adopted by several codes and standards for the design and evaluation of threaded connections. In the BS 7608 standard a design curve with an endurance limit at 2×10^6 cycles is given for threaded fasteners, mainly bolts, subjected to a repeated axial load zero minimum of *R* = 0. As can be seen in Eq. (2.36) the material is accounted for by dividing the applied stress range S_R by the material's tensile strength σ_{UTS}. However, it does not take into account the design or geometry of the threads.

$$(\frac{S_R}{\sigma_{UTS}})^3 . N = 400 \quad (2.36)$$

A different *S-N* curve is provided by the ASME codes and is given by Eq. (2.37) (Rodabaugh, 1983). This relation describes the mean curve of fatigue tests performed on a wide range of welds, fittings and joints and for each type a stress intensification factor i was defined (Mark,1950). This stress intensification factor should not be confused with common stress concertation factors. Markl used the S-N curve of a butt

welded joint as a reference and i describes the relationship between a component and this reference curve. For threaded pipe joints a factor $i = 2.3$ was obtained, which is adopted by the ASME B31.3 code (ASME B31.3-2002). Noting that Eq. (2.37) is a mean curve, a conservative factor of safety of 2 on stress was introduced to obtain the ASME design equation (2.38). No endurance limit is assumed in this standard.

$$i.S_r = 3378.N^{-0.2} \quad (2.37)$$

$$i.S_r = 1689.N^{-0.2} \quad (2.38)$$

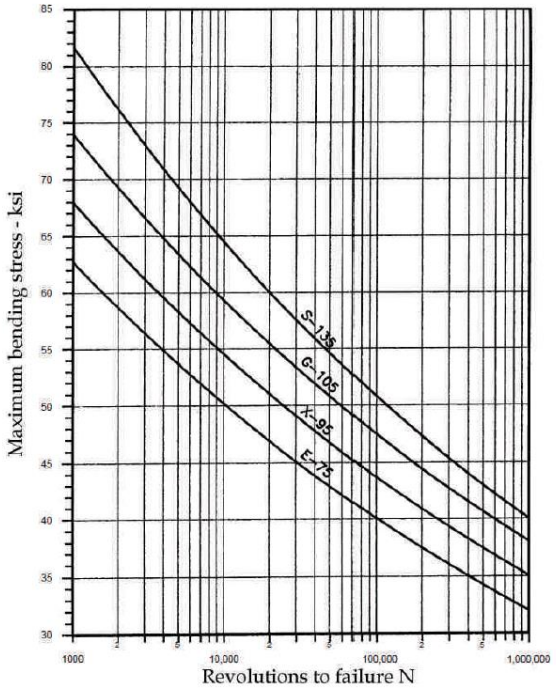

Figure 2.26: Mean S-N curves for API drill pipe connections (American Petroleum Institute, 1998).

In analogy with this approach, number of S-N curves are given in API RP7G (American Petroleum Institute, 1998) for drill pipe connections of different grades. These curves, shown in figure 2.26, can be used for fatigue life calculations of standard API drill pipe joints. The most elaborate specification for the analysis of threaded pipe connections is given by DNV-RP-C203 (Veritas, 2010). In this document, it is recommended to establish a finite element model with contact surfaces on the threads including non-linear material behaviour to allow for local yielding during make-up. A fine mesh is necessary at the threaded roots to describe the stress distribution with sufficient accuracy. By simulating a single load cycle, the local stress range can be obtained. This value can then be used to calculate the stress-life from the *S-N* curve with following equation:

$$S_R = 5151.N^{-0.2128} \quad (2.39)$$

When the calculated stress concentration in the connection is dependent on the load level, it is recommended to use the load that the connection is most likely to experience during the first year of service. Additionally, the results should be supported by experimental test results of full-scale connections. It is noted in the procedure's description based on experience this stress-life approach is more representative for

actual fatigue behaviour than that of the initial strain method which is recommended by ISO 19902 and which leads to overly conservative results. Additionally, a simplified approach is given if a linear elastic finite element analysis is performed. In this case the *S-N* relation (2.40) can be used in combination with the obtained stress range. This approach is more conservative and no experimental validation is required to meet the standard.

$$S_R = 6015.N^{-0.25} \tag{2.40}$$

2.5.6.2 Local strain and fracture mechanics models

A general problem with local strain and fracture mechanics models is that they only describe the crack propagation part of the fatigue process, of crack initiation and propagation phase. This meant that in order to get accurate results, two different models have to be combined. Hence two separate sets of material constants are required, which are generally not available. This was illustrated in the work of Schneider et al. (2010). However, their experimental results were obtained for M10 bolted joint with a solid shaft. This meant that fatigue crack propagation is more important than in the case of threaded connections where the ratio between wall thickness and diameter can be relatively small. As can be derived from experimental results of Newport (1989), the fatigue crack initiation life is about 85% of the total fatigue life for casing connections. However, when looking at connections with a bigger wall thickness to diameter ratio such as drill pipes, the influence of the fatigue crack growth becomes more important to be clear about relative initiation/propagation time. In the work of Brennan (1992) it can be found that the initiation part of the fatigue life can be limited to 10% and less. Hence it should be noted that it is inaccurate to excluding the impact of either crack initiation or propagation from fatigue life calculations without preliminary test results.

An additional complication when using the combination of crack initiation and propagation models is defining the crack size for transition between the two models. Newport (1989) considered a crack to be initiated if it exceeded a length of 2.5 mm. while Brennan (1992) and Schneider et al. (2010) both used the crack depth with critical values of respectively 0.2 mm and 0.1 mm to define crack initiation. This choice depends in most cases rather on practical considerations, e.g. the resolution of the crack sizing technique used, than on fracture mechanical aspects.

2.5.6.3 Multiaxial fatigue models

Multiaxial fatigue models still receive intensive research and new models are developed regularly. But there is no real consensus on what model to use in the case of threaded connections. However, application of the Dang Van criterion was reported in different studies of threaded components. Since the criterion, itself only describes the boundary of infinite life, specific fatigue life calculations are not possible. Therefore, the criterion was extended to encompass finite life calculations. Such an approach was used by Ferjani (2006) in his study on the fatigue life of drill string connections.

When using this approach, first the parameters k and λ from the Dang Van criterion (2.24) are calculated using the endurance limits of the *S-N* curves obtained for the material under cyclic tension and cyclic torsion. The resulting Dang Van relation is plotted as a straight line in a $\sigma_H \; vs \; \tau$ plot. It is assumed that the lines corresponding to a finite fatigue life are parallel to this line. The distance between the lines can be obtained using the *S-N* curve for the material under torsion as shown in figure 2.27.

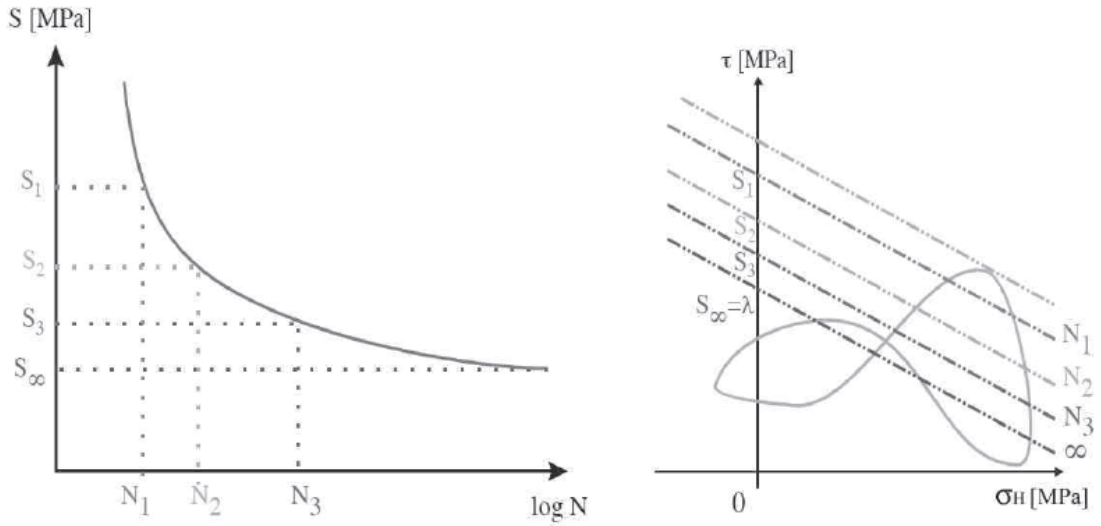

Figure 2.27: Extension of the Dang Van criterion to finite fatigue life calculation (Ferjani, 2006).

A similar approach was used independently by Fares et al. (2006) for the fatigue life calculation of bolts. In their study the *S-N* curve of two bolts under different preloading condition were used to obtaining modify Dang Van's graph, hence obliterating the need for separate material testing and showing the usefulness of this approach for evaluating threaded connections.

2.6 Summary and Conclusion

In this chapter, an overview has been given of the current knowledge on fatigue behaviour of threaded pipe connections. During the last three decades, it is been attempted to improve the fatigue life by changing the connection's global geometry or changing local feature such as the thread type or the interference over the engaged thread length. This resulted in several patented designs. However, it is neither possible to make a qualitative nor a quantitative comparison between these configurations based on published data.

To analyse threaded connections, numerical tools can be used. An overview is given of different analyses for threaded connections that were used in past. Finite element modelling has been identified as the most commonly used method to calculate stress and strain distribution over the connections. 2D axisymmetric models are preferred due to their calculation efficiency compared to full 3D models. However, it is of

uppermost importance to take into account the non-linearities of material behaviour and contact conditions. If not, the data obtained will not represent the real situation. Even though some basic parameter studies were carried out using previous modelling techniques, no parametric studies using finite element models have been published. The finite element model developed in the present research will be presented in chapter 6. This model is constructed in such a way that parametric studies on a connection can reveal the influence of its geometry on fatigue life.

To perform elaborate fatigue analyses different fatigue models are available which use the stress and strain provided by finite elements. The stress-life approach is chosen to present the experimental data obtained by testing, for comparison with results from literature and design curves from standards. However, due to the fact that this approach does not take into account the complex stress distribution at the threads, additional multiaxial fatigue analyses are required.

Since every modelling technique is based on certain assumptions and simplifications, experimental tests continue to play an important role in the design process of threaded connections. Different setups for fatigue testing of threaded pipe connections are compared. They are categorized by the way the load is introduced on the pipe.

The amount of published experimental data is rather limited. Hence, for the present study a strong experimental basis is needed. For this reason, fatigue tests are carried out under axial loading on two different connection sizes. From the above literature review and suggested method in table 2.2 it can be suggested that:

Fatigue life = Initiation + Propagation

LCF (Strain analysis) N_i from Eq 2.20 + HCF (Stress analysis) N_p from Eq 2.37 (typically)

Fatigue analysis Technique	**Advantages**	**Disadvantages**
Multiaxial models	• Described appearing stress concentrations more accurately by considering multiaxiality • Data of S-N curves can be used as an input	• A complex stress analysis is required. • Multiaxial models are less common, which means there is no consensus on what models to use.
Local Strain Models	• A strain-life curve can be used for any geometry. • For a, given material, the results of a set of standard specimens is sufficient, no component testing is required.	• A complex stress analysis is required. Depending on the method used, the obtained stress intensity factor can be significantly different. • Only the crack initiation phase is taken into account, not the total fatigue life. • The required material data is generally not available.
Stress-Life approach	• This technique is broadly used because it is relatively simple and quick. • The total connection life is predicted. • The stress to which the fatigue life is related can be the nominal stress, removing the need for complex stress analysis.	• A large number of tests is needed to produce an S-N curve that relates to one specific connection. • S-N curves can rarely be used for other geometries since results are highly dependent on the used theories and calculation. • No distinction is made between crack initiation and propagation. This information can be required for in service inspection.
Fracture Mechanics	• The local behaviour of crack is addressed. • It can be used for the non-destructive evaluation of remaining fatigue life and for defining inspection intervals.	• A complex stress analysis with several uncertainties is required. • Only the crack propagation phase is considered. • The required material data is generally not available.

Table 2.2: Trade-off of different fatigue analysis techniques.

Reference

- American Petroleum Institute, 1998. *Standard API RP 7G: Recommended Practice for Drill Stem Design and Operating Limits*. American Petroleum Institute.
- ASME B31.3-2002, Process Piping, American Society of Mechanical Engineers, 2002.
- Assanelli, A.P. and E.N. Dvorkin (1993). “Finite element models of OCTG threaded connections.” Computers and Structures 47:725-734.
- Assanelli, A.P.,Xu, Q., Benedetto, F., Johnson, D.H. and Dvorkin, E.N., 1997. Numerical/experimental analysis of an API 8-round connection. *Journal of energy resources technology*, *119*, p.81.
- Axisymmetric analysis of a threaded connection,2006. Abaqus 6.6 Example Problems Manual, Section 1.1.19.
- Bahai, H. and Esat I. I., et al. (1992). “A hybrid modelling approach to 3-D stress analysis of threaded connections.” Engineering System Design and Analysis 1(1): 235-241.
- Bahai, H., 2001. A parametric model for axial and bending stress concentration factors in API drillstring threaded connectors. *International journal of pressure vessels and piping*, *78*(7), pp.495-505.
- Bahai, H., Esat I. I., et al. (1992). “ A hybrid modelling approach to 3D Stress analysis of threaded connections.” Engineering systems Design and Analysis 1(1): 235-241.
- Bahai, H., Glinka, G. and Esat, I.I., 1996. Numerical and experimental evaluation of SIF for threaded connectors. *Engineering fracture mechanics*, *54*(6), pp.835-845.
- Basquin, O.H., 1910. The exponential law of endurance tests. In *Proc. Astm*(Vol. 10, No. 2, pp. 625-630).
- Bertini, L., Beghini, M., Santus, C. and Baryshnikov, A., 2006. Fatigue on drill string conical threaded connections, test results and simulations. In *9th International Fatigue Congress, Atlanta, GA, May* (pp. 14-19).
- Bole, W.A., 1885. *Half to ralph bagaley*. U.S. Patent 331,940.
- Bole, W.A., 1885. *William a*. U.S. Patent 332,184.
- Bole, W.A., 1885.Tube Expander, United State Patent, US 319879.
- Brennan, F.P., 1992. *Fatigue and fracture mechanics analysis of threaded connections* (Doctoral dissertation, University of London).
- Bretl, J. and Cook, R.D. (1979). “modelling the load transfer in threaded connections by the finite element method” international Journal for Numerical Methods in engineering 14:1359-1377
- Campbell, F.C. ed., 2008. *Elements of metallurgy and engineering alloys*. ASM International.
- Chen, J.J. and Shih, Y.S., 1999. A study of the helical effect on the thread connection by three dimensional finite element analysis. *Nuclear engineering and design*, *191*(2), pp.109-116.

- Curley, J.A. and Prinja, N.K., Failure Investigation of an offshore drilling component. In *Abaqus Users' Conference* (pp. 1-14).
- Daabin, A, and Y.M. Chow (1991). " A Theoretical Model to study thread loosening." Mechanism and mechanic Theory 27: 69-74.
- Daabin, A. (1990). " Static and Dynamic Analysis of Knuckle shape threaded joint." Mechanism and Mechanic Theory 25: 225-232.
- DeLange, R.W. and Evans, M.E., Grant Prideco, LP, 2003. *Threaded and coupled connection for improved fatigue resistance*. U.S. Patent 6,609,735.
- Dragoni, E., 1992. Effect of nut geometries on screw thread stress distribution: Photoelastic results. *The Journal of Strain Analysis for Engineering Design*, *27*(1), pp.1-6.
- Dvorkin, E.N. and Toscano, R.G., 2003. Finite element models in the steel industry: Part II: Analyses of tubular products performance. *Computers & Structures*, *81*(8), pp.575-594.
- Dvorkin, E.N., Assanelli, A.P. and Toscano, R.G., 1996. Performance of the QMITC element in two-dimensional elasto-plastic analyses. *Computers & Structures*, *58*(6), pp.1099-1129.
- Elster, J., 1989. *Nuts and bolts for the social sciences* (pp. 410-465). Cambridge: Cambridge University Press.
- Ertas, A., Cuvalci, O. and Carper Jr, H.J., 1999. Determination of friction characteristics of J-55 OCTG connections lubricated with environmentally safe thread compound. *Tribology transactions*, *42*(4), pp.881-887.
- Fares, Y., Chaussumier, M., Daidie, A. and Guillot, J., 2006. Determining the life cycle of bolts using a local approach and the Dang Van criterion. *Fatigue & Fracture of Engineering Materials & Structures*, *29*(8), pp.588-596.
- Ferjani, M., 2006. *INTEGRATION DES PHENOMENES DYNAMIQUES DANS L'ANALYSE EN FATIGUE DES GARNITURES DE FORAGES*(Doctoral dissertation, Ecole Polytechnique X).
- Gerber, W.Z., 1874. Calculation of the allowable stresses in iron structures. *Z. Bayer Archit. Ing. Ver*, *6*(6), pp.101-110.
- Glinka, G., Dover, W.D. and Topp, D., 1986. Fatigue assessment of tethers. *Fatigue and Crack Growth in Offshore Structures*, pp.187-198.
- Goodier, J. N. (1940). " The Distribution of load on the threads of screws." Journal of Applied Mechanics: A10-A16.
- Grewal, A.S. and M.Sabbaghian (1997). "Load Distribution between Thread in Threaded Connections. " Journal of Pressure Vessel Technology 119: 91-95.
- Guangjie, Y., Zhenqiang, Y., Qinghua, W. and Zhentong, T., 2006. Numerical and experimental distribution of temperature and stress fields in API round threaded connection. *Engineering Failure Analysis*, *13*(8), pp.1275-1284.
- Hagiwara, M., S. Itoh, et al. (1995). "Loadability of nut and bolt Assemblies determination of critical Nur Height by Staircase Method." International Journal- Japan Society of Precision Engineering 29: 356-360.
- Hetenyi, M., 1943. The distribution of stress in threaded connections. *Expt. Stress Anal*, *1*(1), pp.147-156.
- Higbee, C.A., 1900. *Screw-coupling*. U.S. Patent 658,087.

- Hilbert Jr, L.B. and Kalil, I.A., 1992, January. Evaluation of premium threaded connections using finite-element analysis and full-scale testing. In *SPE/IADC Drilling Conference*. Society of Petroleum Engineers.
- Hosokawa, S., S. Sato, et al. (1989). " Deformation of Nut in Threaded connection." Bulletin of the Japan Society of Prec. Engineering 23(1):47-52.
- ISO 10407-1, 2004.Petroleum and natural gas industrie- Drilling and production equipment- Part 1: Drill Stem Design and operating limits, international organization for standardization.
- Kachanov, L.M., 1958. Time of the rupture process under creep conditions. *Isv. Akad. Nauk. SSR. Otd Tekh. Nauk*, *8*, pp.26-31.
- Kristensen, A.S., Toor, K. and Solem, S., 2005, January. Finite Element analysis of jar connections: Modeling considerations. In *SPECIAL ISSUE FOR THE 18 TH NORDIC SEMINAR ON COMPUTATIONAL MECHANICS OCTOBER, 27 TH–30 TH 2005* (p. 37).
- Lemaitre, J. and Chaboche, J.L., 1994. *Mechanics of solid materials*. Cambridge university press.
- Lemaitre, J. and Desmorat, R., 2005. *Engineering damage mechanics: ductile, creep, fatigue and brittle failures*. Springer Science & Business Media.
- Lemaitre, J., 1985. Coupled elasto-plasticity and damage constitutive equations. *Computer Methods in Applied Mechanics and Engineering*, *51*(1-3), pp.31-49.
- Liebster, D. T. and Glinka (1994). " Development of numerical model for predicting fatigue lives of tubular threaded connections." American Society for testing and materials: 156-173.
- Lundberg, B., R. Beccu, et al. (1989). "Nonlinear dissipative spring mass model for a percussive drill road joint of the coupling sleeve type." International Journal of Impact Engineering 8: 303-313.
- Macdonald, K.A. and Deans, W.F., 1995. Stress analysis of drillstring threaded connections using the finite element method. *Engineering Failure Analysis*, *2*(1), pp.1-30.
- Macdonald, K.A., 1996. The effectiveness of stress relief features in austenitic drillcollar connections. *Engineering Failure Analysis*, *3*(4), pp.267-279.
- Miller, D. L., M. Marshek, et al. (1983). "Determination of Load Distribution in a threaded connection." Mechanism and Mechanic theory 18(6): 421-430.
- Morrow, J., 1968. Fatigue properties of metals. *Fatigue design handbook*, pp.21-30.
- Morse, J.O., 1882. Wrought Iron coupling for pipe sections, United States Patent, US 263943.
- Newport, A. and Glinka, G., 1991. Concentration of cyclic stresses in preloaded threaded connections. *Journal of engineering mechanics*, *117*(6), pp.1257-1273.
- Newport, A., 1989. *Stress and fatigue analysis of threaded tether connections*(Doctoral dissertation, University College London (University of London)).

- Noel, T. and Roussie, G., Vallourec Mannesmann Oil & Gas France and Sumitomo Metal Industries, Ltd., 2009. *Fatigue-resistant threaded component for a tubular threaded joint*. U.S. Patent 7,513,534.
- O'Hara, P.(1974). " Finite Element Analysis of Threaded Connections." Army Symposium on Solid Mechanics: 99-119.
- Olivier, H.P., 2002. *Connection*. U.S. Patent 6,485,063.
- Percy, J. L. and Sato A. (1918). "Analysis of threaded joints by Finite Element Method." Centro Tecnico Aeroespecial.
- Pilkey, W.D., 2003. Peterson's stress concentration factors, (1997).
- Placido, J.C.R., Valadao de Miranda, P.E., Netto, T.A., Pasqualino, I.P., Micsow, G.F., de Carvalho Pinheiro., B., 2005.Fatigue analysis of aluminium drill pipes, Material Research, 8(4), 409-415.
- Premium Joint, 2006."JFEBAR" for OCTG, JFE Technical Report, 7, 50-54.
- Radhakrishnan, V.M., 1992. On bilinearity of Manson-Coffin low-cycle-fatigue relationship.
- Rhee, H.C. (1990). "Three-Dimensional Finite Element Analysis of Threaded Joint." Offshore Mechanics and Arctic Engineering 3:293-297.
- Rodabaugh, E.C., 1983. *Comparisons of ASME Code Fatigue Evaluation Method for Nuclear Class 1 Piping with Class 2 or Class 3 Piping*. NUREG/CR-3243, June.
- roymech. (2017). *mean stress diagram.* Available: http://www.roymech.co.uk/Useful_Tables/Fatigue/Stress_levels.html. Last accessed 17/03/2017.
- Santus, C., Bertini, L., Beghini, M., Merlo, A. and Baryshnikov, A., 2009. Torsional strength comparison between two assembling techniques for aluminium drill pipe to steel tool joint connection. *International Journal of Pressure Vessels and Piping*, *86*(2), pp.177-186.
- Sches, C., Desdoit, E. and Massaglia, J., 2008, January. Fatigue Resistant Threaded and Coupled Connectors for Deepwater Riser Systems: Design and Performance Evaluation by Analysis and Full Scale Tests. In *ASME 2008 27th International Conference on Offshore Mechanics and Arctic Engineering* (pp. 407-420). American Society of Mechanical Engineers.
- Schneider, R., Wuttke, U. and Berger, C., 2010. Fatigue analysis of threaded connections using the local strain approach. *Procedia Engineering*, *2*(1), pp.2357-2366.
- Shahani, A.R. and Sharifi, S.M.H., 2009. Contact stress analysis and calculation of stress concentration factors at the tool joint of a drill pipe. *Materials & Design*, *30*(9), pp.3615-3621.
- Shoji, Y. and Sawa, T., 2010, January. Stress concentration at the ROOT of bolt thread. In *ASME 2010 Pressure Vessels and Piping Division/K-PVP Conference* (pp. 427-432). American Society of Mechanical Engineers.
- Smallman, R.E. and Bishop, R.J., 1999. *Modern physical metallurgy and materials engineering*. Butterworth-Heinemann.
- Sopwith, D. G. (1948) "The Distribution of Load in Screw Threads." Inst. Mech. Engrs. Appl. Mech. Proc. 159: 373-383.

- Stoeckly, E. E. and H. J. Macke (1952). “ effect of taper on screw-thread load distribution.” Transactions of the ASME: 103-112.
- Stromeyer, C.E., 1918. Stress distribution in bolts and nuts. *Trans. Inst. NA*, *60*, pp.112-117.
- Sugino, M., Nakamura, K., Yamaguchi, S., Daly, D., Briquet, G. and Verger, E., 2010, January. Development of an innovative high-performance premium threaded connection for OCTG. In *Offshore Technology Conference*. Offshore Technology Conference.
- Tafreshi, A. (1999). “SIF Evaluation and stress analysis of Drillstring Threaded Joint.” Pressure Vessel and Piping 76(2): 91-103.
- Tafreshi, A. and W. D. Dover (1993). “Stress Analysis of Drillstring Threaded connections using the finite element method.” Int J Fatigue 15(5): 429-438.
- Tafreshi, A., 1999. SIF evaluation and stress analysis of drillstring threaded joints. *International journal of pressure vessels and piping*, *76*(2), pp.91-103.
- Takano, J., Yamaguchi, M. and Kunishige, H., 2002. Development of Premium Connection" KSBEAR" for Withstanding High Compression, High External Pressure, and Severe Bending. *KAWASAKI STEEL TECHNICAL REPORT-ENGLISH EDITION*-, pp.14-22.
- Tanaka, M. and A. Yamada (1986).” The Behaviour of fasteners under eternal loading (Force Ratio Threaded Connections).” Bulletin of the JSME 29: 617-624.
- Tanaka, M. and., H. Miyazama, et al. (1981). “Application of the finite element method to bolt-nut joints- fundamental studies on analysis of Bolt-nut joint using the finite element method.” Bulletin of the JSME 24: 1064-1071.
- Tanaka, M., K. Hongo et al (1982). “Finite Element Analysis of the threaded connections subjected to external loads.” Bulletin of JSME 25:291-298.
- Topper, T.H., Wetzel, R.M. and Morrow, J., 1967. *Neuber's rule applied to fatigue of notched specimens*. ILLINOIS UNIV AT URBANA DEPT OF THEORETICAL AND APPLIED MECHANICS.
- Van, K.D., Cailletaud, G., Flavenot, J.F., Le Douaron, A. and Lieurade, H.P., 2013, October. Criterion for high-cycle fatigue failure under multiaxial loading. In *ICBMFF2*.
- Veritas, D.N., 2010. Fatigue design of offshore steel structures. *No. DNV-RP-C203*.
- Wahab, M.A., Ashcroft, I.A., Crocombe, A.D. and Shaw, S.J., 2001. Prediction of fatigue thresholds in adhesively bonded joints using damage mechanics and fracture mechanics. *Journal of adhesion science and technology*, *15*(7), pp.763-781.
- Wang, W. and K. M. Marshek (1995). “Determination of the Load Distribution in a threaded connector having dissimilar Materials and varying thread stiffiness.” Engineering for industry 117: 1-8.
- Wöhler, A., 1870. *Über die Festigkeits-versuche mit Eisen und Stahl*.
- Wohler, A., 1871. Tests to determine the forces acting on railway carriage axles and the capacity of resistance of the axles. *Engineering*, *11*, p.199.

- Yammoto, K., Kobayashi K., et al. (1990) “Stress Analysis of Premium Threaded Connection “FOX” by Finite Element Method. “Kawasaki Steel Technical Report 22:41-47.
- Yazawa. S. and K. Hongo (1988). “ Distribution of load in a screw Thread of a Bolt-Nut connection subjected to tangential forces and bending moment.” JSME International Journal 31: 174-180.
- Yuan, G., Yao, Z., Han, J. and Wang, Q., 2004. Stress distribution of oil tubing thread connection during make and break process. *Engineering Failure Analysis*, *11*(4), pp.537-545.
- Zadoks, R. I. and D. P. R. Kokatam (1999). “ Investigation of the axial stiffness of a bolt using a Three Dimensional finite element model.” Journal of sound and Vibration 246: 349-373.
- Zadoks, R. I. and X. Yu (1997). “An Investigation of the self-loosening behaviour of bolts under transverse vibration.” Journal of sound and Vibration 208: 189-209.
- Zhao, H. (1994). “Analysis of the load Distribution in a Bolt-Nuts Connector.” Computers and structures 53(6): 1465-1472.
- Zhao, H. (1996). “Numerical Method for load Distribution in Threaded connections.” Journal of Mechanical Design 188: 274-279.
- Zhao, H. (1998). “Stress Concentration factors within Bolt-Nuts Connectors Under Elasto-Plastic Deformation.” Int J Fatigue 20(9): 651-659.
- Zhao, H., Kuang, Z.B. and Li, Z.H., 1996. Stress-intensity factor for a semi-elliptical surface crack at the thread root of a screwed-pipe joint. *Computers & structures*, *59*(3), pp.419-424.
- Zhong, A., 2007, May. Thread Connection Response to Critical Pressures. In *Abaqus Users’ Conference, Paris, France* (pp. 690-706).

Chapter 3 Measurement Techniques

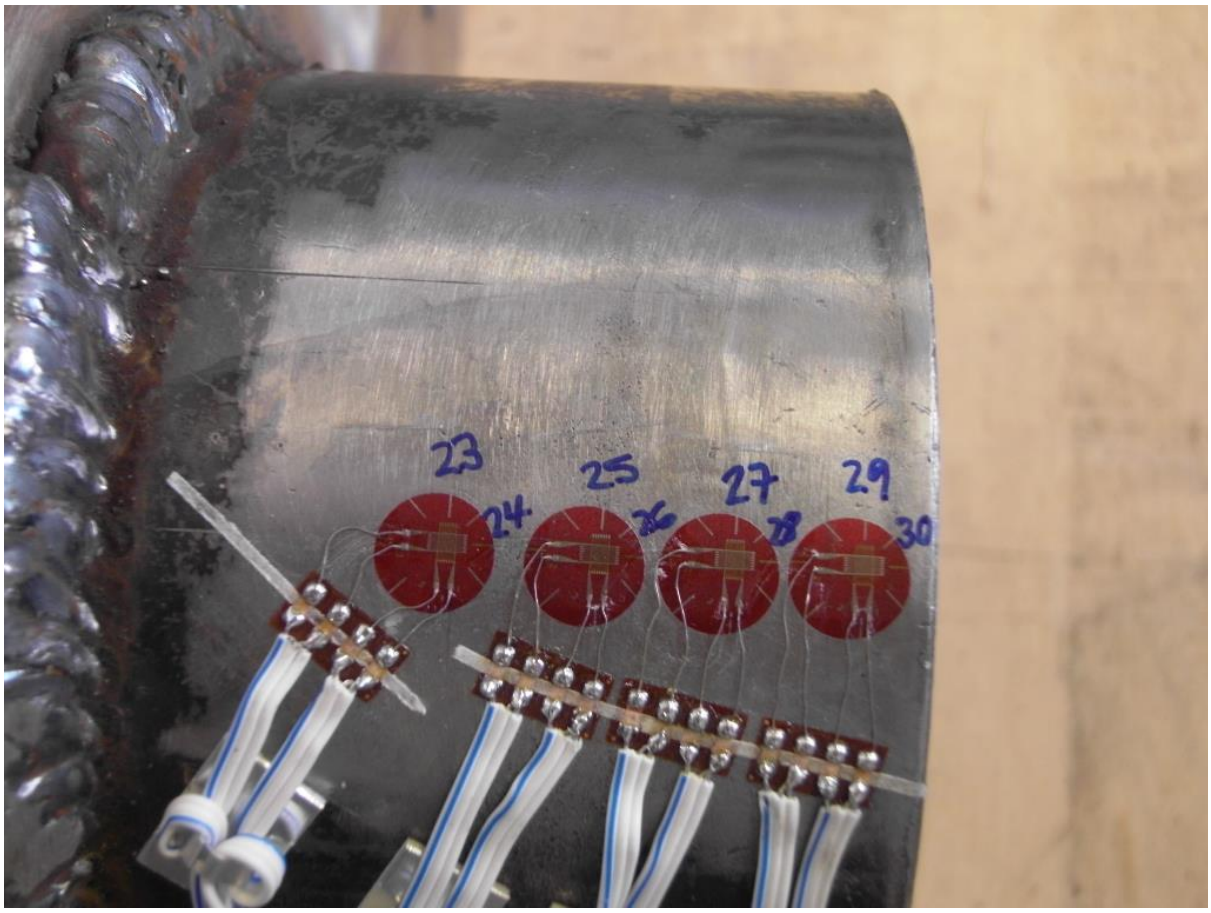

3.1 Summary

In this chapter, an overview is given of measurement techniques that may be suitable for detecting fatigue failure in a threaded pipe connection. It is not aimed to give a complete overview of existing crack sizing techniques, as not all techniques can be applied to threaded connection.

Distinction is made between on line monitoring and off line crack sizing techniques. From the practical viewpoint, on line monitoring techniques are the most interesting as they can be used without interrupting a running fatigue test. However, since fatigue cracks in threaded connections typically initiate at the root of an engaged thread, the region where the crack appears is not directly accessible during the test. This means that with on line techniques a crack is monitored in an indirect way which might result in less accurate measurement than in the case of off line crack sizing techniques. Additional attention is given to other measurement techniques commonly not used for crack sizing purpose, but which are used during the current research.

In the last section of this chapter a final comparison between the techniques is made and the technique is selected that will be used in this study for monitoring the fatigue damage setup described in chapter 4 and for the experiment described in chapter 5. It is beyond the scope of this project to develop new fatigue crack sizing techniques.

3.2 Overview of Crack Inspection Techniques

3.2.1 Online crack monitoring

3.2.1.1 Leak detection

To detect a through wall thickness crack in a tubular specimen, leak detection can be used. This is done by closing both ends of the specimen and applying a certain internal pressure with a fluid or gas (in most cases respectively water or air). The internal pressure is then monitored with a pressure gauge. When a sudden pressure drop is detected, a fatigue crack has propagated through the specimen’s wall thickness, creating a leak. Due to its simplicity, this method is common practice for fatigue testing of both threaded and welded pipes and it was used in most experimental studies described in the previous chapter. The only downside of this method is that it only provides information about the specific moment that the through wall thickness crack appears. It does not deliver any additional information on the crack growth rate while penetrating the pipe wall, nor does it give any measure of the actual crack length or shape.

3.2.1.2 Crack opening measurement

With crack opening measurements, the propagation of a fatigue crack can be monitored continuously. This technique is widely used for the characterisation of material fatigue crack growth properties and adopted by several standards. As an example, the compact tension or CT specimen as described in the ASTM E647

standard (ASTM International, 2011), is shown in figure 3.1. This kind of specimen contains a machined notch at the root of the which a fatigue crack will initiate. During the fatigue test the crack opening δ_o is measured using a clip gauge or linear variable displacement transducer (LVDT). To relate the measured crack opening to the crack depth a, the compliance method has to be used. This method is based on analytical solutions, in which the crack depth is a function of the ratio of crack opening to applied load. However, this analytical solution only exists for standard test specimen so no direct method is available to translate measured crack opening values to crack size in a threaded connection. Nevertheless, crack opening measurements have been successfully used on non-standard tubular specimen to provide a qualitative indication of the crack growth rate e.g. to monitor fatigue propagation in pipeline welds (Lefevre, 2011).

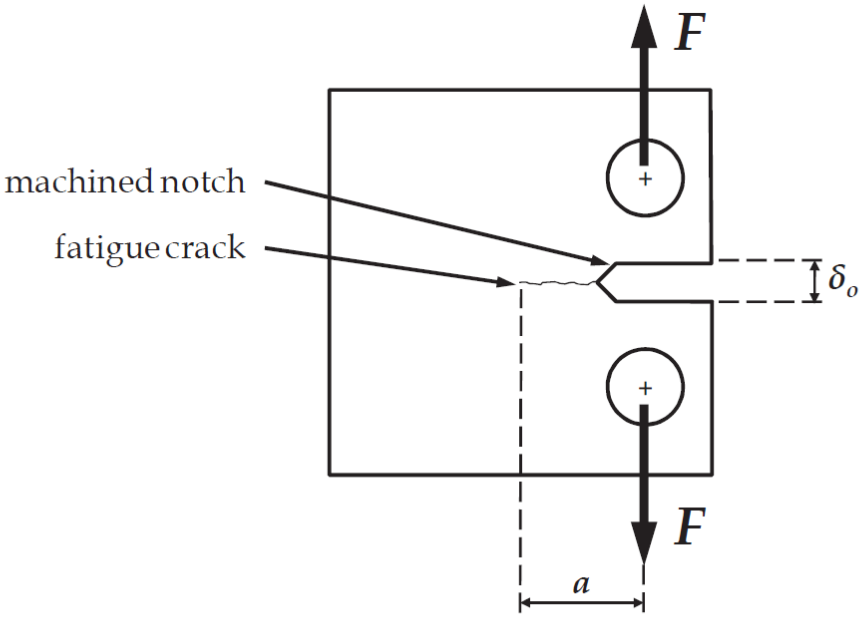

Figure 3.1: Compact tension specimen with crack opening measurement.

3.2.1.3 Ultrasonic inspection

Ultrasonic inspection is a well stablished crack sizing technique and can be applied to threaded connections (Suh, 1999). During a measurement, an ultrasonic signal is pulsed into a test specimen. When these pulses encounter a surface, e.g. an edge or a thread, they are reflected and captured by the same transducer. This is illustrated schematically in figure 3.2. if a fatigue crack appears, an extra surface is created on which the pulses are reflected. By monitoring the changes in the reflected signals, the crack growth can be quantified. As the transducer, can be placed outside the thread contact zone, the connection can remain coupled. The ultrasonic method testing it not the most convenient way as it is very difficult to distinguish flaws from the signal reflected by the different threads. Online monitoring of the fatigue crack growth using ultrasonic testing require more advance signal processing. Additionally, the test should be paused since local displacements due to a variable load can introduce inaccurate

readings. Nevertheless, this technique can be considered as an on-line measuring method since there is no need to remove the threaded connection from the test rig.

Although this technique exists and its feasibility was demonstrated by Suh (1999) by sizing cracks in bolts with a minimum depth of 0.5 mm to an accuracy of 0.2 mm, there exists no off-the-shelf equipment to implement this technique to threaded pipe connections. Consequently, this technique is not applied in this study.

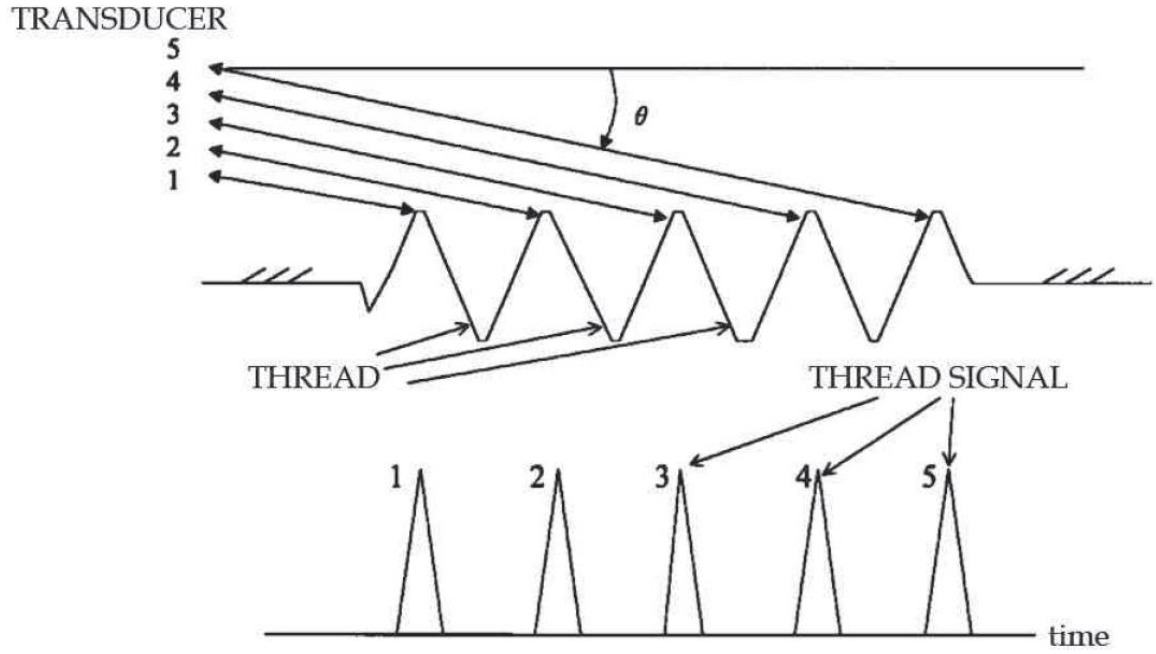

*Figure 3.2: Ultrasonic inspection technique for bolts (*Suh, 1999).

3.2.1.4 Modal analysis

Damage tends to reduce a structure's stiffness and as a consequence also its Eigen frequencies are reduced. With knowledge of these changes it becomes possible to determine the extent of cracks or damage in the structure. Also, when changes in the mode shapes are analysed, both crack size and crack location can be possibly determined (Swamidas and Chen,1995.) and order to use this technique in practical applications, the modal accelerations and modal strains are measured with accelerometers would modal strain sensors respectively. These sensors would be attached at different locations over the test specimen.

The structure is excited by one or more measured dynamic forces for modal analysis. The result from these excitations induced by force is recorded and the require modal parameters in the frequency range of the interest are extracted from the analysed data. In modal analysis, it is very important to isolate the structure from its operating environment and tested in laboratory conditions. One of the disadvantages the isolation cause, the excitation and the boundary condition differ significantly those of a structure's real life operation. One of the limitation this method creates is less

suitable for large structure, since it is very difficult or not possible, to create laboratory conditions for testing.

As an alternative, the output-only or operational modal analysis (OMA) technique has been developed and applied by Peeters and De Roeck (2001). These extract the modal parameters from the dynamic response to ambient force and in operational condition. As a result, a linear modal of the structure around the real working point of operation is delivered. The unmeasured, ambient forces are usually modelled as stochastic quantities with unknown parameters but with known behaviour.

The OMA technique like many other techniques suffers from several shortcomings. A complete modal model cannot be done by first output-only measurements, since the modal shapes cannot be scaled in an absolute sense. For ambient excitation, a narrow frequency band is used and as a result only a limited number of modes can be extracted with high quality from the ambient vibration data. In the past few years, special attention was given toward combined experimental modal testing techniques, also called operational modal analysis with exogenous inputs (OMAX) (Guillaume,2007). This technique uses artificial forces in operational conditions. The difference between OMAX and the traditional modal analysis approach is that the operational forces are included in the identified system model. They are considered as useful excitation and not as an unwanted noise source. Consequently, the amplitude of the artificial forces can be equal to or lower than amplitude of the unmeasured operational forces. This is of crucial importance for the modal testing of large structures, since it allows to use small excitation device like impact hammers or shakers.

When OMAX is applied to fatigue crack growth, crack size and locations are determined by change in the modal parameters of the structure. Hence, advanced calculation techniques have to be used to relate the measurements to the crack data.

3.2.2 Off line crack sizing

3.2.2.1 Dye penetrant

Dye penetrant can be used to highlight cracks during visual inspection. The working principles are illustrated in figure 3.3. After the surface is cleaned and grease free, a dye penetrant is applied to the surface and enters the defect (step a in figure 3.3). This dye has a bright red colour. After a certain dwelling time, that enables the dye to penetrate all cracks, the superficial dye is removed (step b). In the next step a thin layer of white developer is sprayed on the surface. The developer has the property to absorb the red dye from the crack which clearly colours the white layer of the developer.

This technique can be used to help locating surface cracks and viewing crack lengths during visual inspection, but it does not provide additional information about the crack depth.

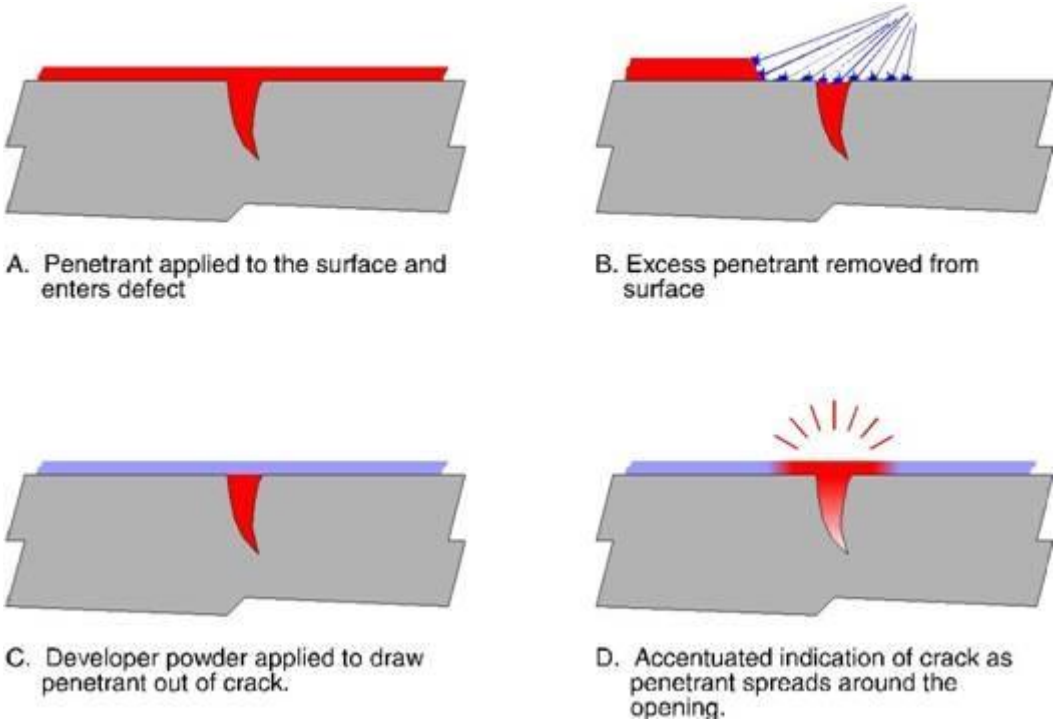

Figure 3.3: Illustrations of dye penetrant testing (*Mechjob, 2017).*

3.2.2.2 Magnetic Flux Leakage (MFL)

Magnetic flux leakage (MFL) detection is a magnetic non-destructive testing (NDT) method in which a very high magnetic field is induced in the test specimen. Sensing coils or Hall probes are used to detect the flux leakage around a flaw. Alternatively, the magnetic field outside the surface of the material can be detected visually with the so called magnetic particle inspection (MPI) technique where the crack is revealed by an accumulation of magnetic particles trapped in it leakage filed.

It is possible to use MFL to size crack in threaded pipe connections as was shown in two studies, respectively on tubing (Jinfeng,2006) and drill pipe threads (Ding,2006). The latter setup is illustrated by figure 3.4. A magnetizing exciter, which consist of a soft iron yoke (2) and the electrical coil (3), is inserted in the threaded pipe (1) and magnetizes it to saturation. When the threaded connection is saturated, the magnetic flux will leak in to the air at the location of the crack (4). This flux can be detected by the probe (5). This probe contains 8 Hall sensors and is pulled by a linear motor scan the threads along the axial direction.

With this method, the authors where able to detect cracks with a minimum depth of 0.3 mm and with a measurement accuracy of about 0.3 mm. MFL equipment is not is not available for this project.

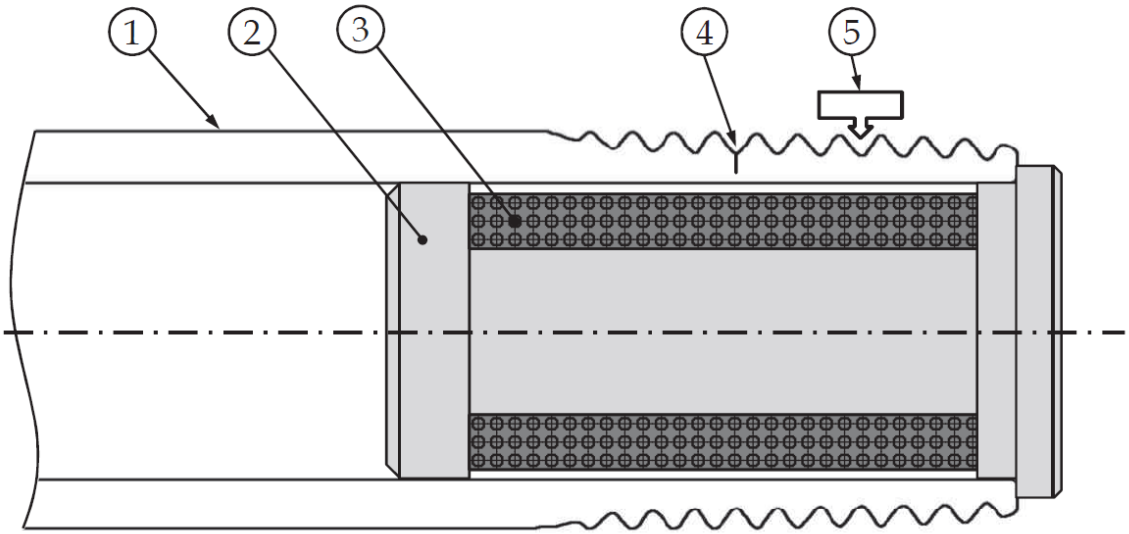

Figure 3.4: Thread inspection by magnetic flux leakage.

3.2.2.3 Eddy current testing

When a coil with an alternating current passing through is brought in the proximity of an electrically conducting material, the impedance measured at the terminals of the coil changes. As illustrated by figure 3.5, the magnetic field associated with the current flowing in the coil induces eddy currents in the conducting specimen. These eddy currents create a secondary magnetic field opposite to the magnetic field of the coil, which affects the coil's impedance. When a surface defect is present in the test object, the eddy current is not able to flow through it and its presence can be detected.

This technique can be applied to detect flaws of approximately 1 mm in depth in bolt threads of non-magnetic metals (Koshti, 2011) but its practical applicability for ferromagnetic materials is less straightforward. Here mechanical and thermal production and handling processes can introduce magnetic anomalies or local magnetisation which can interfere with the crack detection process. Consequently, this technique is not used in the current work.

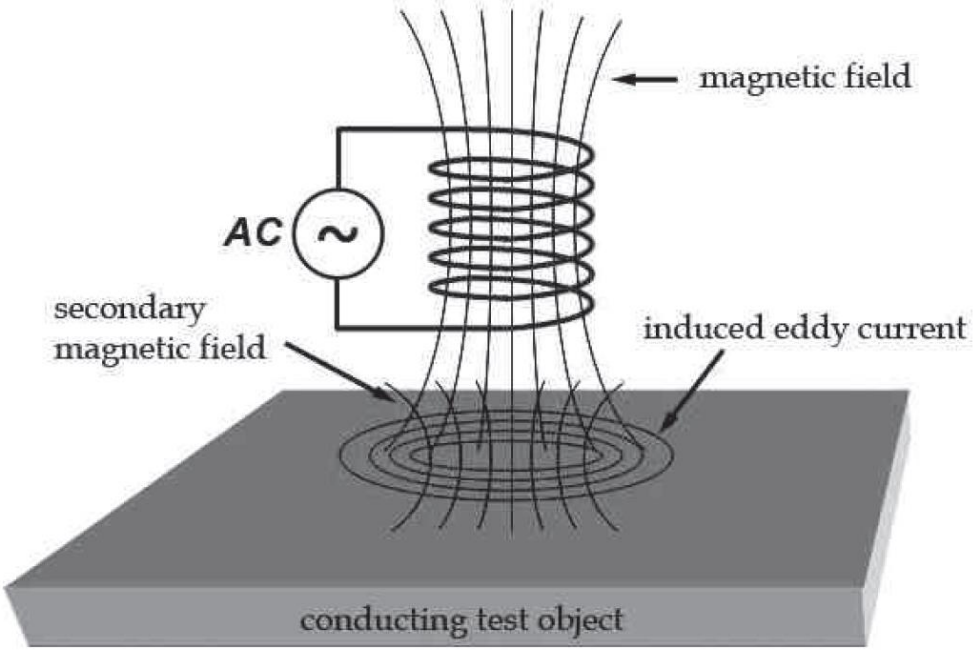

Figure 3.5: Eddy current testing.

3.2.2.4 Direct Current Potential Drop technique (DCPD)

The direct current potential drop (DCPD) technique is among the oldest electromagnetic NDT techniques and has been used for decades to estimate crack depths in plates and to monitor crack initiation and propagation during laboratory tests (Andersson, 2009). In this relatively simple technique an electrical DC current is injected into a conducting specimen through one pair of electrodes, while a second pair straddles the crack or the area where crack initiation is expected, as illustrated in figure 3.6 (Sposito,2009). The injecting electrodes should be positioned at a sufficient distance to ensure field uniformity at the inspection area.

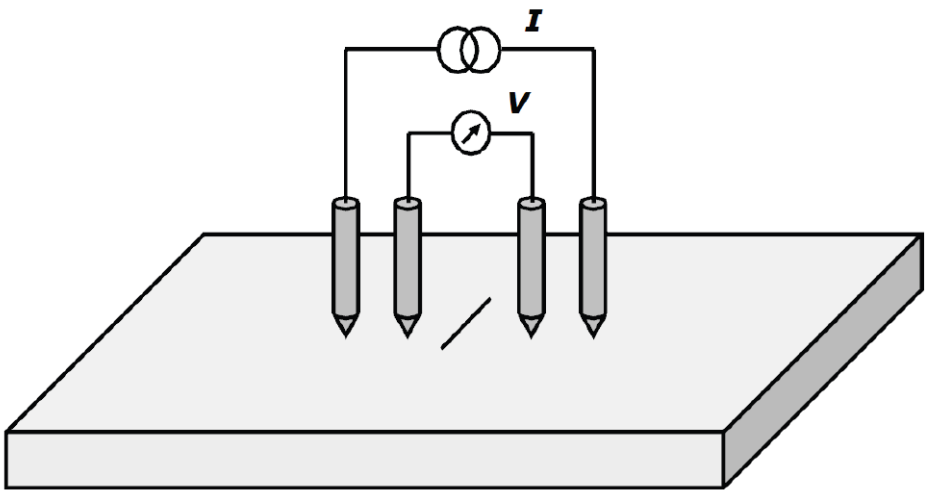

Figure 3.6: Direct current potential drop (Sposito, 2009).

As the crack size increases, the cross-section of the specimen is reduced, hence increasing the electrical resistance and the potential difference measured between the inner probs. Since the potential difference change is relatively small (in the order of μV), large current ($100A$ and more) have to be used. In addition, the method is very sensitive to changes in distance between the measuring probes and good electrical contact of the measuring probes is necessary. This means in practice that the probes should be spot welded to the part, which makes this method unsuitable to use on threaded pipe connections.

3.2.2.5 Alternating Current Potential Drop technique (ACPD)

The working principle of the alternating current potential drop (ACPD) technique is very similar to DCPD, the main difference being the use of an alternating instead of a direct current. Irregular current is passed through a conductor, this so-called skin effect forces the current to flow in a thin layer on the outer surface. This mean the effective cross-section carrying the current is small. As a consequence, sufficiently high potential differences can be generated by relatively low currents (3 A and smaller) see Sposito, (2009), Venkatsubramanian, and Unvala, (1984), Lugg, (2002). The thickness of the current-carrying layer, or skin depth θ can be calculated by eq. (3.1):

$$\theta = \frac{1}{\sqrt{\pi f \sigma_e \mu}} \qquad (3.1)$$

Where F is the frequency of the applied alternating current, which can be up to 10 kHz, σ_e is the electrical conductivity and μ is the magnetic permeability. At a frequency of about 5 kHz, for example, ferromagnetic mild steel has a skin depth in the order of 0.1 mm. The presence of an electrically insulating defect, such as a crack, forces the current to flow around and below it. The longer current path results in a higher resistance and a larger potential drop.

ACPD can be used to size cracks in threads (Lugg, 2002) as illustrated in figure 3.7. Since the fatigue cracks tend to initiate along the thread roots, where the position around the root radius is not known in advance, special voltage probes should be used that contact adjacent thread crests as illustrated in figure 3.7. If the thread applies to a solid component like a bolt, the alternating current is injected along the bolt's axis as shown. This delivers a uniform current field distribution around the thread circumference. For a tubular specimen, it may be better to induce the field using an additional coil that moves with the voltage probe.

Although ACPD can reach sub-micrometre accuracy if the probes are welded to the specimen, the accuracy of a system with travelling probes is only 0.1 mm and the minimum detectable crack size is approximately 1 mm.

In addition, the accuracy is highly dependent on the electrical contact between the probe and the thread crests. This technique is not applied in the current work. Since the thread connection is inaccessible.

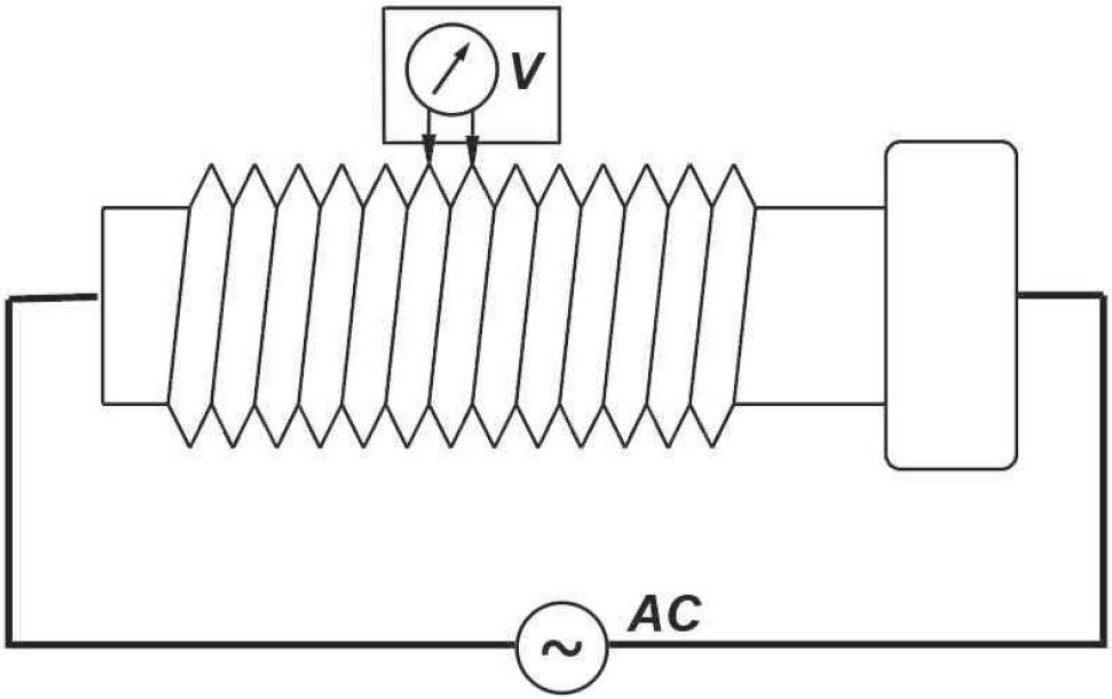

Figure 3.7: ACPD measurement for bolt inspection.

3.2.2.6 Alternating Current Field measurement (ACFM)

The alternating current field measurement ACFM technique was developed to combine the ability of ACPD to size cracks accurately in ferromagnetic materials with the ability of the eddy current technique to work without electrical contact. The latter is achieved by inducing (rather than injecting) uniform currents on the surface of the inspected specimen and by measuring the magnetic field above the surface instead of measuring the surface voltage.

During ACFM inspection two components of the magnetic field B are considered. The x-component B_x according to the coordinate system shown in figure 3.8 is parallel to the crack, while B_z is perpendicular to the object's surface (Knight, Brennan and Dover, 2004). When no crack is present, both the electric field induced by the current flow in the y-direction and the B_x-component are uniform. A surface flaw diverts the current away from the deepest point of the crack where it and concentrates near the end of the defect (see figure 3.9). Above the crack end in the B_z a strong field is generated, while the B_x field drops in strength. Interpretation of crack depth is based upon the ratio of uniform to minimum B_x levels, whilst crack length is determined by the local maxima and minima in the B_z signal. The magnitude of these two parameters are recorded over time as the ACFM probe scans the surface under inspection.

Since the 1980's special probes have been developed to optimize ACFM measurement for thread inspection. Consequently, AFCM has been used successfully to size cracks in bolts (Dover,1988) and drill pipe threads see Knight, Brennan and Dover, (2004), Topp and Lugg (2005). A example of a drill pipe thread inspection probe

is given in figure 3.10. It incorporates an induction coil to generate the surface current and a pick-up coil to measure the B_x and B_z field components. The detection threshold for crack depths in threads is less than 1mm and the technique has an accuracy of about 0.3 mm. The main disadvantage of this technique is that a relatively expensive probe has to be made for every thread type and size. It has not been applied during this project, where stopping test and disassembly is necessary.

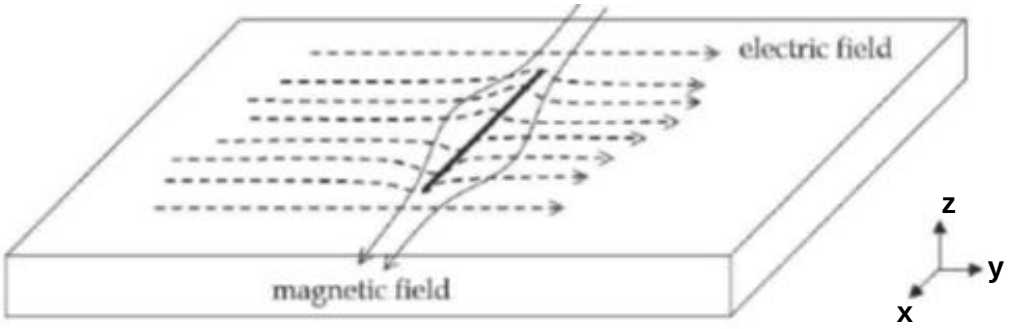

Figure 3.8: Field direction and coordinate system used in ACFM (Knight, Brennan and Dover, 2004).

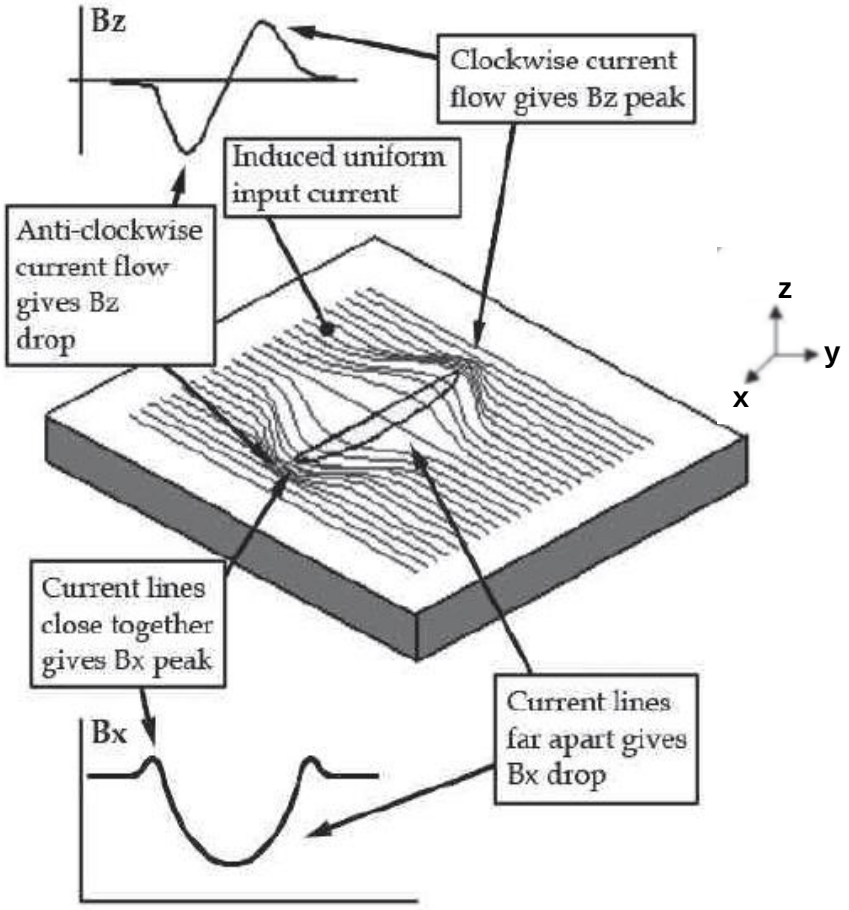

Figure 3.9: Magnetic field components in the vicinity of a defected (Knight, Brennan and Dover, 2004).

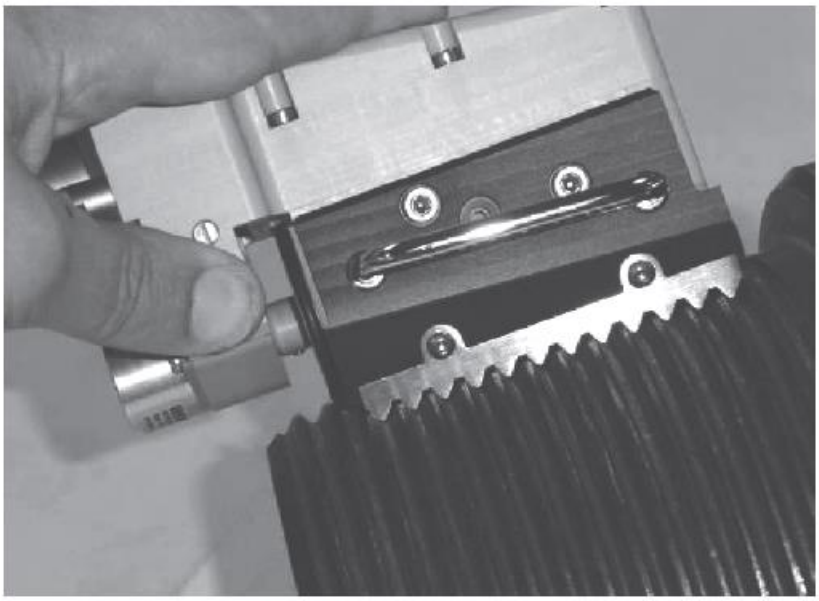

Figure 3.10: Probe for ACFM inspection of drill pipe threads (Topp and Lugg, 2005).

3.2.2.7 Beach marking

This technique is based on the principle of the crack propagation law of Paris-Erdogan eq. (2.22) as introduced in chapter 2. From this theory, it is known that the crack growth rate depends on the applied stress range. When the stress range is reduced, the crack growth rate is reduced as well. This changed propagation rate will mark a clear line in the fracture surface of the test specimen as illustrated in figure 3.11.

In practice this is done by applying a number of load cycles at a higher stress ratio while keeping the same value of the maximum stress (see figure 3.12). The majority of the fatigue damage is produced by the stress range $S_{r,test}$. The lower stress range $S_{r,beach}$ can be chosen in such a way that its contribution to the total fatigue damage is negligible.

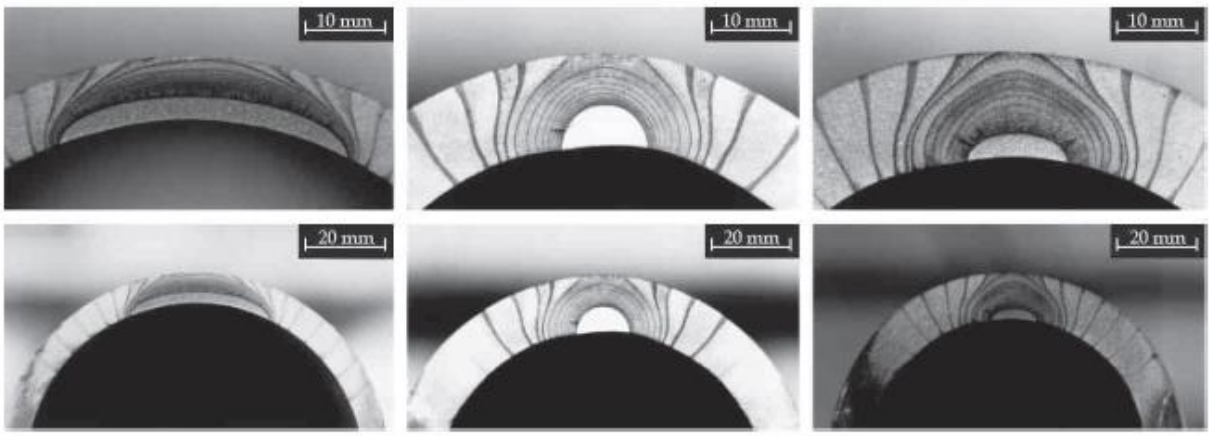

Figure 3.11: Fracture surface with beach mark lines of tubes with internal notches of different initials size (Yoo and Ando, 2000).

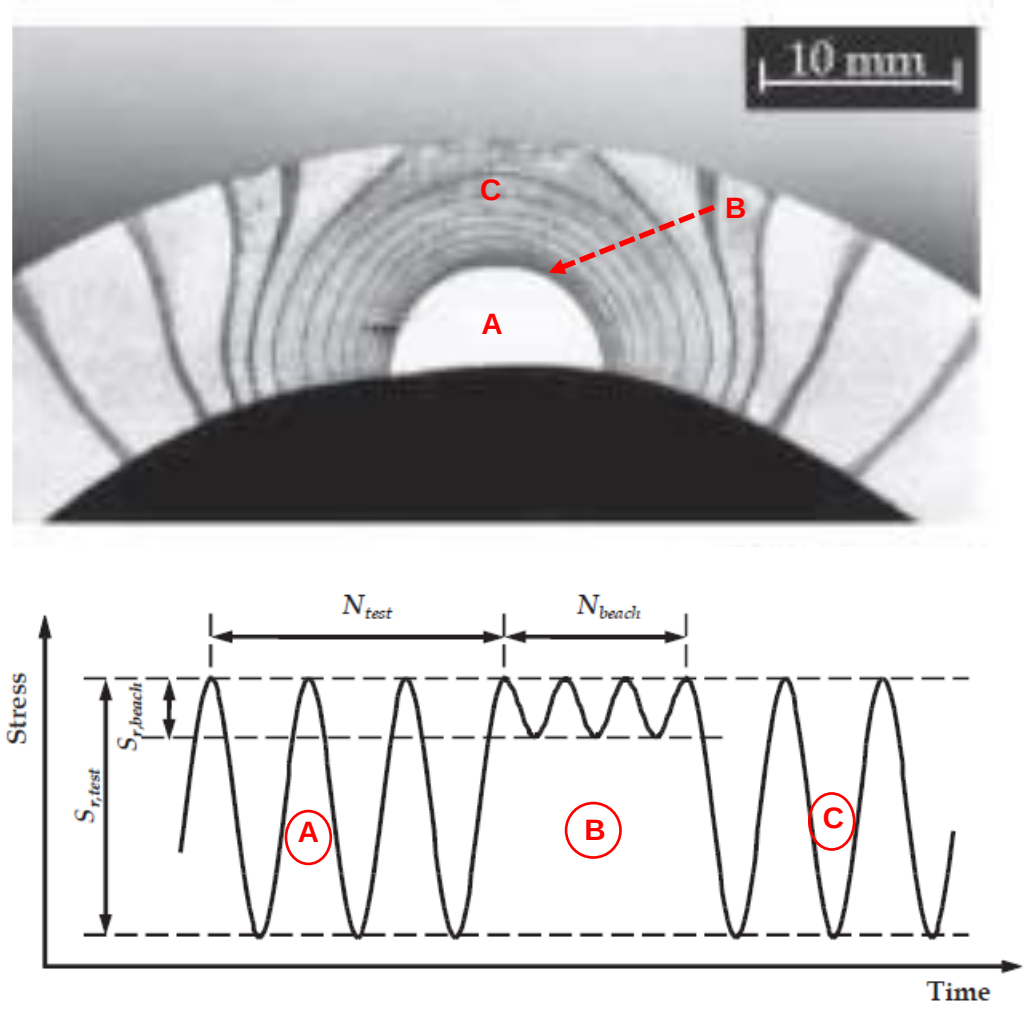

Figure 3.12: Schematic overview of the beach marking technique.

Multiple beach mark load blocks may be applied to create several lines in the fracture surface. The results, however, can only be seen after the test by breaking open the fracture surface. The cracks can then be measured by using an optical measuring microscope. Since this can only done after the test is finished, the beach marking technique requires a certain amount of expertise to determine when to apply the beach mark blocks and to select the correct number of cycles. If the beach mark cycles are applied too early or too few cycles are applied, no beach mark lines will be visible. On the other hand, if too many beach mark blocks or cycles are applied, the crack propagation will be affected by the technique.

Nevertheless, beach marking has been used successfully in different application see Yoo and Ando, (2000), Liu and Bowen, (2003), Raghava, (2005), Cai, and Shin, (2005) and Lihavainen, (2007) including the work of Brennan on drill pipe connections (Brennan, 1992). In most case, however, the beach mark lines are used as a validation or calibration for an indirect crack sizing technique as described earlier in this chapter.

In this study, the beach marking technique will be used to investigate the fatigue crack growth in threaded pipe connections in more detail.

3.2.3 Other measurement technique

In this section two additional measurement techniques are discussed. They are not specifically developed for crack detection, but will be used in the current research.

3.2.3.1 Strain gauge

Strain gauge are widely used to measure strain locally in either static or dynamic applications. As mentioned in the review in section 2.2.3 of chapter 2, strain gauge measurements during static tests have been used for validation of finite element simulation of threaded pipe connections is several studies. In addition, dynamic strain gauge measurement has been used to control the bending stress of threaded pipe connection in a resonant bending fatigue setup (Sches, 2008).

The working principle of a strain gauge is based on the fact that the resistance of a conductor is both material and geometry dependent. For a wire material of constant resistivity, the total resistance increases with length and decrease with cross-sectional area. Example of a strain gauges are shown in figure 3.13.a. Each consists of a fine wire which runs several times in parallel over the gauge area. When the strain gauge is properly bonded to a surface the change in length of the surface can be accurately measured by the change in resistance of the wire. Strain gauges are constructed in such a way that the change in resistance occurs in a known proportion (gauge factors) to the applied tensile or compressive strain value (Lee, 2005).

In the present fatigue application strain gauge are applied to monitor local strains around stress concentrations. A measured strain value can also be used as feedback signal for a strain controlled fatigue test.

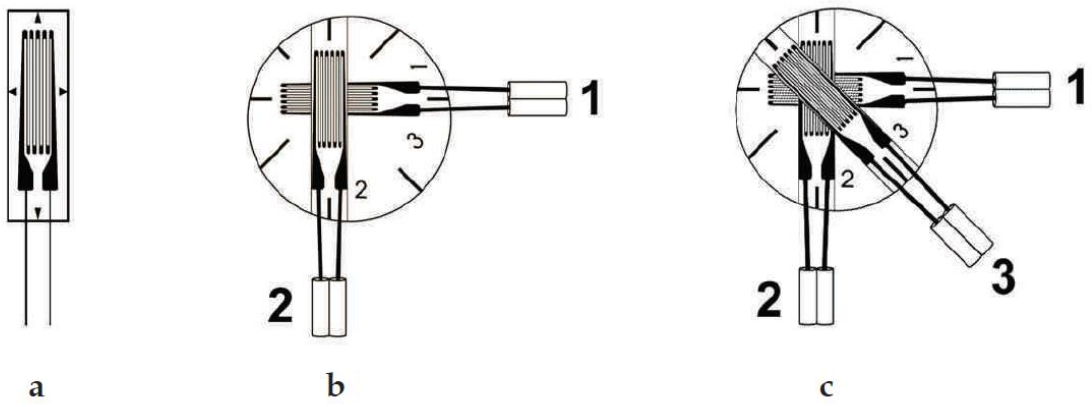

Figure 3.13: Strain gauges: a) Line gauge, b) Cross gauge, c) Rosette gauge.

For the line gauge illustrated in figure 3.13.a, only the strain in the vertical direction can be measured. They are applied to directions where a uniaxial strain situation is expected to appear. In the elastic region, the uniaxial stress component σ can be calculated from the measured strain ε according to Hooke's law, with E young's modulus of elasticity:

$$\sigma = \varepsilon E \tag{3.2}$$

For a biaxial strain situation, a cross gauge as in figure 3.13.b can be used. With the strain gauge aligned along the principle directions, the elastic stress components σ_1 and σ_2 can be calculated according Eq. (3.3-4), with v the Poisson ratio.

When:

$$\sigma_1 = \frac{E}{1-v^2}(\varepsilon_1 + v.\varepsilon_2) \tag{3.3}$$

$$\sigma_2 = \frac{E}{1-v^2}(\varepsilon_2 + v.\varepsilon_1) \tag{3.4}$$

To determine the principal stress directions, a rosette gauge, shown in figure 3.13.c, can be used. The principal strain may be calculated or constructed within a Mohr's circles from the three gauge readings, shear strain in each non-principal gauge directions may also be found as required.

3.2.3.2 Photogrammetry

Photogrammetry is the practice of determining geometric properties of an object from photographic images. Photogrammetric measurement techniques have been improved extensively and optimized during the last two decades thanks to the development of low cost, high resolution digital camera. When images of the same object, taken from different orientations are analysed, very accurate 3D information related to the coordinates of an object can be obtained, although the images themselves only contain 2D information.

Originally photogrammetry was developed a fast way to acquire dimensional data of civil engineering constructions. Using a single digital camera to photograph a construction from different angles, a 3D model of the construction can be generated by post-processing the images (Armesto, 2009, Ozbek, 2010)

Moreover, when an object is photographed at different moments, photogrammetry can be used to detected deformation or displacements. Reference points, such as reflective marker, are added to the object in order to size the displacement. System have been developed with two cameras positioned on a fixed distance and under a fixed angle, which enables the acquisition of 3D displacement data. Additionally, system exist with more than two cameras. These can be used when very large objects are to be analysed. An example of this is given by Ozbek et al (2010) in their analysis

of the displacement of a wind turbine with a rotor diameter of 80 m. Due to advanced post-processing techniques a sub-pixel accuracy can be obtained. This makes it possible to detect small displacement and deformations.

Dynamic 3D optical measurement system as illustrated in figure 3.14 (Techniques, G.O.M., 2005) the system delivers accurate 3D displacement data for a number of reflective markers attached to a test object. When image are captured, the reflective markers are illuminated by an integrated flash LED system. After the data is captured, it is post-processed to identify the markers and to calculate their displacement (see figure 3.15). The system consists of two high-speed digital cameras placed on a rigid bar with calibrated length L of 1200 mm and under a certain angle α which can be changed between 15° and 40°. This way the focal point of the system is located at the measuring distance D. All markers inside a certain cubic measuring volume around this point can be captured.

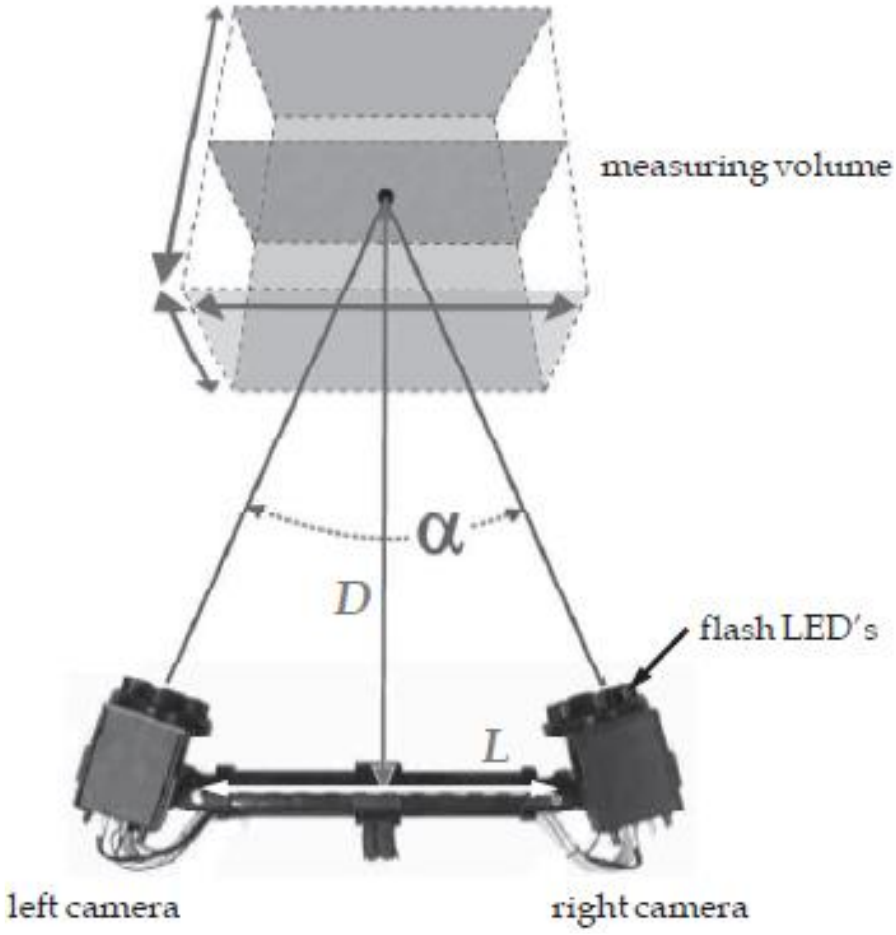

Figure 3.14: Dynamic 3D optical measurement system.

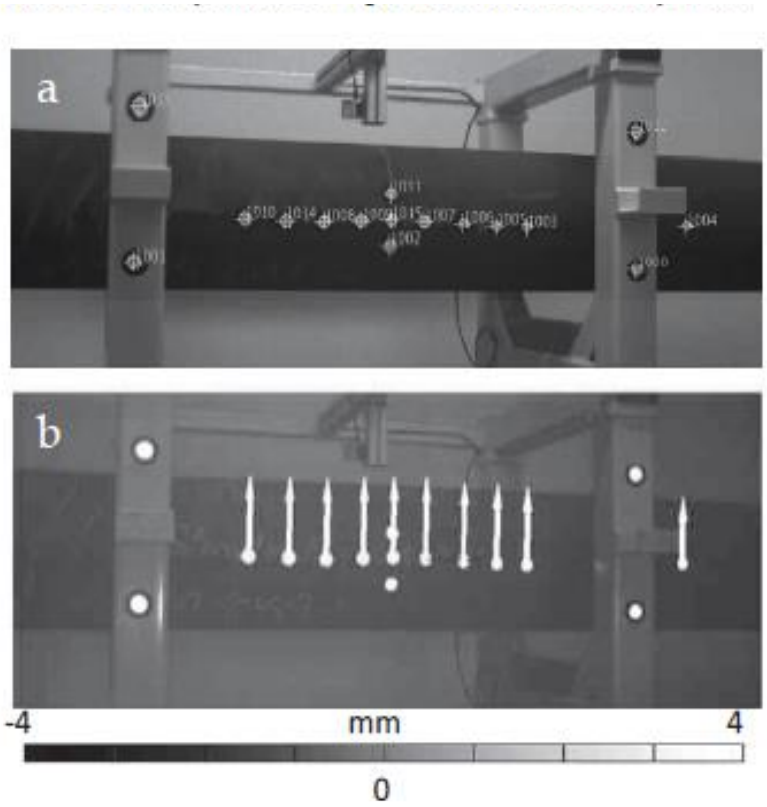

Figure 3.15: a) Identified markers, b) Calculated displacement.

With this configuration, the measuring distance D can be altered from 1.6 m to 4.6 m and the corresponding edge length of the measuring volume is between 1.6 m and 3.5 m. The dynamic 3D optical measurement system uses digital cameras with 20 mm lens and 1.3 MPixel resolution that can capture images at a rate up to 500 Hz. The system's accuracy is typically 0.02 pixels, which corresponds to 20 μm to 50 μm, depending on the measuring volume.

3.2.3.3 Photoelastic

Since threaded joint connection is a closed section, it is difficult to measure strains experimentally through sections of the joint. The Photoelastic method was the first method used for measuring the stress distribution within connection models. Figure 3.16 and 3.17 show a quantitative estimate of stress in three dimensions of even the most complex geometries such as threaded joint connection. Static stress freezing technique is the most common Photoelastic method. Specimens can be cast or machined out of Photoelastic bakelite or similar material. First the threaded joint connection is loaded statically and then heated in controlled manner, followed by cooling, effectively freezing the stresses which can be sectioned and viewed with fringe multiplying polariscope. One of the advantages of this method is that it allows study of the overall stress field and in particular the stress distribution through the tube wall thickness. It is this distribution that determine the crack propagation.

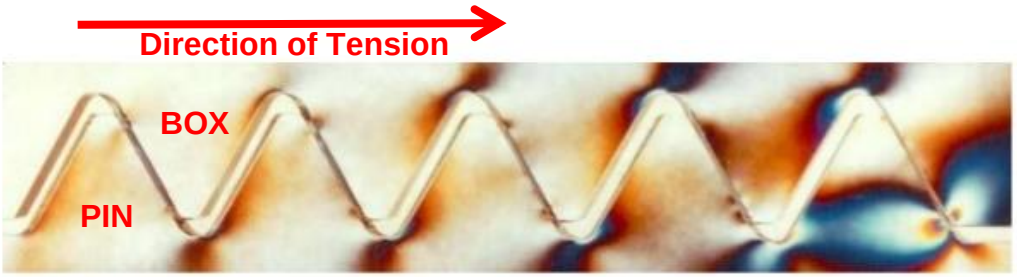

Figure 3.16. Standard 60-degree thread, stress concentrated on last engaged thread (Prweb,2017).

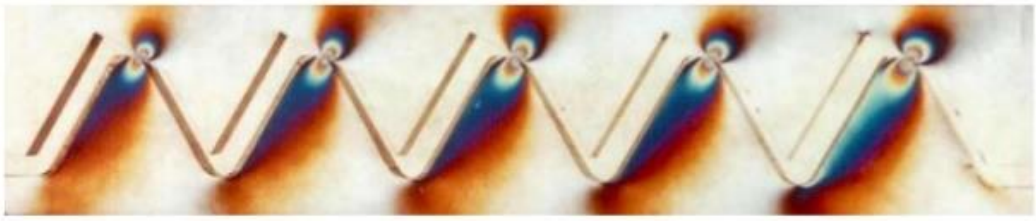

Figure 3.17. Radial stress distribution, to improve thread fatigue life (Prweb,2017).

3.3 Summary and Conclusions

3.3.1 Comparison of crack sizing techniques

In Table 3.1 an overview is given of the quantitative crack sizing techniques described in pervious sections that were used for inspection threads or threaded connection in the past. All techniques can detect crack with a minimum depth between 0.3 mm and 1 mm and have a crack measurement accuracy from 0.1 mm to 0.5 mm. These techniques all require specialised equipment and it should be noted that the only on line crack sizing technique for threaded connections it is ultrasonic inspection, while the other technique require the connection to be uncoupled for inspection. Next to this, the ultrasonic technique described in (Suh, 1999) require advanced signal processing and no systems are currently available that include this option.

Table 3.1: Overview of crack sizing technique applied to threads.

Measurement technique	Crack detection threshold [mm]	Crack depth accuracy [mm]	Online/Offline
Ultrasonic inspection	0.5	0.2	Online
MFL	0.3	0.3	Offline
Eddy current	1	0.5	Offline
ACPD	1	0.1	Offline
ACFM	1	0.3	Offline

3.3.2 Applied techniques

In order to relate the measure the crack size, beach marking will be applied to visualize crack fronts which are sized by a measuring microscope after the test.

During the static and fatigue test described in chapter 5 strain gauges are attached to the specimens in order to validate strain distribution simulated by the finite element model described in chapter 6.

The following techniques mentioned in Table 3.1, were not available for this research due to limited funding and resources, therefore for easy accessibilities and convenience (i.e. decoupling not wanted), and for validation for simulations (experiment were done simple as possible) the available mentioned technique was used.

Refrences

- Andersson, M., Persson, C. and Melin, S., 2006. Experimental and numerical investigation of crack closure measurements with electrical potential drop technique. *International journal of fatigue*, *28*(9), pp.1059-1068.
- Armesto, J., Lubowiecka, I., Ordóñez, C. and Rial, F.I., 2009. FEM modeling of structures based on close range digital photogrammetry. *Automation in Construction*, *18*(5), pp.559-569.
- ASTM International, 2011. *Standard test method for measurement of fatigue crack growth rates*. ASTM International.
- Brennan, F.P., 1992. *Fatigue and fracture mechanics analysis of threaded connections* (Doctoral dissertation, University of London).
- Cai, C.Q. and Shin, C.S., 2005. A normalized area-compliance method for monitoring surface crack development in a cylindrical rod. *International journal of fatigue*, *27*(7), pp.801-809.
- Ding, J.F., Kang, Y.H. and Wu, X.J., 2006. Research on the method for Drill Pipe Thread Inspection. In *Key Engineering Materials* (Vol. 321, pp. 472-475). Trans Tech Publications.
- Dover, W.D. and Dharmavasan, S., 1988. Inspection of threaded components using ACFM. *Fatigue of Large Diameter Threaded Connections*, pp.57-70.
- Guillaume, P., De Troyer, T., Devriendt, C. and De Sitter, G., 2007, February. OMAX–operational modal analysis in presence of eXogenous inputs. In *Proceedings of the 25th IMAC, a conference on structural dynamics, society for experimental mechanics, Orlando, FL*.
- Henze, F., Siedler, G. and Vetter, S., 2006. Integration of digital image analysis for automated measurements into a photogrammetric stereo evaluation system. In *Proc. of the ISPRS Commission V Symposium'Image Engineering and Vision Metrology', Dresden, Germany, Sep* (pp. 25-27).
- Jinfeng, D., Yihua, K. and Xinjun, W., 2006. Tubing thread inspection by magnetic flux leakage. *NDT & E International*, *39*(1), pp.53-56.
- Knight, M.J., Brennan, F.P. and Dover, W.D., 2004. Effect of residual stress on ACFM crack measurements in drill collar threaded connections. *Ndt & E International*, *37*(5), pp.337-343.
- Koshti, A., 2011. Process Specification for Eddy Current Inspection.
- Lee, Y.L., 2005. *Fatigue testing and analysis: theory and practice* (Vol. 13). Butterworth-Heinemann.
- Lefevre, A.A., Waaijenberg, M., Aylwin, E. and Triel, H.M., 2011. Defect propagation from fatigue loading in 13% Cr pipelines. *Journal of Pipeline Engineering*, *10*(3).
- Lihavainen, V.M., 2007. A novel approachfor assessing the fatigue strength of ultrasonic impact treated welded structures. *Acta Universitatis Lappeenrantaensis*.
- Liu, J. and Bowen, P., 2003. DC potential drop calibration in matrix-cladded Ti MMC specimens with a corner notch. *International journal of fatigue*, *25*(7), pp.671-676.

- Lugg, M.C., 2002. An introduction to ACPD. *Technical Software Consultants Ltd., TSC/MCL/1146, United Kingdom*, *20*.
- Mechjob (2017) *dye penetrant testing,* Available at: *http://www.mechjobs.in/2015/06/introduction-to-dye-penetrant-testing.html* (Accessed: 18th March 2017). Mechjob (2017) *dye penetrant testing,* Available at: *http://www.mechjobs.in/2015/06/introduction-to-dye-penetrant-testing.html* (Accessed: 18th March 2017).
- Ozbek, M., Rixen, D.J., Erne, O. and Sanow, G., 2010. Feasibility of monitoring large wind turbines using photogrammetry. *Energy*, *35*(12), pp.4802-4811.
- Peeters, B. and De Roeck, G., 2001. Stochastic system identification for operational modal analysis: a review. *Journal of Dynamic Systems, Measurement, and Control*, *123*(4), pp.659-667.
- Prweb (2017) *Photoelastic,* Available at: *http://www.prweb.com/releases/2006/09/prweb443559.htm* (Accessed: 18th March 2017).
- Raghava, G., Mithun, I.K., Gandhi, P., Vaze, K.K., Bhate, S.R. and Bhattacharya, A., 2005. Application of beach marking technique to the study of fatigue crack growth in steel plate specimens subjected to tensile loads. *Journal of Structural Engineering*, *32*(3), pp.229-232.
- Sches, C., Desdoit, E. and Massaglia, J., 2008, January. Fatigue Resistant Threaded and Coupled Connectors for Deepwater Riser Systems: Design and Performance Evaluation by Analysis and Full Scale Tests. In *ASME 2008 27th International Conference on Offshore Mechanics and Arctic Engineering*(pp. 407-420). American Society of Mechanical Engineers.
- Sposito, G., 2009. Advances in potential drop techniques for non–destructive testing. *Doctor of Philosophy, Imperial College London*.
- Suh, D.M., Kim, W.W. and Chung, J.G., 1999. Ultrasonic inspection of studs (bolts) using dynamic predictive deconvolution and wave shaping. *IEEE transactions on ultrasonics, ferroelectrics, and frequency control*, *46*(2), pp.457-463.
- Swamidas, A.S.J. and Chen, Y., 1995. Monitoring crack growth through change of modal parameters. *Journal of Sound and Vibration*, *186*(2), pp.325-343.
- Techniques, G.O.M., 2005. Aramis v5. 4 user manual. *GOM mbH*.
- Topp, D. and Lugg, M., 2005. Advances in thread inspection using ACFM. In *3rd Middle East NDT Conference and Exhibition, Bahrain, Manama 27-30th Nov 2005*.
- Venkatsubramanian, T.V. and Unvala, B.A., 1984. An AC potential drop system for monitoring crack length. *Journal of Physics E: Scientific Instruments*, *17*(9), p.765.
- Yoo, Y.S. and Ando, K., 2000. Circumferential inner fatigue crack growth and penetration behaviour in pipe subjected to a bending moment. *Fatigue and Fracture of Engineering Materials and Structures*, *23*(1), pp.1-8.

Chapter 4 Axial Fatigue Setup

4.0 Summary

In this chapter, the experiment set up will be explained, the obtained test data will be used to validate the performed simulations and is analysed more in detail to reveal the general trends in the fatigue behaviour of threaded pipe connections in chapter 5.

In this chapter, the design and working principle of the fatigue setup developed are discussed. The setup is completely designed, produced, assembled and operated as a part of this PhD project. The advantage of this development over a conventional experimental setup is its low energy consumption.

Even through computer simulations like finite element analysis can significantly increase the efficiency of the design process, experimental test remains important to obtain reliable predictions of the fatigue life of a threaded connection. Since the stress distribution resulting from make-up and dynamic loads cannot be applied to small strip-like specimens, it is required to perform the experiments on threaded tubular specimens.

4.2 Experimental Test Program

4.2.1 Test program overview

An overview of the experimental test program is given in Table 4.1. Both static tests and fatigue tests are performed. Static torque, axial tension test is performed on threaded pipe connections. Next to this, the torque test is used to determine the coefficient of friction of the contact between the threads of pin and box.

Table 4.1: Overview of the experimental test program.

Experimental test program		
Test Types	**Static Tests**	**Fatigue Tests**
	• Torque test	• Axial tension
	• Axial tension	• Small scale 1-inch pipe
	• Small scale 1-inch pipe	• Medium scale 4.5-inch pipe
Goals	• Model validation	• Determining fatigue live
	• Determining connection properties	• Compare different connection type

The fatigue tests are performed in two different setups: axial tension small scale 1-inch and medium scale 4.5-inch test. During this test, the fatigue lives for different threaded connection types subjected to a range of loads are determined.

Additionally, the specimen's material properties are determined by tensile tests on the pipe material. Figure 4.1 and 4.2 show the flat and round tensile test.

Tensile test performed on an Instron model 5967, this being a screw driven machine with a load capacity of $30\ kN$, load measurement accuracy to +/- 0.5% of reading down to 1/1000 of load cell capacity and fast, synchronized data acquisition rates up to 2,500 points per second.

Figure 4.1: The tensile test performed on the sample.

Two different samples were tested to check the accuracy of the tensile test. Sample **A** in figure 4.2 is a rounded sample cut out from a 5.5-inch API pipe with a 16-mm wall thickness. Sample **B** is a flat sample cut out from a 4.5-inch API pipe with a wall thickness of 6 mm.

Contact extensometers have been used to measure changes in the length as shown right hand side of figure 4.1, These devices are used for applications where high precision strain measurement is required (most ASTM based tests). They have the advantage of lower cost and ease of use, however, they can influence small / delicate specimens. One disadvantage of the contact extensometer is as the length changes due to tensile load the blade contacted extensometer slip on the surface and alter the reading. Therefore, it is highly recommended for very accurate tensile test data non-contact extensometer be used such as laser or video recording.

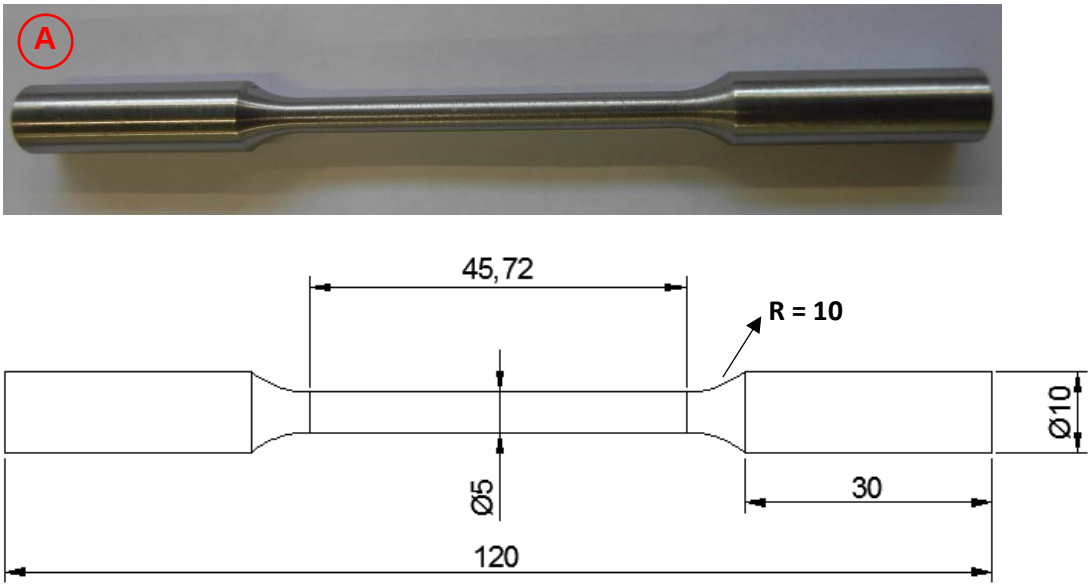

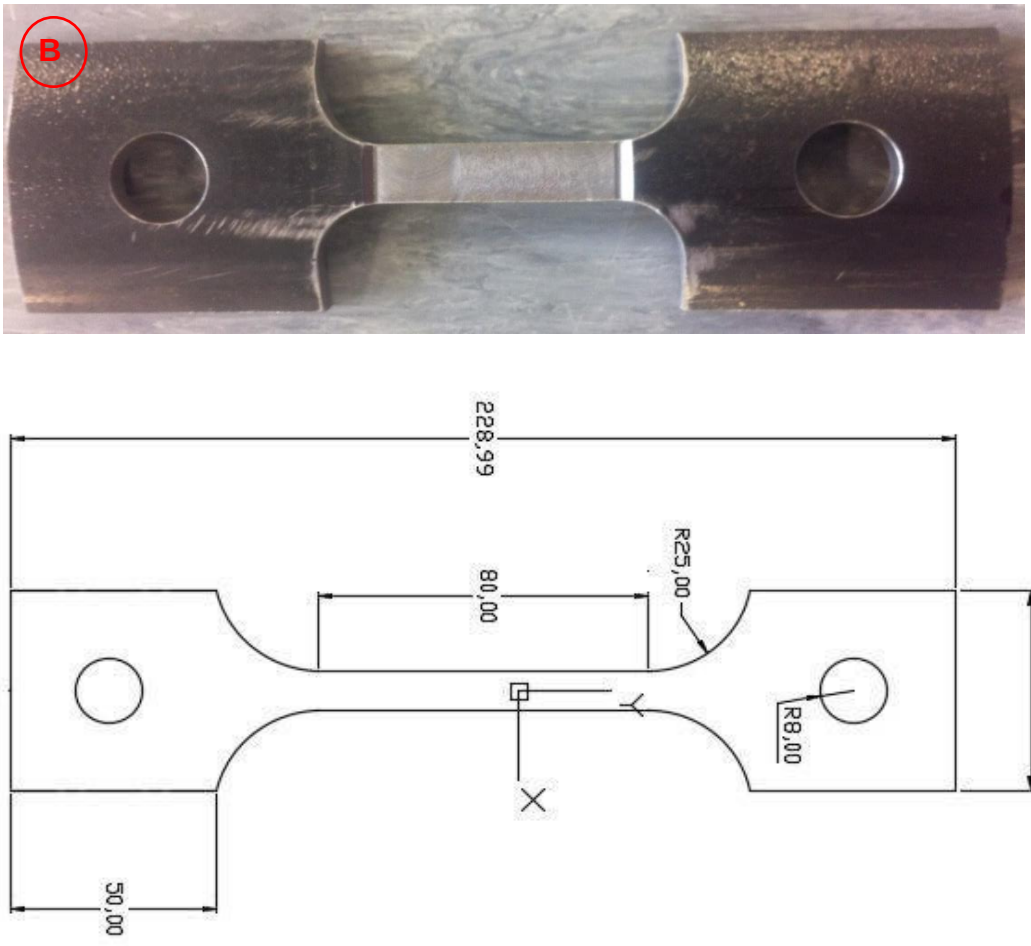

Figure 4.2: Tensile sample A) Round sample (mm), B) Strip sample (mm).

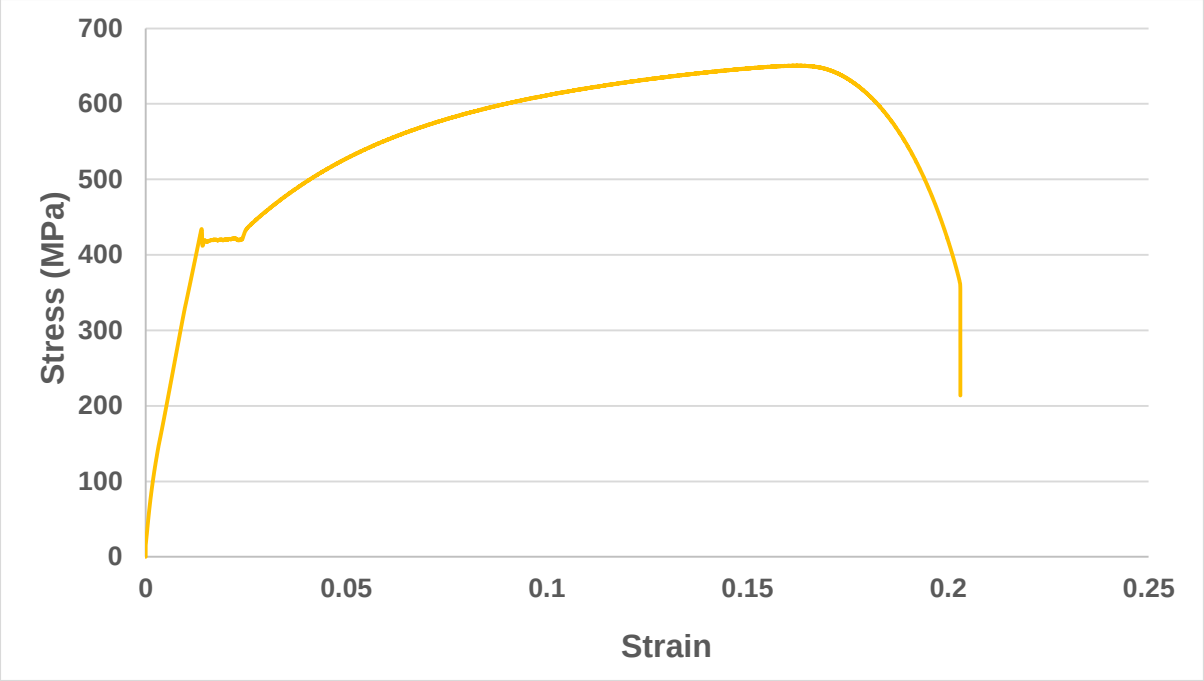

Figure 4.3: Tensile test on API specimen.

The tensile test was performed as shown in figure 4.3 on both round and strip sample and the result is presented here.

It is important to point out that all the samples were cut from the same pipe and they were all tested under the same condition to rule out other influences such as environment and material defect. Despite all these considerations none of the result were similar. Tensile test was repeated ten times and interestingly none of the test results were identical, this topic will be discussed in chapter 5 further.

4.2.1.1 Chemical composition of API Grade B materials

The chemical composition shall comply with requirements of API 5L Grade B/X42 and A106/SA106 Grade B.

The following instruction shall be imposed:

- C 0.20% Max
- Mn 1.15% Max
- Si 0.10% Min
- P 0.030% Max
- S 0.010% Max
- CEV 0.41% (Long Formula)

4.2.2 Test specimen selection

4.2.2.1 API line pipe connection

In this study, the API Line Pipe connection is used as a reference. As illustrated in figure 4.4, this is T&C connections with truncated triangular threads. The male and female threads both have a thread angle of 60° for API and 55° for BSPT, both thread is a parallel thread as can be seen in figure 4.4 and Figure 4.5.

Figure 4.4: Medium scale 4.5-inch male and female.

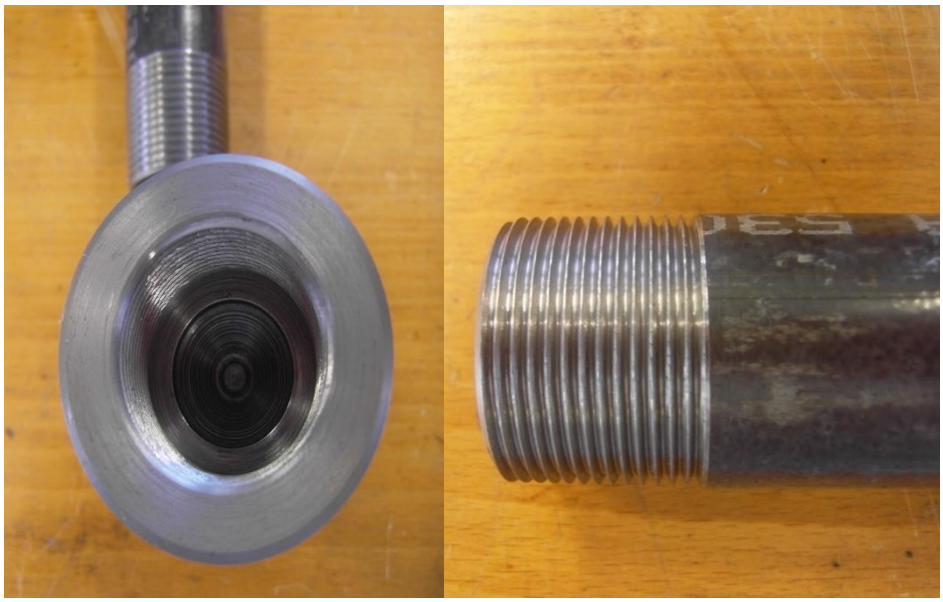

Figure 4.5: Small scale 1-inch API, left side female and right side male.

The thread geometry is specified by A.P.I., (2008) (5B Specification for Threading) and is within the tolerance of the *National Pipe Thread Taper* (NPT) described in ASME Codes and Standards. The box dimensions as well as the mechanical properties of the API Grade B material used for all API Line Pipe samples, are specified by A.P.I., (2004) 5L specification for line pipe thread. Although not optimized for fatigue service, this connection is selected because it is widely available as a standardized connection type. Moreover, it is available in a wide diameter range; API Line Pipe coupling are available with a male diameter starting from $D_p = 10.3\,mm$ (1/8") to as large as 508 mm (4.5"). This makes it possible to perform small and larger scale tests on the same connection type. As a comparison, the API buttress connection is only available starting from a diameter $D_P = 114.3\,mm$. A final practical reason to use the API Line Pipe connection is the make-up torque which is lower than other standard API connection types of the same size. Consequently, the make-up can be performed in laboratory conditions by the torque described in section 4.2.

Two sizes of API Line Pipe connections are tested: the 1" and 4.5" size. The 1" connection has a pin diameter $D_P = 33.4\,mm$, for the 4.5" size $D_P = 114.3\,mm$. The pin wall thickness WT, box diameter D_P, box length L_b(as in figure 4.6 and figure 4.7), and the number of threads per inch tpi for both connection sizes are given in table 4.2. Both the minimum specified material properties and values obtained by tensile testing are summarized in table 4.3. The tabulated values are the mean of three tensile test. For 1" specimen, a tubular specimen is tested, while the properties of the 4.5" connection are determined by five tests on strip specimens and ten round specimens.

The 1" size is extensively tested in both static and fatigue tests to validate the finite element model that will be described later and also 4.5" size tested for fatigue. The 1" size samples are easy to handle and to modify. Hence, large number of fatigue tests is carried out on this connection size to study the influence of cyclic load and variable load on its fatigue life.

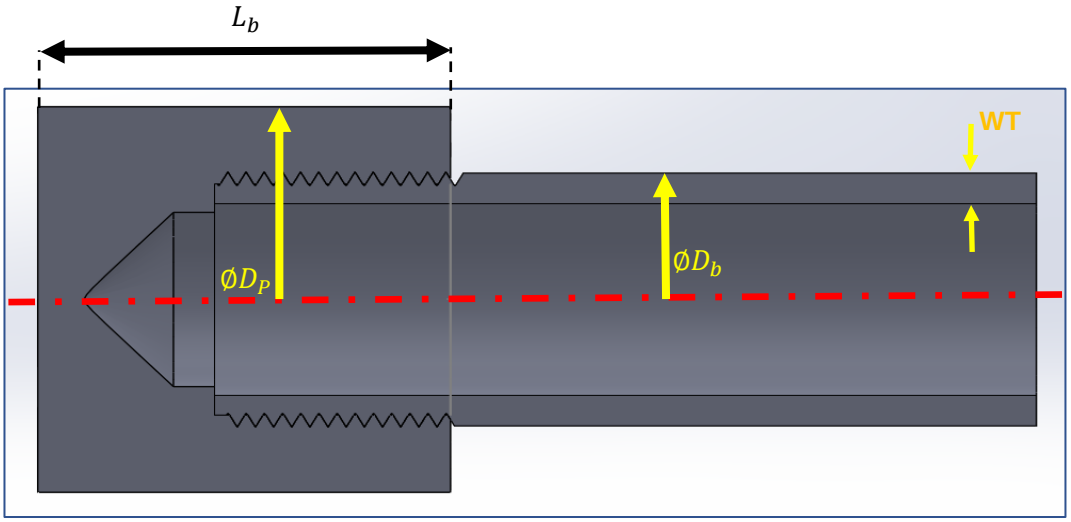

Figure 4.6: Schematic view of the API Line Pipe connection.

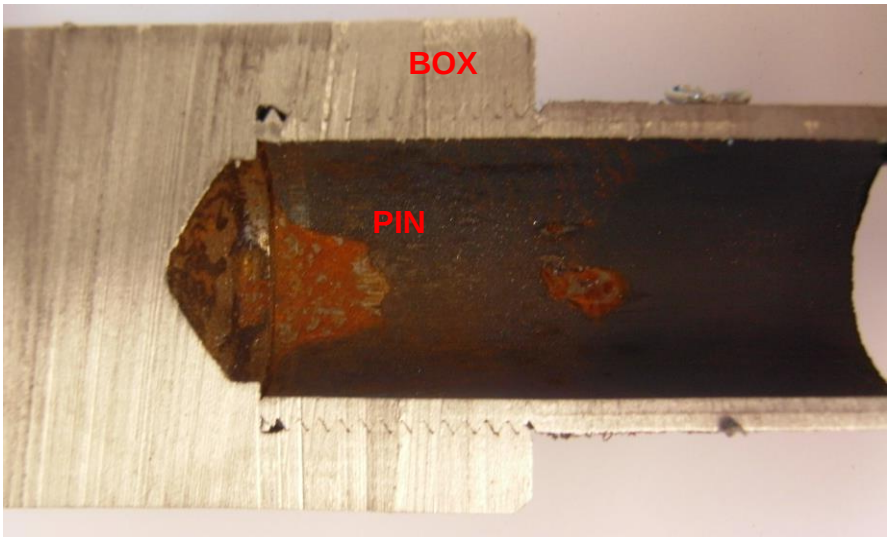

Figure 4.7. Cross-section of 1-inch pipe (Pin and Box).

Table 4.2: Geometrical properties of the used specimens.

Connection type	D_p [mm]	WT [mm]	D_b [mm]	L_b [mm]	tpi	Thread type
1" API Line Pipe	33.4	3.4	40.0	66.7	11.5	Triangular
4.5" API Line Pipe	114.3	6.0	132.1	114.3	8	Triangular
4.5" BSPT	114.3	6.0	132	114.3	11	Round

Table 4.3: Material properties of the test specimens.

Material	σ_y [MPa]	σ_{UTS} [MPa]	ε [%]
API Grade B: minimum specified	241	414	27.0
API Grade B: 1" samples	356	482	31.1
API Grade B: 4.5" samples	355	502	30.9
St minimum specified	185	290	18
St33: 1" BSPT sample	285	410	>20

4.2.2.2 BSPT connection

The second connection type used in the experiments is the British BSPT connection as specified by (European Committee for Standardization, 2004) and illustrated in Figure 4.8. In this T&C connection, only the male threads are parallel, while the female thread is straight. The connection uses round triangular threads with thread angle of 55° and 11 threads per inch.

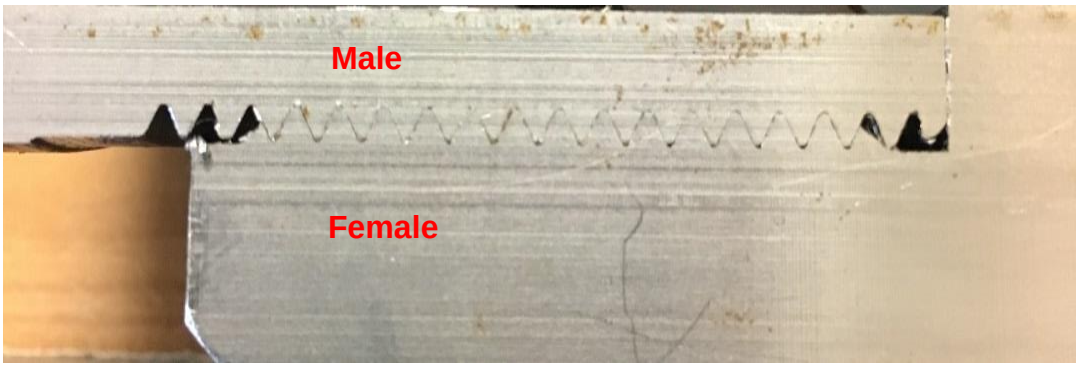

Figure 4.8: Schematic view of the BSPT connection.

The test specimen used in this study have a nominal size of 4.5" or $D_P = 114.3\,mm$, so they can be tested in the same setup as the 4.5" API Line Pipe samples. The other sample dimensions are summarized in Table 4.1, the material properties are given in Table 4.3.

4.3 Static tests

4.3.1 Overview of the static tests

The performed static test is schematically summarized in Table 4.4, first the result of the torque test is presented, performed on a 4.5" API Line Pipe connection using a torque machine. These tests are used to characterize the make-up behaviour of the connection. The test sample is prepared in such a way that an additional tensile test can be performed after make-up.

Table 4.4: Overview of static test.

Static tests			
	Torque Test	Axial Tension	Axial Tension
Setup	Torque Wrench	Instron 100kN	Instron 100kN
Connection	4.5" API Line Pipe	4.5" API Line Pipe	1" API Line Pipe
Number of test	4	2	20
Measured signals	• Strains • Torque • rotation	• Strains • load	• Strains • load

4.3.2 Torque test

4.3.2.1 Setup description

To make-up a threaded connection properly, it is necessary to accurately control the applied rotation and to measure the resulting torque. In order to perform fully instrumented make-up tests with this setup, several parts are modified or added and its original capacity is increased. The make-up creates an effect called preloading between the pin and box, which cause pre-tension between the thread in order to distribute the load more equally between the thread and increase the fatigue life of the connection, further explanation will be given in chapter 5 regarding preload and the effect on the connection and performance of the thread.

The resulting torque-turn graphs of the tests will be shown and discussed in detail in chapter 5 and 6. The number of rotations is put to zero at the point where the torque start to increase, this is the so-called hand-tight situation. The torque increase during the first 0.4 rotations remain limited. This is because every connection has some geometrical deviations and the connection needs to settle before the threads of male and female are completely in contact with each other.

After the total number of 1 make-up turn a torque value of about reached 1200 Nm is reached in both two test. This value of 1 rotation lays within the specified 1 to 3 make-up turn according to API 5B (Spec, A.P.I., 2008. 5B Specification for Threading) and the measured make-up torque of 1200 Nm confirms API5C3 (Bull, A.P.I., 1994. 5C3), that specifies the make-up torque should be between 1149 Nm and 1915 Nm and for 1 inch API make-up torque should be between 140 Nm to 190 Nm, the optimal torque for 1" API pipe is 152 Nm.

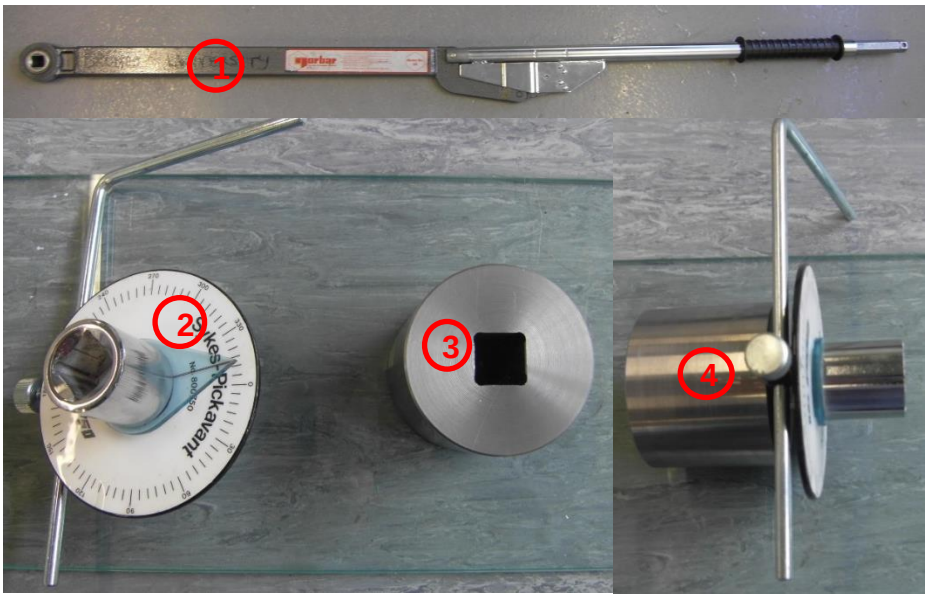

Figure 4.9: Schematic view of the torque machine.

The most important modification made to the set-up was the toque wrench. In order to apply the required make-up force to threaded pipe connection a few part must be crafted and designed as it can be seen in figure 4.9 which transfers torque to the pipe (i.e. part 3 in figure 4.9). The new adapted setup is presented in figure 4.9. the test specimen consisting of a pin and box, the special left hand side threaded socket (3) were made to be screw on the top of the male section, the torque meter device (2) is fitted on the top of the socket (4), the assembly can be seen in number 4, using the torque wrench (1) can be fitted on top of the torque meter and then applying the right torque to the connection using the wrench. The torque wrench has a capacity of 1300 Nm, and the maximum test specimen length (pin and box) is 600 mm.

The test specimen is instrumented with 12 strain gauges at the positions shown in figure 4.10. Strain gauges 1 to 6 are attached in outer surface and strain gauges 7 to 22 are attached to the inner surface of the pin.

Before attaching the strain gauges, it is very important to prepare the specimen and get them ready for installation, as can be seen in figure 4.10. This require using sand paper to clean the black coating of the pipe. If the strain gauges attached directly on the coating of the pipe the strain gauge are not able to collect all the data from the surface as the coating surface is not a smooth surface. Strain gauge installation procedures have been explained in more detail by MicroElectroMechanicalsystems (MEMS) (TML. 2017).

Next step is to clean the surface using sand paper and acid in order to make the surface smooth as possible. This process should be done in quick timing as the acid is very corrosive liquid and eats through the metal and eventually effect the strength of the material. Immediately after using the acid, alkaline should be applied to the surface using sand papers to cancel the effect of the acid on the metal, the final step is to dry the surface and apply the strain gauges to the marked locations. As can be seen in figure 4.10b all the strain gauges are marked which make tracking the strain gauge performance during the test much easier as will be seen.

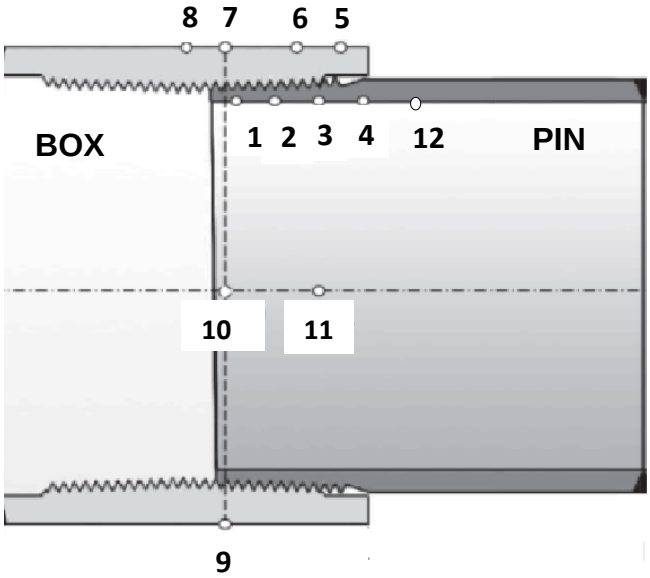

Figure 4.10: View of the test specimen with the strain gauge locations.

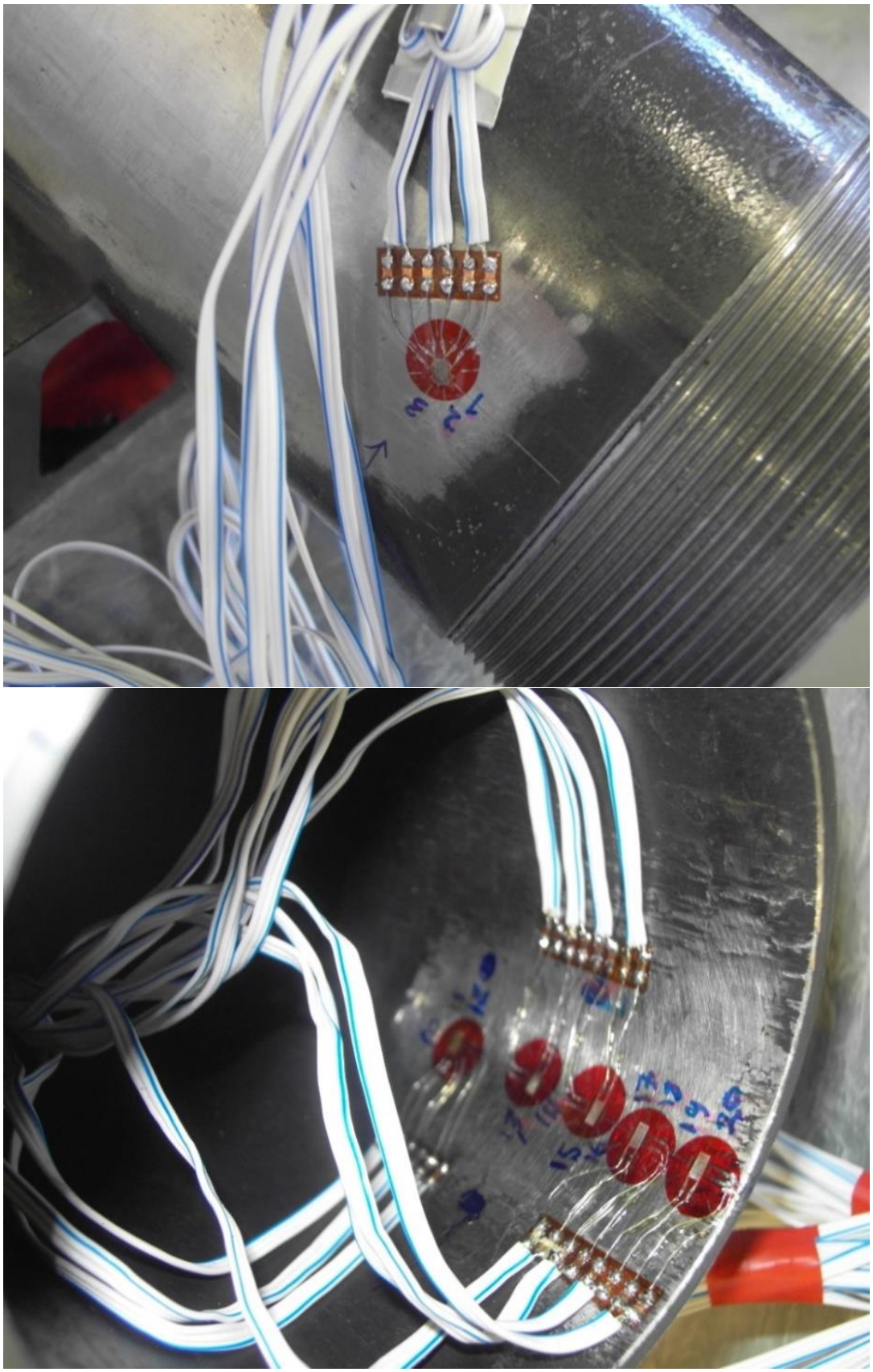

Figure 4.10b: Strain gauges' location on the pin.

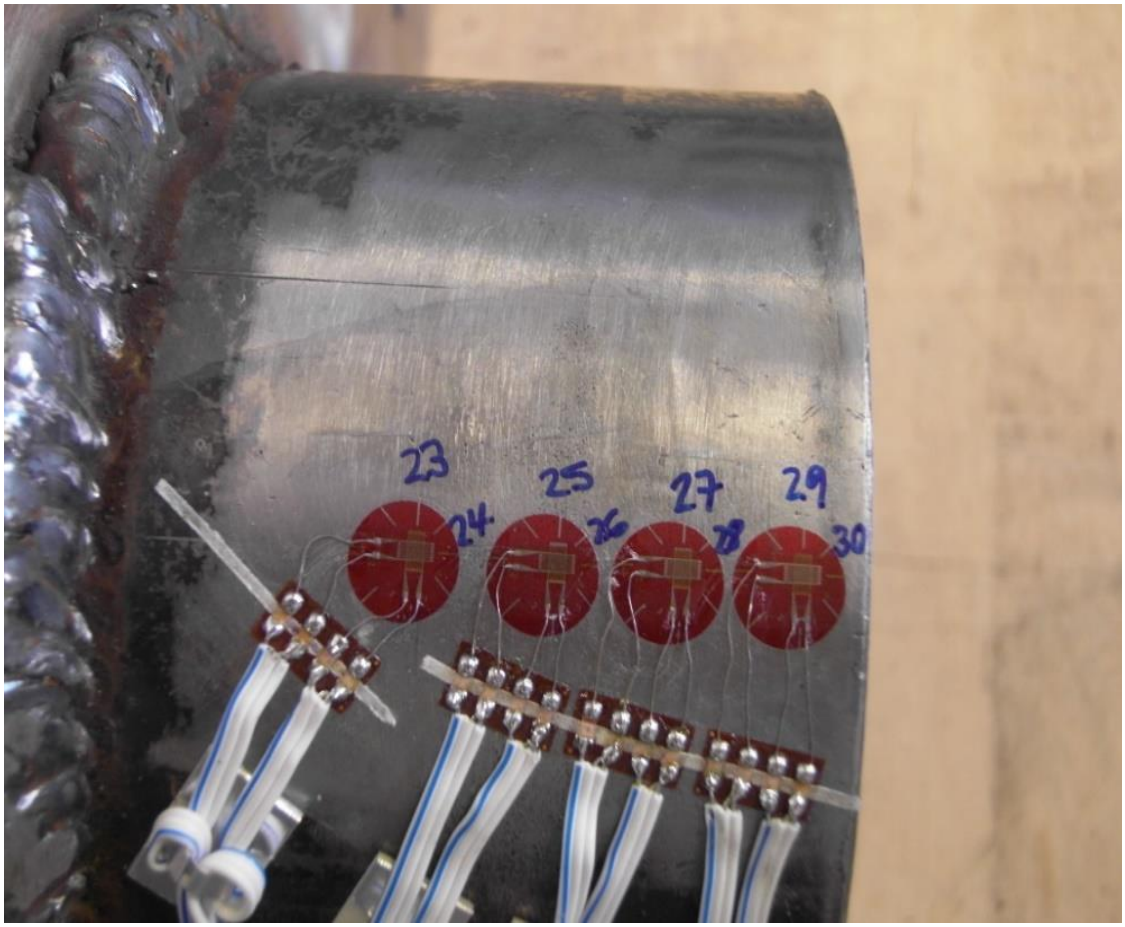

Figure 4.11: Strain gauge location on the box.

Strain gauges 23 to 30 are attached to the outer surface of the box as can be seen in figure 4.11. Strain gauge 1 to 9 are biaxial cross gauge (type TML FCA-3-11 with a gauge length of 3 mm for mild steel applications) to measure both axial and circumferential strains, gauges 10 and 11 are triaxial rosette gauges (type TML FRA-3-11 with a gauge length of 3 mm for mild steel applications) that additionally measure the shear strain.

Gauges 1 to 8 are located on the same circumferential position, while gauges 9 and 10 are located on the box at the same axial position as gauge 7, at respectively 180° and 90° along the box circumference. Strain gauge 11 is on the pin at the axial position of gauge 3 but at 90° along the circumference.

For the $1''$ pipe the test specimen is instrumented with 8 strain gauge at the position shown in figure 4.12. The strain gauge 1 to 4 are attached to the outer surface of pin and strain gauge 5 to 8 are connected to the outer surface of the box. The strain gauge 1 to 8 are biaxial strain gauge (type TML FCA-3-11 with a gauge length of 3 mm for mild steel applications).

Gauge 1 to 8 are located on the same circumferential positions. It is important to mentioned installing strain gauge inside the 1-inch pipe was not possible due to the

small circumferential area, alternatively there was an option of using wireless strain gauge but due to lack of funding and equipment this option was not available for this research. 8 strain gauges were used, two biaxial on the male near to the last engaged thread on the male pipe and two biaxial on the outside of female surface mid-point.

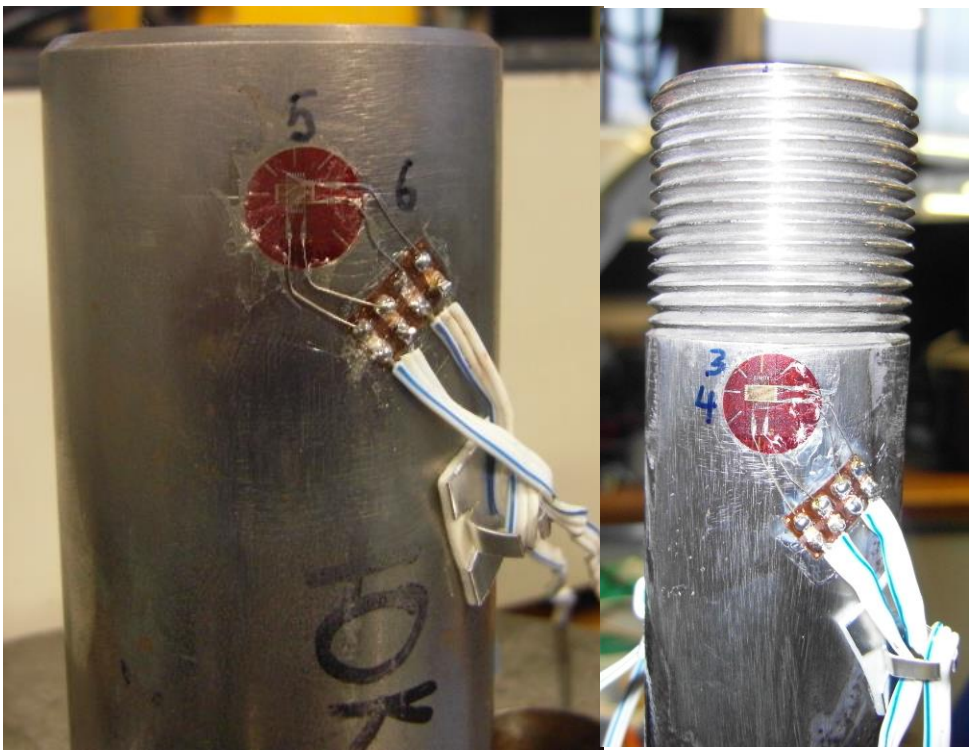

Figure 4.12: Strain gauge location on male and female 1-inch pipe.

Figure 4.13: Solatron 3535D Scorpio, on left hand side data logger and on the right-hand side module card.

The first data logger used is shown in figure 4.13. The solatron 3535D Scorpio" data logger was used to activate/energise the strain gauges and collect data. This device interprets the resistance change from the strain gauges and sends an output to a computer where 'Scorpio' software was used to register and display the results, labelled strain gauges first must be connected to the module card, as can be seen in figure 4.13 on the right-hand side and after that the module card must be connected to the actual data logger. The problem occurs with this data logger when the test moved from static to cyclic load, since the device was old it was not capable and fast enough to collect all the data during a cyclic testing and most of the test data were lost, this data logger is good enough for static test only. Therefore, for cyclic testing the new national instrument device was used as shown in figure 4.14.

All signals from the loadcell and strain gauges are recorded at a frequency of 10 Hz by a 16 bit 24 channel data acquisition system with internal conditioner type NI SCXI-1001, manufactured by National Instrument (NI). Figure 4.14 showing the National Instrument chassis and a module.

Figure 4.14: National instrument device.

Since there was a large number of strain gauge used (in total 12 strain gauges), it is important to label them so during the test reading, analysing data would be easier. A new finding was, strain gauge failure happens during test for which the explanation will be given in chapter 5. Figure 4.15 show the strain gauge connection and figure 4.16 show the reading capturing by PC from national instrument chassis.

Figure 4.15: 34 strain gauge is connected to the chasse and module.

As can be seen in figure 4.15 $NI\ cDAQ-9174$ chassis is used with four NI 9235 modules where all the strain gauged were connected. The chasses are connected to PC with a USB cable. Using LabVIEW software as shown in figure 4.16 in order to monitor the performance of the fatigue during the test.

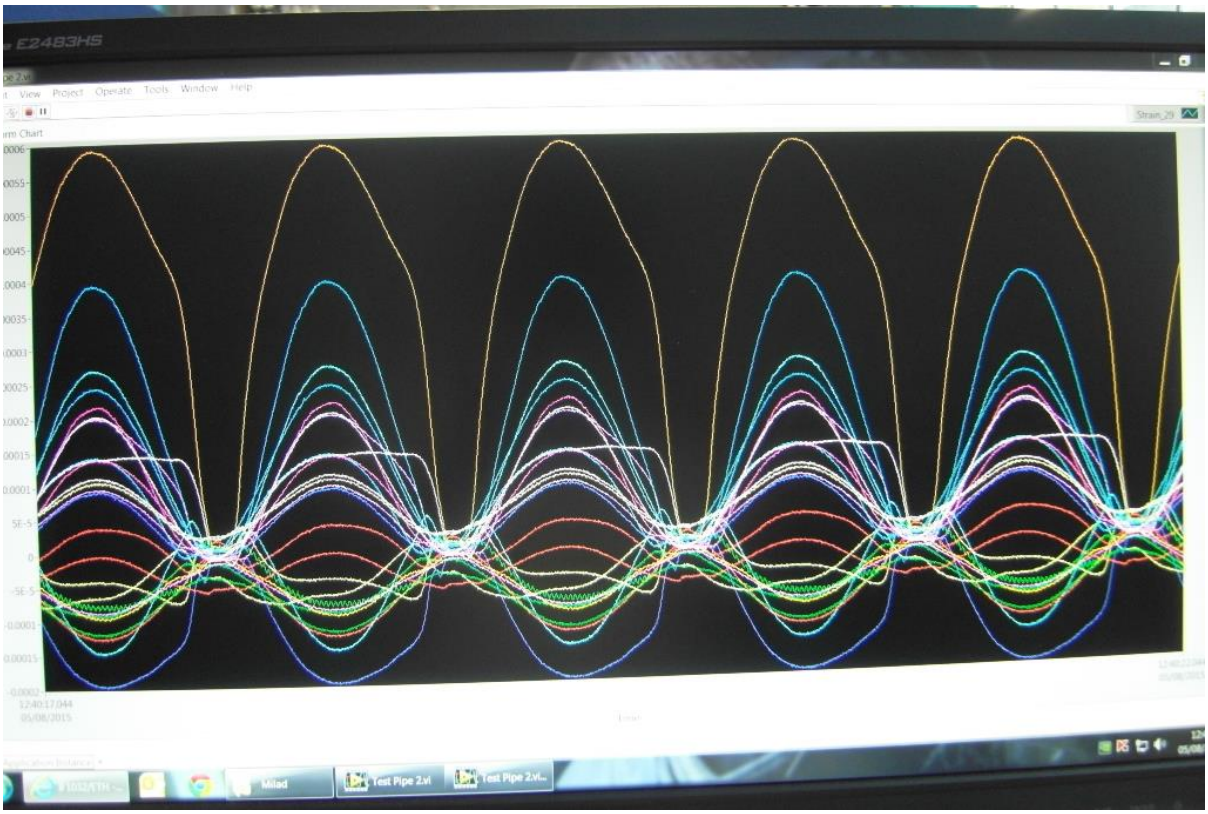

Figure 4.16: Strain gauge reading done by PC from national instrument chasses.

Figure 4.16 show the strain gauge during a cyclic load, as mentioned earlier marking strain gauge it helps the researcher to monitor the performance of the strain gauge and from the legend it can be seen which colour is related to which strain gauge, as an example the dark green line in the figure 4.16 is related to strain gauge number 29 which if check figure 4.11 is connected on female section.

During the test, it was observed the fatigue occurs on the actual strain gauges on the pin section, which further explanation is given in chapter 6 and therefore no data were collected by that strain gauge, strain gauge in direction which the load were applied to the sample were the one effected by fatigue, for example strain gauge number 12 on the outer surface of the pin were the one effected by fatigue and stopped recording data as a result. Fatigue of a strain gauge is an interesting topic for future research. The strain gauges on the male section were the first strain gauge to fail and interestingly the strain gauge lay in the cyclic load direction in this case the axial direction was the one which both gauge and test piece failed.

4.3.2.2 Measuring relevant to the thread displacement

The displacement is measured relevant to the cross head of the Instron machine. A new device used from Micro-Epsilon which measures the displacement more accurately is relevant to the threaded joint connection.

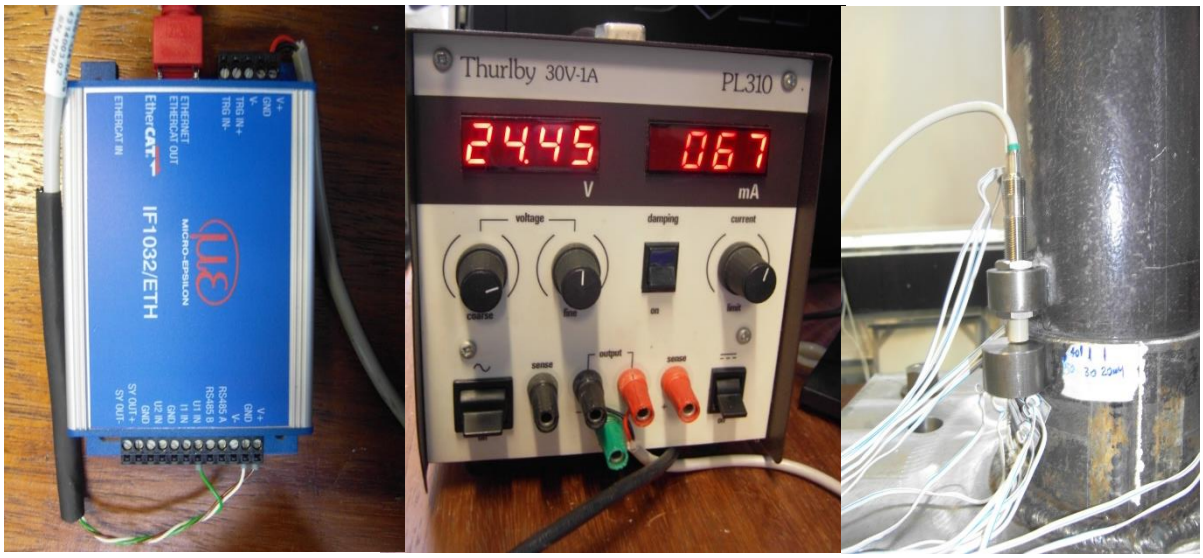

Figure 4.17: Micro-epsilon module on the left-hand side, the amplifier in the middle and the micro-epsilon sensor on the right-hand side.

As can be seen in figure 4.17, on the left-hand side the module (IF1032/ETH) is connected to the amplifier for which current and voltage must be set. The sensor is connected to the module and the module is connected to a PC through a USB cable.

The module is useful since it can measure the displacement in micro-millimeter. The only source of measuring displacement is through the cross head of Instron machine, this device will give us more accurate displacement relevant to displacement of the male and box and not the cross head. Micro-epsilon sensor can measure local displacement more accurately. The results will be discussed in chapter 5.

4.3.2.3 Test specimen configuration

The test specimen configuration has dimensions according to table 4.2. The total length L_{tot} does not exceed 600 mm. The length of the flanges L_f at both end 80 mm. A complete API Line Pipe coupling with box length $L_b = 114.3\,mm$ welded to the left flange is shown in figure 4.18.

It is very important to make sure no deformation or failure occur in the welded region as this is not the area of this research. The thick base plate was chosen for avoiding bending of failure in the plate as shown figure 4.18.

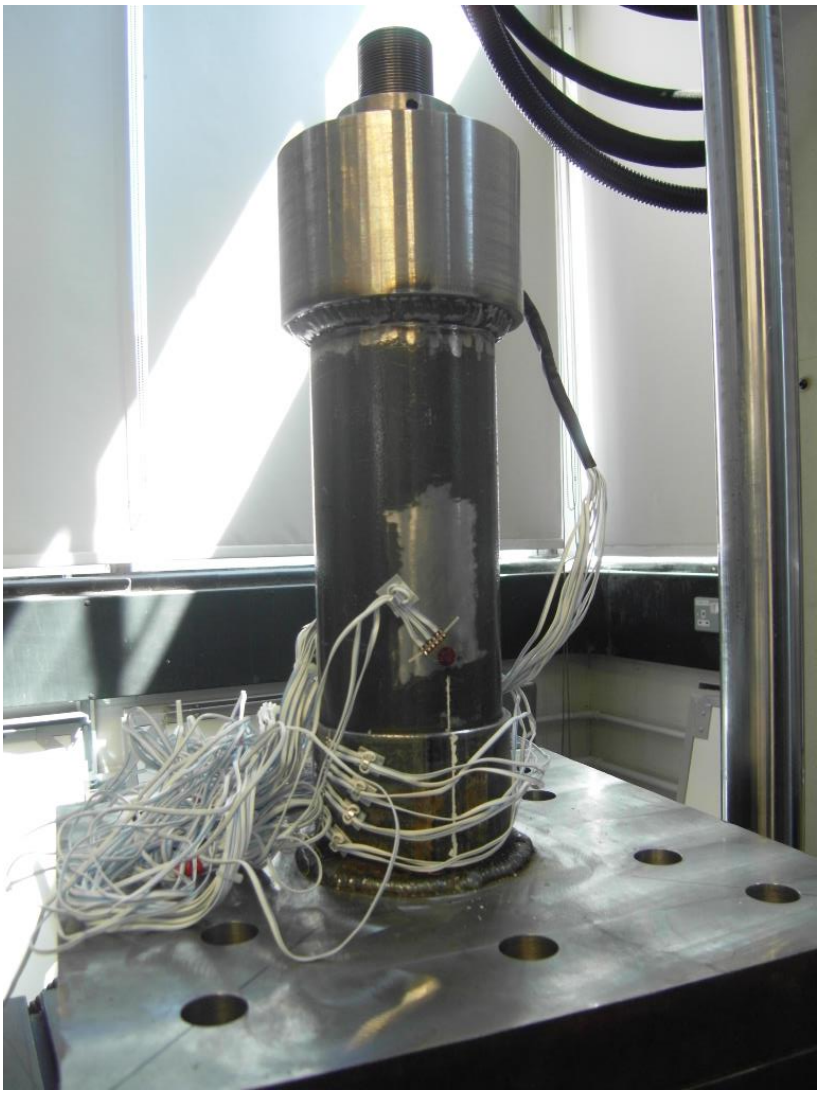

Figure 4.18: Test specimen instrumented with strain gauges.

In order to fit in the setup, the pipe length of the pin L_b should be smaller than 136 mm. to avoid any influence of the boundary conditions in the threaded region of the specimen, L_b should exceed a minimum required value by Eq. (4.1), with R the pin outside radius and WT the pin wall thickness.

$$L_P \geq 4.\sqrt{R.WT} \quad (4.1)$$

This distance is defined in the shell theory (Vinson, 1974) as the so called bending boundary layer for, which 99.4% of any oscillation in a tube caused by its boundaries is decayed. For the 4.5" API Line Pipe pin dimensions, this results in a minimum length of 74 mm, for the test specimens $L_p = 130\ mm$ which makes that the configuration fit in the setup without significant disturbance to the boundary conditions.

4.3.3 Axial tension

4.3.3.1 Setup description

The flanges welded to the test specimen are designed to be compatible with the $100\ kN$ Instron servo-hydraulic universal testing machine. Hence, after the make-up the test, the sample was prepared for an axial tensile test.

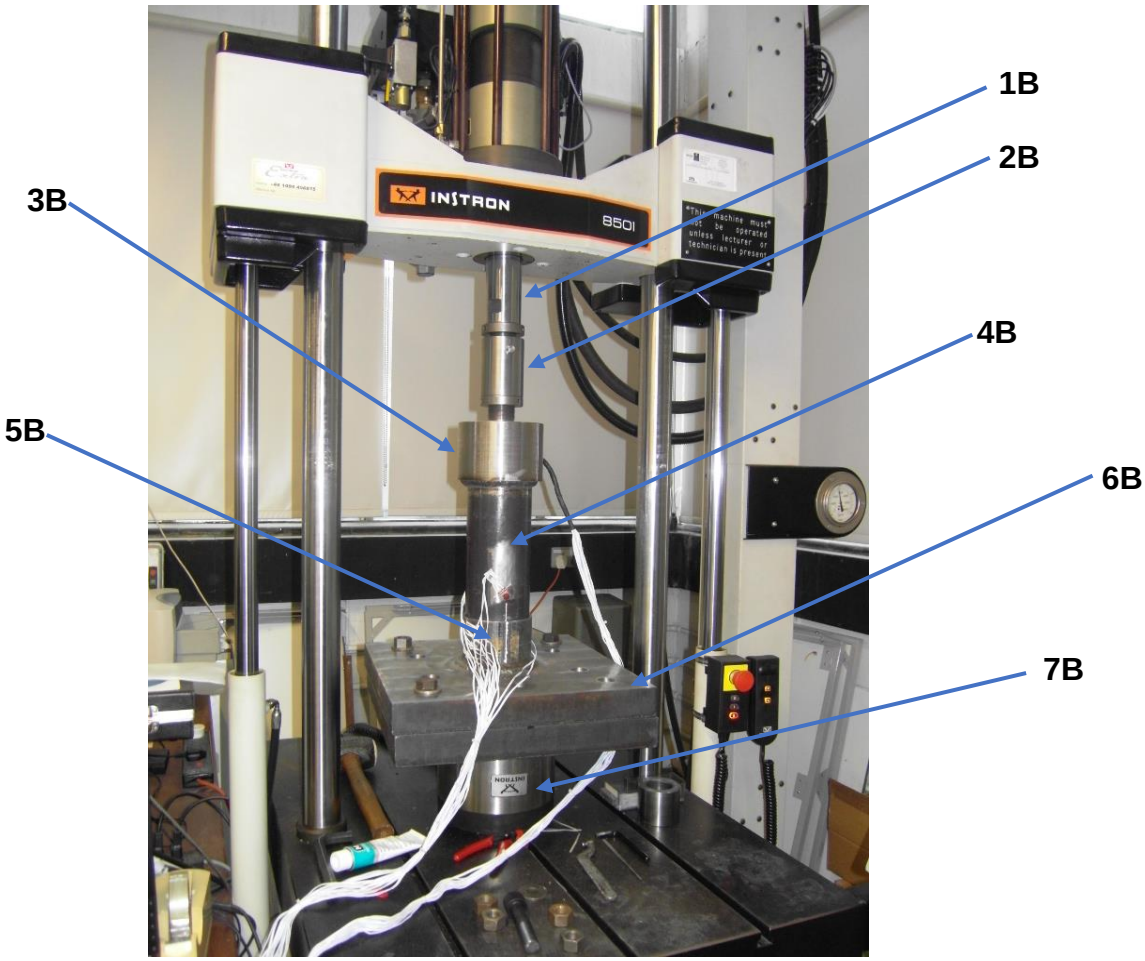

Figure 4.19: Axial tensile test on 4.5" API Line Pipe Connection.

The final test setup appears in figure 4.19. The specimen, consisting of the male (4B) and the female (5B), is placed vertically in the test rig. To compensate for any misalignment errors, the sample is connected to ball joint (3B) at the top and square plate at the bottom (6B). The lower plate is connected to the load cell (7B) that measures the load applied by the vertical hydraulic actuator (1B), the connection between pin connector and vertical hydraulic actuator (2B). During the test an axial tensile load is gradually applied. The corresponding strains measured by the strains gauge configuration according to figure 4.10 and figure 4.11 are continuously logged.

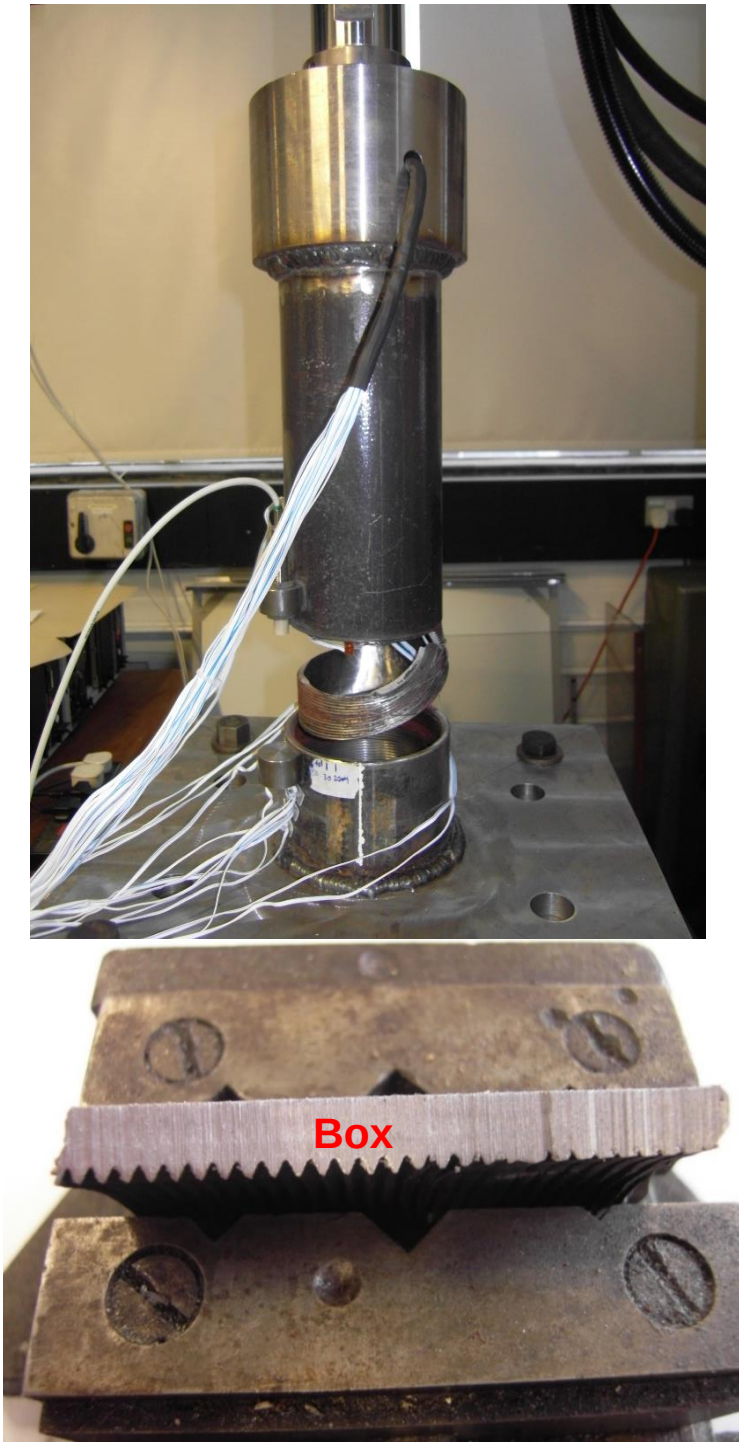

Figure 4.20: (Top) failure due to cyclic load on 4.5-inch pipe. (Bottom) box thread bending.

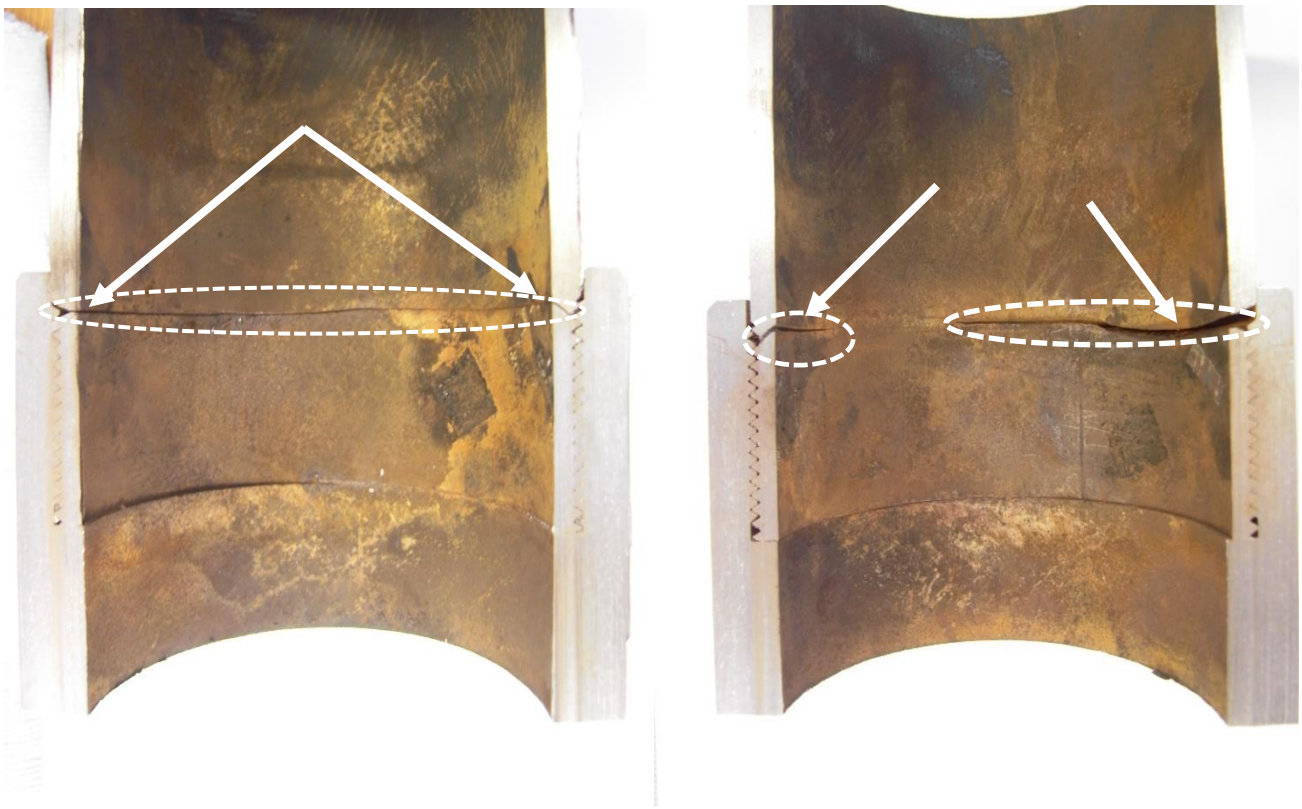

Figure 4.21: Crack propagation circumferentially around a 4.5-inch pipe.

Figure 4.20 shows a 4.5-inch connection failure due to cyclic load. As it has been established in chapter 2, failure always happens in the pin and at the LET, where the stress concentration is highest. It shows a crack initiated at the very last engaged thread in the pin and has propagated circumferentially around the pipe. Figure 4.20 is a BSPT thread connection, the picture at the bottom of figure 4.20 shows a cross section of the box cut out for analysis. It is very clear thread bending occurs as some of the teeth lost their shape due the pin was pull out from the socket.

Figure 4.21 is the API threaded connection. The cross section of a 4.5-inch male and 5.5-inch female section. The figure on the left shows the crack has propagated from the LET and grown circumferentially around the pipe. On the other hand, the right-hand side figure 4.21 shows the crack propagated at the LET on the both sides, in which the propagation is not uniform. Further explanation of propagations in a threaded pipe connection will be given in chapter 5 and 6.

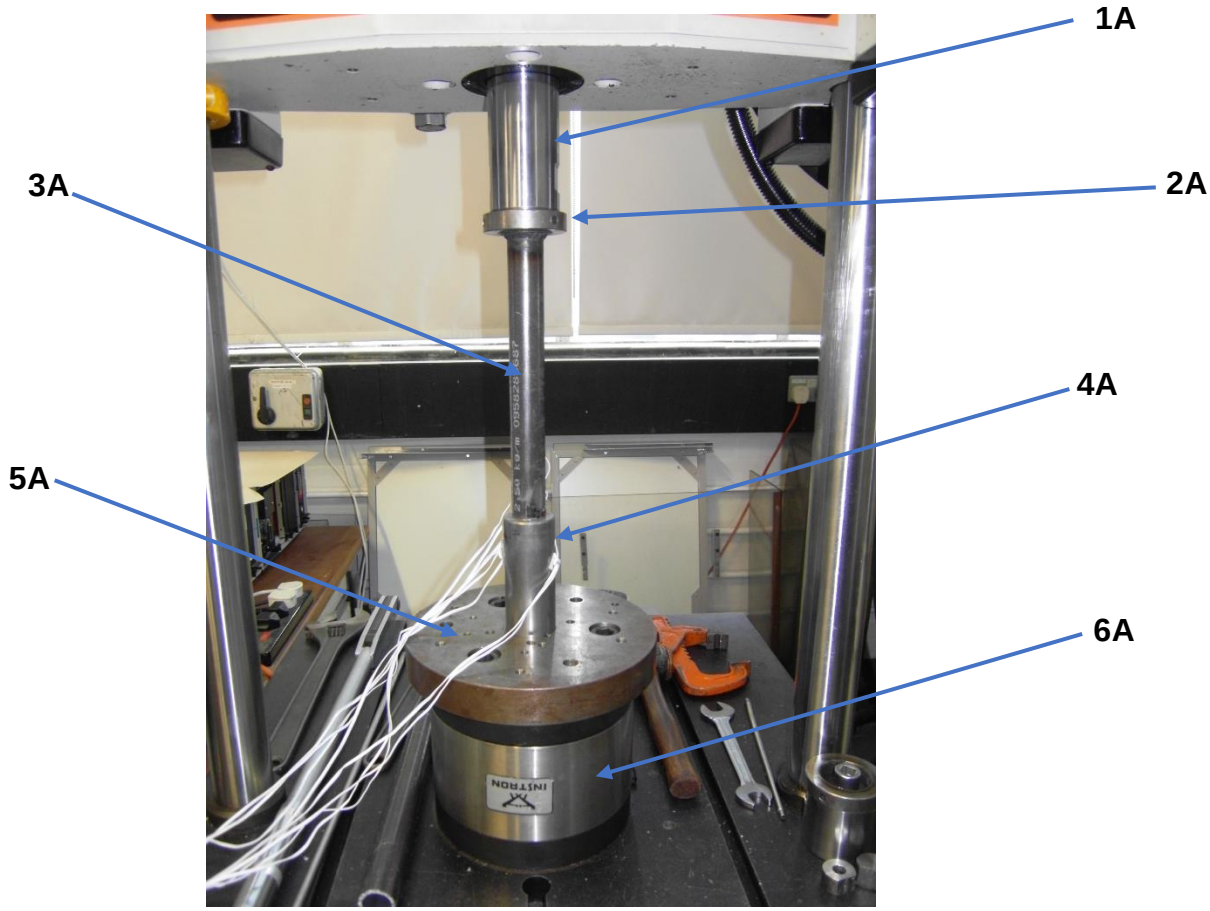

Figure 4.22: 1-inch test setup.

The total test setup in figure 4.22. Refers to a 1-inch pipe, consisting of the pin (3A) and the box (4A), placed vertically in the test rig. To compensate for any misalignment errors, the sample is connected to circular plate joint (5A) at the bottom. The lower plate is connected to the load cell (6A) that measures the load applied by the vertical hydraulic actuator (1A).

As can be seen in figure 4.22 the setup for 1-inch pipe is less bulky and heavier then setup for 4.5-inch test setup, this is due to weight of the sample which influences the connection in long run during the cyclic fatigue test.

Figure 4.23 and 4.24 is the test on 1-inch pipe which serves as validate the 4.5-inch pipe test. That is initiation and failure occurred in the LET, where the stress concentration is the highest and it propagated circumferentially around the pin. Further analysis will be done in chapter 6.

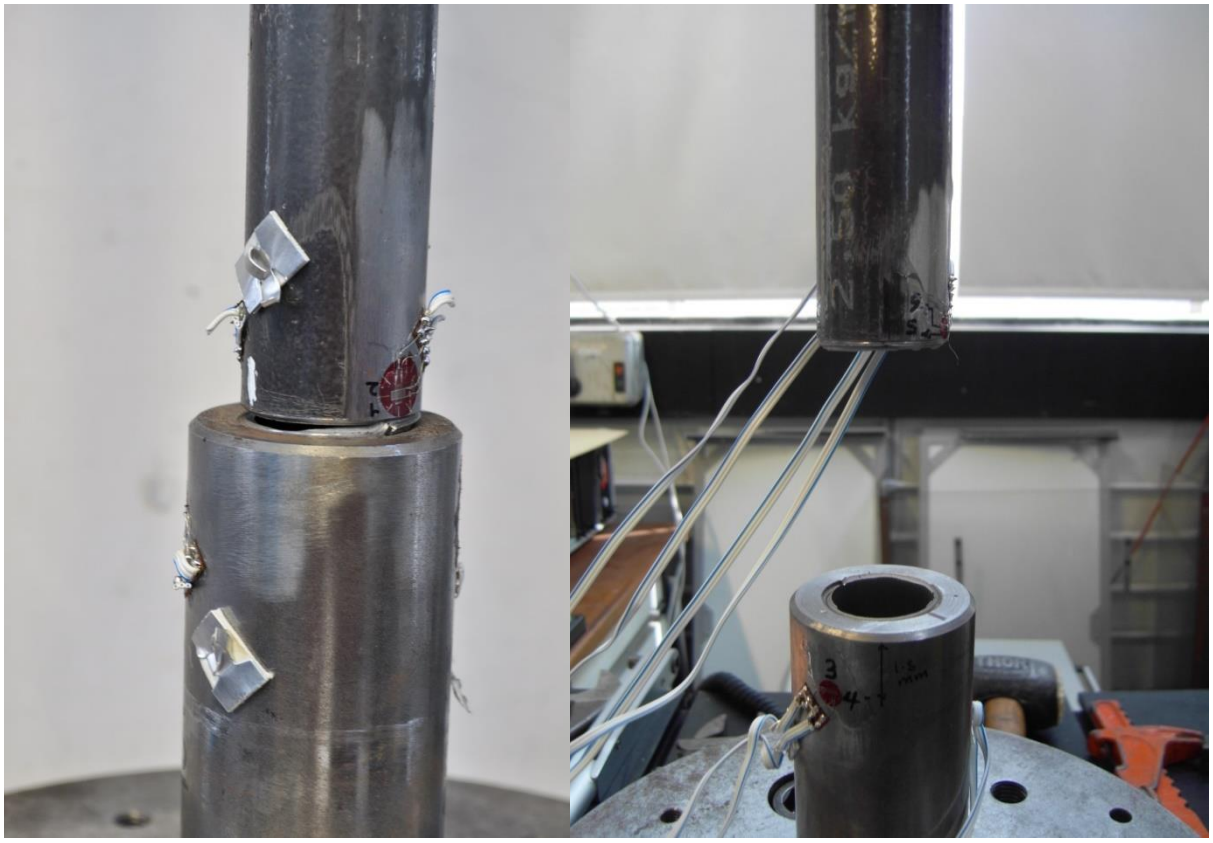

Figure 4.23: Failure in 1-inch API threaded pipe connection.

Figure 24: Failure on the threaded connection pin and box.

4.4 Fatigue tests

4.4.1 Overview of the fatigue tests

In the following sections the fatigue test results are discussed. They refer to figures 4.20 and 4.21, in which two setups have been used. Axial tension fatigue test is performed in the $100kN$ universal tensile testing machine on the $1''$ and $4.5''$ API Line Pipe specimen used in the static torque tests and axial tension test.

Table 4.5: Overview of experimental fatigue tests.

Fatigue Tests		
	Axial Tension	Axial Tension
Setup	100KN Instron	100KN Instron
Connection	4.5" API Line Pipe 4.5" BSPT	1" API Line Pipe
Number of tests	3	20
Measured signals	• load • number of cycle • strain	• load • number of cycle • strain

Reference

- Bull, A.P.I., 1994. 5C3. Bulletin on formulas and calculations for casing, tubing, drill pipe and line pipe properties.
- EN10226-1:2204: E, Pipe threads where pressure tight joints are made on the threads- Dimensions, tolerance and designation, European Committee for Standardization, 2004.
- McHargue, M.C.C.J., ASME Codes and Standards.
- Spec, A.P.I., 2008. 5B Specification for Threading. Gauging and Thread Inspection of Casing, Tubing, and Line Pipe Threads.
- Specification, A.P.I., 2004. 5L, Specification for Line Pipe. Edition March.
- TML. 2017. *TML*. [ONLINE] Available at: http://www.tml.jp/. [Accessed 30 June 2017].
- Vinson, J.R., Structural Mechanics: The Behaviour of Plates and Shells, John Wiley and Sons, New York, p.119, 1974.

Chapter 5 Experimental Results

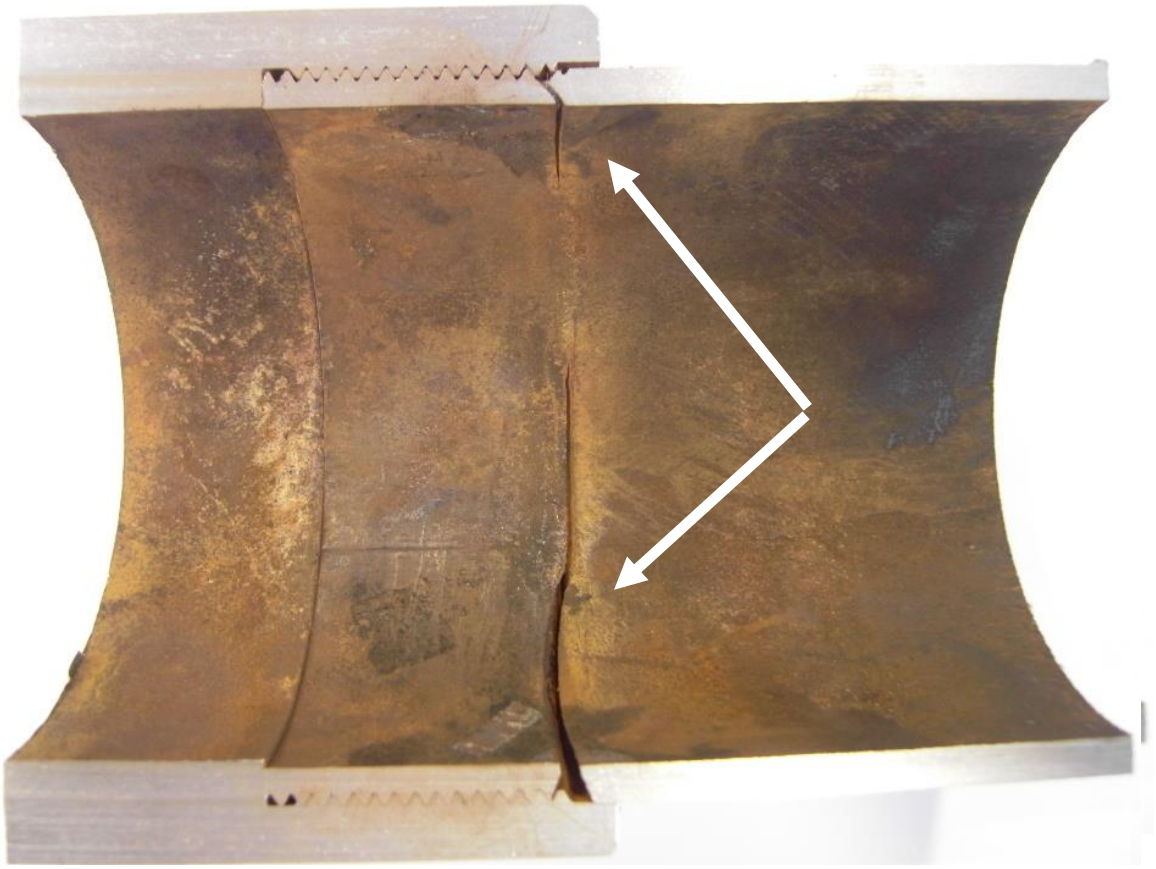

5.1 Summary

In this chapter, the experimental test program conducted in the framework of this study is presented. The experiments are conducted to generate the data needed to validate the numerical model described in chapter 6 and to create a database with fatigue data of threaded pipe connection. The tests have been performed on different setups that are designed and constructed in this study. Next to providing the experimental results, the relevant aspect of the setup developed is discussed as well as implementation of the selected measurement technique of chapter 3 and methodology used to perform the fatigue tests.

In the following chapters, the test data obtained will be used to validate the performed simulations and is analysed more in detail to reveal the general trends in the fatigue behaviour of threaded pipe connections.

5.2 Experimental Test Program

5.2.1 Test program overview

An overview of the experimental test program is given in table 5.1. Both static tests and fatigue tests are performed. Static torque, axial tension tests are performed on threaded pipe connections. Next to this, the torque test is used to determine the coefficient of friction for the contact between the threads of male and female.

Table 5.1: Overview of the experimental test program.

Experimental test program		
Test Types	**Static Tests**	**Fatigue Tests**
	Torque test	Axial tension
	Axial tension	Small scale 1-inch pipe
		Medium scale 4.5-inch pipe
Goals	Model validation	Determining fatigue live
	Determining connection properties	Compare different connection type

Linear-Elastic Fracture Mechanics (LEFM) is the most common method for analyzing fatigue crack growth in structural components. The general assumption is that the relationship between the applied loads and resulting displacements to a component is linear.

Based on LEFM, the Paris law is given by:

$$da/_{dN} = C\Delta K^m \qquad (2.22)$$

The relationship between crack growth rate $da/_{dN}$ and stress intensity factor range ΔK, suggested by Paris and Erdogan, which is widely accepted. In this relationship stress

intensity factor describes the crack tip stress field as a single parameter, and is a function of the nominal stress and geometry of the component. The stress intensity factor also depends upon the mode in which the crack grown, i.e. opening, edge sliding or shear mode. In this research, it is assumed that any significant crack growth we are interested in occurs entirely in mode I (opening mode). The parameters m and C are material properties for inert environment. These material constants are needed so that the crack propagation data from the threaded connections, fabricated from the material, can be interpreted in terms of K.

In the LEFM method for analysis of the crack growth it is assume the yielding and plastic zone size at the crack tip is confined to a relatively small region of the overall component, so that the elastic stress field is hardly affected. It is important when deciding upon the dimensions of the specimens to be tested in order to acquire the constants C and m.

Predicting the occurrence of fatigue in engineering structures is a major challenge as mentioned in chapter 1. In this research predicting fatigue and fracture in threaded joint connection consider to be complex due to load and geometry of the thread. This problem considers to be a closed system problem as there is not visual view on how and where the problem occurs. The step above will be studied in detailed and analysis for predicting fatigue life of threaded joint connection, presented in section 5.5.1.

5.3 Torque and Preloading

The application of preload to threaded connection has long been accepted as a very useful means to improving the life of the couplings. The benefit of preload on these connections is two-fold. First by creating a friction force between the two parts it ensures that the joint stays tightly connected during the service and, secondly, it reduces the load on some of the threads very significantly. The latter effect is very important in fatigue loading as the amplitude of cyclic loading reduced, at the expense of creating a mean stress in the connector.

In the majority of connections used in drill string application, the preload is applied at the free end of the box. This application the pin is torqued against a shoulder on the box, creating a compressive load in the box and a tensile load in the pin see figure 5.1. When an external tensile load is now applied to this preloaded joint, there is a change in the deformation of the pin and box. The pin initially in tension now undergoes further elongation and the compression in the box will reduce. The two deformations are equal as the joint remains in equilibrium.

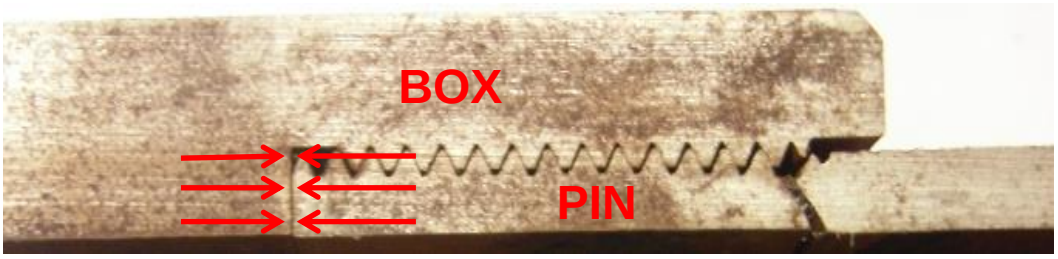

Figure 5.1: preloading and force-displacement in threaded joint.

The concept of preload and its effect on the loading mechanism can be best described by joint force-displacement diagram shown in figure 5.2.

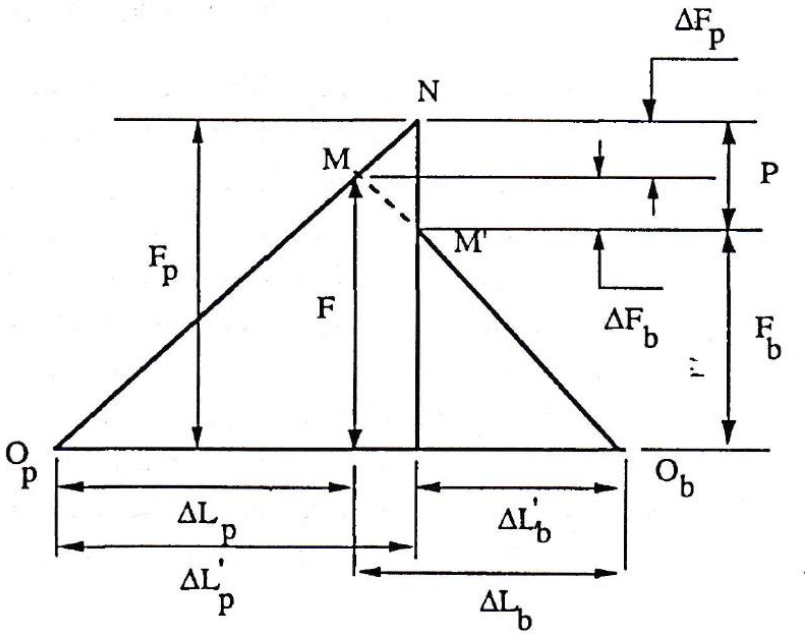

Figure 5.2: Joint Force-Displacement diagram.

Notation for figure 5.2:

F= initial preload

P= External applied load

F_p=Load taken by the pin due to preload and applied load

F_b=Load taken by the box due to preload and applied load

$\Delta L'_P, \Delta L_P$= Elongation of the pin before and after application of external load

$\Delta L_b, \Delta L'_b$=Compression of the box before and after application of external load

ΔF_p=change of load in the pin due to the external load

ΔF_b=change of load in the box due to external load

This figure shows the force and displacement set up in a joint as a result of preload and an external axial force. The line O_pM is the force displacement curve for the pin and the line O_bM is that of the box. Point M is the equilibrium position due to preload only after the initial stretching of the pin (ΔL_p) and shortening of the box (ΔL_P). It can be seen from this diagram that for an equal change in the deformation of the pin and box i.e.:

$$(\Delta L'_P - \Delta L_P) = (\Delta L_b - \Delta L'_b) \quad (5.1)$$

the change in the load in the pin is only a portion (depending on the stiffness ratio between pin and box) of the external force. This implies that any external tension load, P will only be partially absorbed as new added force in the pin (ΔF_P) and partially absorbed in replacing the reduction in the force that the box originally extracted on the pin (ΔF_b). The force of the box on the pin plus the external load, equals the new total tension force in the pin which is greater than the previous total. The change in the pin load, which is also referred to as 'dynamic' load, is, however, less than the external load applied to the pin.

By changing the stiffness ratio between pin and box, one can control the amount of load taken by each component of the joint. For example, a stiffer pin will absorb a larger percentage of the external load. Internal and external diameters of pin and box respectively are two important parameters which determine this ratio are indeed two of the variable which are varied in the parametric study, in order to investigate their effect on load and stress concentration in the joint.

The precise amount of preload in the joint is often difficult to determine or achieve. It has generally been assumed that there is a linear relationship between the torque applied to a threaded coupling and the preload developed in it and there have been a number of different equation derived to be define this constant of proportionality. It is, however, also recognised that preload is not simply a linear function of torque. As a torque is applied to a pin/box connection the box turns and the pin stretches creating preload. Preload is therefore developed as a function of both torque and turn simultaneously and its magnitude varies at different stages of tightening. In view of the local plastic deformations that take place during this process, preload has a very complicated influence. For the present study, it is assuming that the preload is a linear function of torque and that it is sufficiently high for the joint not to be fully unloaded by the external load.

5.3.1 Test results

Two torque test are performed on the same sample by consecutive assembling and disassembling. The resulting torque-turn graphs of the tests are shown in figure 5.2. The number of rotations is put to zero at the point where the torque start to increase, this is so-called hand-tight situation. It can be seen that there is a difference in torque behaviour between the different tests. This is because plastic deformation of the connection occurs during make-up. The most important deformation take place during

the first assembly. This is discussed more in detail in chapter 6, where a comparison is made between the measured strains and strains according to the simulation model.

Nevertheless, both curves show the same trends. The torque increases during the first 0.4 rotations remains limited. This is because every connection has some geometrical deviations and the connection need to settle before the threads of male and female are completely in contact with each other. Due to plastic deformation that took place during the first test, the torque required to force this settlement is smaller during the consecutive tests. The number of rotations needed for this, stay however the same. Once this settlement has taken place, the torque increase becomes more important and follows the path of the linear fit as shown for test 1 in figure 5.4. After the total number of 1 make-up turns a torque value of about 1200 Nm is reached in all tests. This value of 1 rotation lays within the specified 1 to 3 make-up turns according to API (2008) and the measured make-up torque of 1200 Nm conforms to API., (1999) the specifies the make-up should be between 1149 Nm and 1915Nm.

For 1 inch API pipe the torque range lays between 140 Nm to 190 Nm, the optimal torque for 1 inch API pipe is 152 Nm according to, API. (2008).

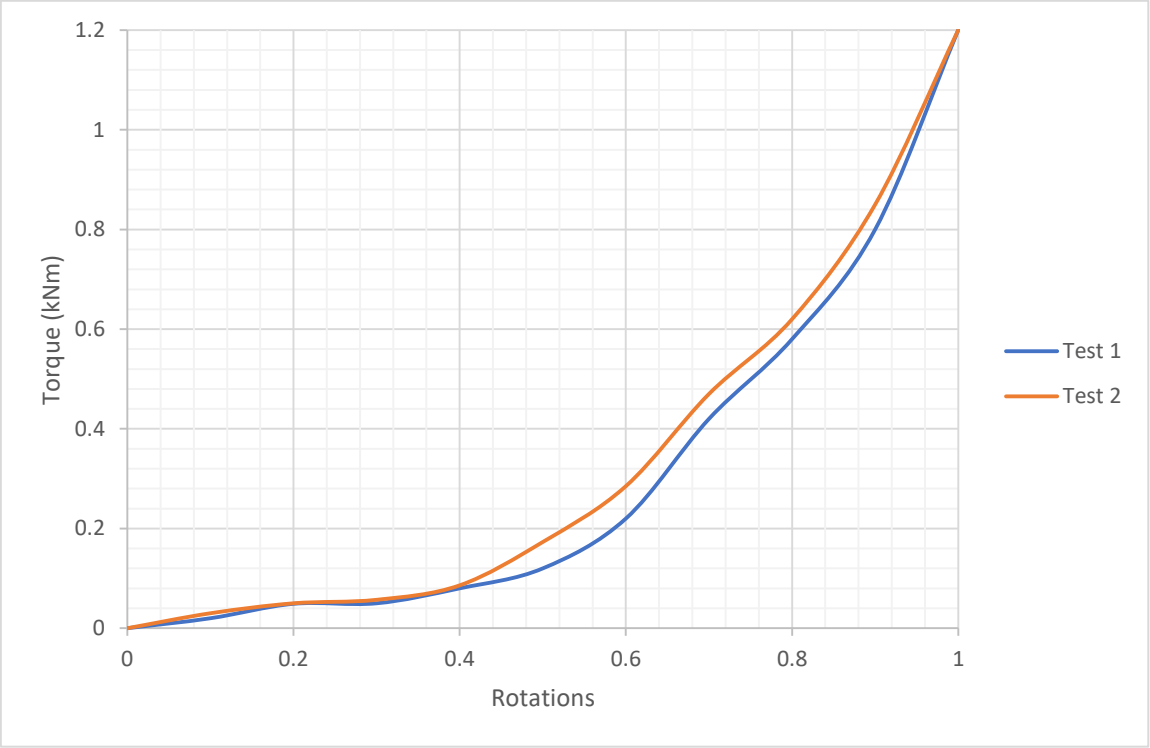

Figure 5.2: Torque vs Number of turns for the two torque tests.

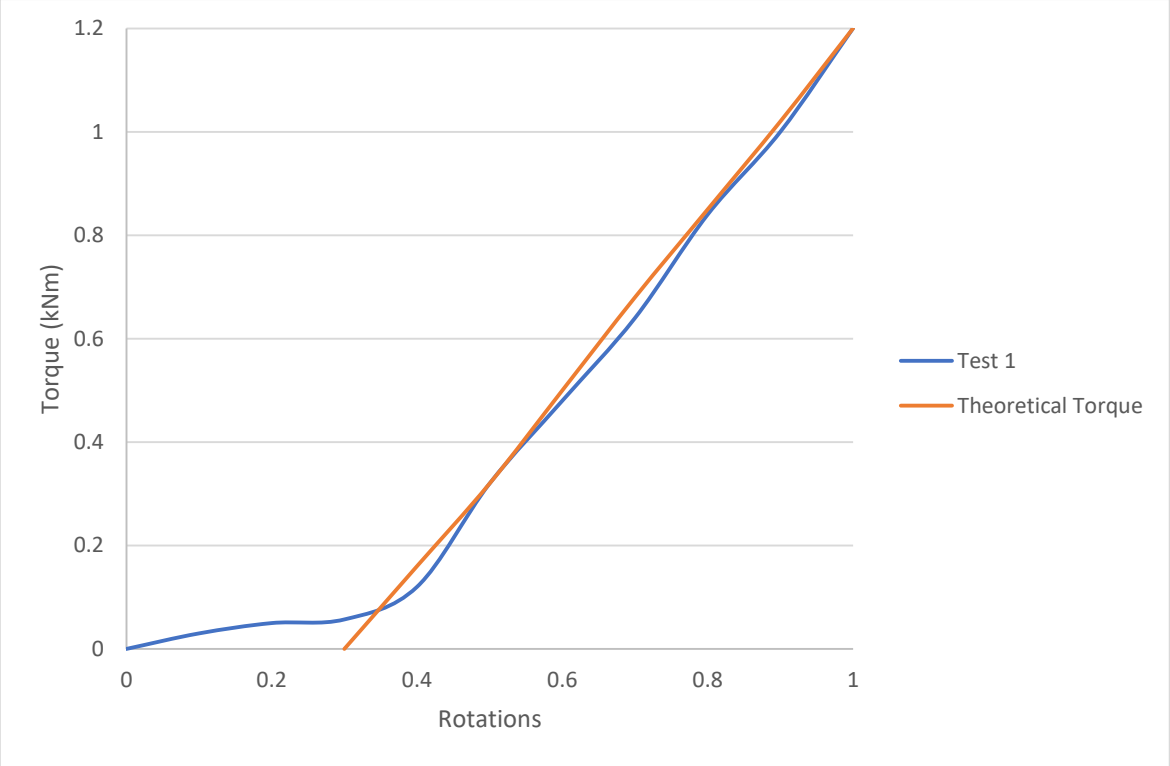

Figure 5.3: Analysis of the torque-turn data of test 1.

The linear fit shown in figure 5.3 becomes zero at a value of 0.3 rotations. Hence, it appears the torque-turn line shifts over this distance and it can be considered that the shifted effective number of make-up turns is only 1 – 0.3 = 0.70. When the make-up behaviour of a connection is analysed or simulated numerically, this effective value of make-up turns should be used as an input since there is a perfect match between the geometry of pin and box in the models. In the previous study Assanelli et al. (1997) an similar shift in torque behaviour was observed for an API 8-round threaded connection.

During the torque tests, strain gauge measurements were made. In figure 5.4 the results of selected strain gauges are shown. For these measurements, the rotation was stopped at certain moments during the make-up in order to get a stable signal. The result are shown for strain gauges 3 and 11, located inside the pin at the same axial distance, but at 90° along on the circumference, and for strain gauge 7 and 9, on the outside of the box at the same axial distance, but 180° rotated. For these four strain gauges the measured axial and circumferential strains are shown in figure 5.4, respectively keyed with a letter A and C.

It can be seen that the corresponding strains on male and female at the same axial position, but rotated over the circumference, correspond well. Differences appear due to the thread helix which changes the axial position of the threads over the circumference, hence influencing the strain distribution.

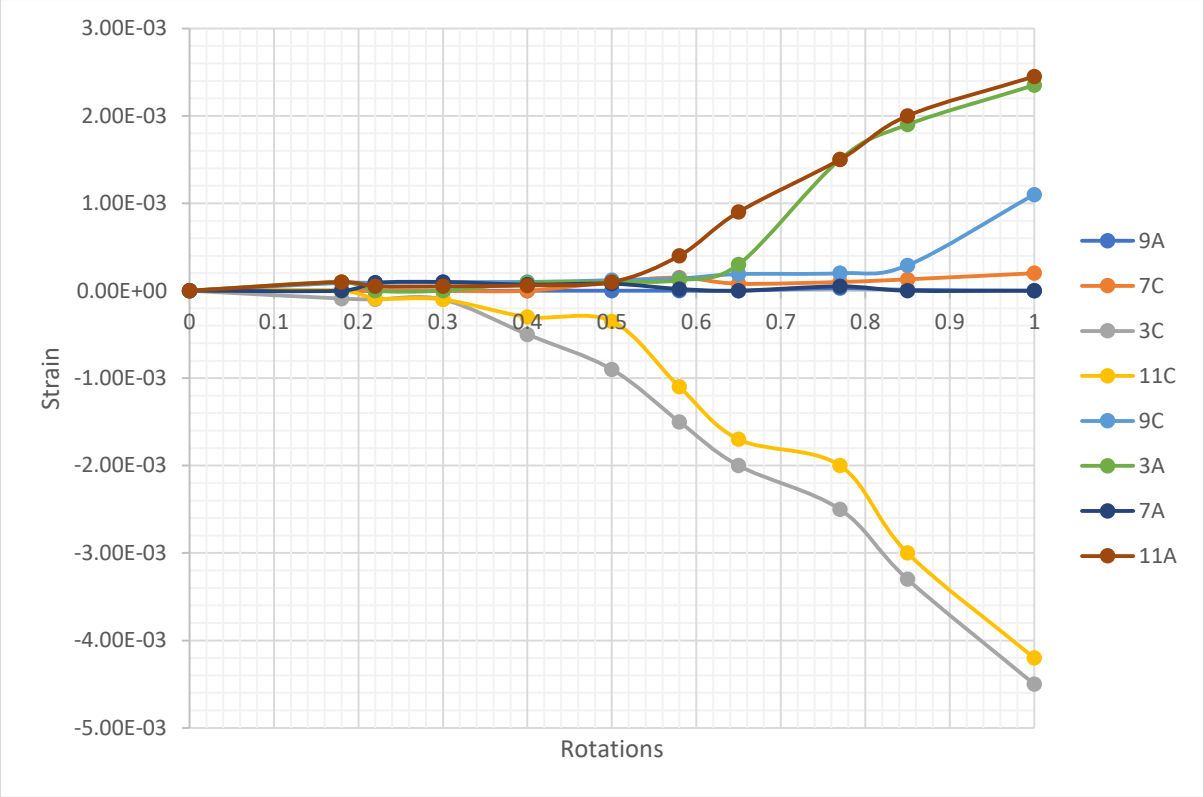

Figure 5.4: Strain measurement during the make-up test.

The resulting strains at the male are much larger than the female, since the box is the more rigid part. The circumferential male hoop strain is negative or compressive, while the hoop strain in the female is positive. This is because the male is shrunk into the female, compressing the male and stretching the female. The strains are not perfect linear function of the number of rotations, as they are affected by small geometrical deviations between male and female. These fluctuations are not unusual, a similar behaviour was reported by Yuan et al (2004).

The strain measured by all the strain gauges will be analysed in more detail in chapter 6, where they are used as a part of validation of finite element model.

5.3.2 Determination of the coefficient of friction

From the torque turn data, the mean coefficient of friction between the contacting threads of male and female can be calculated. This is done by finding the best fit between the experimentally measured and analytically calculated torque versus turn behaviour. The analytical calculating is based on Timoshenko's beam theory (Shigley, 2011). By modifying the analytical solution of the shrink fit of two concentric tubes as shown in figure 5.5.a, this theory can be used to calculate the contact pressure between pin and box of a threaded connection. The contact pressure p between two concentric tubes is given by the following equation:

$$p = \frac{E.\delta}{R_c} \frac{\left(R_c^2 - R_i^2\right).\left(R_o^2 - R_c^2\right)}{2.R_c^2\left(R_o^2 - R_i^2\right)} \qquad (5.2)$$

with R_i, R_O and R_c respectively the internal radius, outside radius and radius at the contact surface between the two tubes. E is Young's modulus of elasticity and δ the radial overlap at the interface between the two tubes.

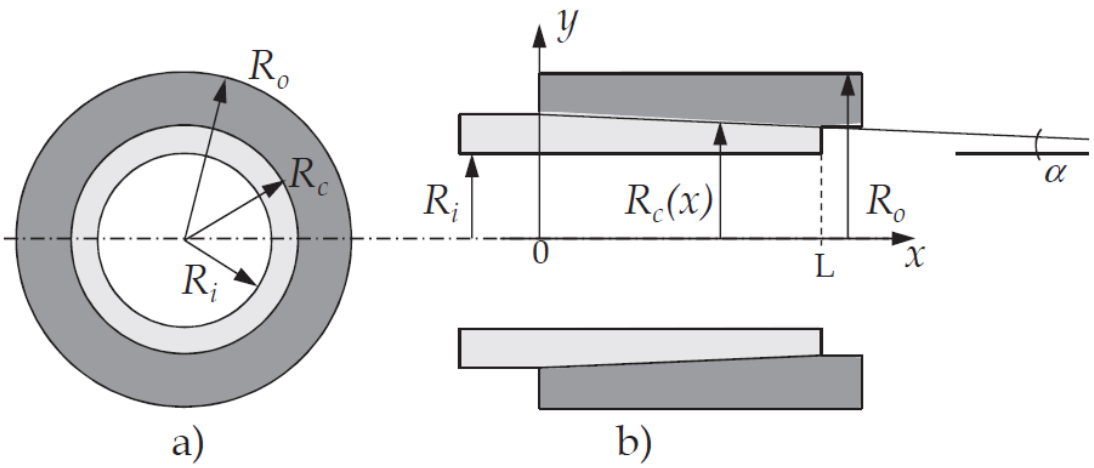

Figure 5.5: Shrink fit symbols (Wittenberghe, 2011).

This theory can be applied to threaded connections since the advancement of a pin into box approximates that of a wedge. The exact thread shape is neglected and radius of the contact surface R_c is a function of the axial position x and changes according to the thread pitch line (see figure 5.5.b).

Hence Eq. (5.2) become a function $p(x)$ that describes the radial contact pressure:

$$p(x) = \frac{E.\delta}{R_c(x)} \frac{\left(R_c(x)^2 - R_i^2\right).\left(R_O^2 - R_c(x)^2\right)}{2.R_c(x)^2\left(R_O^2 - R_i^2\right)} \tag{5.3}$$

where the interference δ is depends upon the number of make-up turn t, thread pitch P, and the taper angle α:

$$\delta = t.P.\tan(\alpha) \tag{5.4}$$

Weiner and Sewell (1967.) showed from strain gauge measurements that this approach can be used to model longitudinal and hoop stresses in a tubular connection. Schneider (1982.) used this same technique to analyse the stresses in standard API casing and tubing threaded connections.

The resulting radial force component dF_r (along the y-direction in figure 5.4, b) on a segment $d\theta$ of the circumference can be calculated from the radial pressure component $p(x)$ as follows:

$$dF_r = \int_0^L p(x).R_c(x).dx.d\theta \tag{5.5}$$

Where L is the length of the contact surface between male and female. A force dF normal to the tapered contact surface corresponds to this radial component dF_r, with dF given by Eq. (5.6).

$$dF = \frac{dF_r}{\cos(\alpha)} \tag{5.6}$$

According to the analytical calculations by Clinedinst (1976.), the contact pressure introduced by make-up results on each fully engaged thread in two equal force components dN normal to thread flanks. This is illustrated in figure 5.6, where both load and stab flank are subjected to the same normal force components during make-up as no external axial load is applied. The normal components dN are calculated by Eq. (5.7), with φ the half thread angle ($\varphi = 30^{\circ}$ for the API Line Pipe Connection).

$$dN = \frac{dF}{2.\sin(\varphi)} \qquad (5.7)$$

During make-up, the normal thread force dN will create a frictional force μdN which contributes to the make-up torque. The coefficient of friction μ, is assumed constant over different threads, so it can be considered as a mean friction value for the entire contact surface. Next to this friction, the wedge effected accounts for an important part of the total torque value. The total make-up torque T can be calculated using the virtual work balance E.q. (5.8).

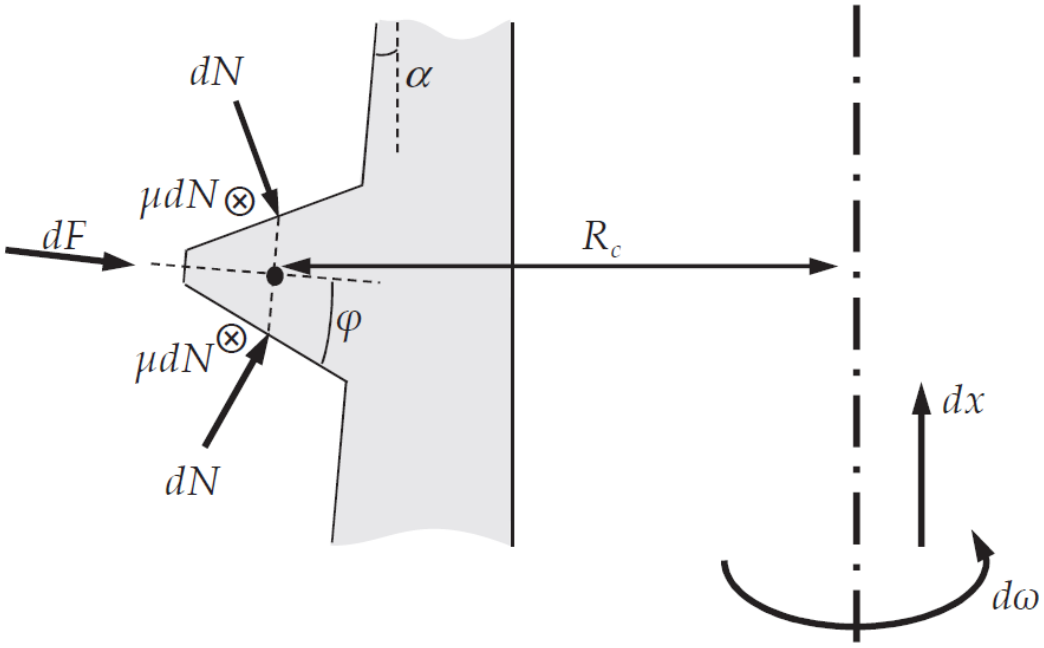

Figure 5.6: Forces acting on a thread (Wittenberghe, 2011).

$$T.d\omega = \left(2.\mu.\int_0^{2\pi} dN\,.R_c(x).d\theta\right).d\omega + \left(\int_0^{2\pi} dF\,.\sin(\alpha)\,.d\theta\right).dx \qquad (5.8)$$

This equation expresses that the virtual work applied by the make-up torque T over a certain virtual angular displacement $d\omega$ consists of two terms. The first term is the work for the virtual angular displacement of the frictional torque caused by the contribution of the frictional force μdN integrated over the circumference.

When the virtual angular displacement is applied, a virtual axial displacement dx will take place due to the helical effects of the threads. This dx is related to $d\omega$ as in Eq. (5.9). The second term in the virtual work balance Eq. (5.8) is the work for dx of the

axial component of the contact force dF integrated over the circumference. Thus, this is the virtual work caused by the wedge effect.

$$d\omega = \frac{dx}{P} 2\pi \tag{5.9}$$

Using Eq. (5.9) and Eq.s (5.5-5.7) the virtual work balance can be used to calculate the make-up torque T:

$$T = \frac{2\pi}{\cos(\alpha)} \int_0^L p(x).R_c(x).\left(\frac{\mu.R_c(x)}{\sin(\varphi)} + \frac{P}{2\pi}\sin(\alpha)\right).dx \tag{5.10}$$

Since the integration length L, which is the length of the contacting surface between pin and box, is a function of the number of make-up turns A. It is hard to solve this Eq. (5.10) analytically. A Nevertheless, numerical evaluation is possible. For a steel connection with known dimensions, the only unknown parameter in this equation is μ. Hence when an experimental torque-turn relation is known, Eq. (5.10) can be fitted to the experimental data to determine the value of the coefficient of friction.

This is done for the two performed make-up tests. In figure 5.3 the theoretical curve is compared to the measured torque-turn data of test 1 and a corresponding value of $\mu = 0.12$ is calculated. For the two consecutive tests a friction value $\mu = 0.15$ was obtained. The difference between the values can be explained by local changes in the connection geometry due to plastic deformation during the first test. Nevertheless, value obtained are within the range that can be found in literature these having been obtained in experimental tests as was discussed earlier in chapter 2.

5.4 API Line Pipe Joint Strength

During the test a constant axial tensile load is applied to the specimen from 10 kN to 100 kN at a constant frequency of 10 Hz. Axial test is given in Table 5.2, the test is paused for 20s to allow for a stable measurement. These measurements will be used as part of the validation of the finite element model in chapter 6.

Load (kN)	Stress Amplitude (MPa)
100	314
90	282
80	251
70	220
60	188
50	157
40	125
30	94
20	63
10	31

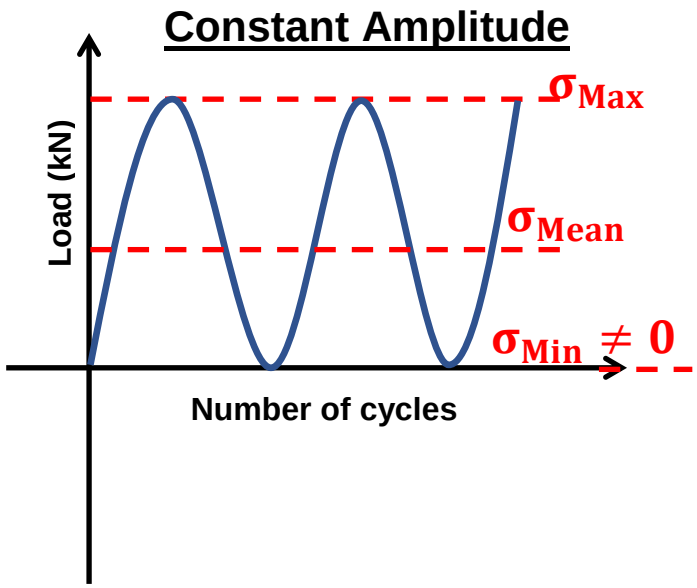

Table 5.2: Load steps for cyclic loading tests.

The tabulated axial stress is the net stress in the pipe body calculated by dividing the axial load by the cross-sectional area of the unthreaded part of the pipe.

The maximum applied axial load is 329 kN, which corresponds to an axial stress in the pipe body of 162 MPa. The joint strength of the 4.5" API Line Pipe connection can be calculated using the empirical formulae given by Clinedints (1976.) these formulae were determined based on 162 tensile test on API Line Pipe connections as reported by Clinedinst, (1965). Two joint strength values are defined: the fracture P_f and pulled out force P_P.

The fracture force P_f is that necessary to break the connection at its minimum cross-section and is calculated by multiplying the specimen's ultimate tensile stress with the cross-sectional area of the pipe wall under last perfect thread. Using the known dimensions and the determined tensile stress, a value of $P_f = 596\,kN$ is calculated. This corresponds to net axial stress of 292 MPa in the pipe body.

It is likely that the connection fails at lower loads due to shearing of the threads or due to thread jumpout. The latter occurs when the connection is separated due to the applied load as explained by figure 5.7.

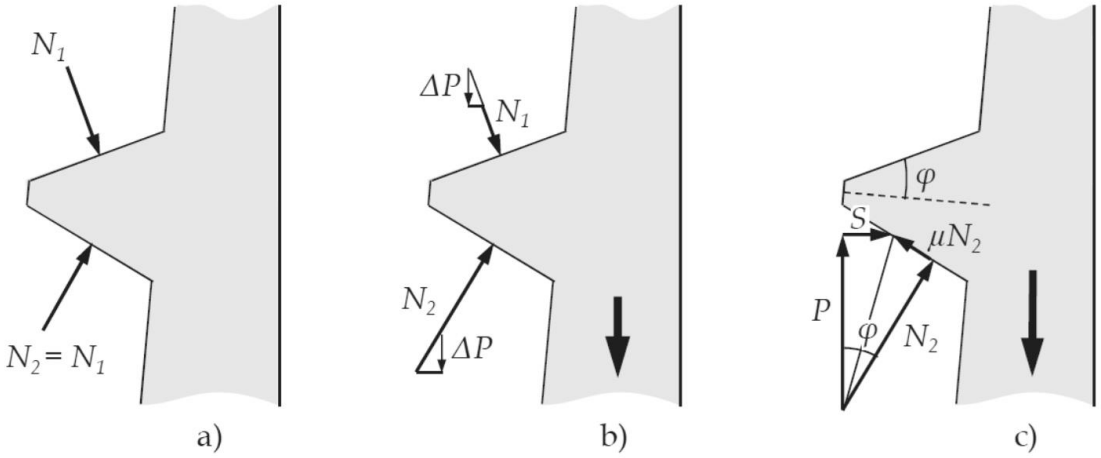

Figure 5.7: Threaded forces during axial loading (Wittenberghe, 2011).

As shown previously, the make-up induces normal forces on the thread flanks indicated by N_1 and N_2 in figure 5.7a. This figure represents a thread of the pin. When no axial load is applied, both normal force is equal. After an increment ΔP of axial load, the amount of normal force on the upper thread flank (the so-called non-load-carrying stab flank) is reduced, while the force on the lower flank (the load flank) is increased. This is shown schematically in figure 5.7.b. When a certain amount of axial load is exceeded, the normal load on the stab flank will become zero and all the load is carried by the load flank. Jumpout cannot occur until this condition is reached. The forces acting on thread at that time are shown in figure 5.7.c. due to the large threaded angle φ, the axial load does not only cause a normal force N_2 on the load flank, but also an important separation force S that tries to disengage the threads. The separation force is partly countered by the friction force μN_2. As soon as this friction force is exceeded, the threads can start to slide, and due to sliding, the resulting load will act closer to the thread crest where the thread cross-section is smaller. If the sliding become too high, the threads can be completely disengaged or thread shearing can occur. These separations are called respectively thread jumpout and thread pull-out.

The API Line Pipe thread pull-out strength P_p can be calculated according to empirical equation (5.11) given by Clinedinst (1976).

$$P_p = A.L_e\left[\frac{2.39(2h)^{0.59}D_p^{-0.59}\sigma_{UTS}}{0.5L_e+0.14D_p}+\frac{\sigma_y}{L_e+0.14D_p}\right] \qquad (5.11)$$

Where A is the cross-sectional area of the pipe wall under the last perfect thread, L_e is the engaged thread length, h is the thread height, D_p is the pin outside diameter, σ_y is the yield strength and σ_{UTS} the ultimate tensile strength. It should be noted that for this empirical equation all lengths should be the unit in inches and the stress values in psi.

Conversions show a pull-out strength $P_p = 503\ kN$ is obtained, corresponding to an axial pipe body stress of 246 MPa. The maximum applied axial load during the test is 100 kN or 20% of the connection pull-out strength.

5.4.1 Test results

During the application of the load, the strain gauge signals were monitored continuously. In figure 5.8 a selection of the measured signals is shown. All measured signals will be discussed more in details in chapter 6 where they are compared to the model strains. Two axial strain values (A) and circumferential strain value (C) are plotted.

The strain numbering is in accordance with figure 5.8. The strain values are relative strains compared to the made-up situation. The absolute values of the strains can be obtained by adding the strains caused by make-up to the values caused by axial tension.

It can be seen that strain gauge 8A and 5C follow a linear path as a function of the applied axial stress, which means they are behaving linear elastic. The strain in 11A, located at the inside pin wall at the LET, is non-linear caused by local plasticity at this location.

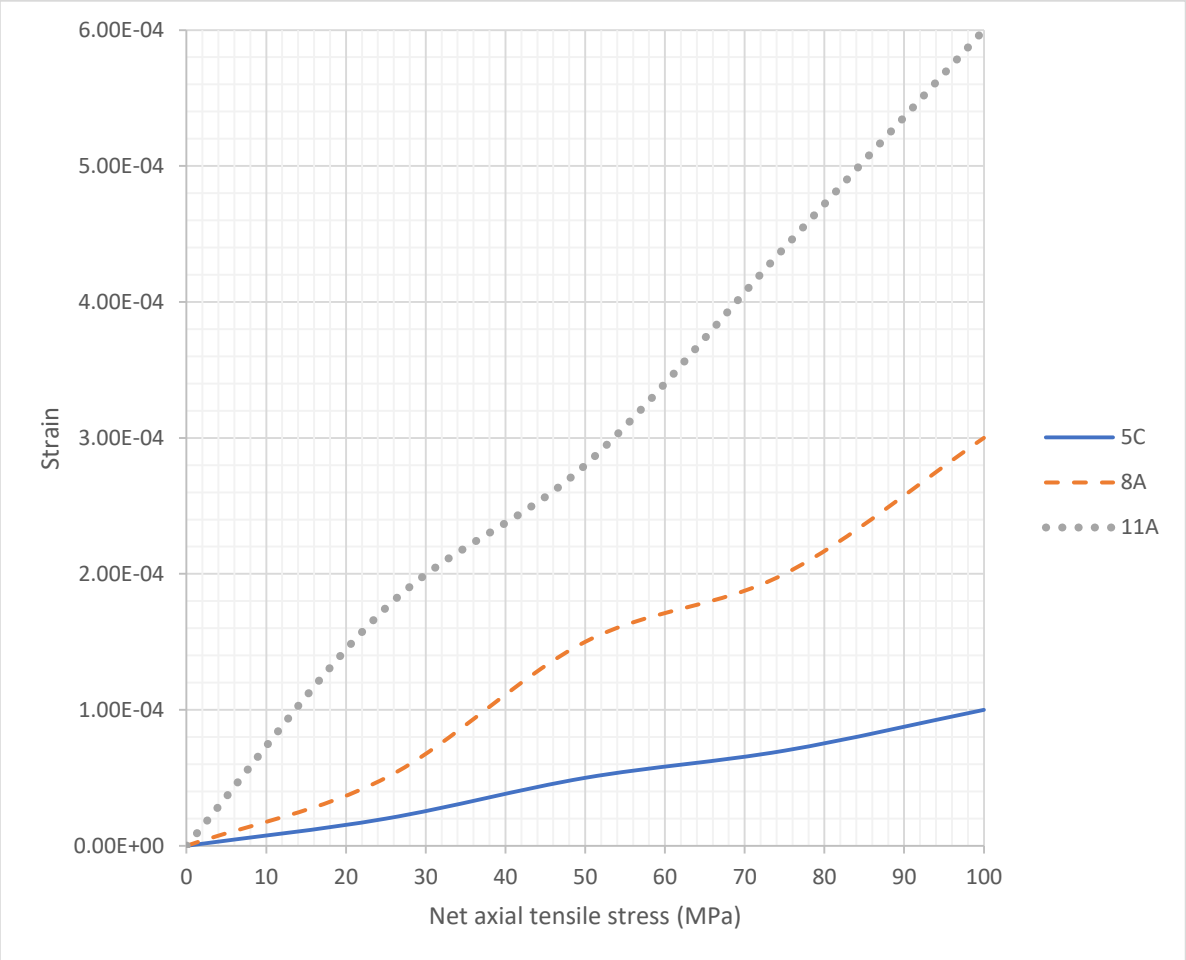

Figure 5.8: Strain measurement during axial tension.

5.4.2 Axial tension fatigue test

Following the quasistatic axial tensile dynamic fatigue test is carried out on the same $4.5''$ and $1''$ API Line Pipe specimen in the 100 kN setup illustrated in chapter 4, this test serves mostly as a comparison for the sample of the same connection type tested in the medium scale and small axial setup.

Figure 5.9: Failed 4.5" and 1" API Line Pipe specimen.

The fatigue test is performed at a load ratio $R = 0.1$, with a maximum net stress in the pipe body of 162 MPa or 33% of σ_{UTS}. The corresponding stress amplitude S_a is 73 MPa and the test frequency is 10 Hz.

The connection for 4.5-inch failed after 567909 cycles and for 1-inch failed after 846 cycles as shown in figure 5.9. There are different mechanisms contributed to the connection's failure. A fatigue crack initiated at the LET of the pin and propagated over part of the pin's cross-section. This effect will concentrate the load on the remaining section and the partition of the threads in this area figure 4.21. Once this area became too small, the threads sheared of in this region and finally jumpout occurred as can be seen in figure 5.9.

5.4.3 Standard $1''$ API Line Pipe

5.4.3.1 S-N curve

In total 20 test are conducted on standard 1" API Line Pipe specimens (shown in figure 4.5), 18 of which failed with a fatigue crack. The other two specimens did not fail and cycling was stopped after exceeding 2 million cycles. Each test is represented by a single data point in figure 5.10. The number of cycles to failure N is shown together with applied net stress amplitude S_a. This is the amplitude of the maximum stress in the pipe material of the pin calculated by Eq. (5.11) without taking into account the stress concentration of the threads.

The data is processed according the BS7608 fatigue standard (BS7608, B.S., 1993.), in which a fatigue limited is assumed at 2 million cycles. The fatigue data is expected to follow a Basquin relation, as introduced in chapter 2, written in the form Eq. (5.13).

$$S_a = A.N^{-B} \tag{5.13}$$

The factors A and B of this curve are found by regression analysis of data points of the test for which crack occurred. The best least-squares fit of the curve to the data points has a standard deviation STD = 5.14 MPa and is given in by Eq. (5.14). The design curve shown in figure 5.9 is calculated according to (BS7608, B.S., and 1993.) as the mean curve minus two times the standard deviation. Hence, the design curve is associated with a 95.4% probability of survival.

$$S_a = 848.7 \times N^{-0.2233} \tag{5.14}$$

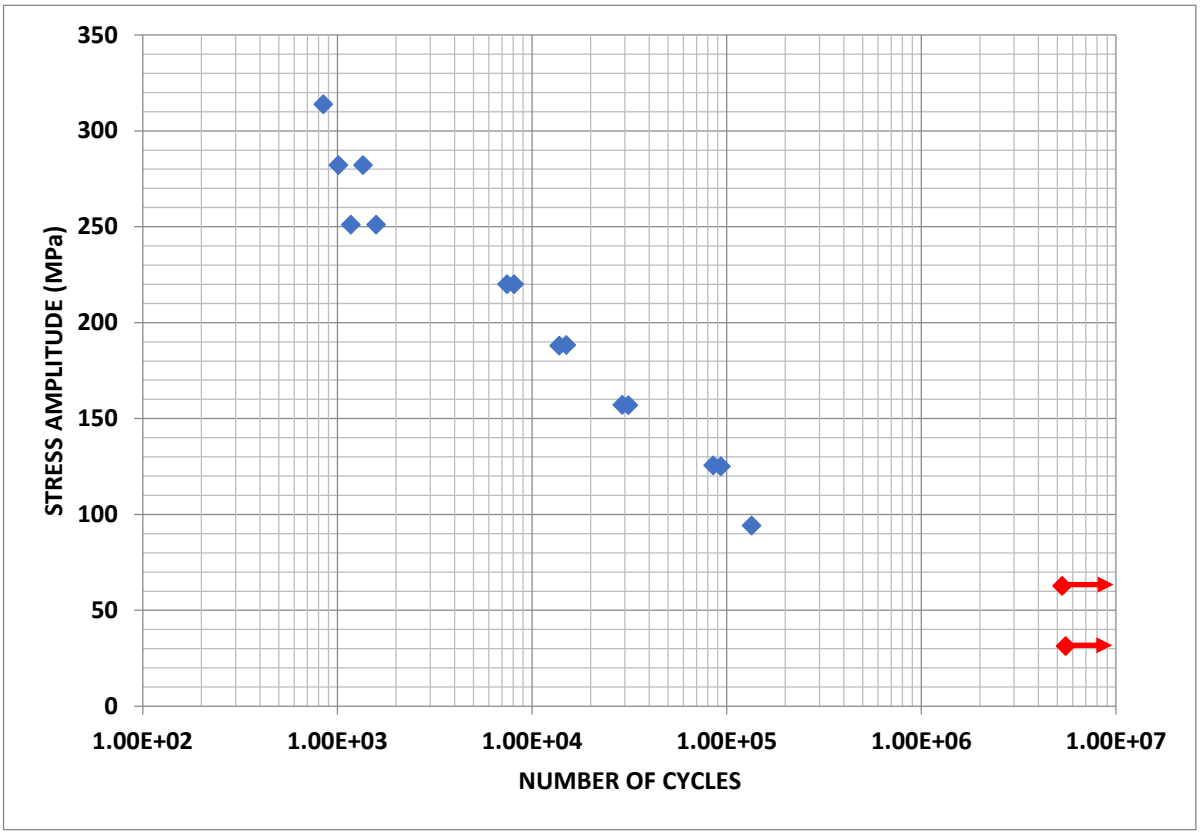

Figure 5.10: S-N curve for the standard 1" API Line Pipe Connection (stress ratio R = 0.1)

5.4.3.2 Fracture surface analysis

For the standard 1″ API Line Pipe connection a detailed analysis is made of the fracture surface to get a better understanding of the fatigue crack growth behaviour of the connection. In order to do this, either longitudinal or transvers sections were made by cutting the specimen or by forcing brittle fracture of the pin after cooling the samples in liquid air.

All observed cracks appear at the last fully engaged thread of the pin as illustrated in the section view in figure 5.11. The crack indicated by the arrow and is oriented perpendicular to the cutting surface. The root of the LET of the pin is the expected location for the cracks to initiate, according to reported failure case and laboratory tests as described in chapter 1. This also corresponds to the location where the highest stress concentration occurs.

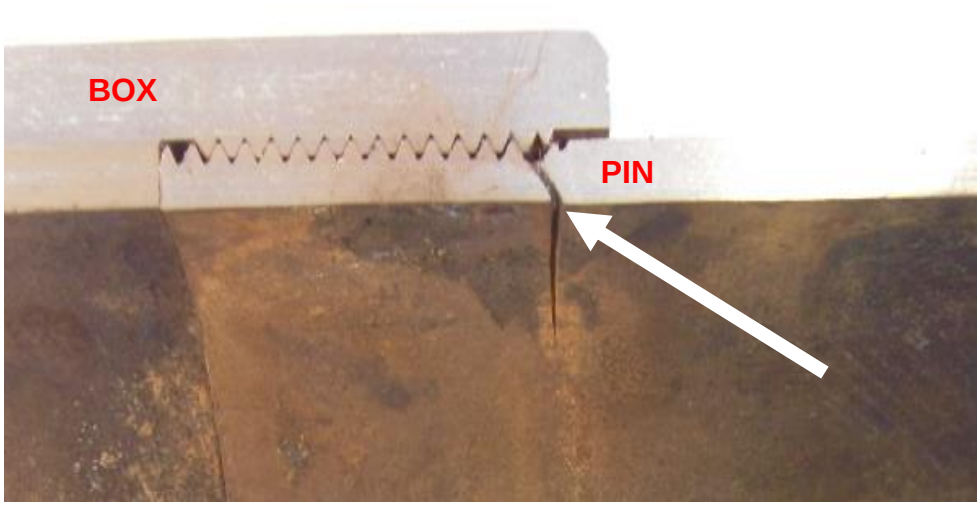

Figure 5.11: fatigue crack initiated at the LET of the pin of a standard 1" API Line Pipe specimen.

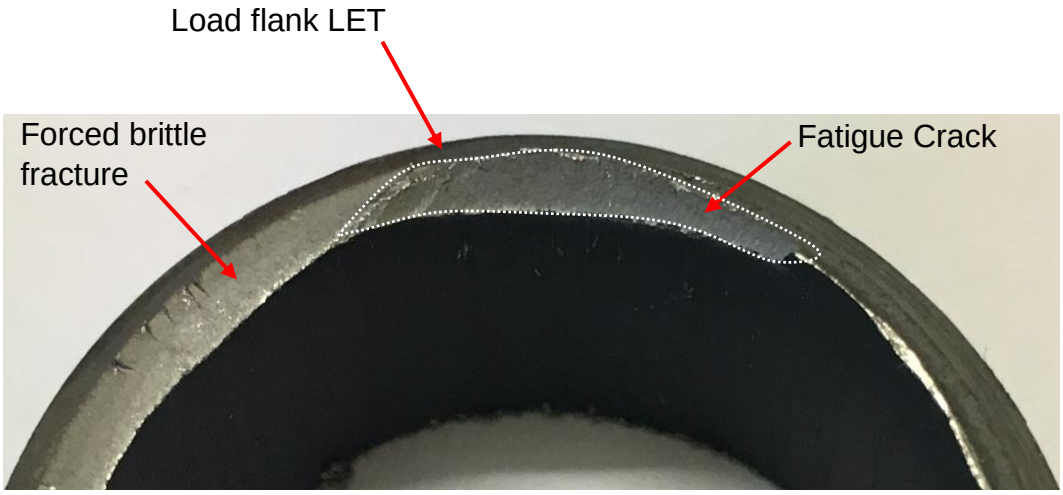

Figure 5.12: Fracture surface of a fatigue crack in a 1" API Line Pipe specimen.

In the fracture surface shown in figure 5.12 the shape of the fatigue crack for a test with stress amplitude $S_a = 94\ MPa$ can be seen. To obtained this view, the sample is cooled down in liquid air to a temperature of about $-180^{\circ}C$ and a brittle fracture is forced to open up the fracture. From the figure 5.12 it can be seen that the fatigue crack initiated along the root of the LET and propagated through the wall of the pin. While doing this, the crack propagates over a wide segment of the circumference. When the remaining overload fracture occurred, creating a through-thickness crack. In several cases the ductile overload is much smaller or negligible, but the global shape of the entire fatigue crack is comparable for observed fracture surfaces.

5.4.3.3 Fracture surface

The fracture surface for a fatigue test with a stress amplitude of $S_a = 90\ MPa$ is shown in figure 5.13. A fatigue crack appeared in the specimen after 134554 cycles. In order

to quantify the fatigue crack growth, this surface is investigated using scanning electron microscopy (SEM). With this microscopic technique magnification factors of several thousand can be achieved and individual fatigue striations can be visualised. Hence cyclic crack depth increments can be measured. This was done at three location indicated in figure 5.13. Location 1 is near the thread root where the fatigue crack initiated. Location 2 is near the inside wall of the pin and location 3 is at the border between the fatigue crack and the forced brittle fracture zone.

In figure 5.14 a SEM micrograph of locations at a magnification of 1000 times is shown. Two different regions, divided by the dotted line, can be clearly observed. The left region is the brittle fracture surface. It has a faceted aspect of a cleavage fracture pattern caused by the brittle fracture of the pin. In the region above the dotted line striations can be observed, which are caused by fatigue crack propagation. A detailed view of the region inside the white rectangle in figure 5.14 with a magnification of 3000 is given in figure 5.15. In this figure, individual fatigue striations can be clearly distinguished (two striations are indicated by the white arrows). The crack propagation direction is perpendicular to the striations or upwards in the figure. The mean cyclic crack depth increase in this region is determined to be $\frac{da}{dN} = 0.56\ \mu m$ as it mentioned above microscopic technique magnification factors were used. The same procedure is used to determine the $\frac{da}{dN}$ values at location 1 and 2. The total crack depth, measured as the distance between the thread root where the crack initiated at the pin inner wall, is 1.889 mm.

Additionally, crack depth increases are measured in a second sample tested at the same stress amplitude of $S_a = 90\ MPa$ and with a total fatigue life $N = 134500$ cycles. The three measured locations in this additional sample are numbered in the same way as in the sample shown in figure 5.13. The measured $\frac{da}{dN}$ and total crack depth values in both samples are summarized in table 5.3. The fatigue crack behaviour will be discussed further in later section

Table 5.3: Cyclic crack depth increase values.

Fatigue Life N	134554
Crack depth (mm)	1.812
$\frac{da}{dN}$ location 1 (μm)	0.40
$\frac{da}{dN}$ location 2 (μm)	0.48
$\frac{da}{dN}$ location 3 (μm)	0.48

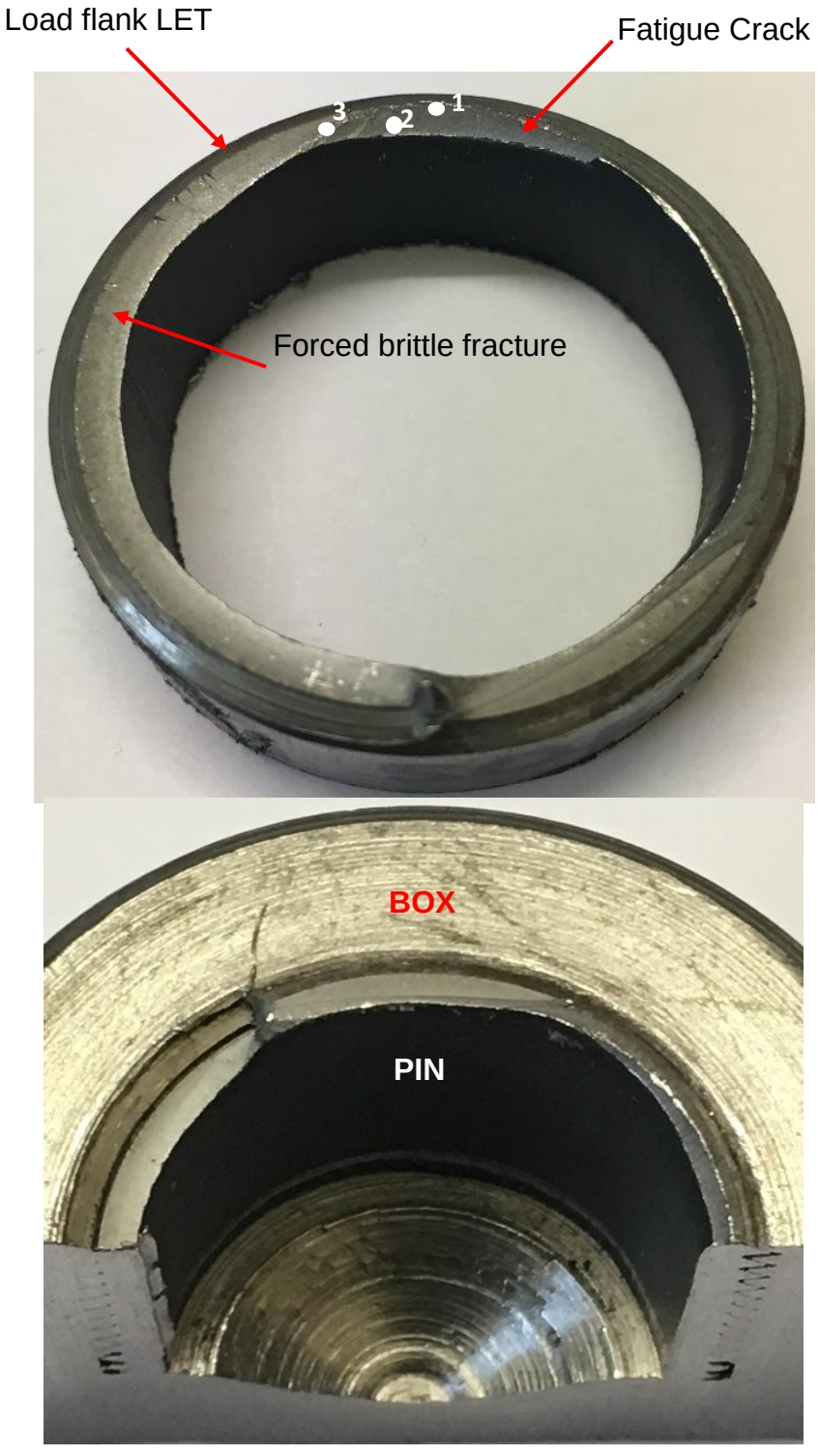

Figure 5.13: fracture surface of a 1" API Line Pipe specimen.

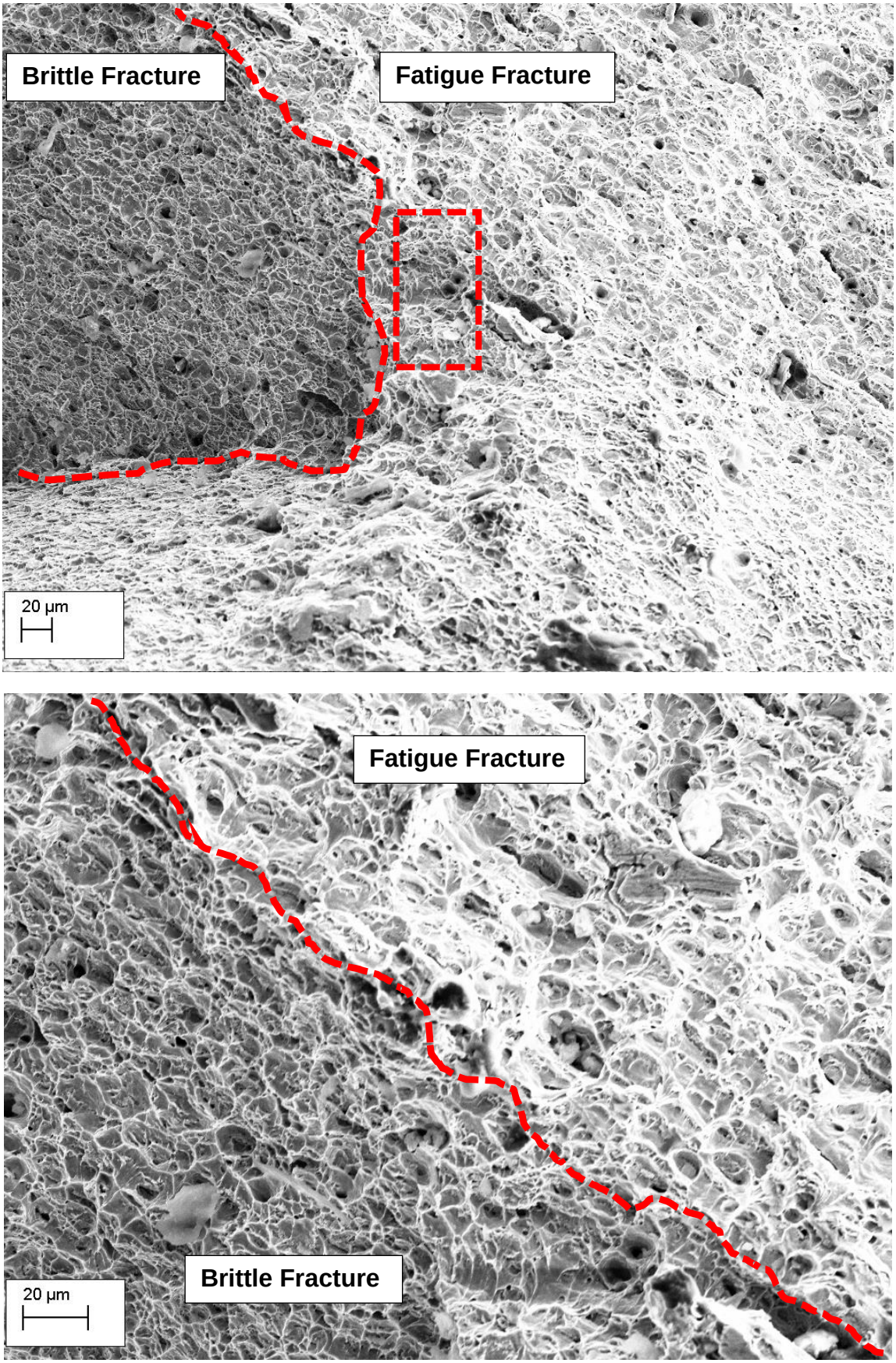

Figure 5.14: SEM micrograph of the boundary between the fatigue crack and forced brittle fracture.

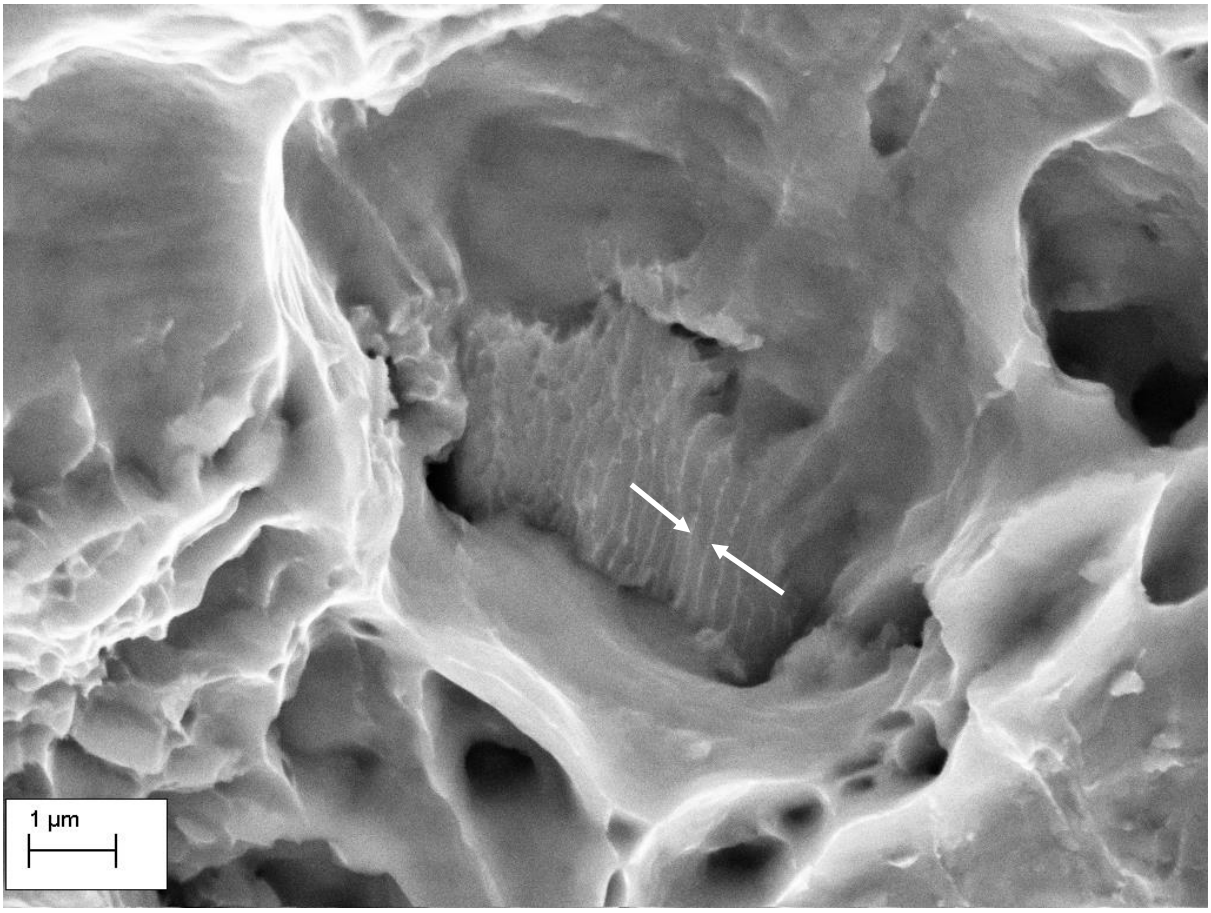

Figure 5.15: SEM micrograph of fatigue crack surface showing fatigue stations.

5.4.4 Small scale test result discussion

5.4.4.1 Comparison of the S-N curves

The respective relations of the mean *S-N* curves are given in figure 5.16. A comparison is made between the API Line Pipe and BSPT configurations. It can be seen that the API Line Pipe has the poorer fatigue properties, as the other *S-N* curve lies above the API Line Pipe curve. Hence, it is experimentally shown that geometrical changes of a threaded connection, without altering the thread shape itself, can affect the connection's life. Consequently, the idea introduced in chapter 2 that a connection's stiffness change can improve its fatigue life it's hereby confirmed. Also, BSPT samples, that have a rounded thread shape, show a better fatigue life than the API Line Pipe connection.

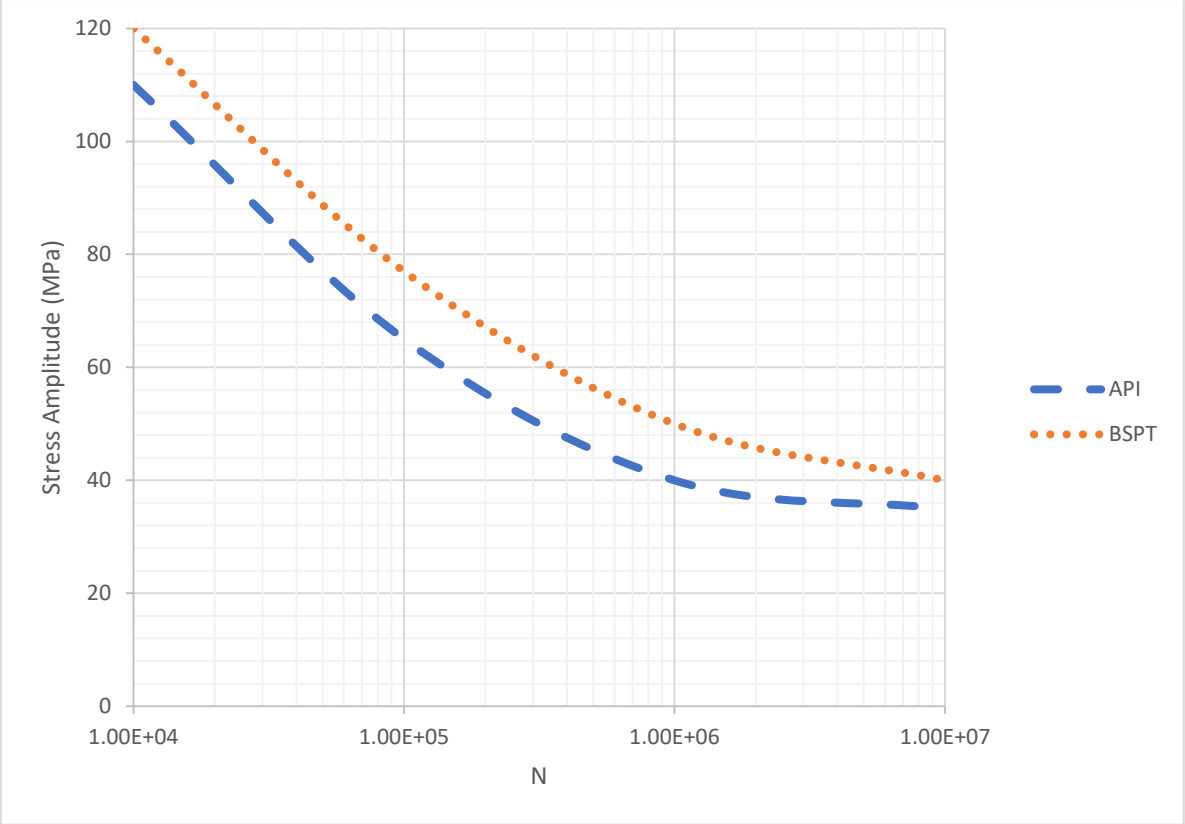

Figure 5.16: Comparison of the mean S-N curves of all experiments carried out on the small scale axial load setup.

The fatigue for connection of the pin can be improved by increasing the wall thickness configuration. Although it has an improved load distribution it does not exhibit better fatigue properties compared to the thick-walled configuration.

5.4: Summary of the performed small scale axial loading tests.

Connection type	S-N relation	STD (MPa)	Number of test
Standard API Line Pipe	$S_a = 848.7.N^{-0.2233}$	5.14	20
Standard BSPT	$S_a = 811.8.N^{-0.2075}$	10.4	3

A detailed analysis of the presented fatigue data is made in later section by comparing the experimental results to standard design curves and using the results of the finite element model described in chapter 6.

5.4.4.2 Crack growth behaviour

Using the crack depth increase value $\frac{da}{dN}$ given in table 5.4 an estimation can be made of the contribution of the crack propagation life N_P to the total fatigue life N. For the four sample that are investigated using SEM, the applied stress amplitude, resulting fatigue life and the crack depth are given in table 5.5. Additionally, the mean value of

the crack depth increase $\frac{da}{dN}$ is calculated with the crack depth increase at initiation measured at the thread root (location 1 in figure 5.12 and figure 5.13) and at the end of propagation measured at the boundary between the fatigue fracture and brittle fracture region (location 3).

The tabulated crack propagation lives are calculated by dividing the crack depth by the mean crack depth increase value. The total fatigue life N is considered to be the sum of both the initiation life N_i and propagation life N_P. As in equation (5.15). Hence N_i can also be determined.

$$N = N_i + N_p \tag{5.15}$$

Given the facts that this analysis is subjected to a certain amount of scatter and that determination of the $\frac{da}{dN}$ values is based on microscopic measurements, the following conclusions can be made: from the results in table 5.5 it can be seen that the mean $\frac{da}{dN}$ value is larger when the total fatigue life is shorter. Since the total crack depth is constant within the tolerances of the connection, this result also in a shorter crack propagation life. Nevertheless, the contribution of the crack propagation life relative to the total connection life is more important in the case of lower values of N. When the total fatigue life is 253836 cycles, the crack propagation life take less than 2% of total life, while when $N = 19663$ the crack propagation takes 17% of the fatigue life. These results are comparable to the values of 15% and less for the ratio of the crack propagation life to total life found in literature as previously mentioned in chapter 2.

Table 5.5: Crack propagation data.

Connection type	API Line Pipe
Stress amplitude S_a(MPa)	90
Total fatigue life N	35320
Crack depth (mm)	1.89
Mean value of $\frac{da}{dN}$ (μm)	0.50
Crack propagation life N_p	3778
Crack initiation life N_i	31450
N_p/N	0.107

5.5 Thread Type

The influence of thread type on a connection's fatigue performance is mainly determined by its stress concentration factor.

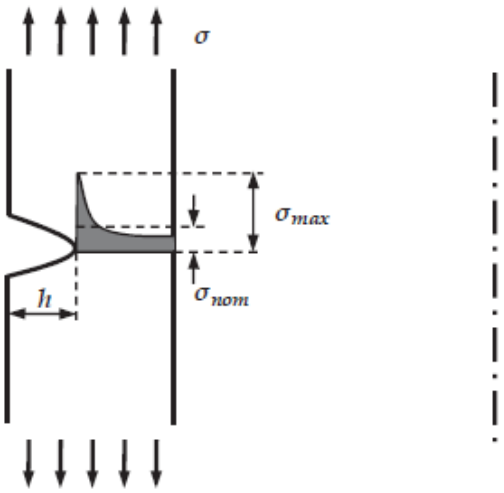

(a) Figure 5.17: Local stresses at a notch tube. (Van Wittenberghe, 2011)

When evaluating stress concentrations, it is common practice to make a comparison between the gross stress concertation factor K_{tg} and the net stress concentration factor K_{tn}. Both factors are explained using figure 5.17. When a notched tube is subjected to a certain gross stress σ, a stress concentration with a maximum value σ_{max} is induced. This relation (5.16) between this gross stress and maximum value defines K_{tg}. This factor, however, includes a certain size effect, since it will change e.g. when the wall thickness is increased while keeping the same notched size.

$$K_{tg} = \frac{\sigma_{max}}{\sigma} \qquad (5.16)$$

$$K_{tn} = \frac{\sigma_{max}}{\sigma_{nom}} \qquad (5.17)$$

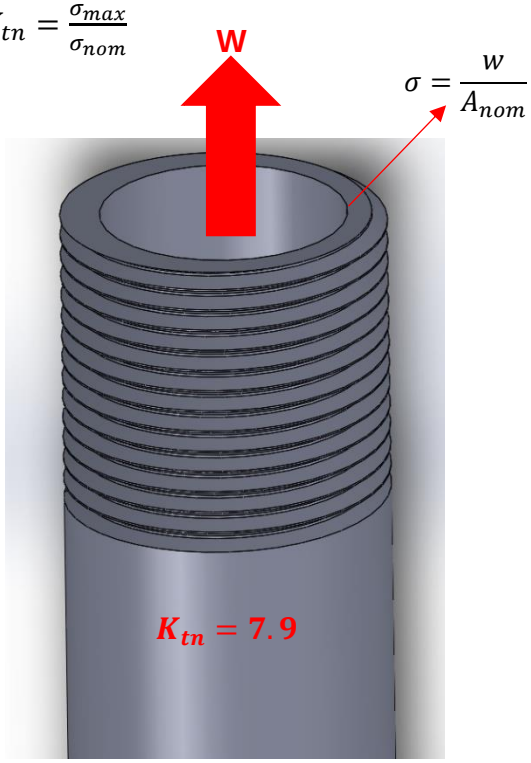

If $A_{nom} < A_g$ then $K_{tn} > K_{tg}$

In order to obtain a stress concentration factor which is more dependent on the notch than on the tube geometry, the net stress concentration factor is defined. This factor is given by the relation (5.17) as the ratio between the maximum appearing notch stress and the nominal stress value over the section of the pipe at the notch location.

To compare the geometrical stress concertation factors of different thread type, a tube with an outer diameter of 114.3 mm and wall thickness of 6 mm is modelled in finite element (FE) with a single notch shaped like the considered thread. Linear elastic material properties are used and each thread is meshed with a seed size of 0.01 mm. The obtained stress concentration factors are summarized in table 5.6.

Table 5.6: Geometrical stress concentration factors for different thread type.

Thread type	Thread height h (mm)	Root radius (mm)	Thread angle	K_{tn}	K_{tg}
API Line Pipe	2.413	0.050	60°	7.9	13.6
API Round	1.810	0.432	60°	4.2	6.1
BSPT	1.479	0.317	55°	4.4	5.9

The gross and net stress concentration factors of the standard $4.5''$ API Line Pipe thread shape are respectively 13.6 and 7.9. It can be noted that these values are considerably higher than those obtained with the finite element model, as will be discuss in chapter 6, since in the current evaluation a linear elastic model is used and consequently no plastic relaxation can appear, in addition, the same thread is evaluated in a pipe with a wall thickness of 16 mm instead of 6 mm. for this configuration a decreased value of K_{tg} is found using equation (5.16), while the K_{tn} value is similar (using equation (5.17)). This is illustrating the difference between the two stress concentration factors.

The API Round shape is a triangular thread with rounded crest and roots. This smoother thread shape has a clear influence on the appearing stress concentration since the net stress concentration factor is almost half the value of the API Line Pipe thread. The BSPT thread type is similar to the API round thread, but has a smaller root radius. This results in a slightly higher K_{tn} value of 4.4. Nevertheless, the gross stress concentration factor of the BSPT thread is slightly lower than that of the API Round type since the BSPT thread height is lower.

5.5.1 Fracture mechanics approach

Since four different beach mark line are presented on the fracture surface of tests (see figure 5.18a), a detailed crack growth analysis is carried out on the test specimen. This is done by using the fracture mechanics calculations according to the ASME BPVC VIII-3-app.D (A.S.M.E., 2010). In this approach, a crack at root of a thread is considered as an annular flaw, instead of assuming a semi-elliptical crack shape. Considering the observed crack shapes, seems to be a better assumption.

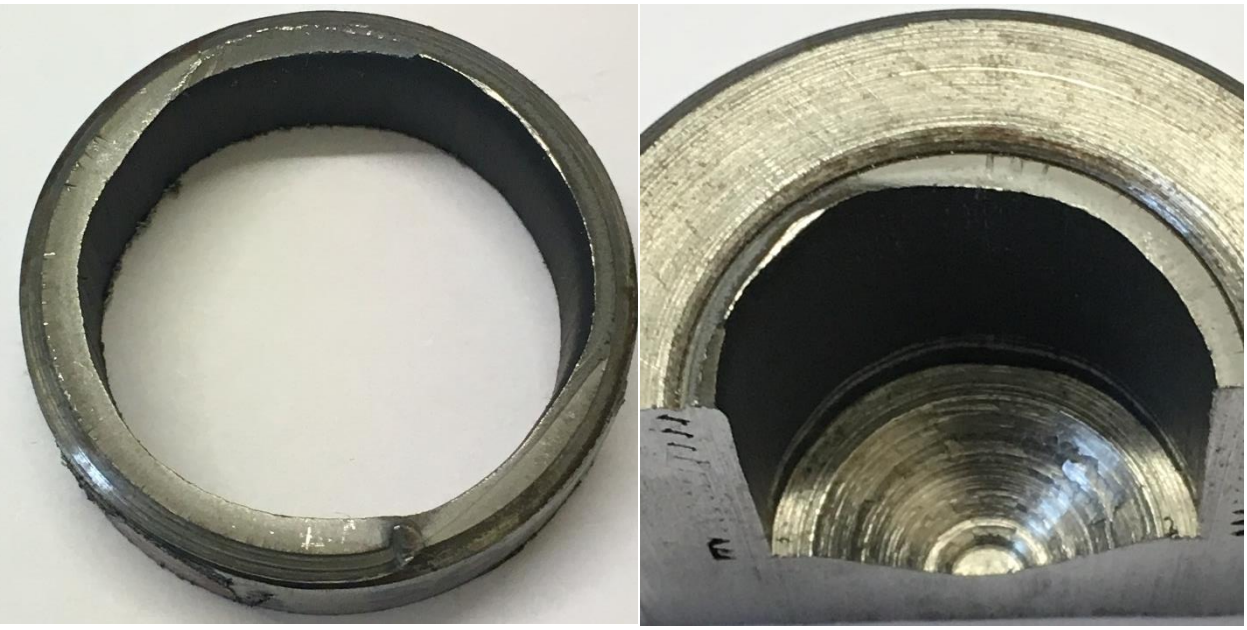

Figure 5.18a: a) Fracture surface test low to high; b) Zone divided by the each marks.

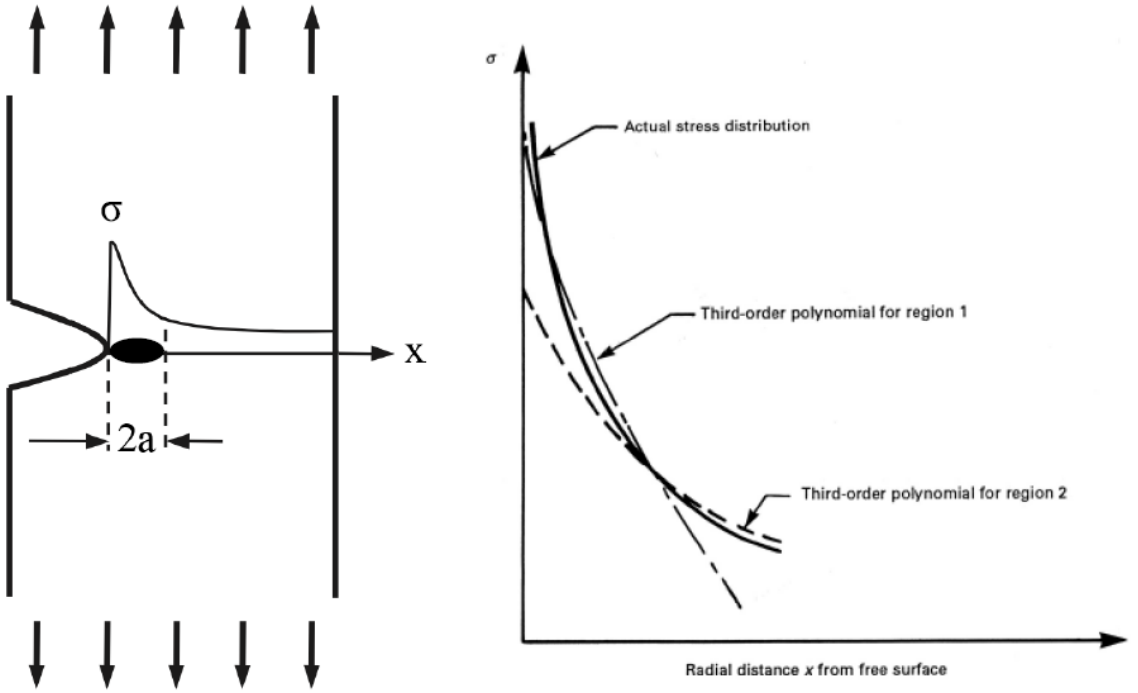

(a) Initial flaw beneath the thread root based on (Wittenberghe, 2011)

(b) Polynomial representation of stress distribution taken from (A.S.M.E., 2007)

Figure 5.18: Basic of ASME crack growth method.

The stress intensity factor K_I for a certain crack depth $2a$ is calculated according to eq. (5.18).

$$K_I = F\sqrt{\pi a} \tag{5.18}$$

where the factor F is defined by:

$$F = A_0 F_1 + \frac{2aA_1F_2}{\pi} + \frac{a^2A_2F_3}{2} + \frac{4a^3A_3F_4}{3\pi} \tag{5.19}$$

In eq. (5.19) the F_1,F_2, F_3 and F_4 are magnification factors relative to the crack geometry. The four coefficients A_0, A_1,A_2 and A_3 are determined by the Buchalet-Bamford method (Buchalet and Bamford,1976) in which the distribution of stresses σ normal to the plane containing the annular crack is approximated by a third order polynomial eq. (5.20).

$$\sigma = A_0 + A_1 x + A_2 x^2 + A_3 x^3 \tag{5.20}$$

where x is the radial distance from the free crack surface or $x = 0$ in the root of the LET see figure 5.20. The stress distribution is calculated by a linear elastic analysis and the coefficients are determined by the best least squares fit of the polynomial. If a single polynomial is not sufficient to fit the stress distribution, it is acceptable to split the distribution into several regions and described each region by a different polynomial.

If a single 3rd-order polynomial is not enough to achieve a sufficient fit of stress field, it is permitted to split the region into several parts for which separated polynomial fits are produced (A.S.M.E., 2007). An example of such a division into two different fits is given in figure 5.18b. For both polynomial fits the stress intensity factor is calculated based on equation 5.17 and to compensate the difference between both stress intensity factors, where the regions join, the difference between them is added to all subsequent values of K_I. To illustrate this assume that 2 polynomial fits are used, as presented figure 5.18b. For the first region, the actual stress intensity factor $K_I(x)$ is based on the fit for the first region. From the point p on, where both regions join, the stress intensity factor $K_{I,region2}$ for the second region will be used, but the difference $\Delta K_{I,2}$ at the joining point will be added. This procedure is also presented in figure 5.18.

$K_I(x) = K_{I,region1}$ for $0 \leq x \leq p$

$K_I(x) = K_{I,region2} + \Delta K_{1,2}$ for $x \geq p$

Based on this procedure the number of cycles to failure has been calculated for 8 combinations of S_{max} and S_{min} with a constant ratio of $R = 0.1$ using the 2D axisymmetric model chapter 6 with 2 sets of polynomials in each case. The first polynomial is fitted to the interval $0 < x < 0.1\ mm$ and the 2nd to the rest stress field. An example of an insufficient form of the stress gradient by one polynomial and the improvement by dividing the gradient into two regions is explained in figure 5.19.

The corresponding fatigue crack growth has then be calculated using Paris Law for different initial defect sizes $2a_i$ from 0.01 mm to 0.1 mm at the root of the LET. Those defect sizes are chosen to cover the range of typical flaw in steel pipes, as found in tests by Zhang et al (2003).

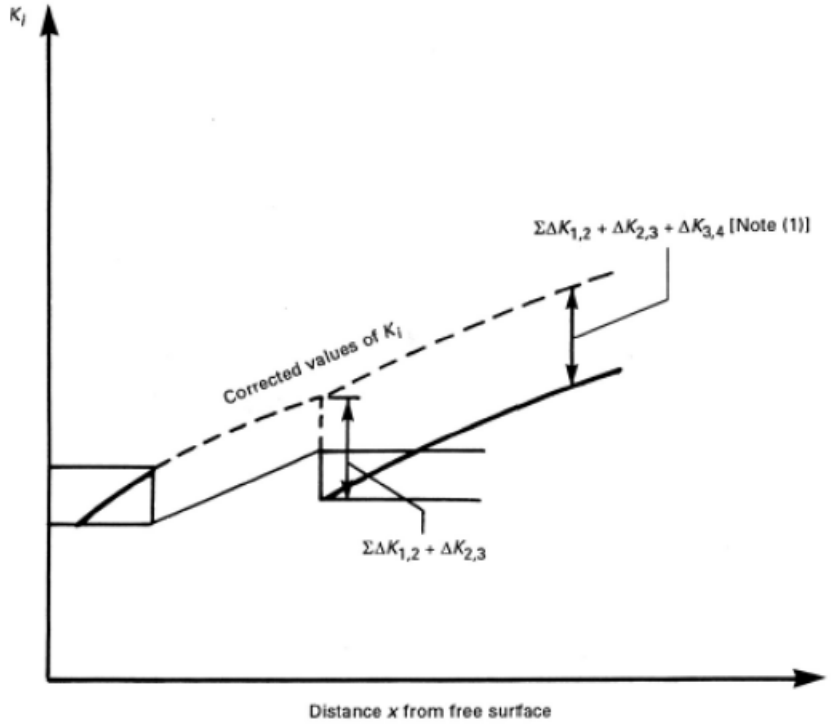

Figure 5.19: Illustration of the method for correcting K_I if several polynomial fits are used described the stress field taken from (A.S.M.E., 2007)

By numerical integration of Paris Law, it is possible to find the number of cycles needed for a crack to grow from the stated initial defect sizes to a through-crack, which is considered as failure of the connection in this case since the experimental test were stopped after the failure was defected. *S-N* curves obtained for different initial defect sizes was established by testing 20 connections under pulsating tension.

Analyze and visualizing crack and crack propagation during the experiment was impossible due to not having access to the threaded joint connection, therefore the best way possible in this research were simulating a 2D axisymmetric model in ABAQUS and analyzing crack and crack propagation for validating experimental results.

Since the crack is considered to be annular, the 2D axisymmetric FE model from chapter 6, now with linear elastic material properties, is used to obtain the stress distribution. In figure 5.20 the resulting axial stress distribution at the LET is plotted for the minimum and maximum axial load. The load is applied as a uniform stress over the wall of the pin with a magnitude of 15 MPa and 150 MPa respectively. Two polynomial are used to described each curve. The first polynomials describe the region $0 < x < 0.35\,mm$, the second describes the region $0.35 < x < 3.6\,mm$. The boundary between both regions is indicated by the dashed vertical line in the graph.

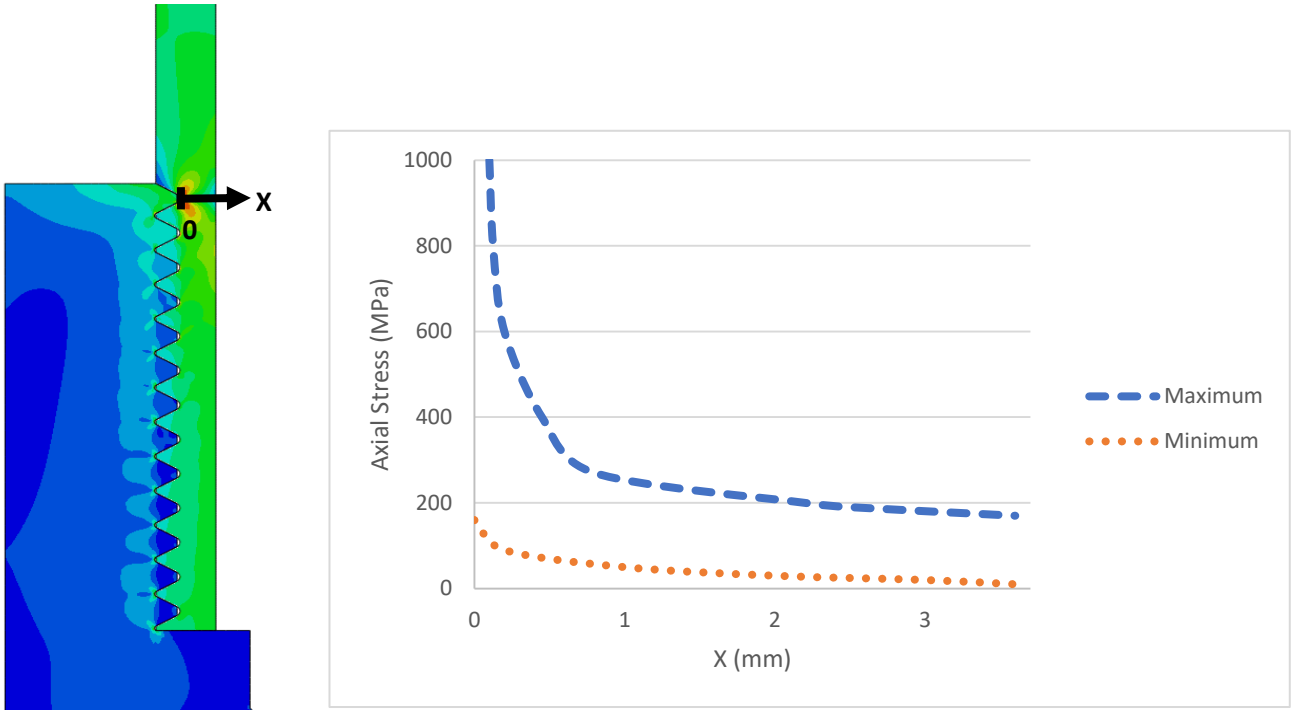

Figure 5.20: Axial stress distribution at the LET using linear elastic properties.

For each polynomial, the coefficient A_0 to A_3 are determined. The fatigue crack growth rate is then calculate using Paris law eq. (5.20), where N is the number of fatigue cycles, f is the crack growth rate factor and ΔK is the range of the stress intensity factor corresponding to the minimum and maximum applied load.

$$\frac{da}{dN} = C.f.\Delta K^m \qquad (5.21)$$

The factor C and m are material constants with values for API 5L Grade B material according to (Lam,2009) $C = 1.38 \times 10^{-12} \left(mPa.m^{\frac{1}{2}}\right)^{-m}$ and $m = 3.37$ the crack growth rate factor *f* is determined by fitting the crack growth rate of eq. (5.21) to the measured crack depth increase between 23000 and 25000 cycles. This resulted in a value of $f = 1.95$.

The number of cycles required to achieve a certain crack depth can be calculated by integrating the Paris Law explained further in section 5.5.2. This is done for the four measured crack depths at the beach mark lines. Table 5.7 show the summarized results. The crack depth increase values, as measured on the fracture surface, are used as inputs in the calculation is shown in second column. In finite element calculation is necessary to set the initial crack depth to be 0.1 mm as a value 0 mm would lead to an infinite number of cycles. The calculated number of cycles are obtained by integrating eq. (5.21). The measured number of cycle is the duration between the applications of the beach marking cycles.

It can be seen that there is a good correlation between the calculated and measured number of cycles. Moreover, it is confirmed by the crack growth calculations that the crack initiated at approximately 20000 cycles as estimated from the crack opening data. Because the total number of calculated cycles to reach the final crack depth of

3.5 mm is 7500 cycles and this crack depth is reached during the experiment at 28500 cycles.

Table 5.7: Crack growth rates during test.

Total number of cycles	Crack depth increase (mm)	Initial crack depth (mm)	Calculated number of cycles	Measured number of cycles
24000	1.2	0.1	3313	3000
26000	1	1.2	2012	2000
28000	1	2.2	1583	2000
28500	0.4	3.2	594	500

5.5.2 Fatigue crack growth (FCG) data and fatigue limit

In order to be able to perform FCG-based fatigue assessment a number of material parameters are required. These parameters will be introduced in this section. For the crack growth analysis by means of numerical integration of Paris law according to equation 5.21 the crack growth parameters for API Grade B steel are required. Both crack growth parameter C for $R = 0.1$ in $\left[(mm/cycle)/(MPa\sqrt{m})^m\right]$ and m have been adopted form Dale (1988) and are summarized in table 5.8. For FCG analysis the parameter C was mean stress corrected to $R = 0$ by using Walker's equation (Walker, 1970).

$$C(R = 0) = C(1 - R_C)^{m - m\gamma} \qquad \text{for } R_C \geq 0 \qquad (5.22)$$

where R_C is the stress ratio for which C was given and γ for various metals are typically around 0.5 if the R-ratio for which the stress intensity factor range ΔK calculated is larger then zero.

Table 5.8: Fatigue crack growth parameter based on test results by Dale (1988).

Material	C	m
API Grade B	1.15e-9	2.68

For low stress amplitude, the stress intensity factor approaches a threshold value, below which no crack growth take place. Unfortunately, no data was found for the fatigue crack growth threshold ΔK_{th} of API Grade B steel. A value for the fatigue crack growth threshold was therefore adopted from BS 7910 (2005), which includes crack growth parameter recommendations for various steel types. In general fatigue crack growth threshold values are highly dependent on environment and R-ratio. Usually, ΔK_{th} is found to increase with decreasing R-ratio (B.S., 2005). For unwelded steel component this taken into account in BS7910 by:

$$\Delta K_{th} = 63 \qquad \text{for } R \geq 0.5$$

$$\Delta K_{th} = 170 - 214R \qquad \text{for } 0 \leq R \leq 0.5 \qquad (5.23)$$

However, the value used in fatigue crack growth analysis should not exceed $63\ MPa\sqrt{mm}$ for assessments of surface-breaking flaws less than 1 mm deep (BSI, 1999). For literature, it is known that fatigue failure of TRCs are usually caused by cracks, which originated at the root of the LET or from surface-breaking flaws beneath the root of the LET (Wittenberghe, 2011). The stress intensity factor threshold ΔK_{th} was therefore set to $63\ MPa\sqrt{mm}$ for all fatigue crack growth methods used in this thesis. Moreover, the local R-ratio close to the crack tip is in case of linear elastic material models higher than 0.5 for all analysed initial cracks.

Based on the stress intensity factor threshold ΔK_{th} it is possible to calculate the fatigue limit S_A for the different FCG-based method and the given initial defect sizes a_i. For this purpose, the geometry factor F is calculated from the effective stress intensity factor range ΔK_{eff} for a given nominal tensile stress range ΔS and the initial crack depth a_i. In order to obtain the number of cycle at which a fatigue limit begins it is then interpolated between the *S-N* results.

$$F = \frac{\Delta K_{eff}}{\Delta S\sqrt{\pi a_i}} \tag{5.24}$$

$$S_A = \frac{\Delta K_{th}}{2F\sqrt{\pi a_i}} \tag{5.25}$$

5.5.4 Application to the finite element model

Before presenting the fatigue analysis using the damage evolution law, it is mentioned that attempts were made to apply the Dang Van criterion according the methodology described in chapter 2. However, the parameters K and λ could not be determined accurately enough.

To account for the local multiaxiality at the root of the LET in the evaluation of a threaded connection's fatigue life, the damage evolution law (DEL) is used, as introduced in chapter 2. The main relation is (2.35).

$$N = \frac{\Delta\sigma_{eq}^{-(\beta+m)} R_V^{\frac{-\beta}{2}}}{a(\beta+m+1)} \tag{5.26}$$

This model combines the values of the von Mises equivalent stress range σ_{eq} and the hydrostatic pressure σ_H (present in the triaxiality function R_V) as determined at the root of the LET in the finite element model. However, the extraction of numerical data from finite element results should be performed rigorously (Stavrovský, Papuga, and Růžička, 2010). Using data from a single element could result in inaccurate or mesh dependent solutions. Therefore, a methodology based on the area method (AM) and the theory of critical distance (TCD) is used.

Due to fatigue thread contact condition, the stress gradient is really high at the edge of contact and therefore all extracted data will be mesh dependent. To overcome this mesh dependency problem a methodology based on process zone method and the theory of critical distance was used to extract the required data for damage model. In this approach, the stresses were averaged over a semi-circular area centered at the

predicted location of crack initiation, having a radius equal to the critical distance L_c (El Haddad et al., 1980). Unfortunately, references data for stress concentration factor is rare and the data found, was mainly obtained from FE models with linear elastic material models.

The average value of triaxiality function R_v and the maximum and minimum equivalent stress i.e. $\sigma_{eq,max}$ and $\sigma_{eq,min}$ show how calculated inside the process zone. Due to lack of information and limited published data for API a typical values for AI2024-T3 were considered for long crack threshold stress intensity factor range, $\Delta K_{th} = 100\ MPa\sqrt{mm}$ (Forman et al., 2005) and plain fatigue strength, $\sigma_o = 263\ MPa$, which results in $L_C \approx 50\ \mu m$.

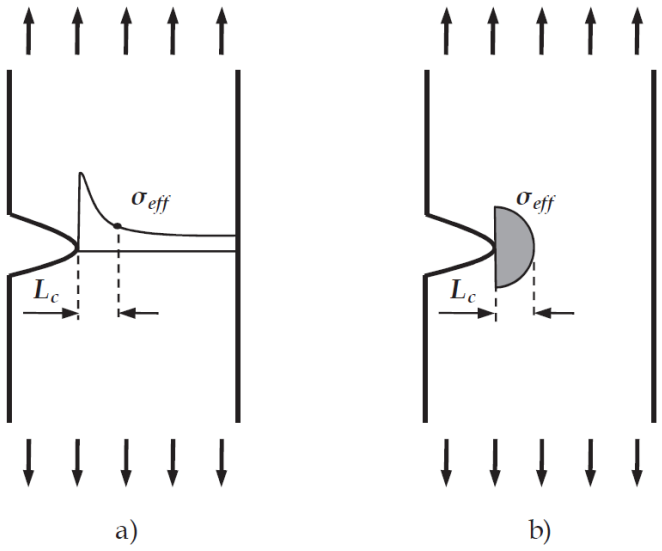

Figure 5.21: a) critical distance evaluation, b) area method.

The TCD (or hot-spot approach) was developed by Peterson (1959) to extract notch factors from linear elastic stress analyses. He assumed that the stress at a certain critical distance L_c from a notch root can be used for fatigue evaluation as illustrated in figure 5.21.a. As this approach only helps to extract data from linear elastic finite element analysis, but still uses data extracted from a single element, the area method was developed by Taylor (1999). In this last approach, the stresses are averaged over a semi-circular area centered at the notch tip having a radius equal to the critical distance L_c as illustrated in figure 5.21.b. Hereby L_c is defined by eq. (5.27).

$$L_c = \frac{1}{\pi}\left(\frac{\Delta K_{th}}{\Delta\sigma_0}\right)^2 \qquad (5.27)$$

where ΔK_{th} is the threshold value of ΔK for fatigue crack growth and $\Delta\sigma_0$ is the plain specimen fatigue limit (stress range) of the material. Common values for medium strength steels (such as API Grade B steel) are $\Delta K_{th} = 8\ MPa.m^{\frac{1}{2}}$ (Boyer, H.E. ed., 1985) and $\sigma_0 = 0.45.\sigma_{UTS}$ (Kocak, 2008) with these values, the critical distance for API Grade B steel becomes 0.1 mm. This corresponds well to the critical distance values from 0.09 to 0.11 mm for V-notches in a steel grade with similar strength properties (Stavrovský, 2010). The area method has been applied to threaded pipe connections

before by Santus (Santus, 2008.) in his study on the fretting fatigue behaviour of drill pipe connections. Furthermore, it is mentioned that even more advanced area methods exist, where the size of the critical area is changed according to the applied fatigue stress (Susmel, and Taylor, 2011).

However, in this study a semi-circular area with a fixed radius of 0.1 mm is used to determine the effective stress values from finite element analyses. The region contains approximately 100 elements in each analysed geometry.

5.5.5 Determination of fatigue parameter

As the damage parameter a and β of the damage model are unknown material constants, experimental tests were chosen to determine and calibrate the damage parameters. Three calibration test were selected covering the broad range of applied axial stress. Therefore, for each of selected experimental test, the average triaxiality function and the maximum and minimum equivalent stress were calculated inside the process zone. Extracted data were then substituted into the damage evolution law equation. The values of the damage parameters were then found using regression to calculate the best least square fit between the predicted cycle for crack initiation and the experimental data for crack initiation. The experimental crack initiation lifetime was calculated by subtracting numerical crack propagation lifetime from observed experimental total life.

In the damage evolution law eq. (5.26) $\Delta\sigma_{eq}$ and R_V are obtained from the simulations, a and β are damage parameters and m is the strain hardening exponent of the connection material ($m = 9.49$ by fitting experimentally determined stress-strain curve of the Grade B steel to the Ramberg-Osgood relation). Since a and β are unknown material constants, the experimental data from the standard API Line Pipe connection is used to determine their values. This is done by evaluating the finite element model at 9 different levels of stress amplitude. For each of these stress levels, the triaxiality function R_V and the equivalent stress range $\Delta\sigma_{eq}$ are calculated and substituted in the damage evolution law. The values of damage parameters are then found using regression analysis to calculate the best least-squares fit between the calculated cycles to failure and the mean curve of the experimental data of the standard API Line Pipe sample given by eq. (5.14). This methodology results in the following values: $a = 1.50 \times 10^{-7}$ and $\beta = -8.23$.

Consequently, the damage evolution law becomes (calculation is shown in Appendix A):

$$N = 2.95 \times 10^{6}.\Delta\sigma_{eq}^{-1.26}.R_V^{4.12} \tag{5.28}$$

In figure 5.22 the corresponding results of the fitted damage evolution law are compared to mean curve of the experimental data of the standard API Line Pipe connection.

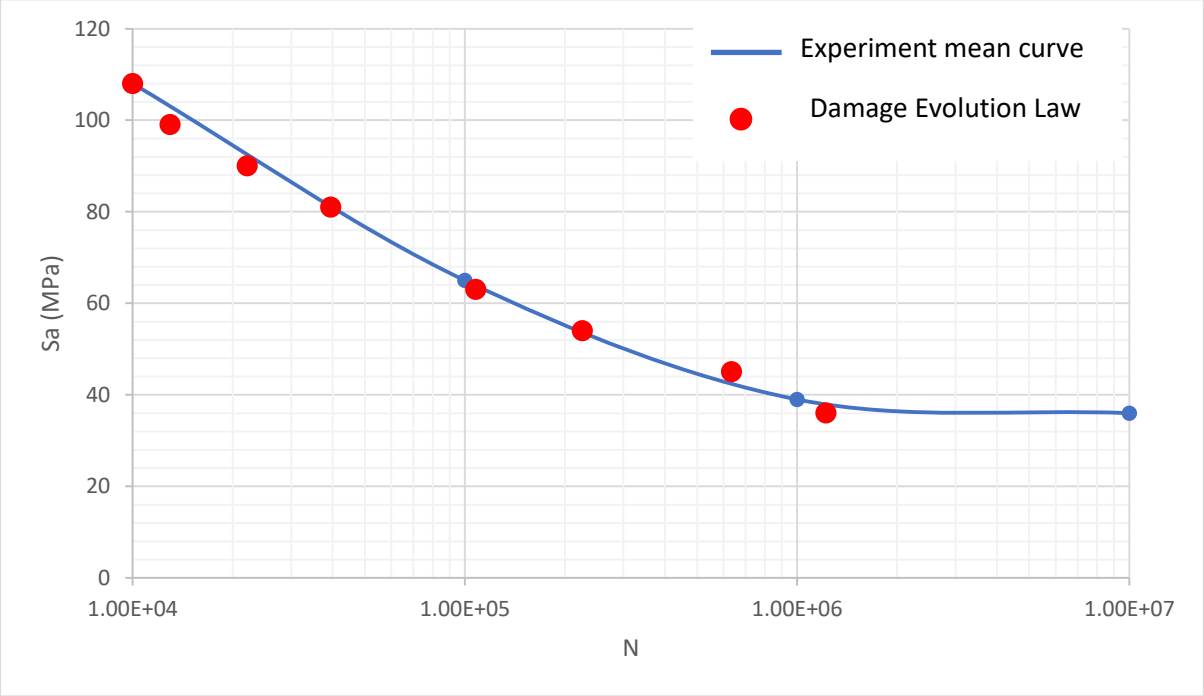

Figure 5.22: Comparison between the mean curve of the 1" standard API Line Pipe results and damage evolution law.

Table 5.9: Numerical data of the damage evolution law.

S_a(MPa)	R_V	$\Delta\sigma_{eq}$(MPa)	N
35	1.14	3	1221250
45	1.15	5	635193
55	1.16	13	225763
65	1.17	23	107975
75	1.18	37	61886
85	1.19	54	39518
90	1.19	87	22125
100	1.19	137	12968
110	1.20	167	10012

It can be seen that for all 9 stress levels where the DEL is evaluated, the obtained fatigue life is in good correspondence with the experimental mean curve. The standard deviation STD is only 1.85 MPa. Also, the values of the fatigue life N, the triaxiality function R_V and von Mises equivalent stress range $\Delta\sigma_{eq}$ are given in table 5.9 for the 9 evaluated values of the stress amplitude S_a. The triaxiality function only slightly increases with increasing stress amplitude, while $\Delta\sigma_{eq}$ is highly dependent of the applied stress level.

To investigate the sensitivity of the critical distance used in the area method, the damage parameter a and β are determined two additional times using the same methodology for a critical of 0.08 and 0.12 mm respectively. The resulting values are

shown in table 5.10. The value of β does not vary greatly. The damage parameter a increases for an increases critical distance. However, the change remains relatively small and it can be stated that small deviations in the number of elements included in the critical area do not affect the value of the damage parameter significantly.

Table 5.10: Damage parameters for different critical distance values.

L_c (mm)	a	β	Number of element in critical area
0.08	1.54×10^{-7}	-8.08	85
0.10	1.50×10^{-7}	-8.23	104
0.12	1.85×10^{-7}	-8.14	126

From the results which was self evidented, it can be concluded that combination of damage and fracture mechanics approach can be a good estimation tool for predicting fatigue behaviour. Moreover, the proposed approach can be applied to real application of fatigue problems with more complicated geometries.

5.5.6 Application to the experimental results

The determined damage parameters a and β should be valid for all types of threaded connections consisting of Grade B steel. The obtained damage evolution law eq. (5.28) is now used to evaluated the fatigue performance of the 5 tested 1" configurations manufactured from the API Line Pipe samples. The DEL data points in the graph in figure 5.23 are obtained by inserting the simulated value of R_V and $\Delta\sigma_{eq}$ in eq. (5.28). It is clear that there is a good correspondence between the predictions of the DEL and the experimental mean curve (STD = 2.97 MPa). As a comparison, the mean curve of the standard API Line Pipe connection is provided. It can be seen that the DEL predicts a similar increase of the connection's fatigue life.

The triaxiality R_V in the connection with reduced box wall thickness higher than for the standard API Line Pipe connection. While only a limited increase of $\Delta\sigma_{eq}$ appears, a change in triaxiality R_V affects the fatigue limit of the S-N curve in the plot. R_V has no influence on the slope of the curve, but $\Delta\sigma_{eq}$ will decrease it.

Table 5.11: Fatigue stress at 10^5 cycles with tested 1" configuration.

Connection configuration	Fatigue stress at 10^5 cycles (MPa)	DEL fatigue stress at 10^5 cycles (MPa)	R_V	$\Delta\sigma_{eq}$ (MPa)
Standard API Pipe Line	65	64.56	1.18	25.6

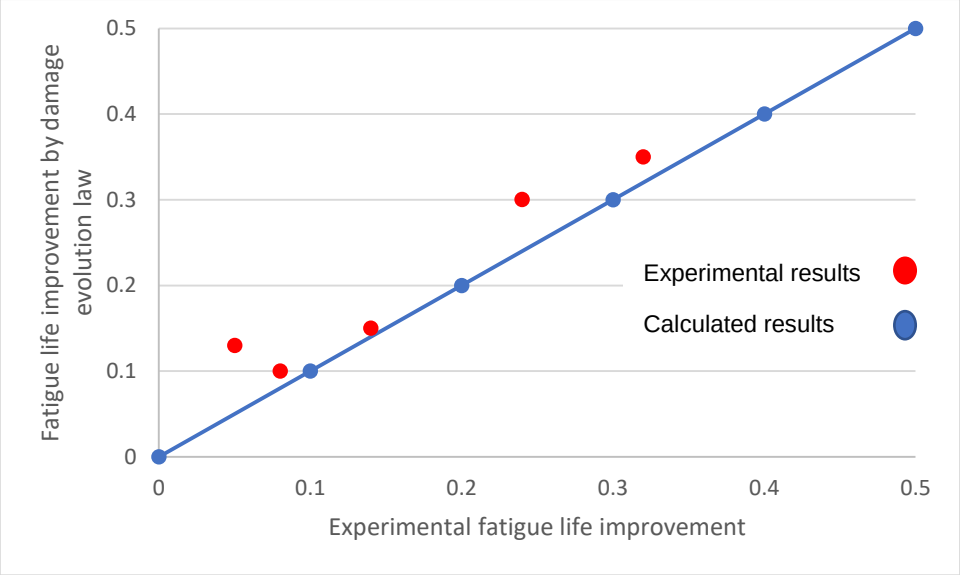

Figure 5.23: Comparison between experimentally obtained and calculated fatigue life improvement values.

For this configuration, there is only a moderate agreement since the DEL predicts a curve with a slope that is too steep. This indicates that the prediction of the von Mises stress range is inaccurate. The standard deviation between the DEL data and the experimental mean curve is 9.15 MPa. This is relatively high.

In table 5.11 the predicated and experimental values are compared based on the fatigue stress values at 10^5 cycles. Next to the values as such, the improvement in terms of percentage are given in table 5.12. From this it is clear that, although the predictions are unconservative for every configuration a higher fatigue stress is predicted than experimentally determined i.e. they follow the same trend. A modified configuration show a higher value of the triaxiality function R_V than the standard API Line Pipe connection, which explains the better fatigue properties. However, the beneficial effect of the increased triaxiality function is in some cases countered by a higher von Mises stress range. The DEL is able to predict the trend observed during the experiments.

For the $4.5''$ API Line Pipe tests on the medium scale axial load setup, insufficient tests have been carried out to construct an experimental fatigue curve. Nevertheless, the results of test 4 are evaluated using the DEL. In this test, a fatigue life of $N = 28250$ cycles was obtained at the stress amplitude of 69.8MPa. For this stress level, following values are obtained from the finite element model: $R_V = 1.41$ and $\Delta\sigma_{eq} = 112.5\ MPa$. When these values are substituted in the DEL eq. (5.28) a fatigue life is obtained of $N = 28000$ cycles, which fit the experimental result.

5.6 Fatigue analysis

5.6.1 Comparison with literature data

In figure 5.24 a comparison is made between the experimentally obtained fatigue data and published results for API steel previously described in chapter 2. This graph the

stress amplitude is expressed relative to the tensile strength of the connection materials. It can be seen that the obtained data is in line with results from previous studies.

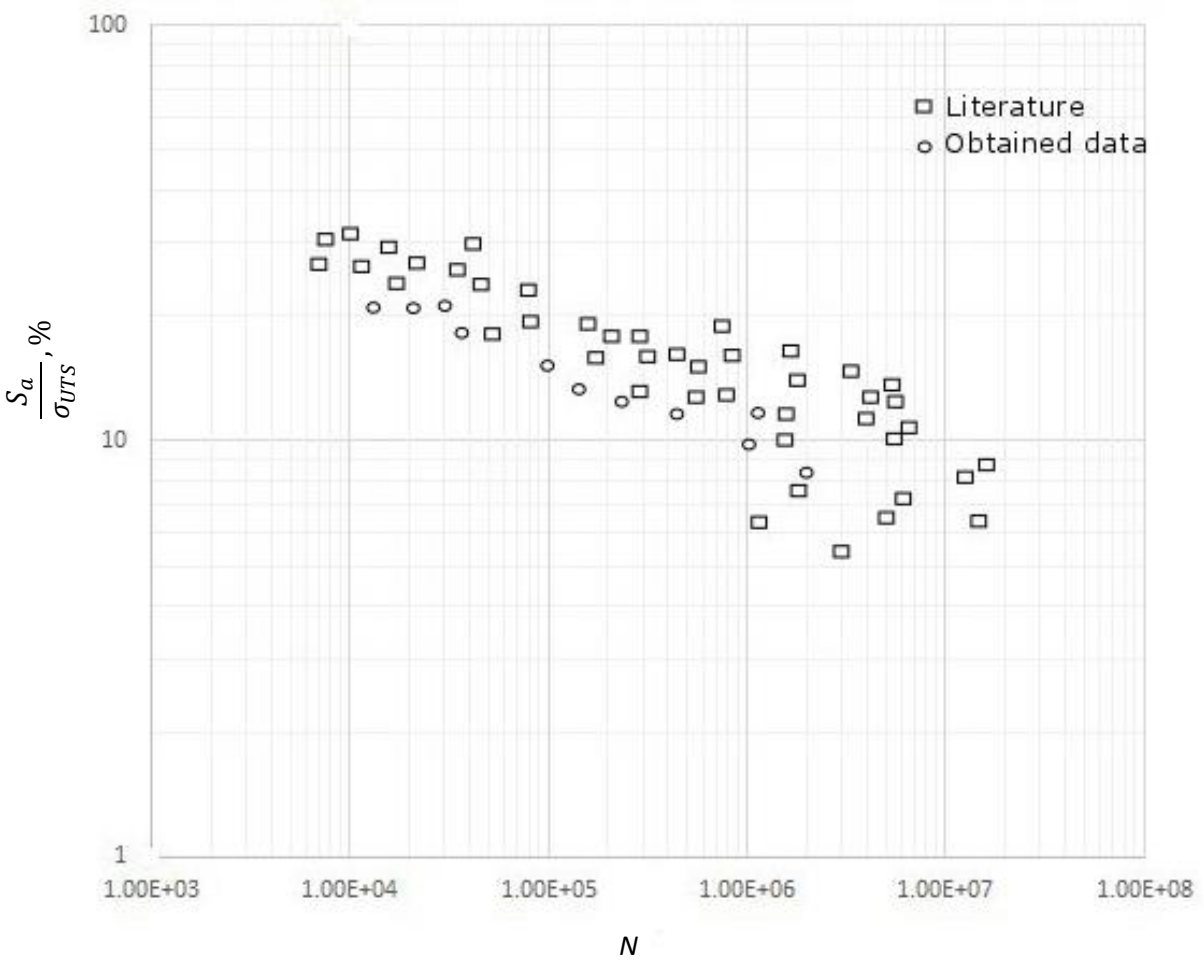

Figure 5.24: Comparison of data obtained in this study with data from literature.

5.6.2 Comparison with Existing Standards

Two standard design curves for threaded pipe connections and a design curve for threaded fasteners were introduced in chapter 2.

In figure 5.25 the results are shown of the 20 failed $1''$ test specimens, obtained using the small scale axial load setup together with the fatigue life data of the 4 tests on the 4.5" API Line Pipe specimens (axial tension). The 1" data points are represented by circles, the 4.5" results are by black squares. Additionally, the ASME-B31 and DNV-B design curves are added. Since these curves are given for a load ratio R = -1, the experiment test data is corrected using Goodman equation (2.16).

Note that all data points are situated well above the ASME-B31 design curve, which means this curve is over-conservative. Hence, the use of this curve would lead to unnecessarily over-dimensioned connections.

The DNV-B curve is obtained by correcting the standard curve eq. (2.39) with the stress concentration factor 3.95 obtained by the finite element model. All these codes used identical producers and it is important to note that only 2 of 20 data points are situated below the DNV-B curve. Accordingly, 98% of the data points are situated above the curve. Since the design curve is based on a mean curve minus twice the standard deviation, it is associated with a 96% probability of survival which is in good correspondence with the obtained value. Due to this good match, it is clear that the DNV approach is more suitable for evaluating the fatigue performance of threaded connections that the ASME-B31 curve. However, more detailed analysis of the different configuration is hard. As plastic deformation occurs during make-up, the von Mises stress at the thread root shows little difference for the different connection types and almost identical stress concentration factors are obtained. Hence the DVN-B can be used as a general design curve, but it is not possible to predict rigorously the influence of different design features on the connection's fatigue life.

The *S-N* plot figure 5.26 compare the fatigue data to the BS 7608 curve. In this curve, the stress amplitude is represented as a percentage of the experimentally determined material's ultimate tensile strength. Both the data points of the failed specimens and of the specimens that did not failed after at least 2×10^6 cycle are plotted. Again only two data points are below the curve, which is acceptable considering the 95.4% probability of survival of the curve. Nevertheless, it can be observed that the 4.5" API Line Pipe results in the low cycle region are lying closely to the curve, while all other data points at the high cycle region are well above it. Hence, the design curve does become more conservative in the high cycle region which make it less accurate than the DNV approach. It can be concluded that the use of standard design curves leads to conservative results and no accurate distinction can be made between different connection designs.

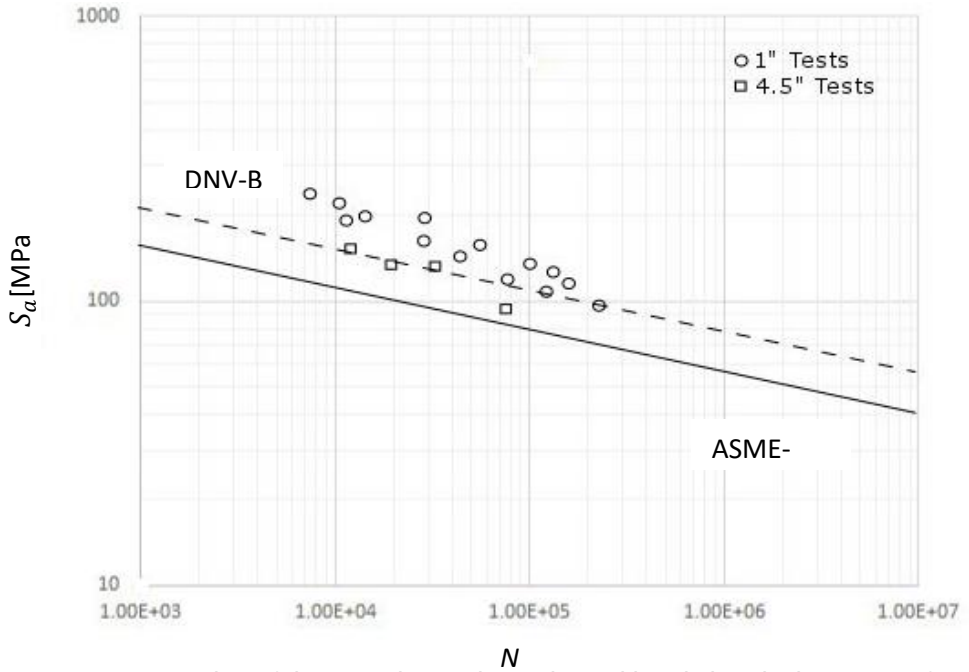

Figure 5.25: Comparsion of the experimental test data with existing design curves for threaded pipe connections (R = -1).

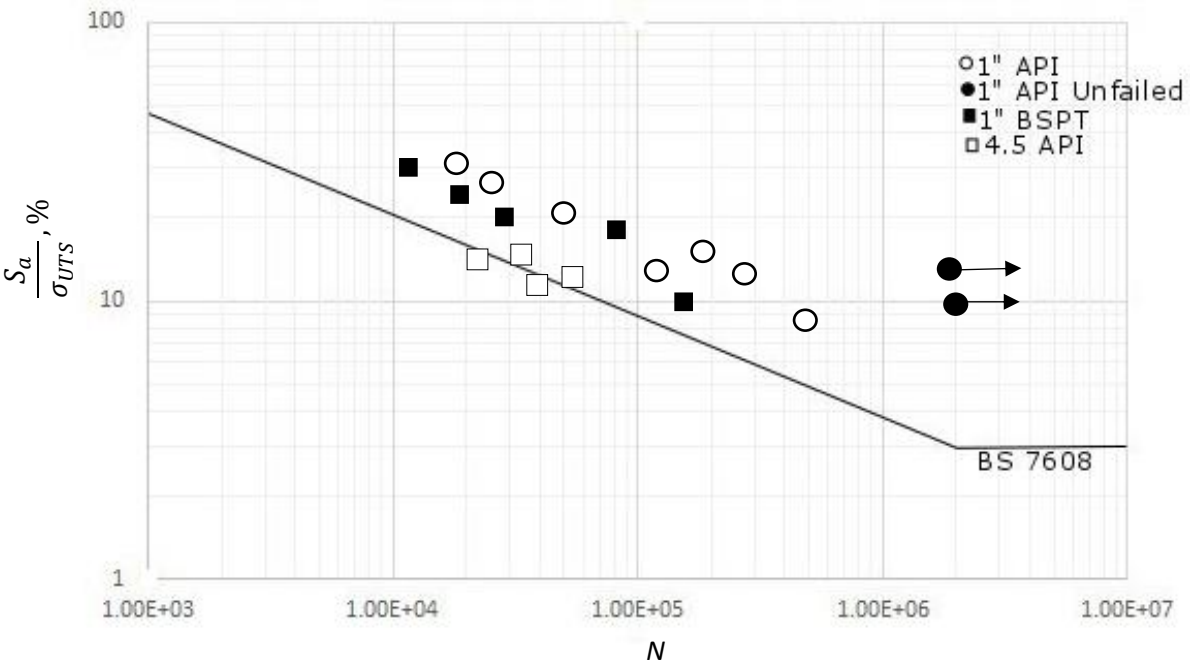

Figure 5.26: Comparison of the experimental data with BS7608 design curve (R = -1).

5.6.3 Comparison with load distribution

It is a common practice to use the thread load distribution as a measure for the fatigue life of a threaded connection. To check this assumption, the thread load distributions are calculated for the 1" configurations tested on the small scale axial load setup as described in chapter 4. The relative load carried by the LET for the different configurations is summarized in table 5.12. The load distributions for two configurations are illustrated in figure 5.27. They are plotted as a percentage of the total load carried by the coupling, where thread 1 corresponds to the LET. Note that for the standard API connection the thread 6 carries a negative load. This is caused by bending of the pin due to make-up deformation, which puts a compressive load on this thread. The standard API Line Pipe connection is used as a reference to other configurations. The LET of this connection carries 53% of the total load. The respective percentages of the load carried by the LET are reduced to 44.5% and 36% which are significantly lower than for the standard API Line Pipe configuration. For the BSPT configuration a relative thread load of 82% at the LET is calculated. This high value is caused by straight pin and box. This results in only four engaged threads and a highly-concentrated load on the LET.

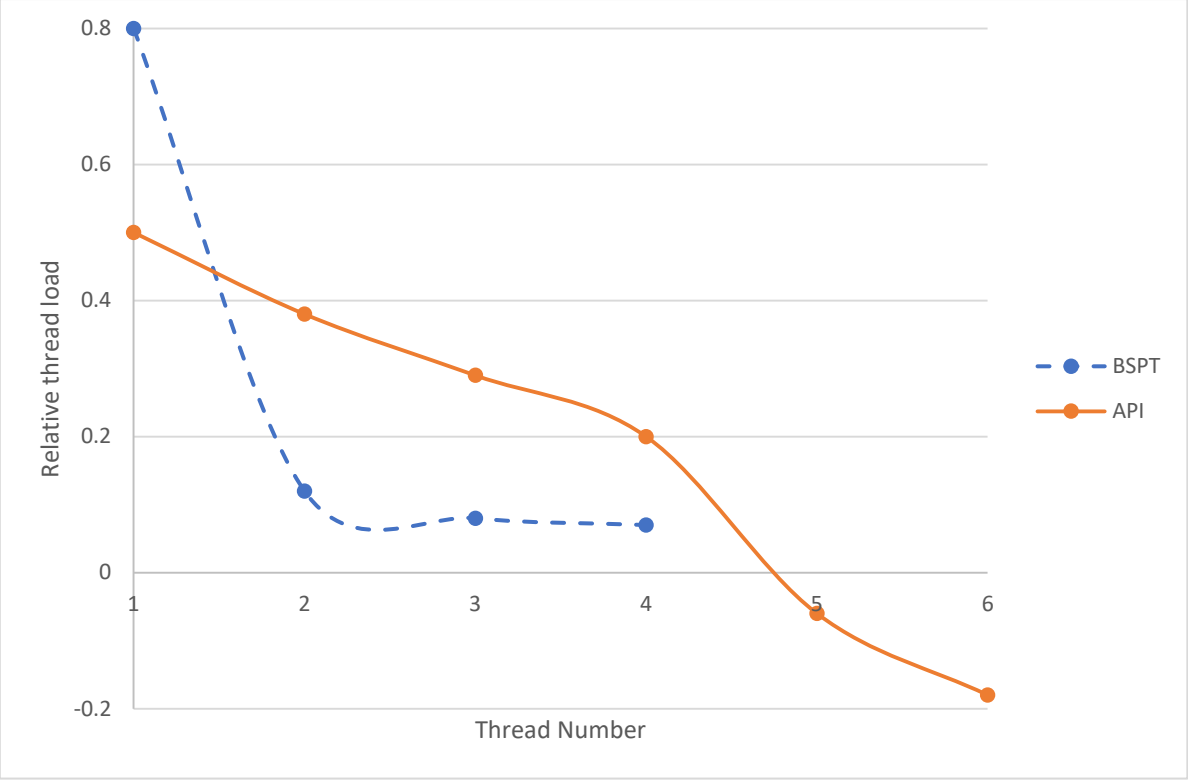

Figure 5.27: Thread load distribution of 1" configurations.

Table 5.12: Comparison of the fatigue stress at 10^5 cycles with the LET relative thread load for tested 1" configuration.

Connection configuration	Fatigue stress at 10^5 cycles (MPa)	Fatigue stress improve (%)	Relative thread load at LET	Thread load improve (%)
Standard API Line Pipe	64.9	-	0.510	-
Standard BSPT	74.5	14.8	0.815	-59.8

In table 5.12 the relative thread load at the LET of the pin as obtained through numerical analyses is put against the allowable fatigue stress at a fatigue life of 10^5 cycles as derived from the experimentally determined *S-N* curve. Additionally, the improvement of the relative thread load at the LET with respect to the standard API configuration is compared to the improvement in fatigue stress amplitude. The results are also plotted in figure 5.28. It is clear that the commonly assumed relation between thread load and fatigue life is not justified. Three configurations exhibit a linear relation between relative thread load and fatigue stress improvement. The BSPT configuration can be subjected to a much higher fatigue stress than expected from the high load carried by the LET. This might be explained by two parameter reasons. First, the crests and roots of the BSPT threads are rounded, while the API Line Pipe threads have a sharper truncated triangular shape. The net stress concentration factor of the BSPT thread ($K_{tn} = 4.4$) is lower than API Line Pipe threads ($K_{tn} = 7.9$) which is beneficial for the fatigue life of the connection. Next to this, the BSPT connection has sealing threads. Hence the thread crests and root of pin and box are in contact with each other

and a certain amount of compressive stress is introduced at the thread root, which can also improve the connection's fatigue life (Knight, Brennan, and Dover, 2004, Korin, and Ipiña, 2010). Despite the unfavorable load distribution, the BSPT exhibits a better fatigue life than the standard API Line Pipe connection due to the improved thread shape.

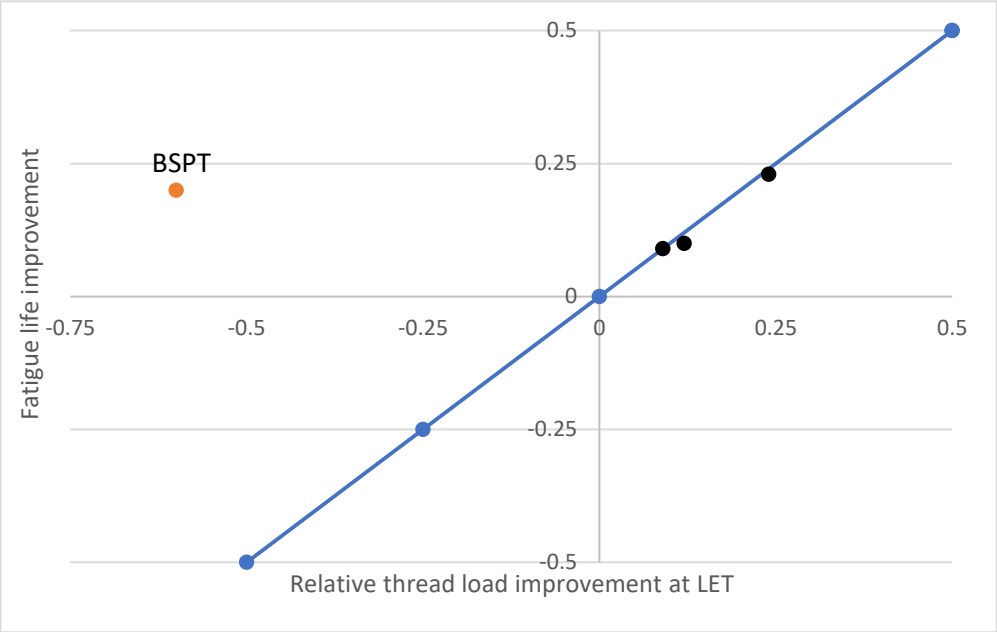

Figure 5.28: Comparison of the relative thread load and fatigue life improvement.

In figure 5.29 the equivalent plastic strain ε_p at the root of the LET (mean value over a certain region, described in section 2.4.1) is plotted as a function of the applied pipe gross axial tensile stress for the API Line Pipe configuration. The equivalent plastic strain at make-up (axial tensile stress = 0 MPa) can be related to the relative thread load at the LET.

This is made clear by the tabulated values of $\varepsilon_{p,make-up}$ and the relative thread load in table 5.13: a decreased equivalent plastic strain at make-up corresponds to a decreased relative thread load. When the pipe axial tensile stress is applied, this relation no longer holds true. The configurations for which the fatigue life improvement is linear to the relative thread load improvement, the plastic strain describes a curve parallel to that of the standard 1" API line pipe connection.

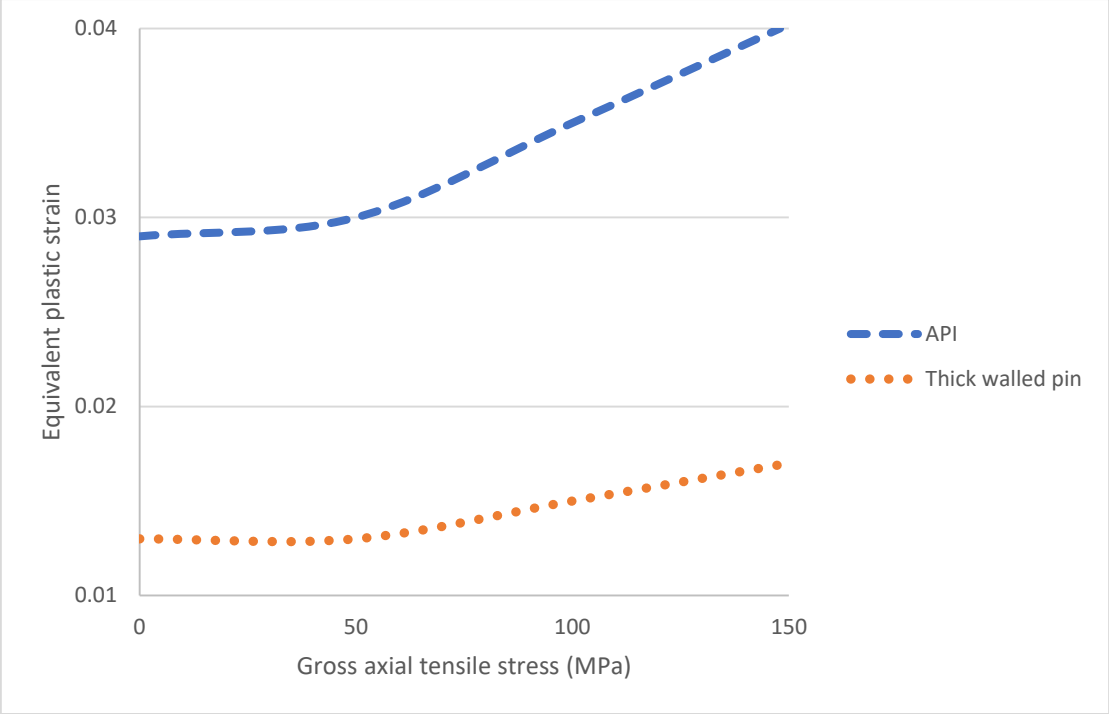

Figure 5.29: Equivalent plastic strain at the LET of the pin as a function of the pipe gross axial tensile stress.

Table 5.13: Equivalent plastic strain and relative thread load data for *1"* API Line Pipe configuration.

Connection configuration	Relative thread load at LET	$\varepsilon_{p,make-up}$ at LET	$\frac{\Delta\varepsilon_p}{\Delta S}$ at 100MPa.10^5 (MPa^{-1})
Standard 1" API Line Pipe	0.510	0.029	9.8
Thick walled pin	0.423	0.012	4.3

To quantify these results, the slope of the plastic strain curve $\Delta\varepsilon_p/\Delta S$ is evaluated at an axial tensile stress of $S = 100\ MPa$ and added in table 5.13. a steep slope means that the strain range during a fatigue test will be higher.

Consequently, a shorter fatigue life might be expected, as it is known from the local strain approach described in chapter 2 that a higher strain range reduces the fatigue life.

It can be concluded that a more uniform load distribution over a threaded connection does not necessarily result in improved fatigue properties. This is because the thread load is a measure for the axial stresses over the connection, while the local stress and strain at the root of the LET are also altered by other stress and strain components such as the hoop stress introduced during make-up, which can additionally be affected by a changed connection stiffness. Hence a connection's fatigue performance cannot be evaluated by its load distribution alone.

5.7 Beach Mark Lines

5.7.1 Beach marking specifications

As mentioned in chapter 3, the load ratio used and number of beach marking cycles applied are important to obtain clear beach mark lines without affecting the crack propagation. In table 5.14 an overview is given of tests found in literature where the beach marking technique has been applied. Shown are the load ratios applied during the test the beach marking blocks as well as applied number of cycles of the test and beach marking blocks.

Table 5.14: Overview of typical beach marking parameter.

Application	R_{test}	R_{beach}	N_{test}	N_{beach}	Source
Drill pipe thread	0.02	0.58	NN	NN	Brennan (1992)
Cube with edge crack	0.1	0.65 to 0.9	NN	6000-110000	Liu and Bowen (2003)
Plate surface crack	0.1	0.64	3000 - 40000	2500-20000	Raghava et al. (2005)
Cylinder surface crack	0.1	0.73	NN	NN	Cai and Shin (2005.)
Welded structure	0.1	0.53	40000	100000	Lihavainen (2007)

In the present study, beach marking cycles are applied under a block loading sequence. The resulting beach marks are fine lines, consequently the number of applied beach mark cycles is excluded from the number of load cycles *N*.

5.7.2 Loading low to high

The fracture of test for 1 inch pipe by applying small load and increase gradually to high load is shown in figure 5.30.a. The crack initiated at the root of the pin's LET. Mentioned earlier a wide load range was chosen for stepped tests. One test was performed from a low load of 20 kN to high load of $60\ kN$.

Since each load was tested separately it was establish total number of cycle to failure for each load. The stepped test was performed at three different load level starting from $0\ to\ 20\ kN$ and run for one million cycles, after that paused for 20 second for test to be stable and moved to second stage of load $40\ kN$ and tested was running for another 31072 cycle and again test was paused for 20 second for stable measurement and final stage of test was running for $60\ kN$, at this stage test was running until it reached the failure. The resulting beach marking line can be clearly distinguished. A magnified view of the zone in the four locations is given in figure 5.30. It can be seen that the beach marking process creates a fine line in the fracture surface.

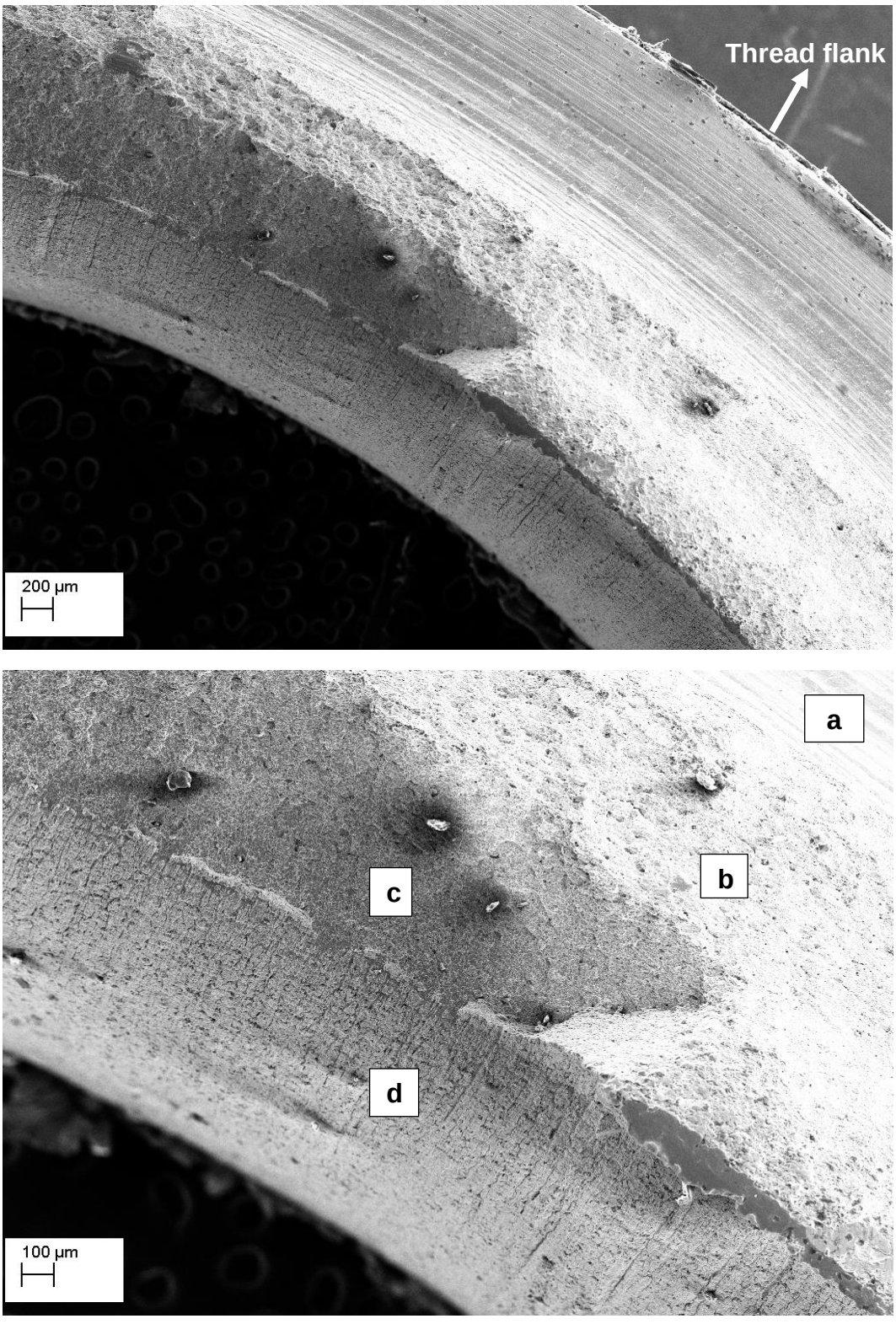

Figure 5.30: a) Fracture surface, zone in rectangles are magnified in Figure 5.27: b) highlighted zones divided by the beach mark line.

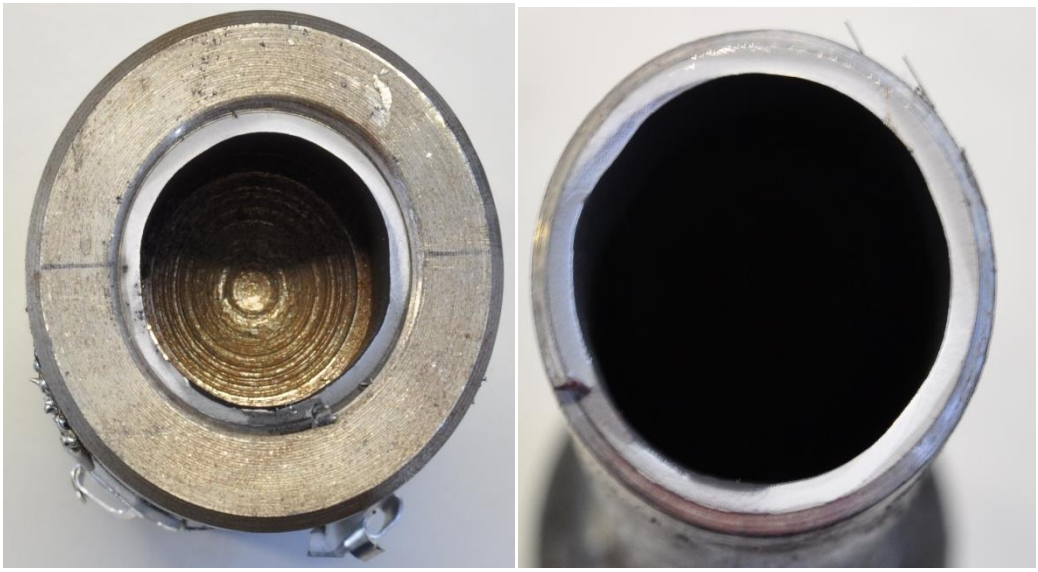

Figure 5.31: a) Fracture surface, zone in rectangles are magnified in Figure 5.27: b) highlighted zones divided by the beach mark line.

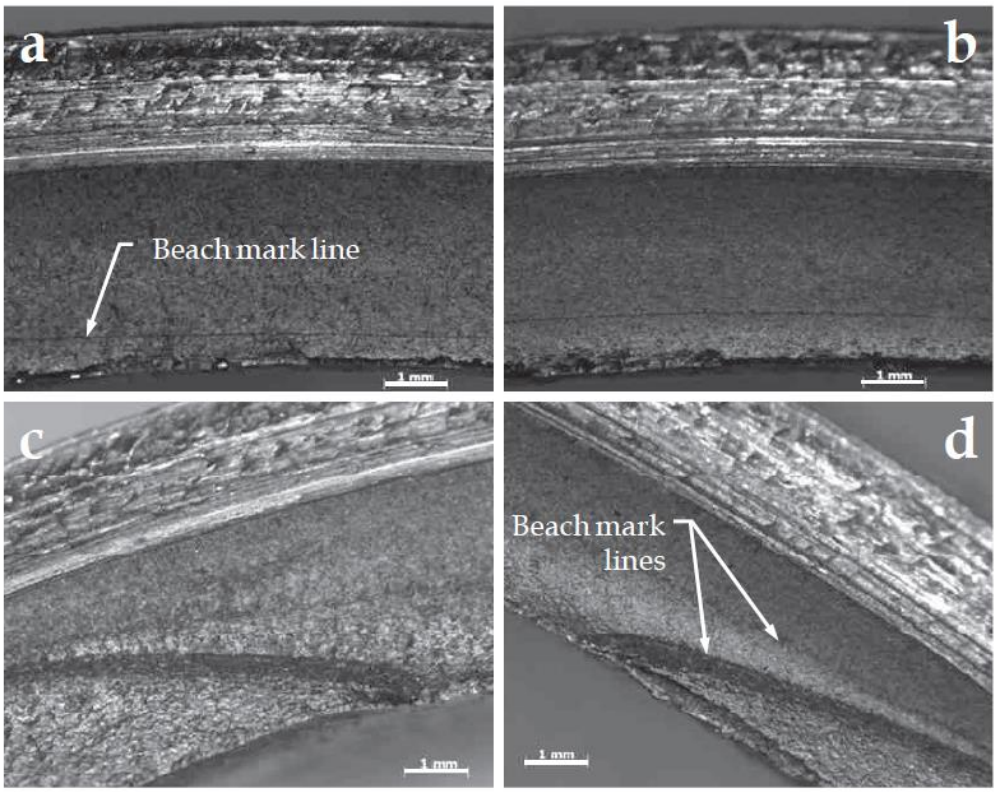

Figure 5.32: Detailed view of the fracture surface with beach mark line.

In figure 5.31.b, the different zones of the fracture are highlighted. It can be seen that the crack initiated along the thread root and propagated over a large segment of the circumference from a low load cycles without creating a through wall thickness crack. During the subsequent load cycles the crack penetrates the pipe wall, while its increase along the pipe circumference is only limited.

In order to determine the crack initiation life N_i and the number of cycles to failure N for the other performed tests, the respective number of cycle is used for a crack opening value of 0.1 mm is used to determine figure 5.33. Since the occurrence of a through-wall crack is used as the failure criterion in this research, it can be seen from the first two beach mark lines that the fatigue life N of this specimen is between peak loads $40\ kN$ and $60\ kN$.

After the pipe wall, has been breached, the crack propagates rapidly over two different crack fronts as can be seen from the crack zone. During the subsequent cycles the crack growth become more and more unstable and the test is finally terminated at 25000 cycles.

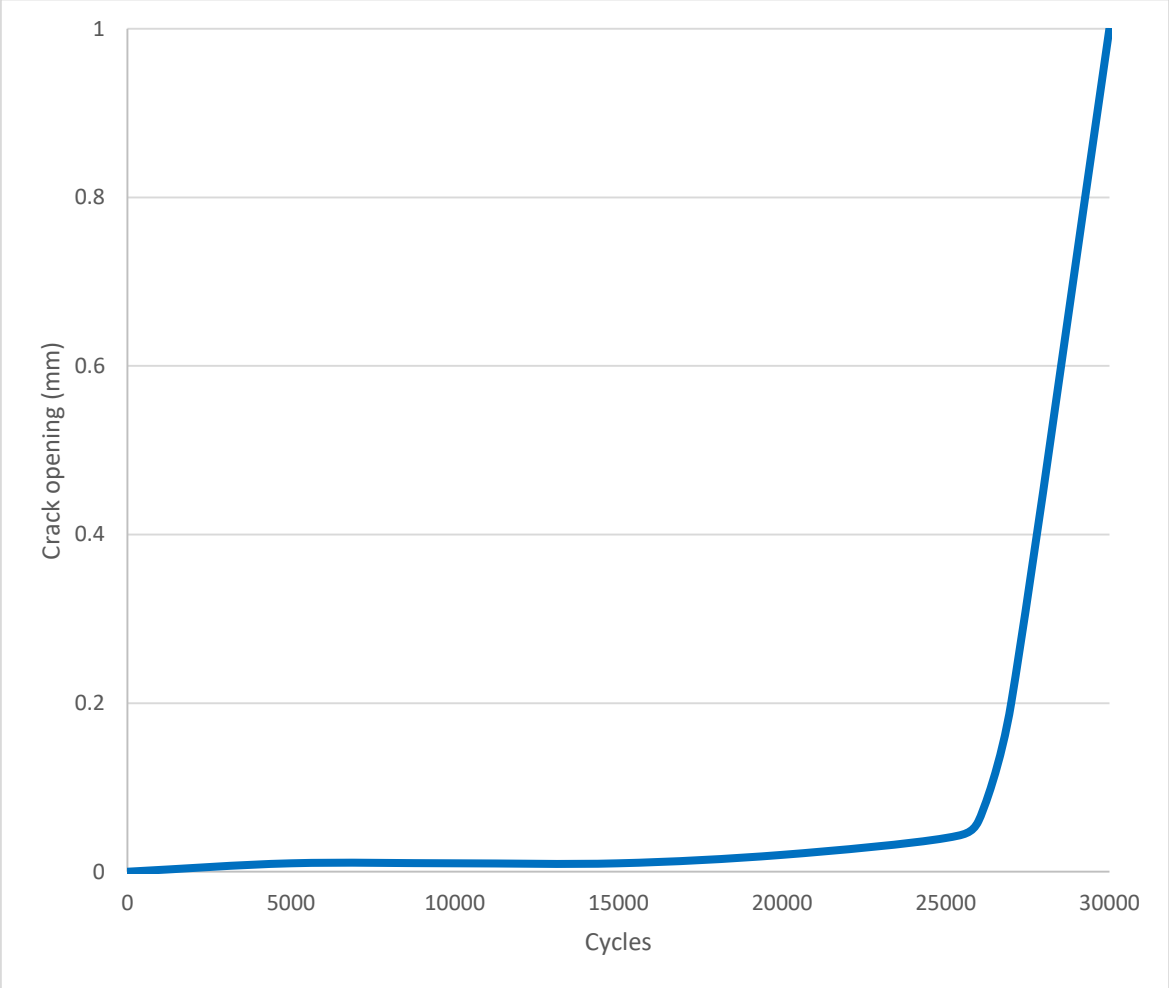

Figure 5.33: Crack propagation of threaded connection from a low load to a high load.

5.7.3 Cyclic load high to low

The same test loads 20, 40 and $60kN$ were applied but in reverse order, so this test started $60kN$ and finished at $20kN$. This test did not reached failure despite the last stage having reached over five million cycle, after that test was stopped and threaded joint was carefully examined, which showed no crack or deformation of the threaded joint connection.

Since in pervious test no failure was observed another block test was performed starting from higher initial load in the sequence $70kN$ to $50kN$ to $30kN$. Failure was achieved in this test as illustrated in the graph figure 5.33. The test was terminated after $N_{test} = 24000$ cycles. Here the beach marking cycles were applied to mark the shape of the fracture surface at certain times before penetrating the pipe wall. The resulting fracture surface of the crack that occurred at the root of the LET of the pin as shown in figure 5.34. With these views the fatigue propagation behaviour, as seen in all previously described small and medium scale tests, is confirmed and the exact crack growth behaviour becomes clearer.

From the highlighted zones in figure 5.34.b it can be seen after 24000 cycles, when the crack depth is limited to about 1.2 mm, it has extended over a considerable length. Hence a long shallow crack is present in the root of the LET of the pin. It continues to propagate in the circumferential direction while only gradually increasing the crack depth. When the total crack length is about one quarter of the entire circumference, the crack fully penetrates the pipe wall and will continue to grow over the two created crack fronts.

Figure 5.34: a) Fracture surface test low to high; b) zone divided by the beach marks.

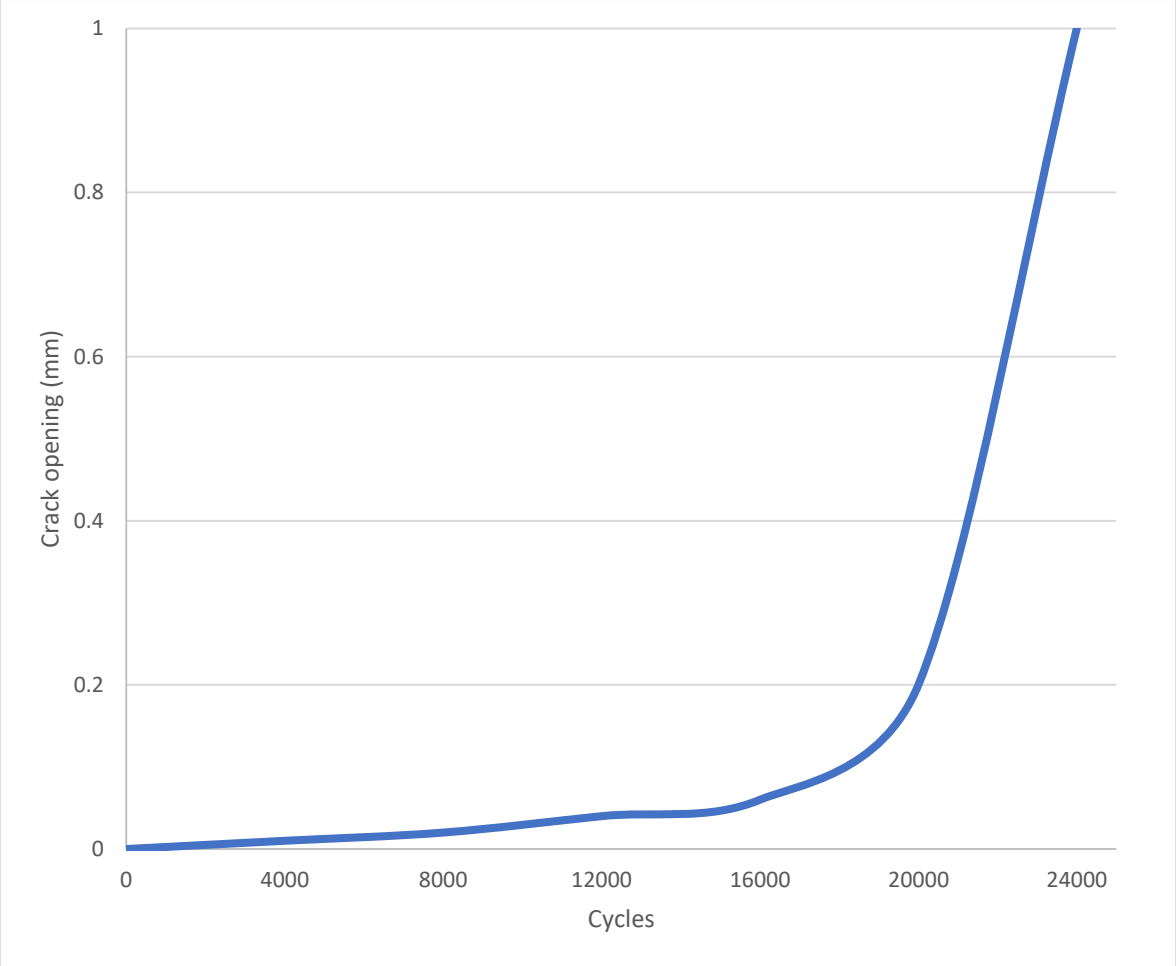

Figure 5.35: Crack propagation from a high cycle to a low cycle.

Other method have been used by researcher in order to analysis the crack initiation and propagation in threaded joint connection. These method were energy dissipation, loss of stiffness, damage law, stress intensity factor and J-integral. In section 5.8 and 5.9 and chapter 6 in detail.

The damage law approach was found to be the most promising method for analysing fatigue and crack propagation in threaded joint connection the results having been illustrated above.

The stress intensity factor and J-integral were alternative methods considered for the FE simulation given in chapter 6.

5.8 Energy dissipation method

The energy method is one of many methods to analysing fatigue failure in threaded joint connection. The figure 5.36 show a graph for a $100\ kN$ test on 1-inch API, energy dissipation method is to analysing how much energy dissipated per cycle and by change of energy it can be seen when and at what cycle failure is going to happen, but unfortunately as it can be seen in the graph below all the loop cycle sharing similar area due to being linear elastic until a sudden failure.

Figure 5.37 it shows the trend of energy dissipated almost in linear pattern until it reaches a sudden failure, this test perfectly proof this problem is fully Linear Elastic Fracture Mechanic (LEFM). Also from this test it can be confirm the sample is brittle and little plasticity is happening.

The remaining result presented in Appendix B.

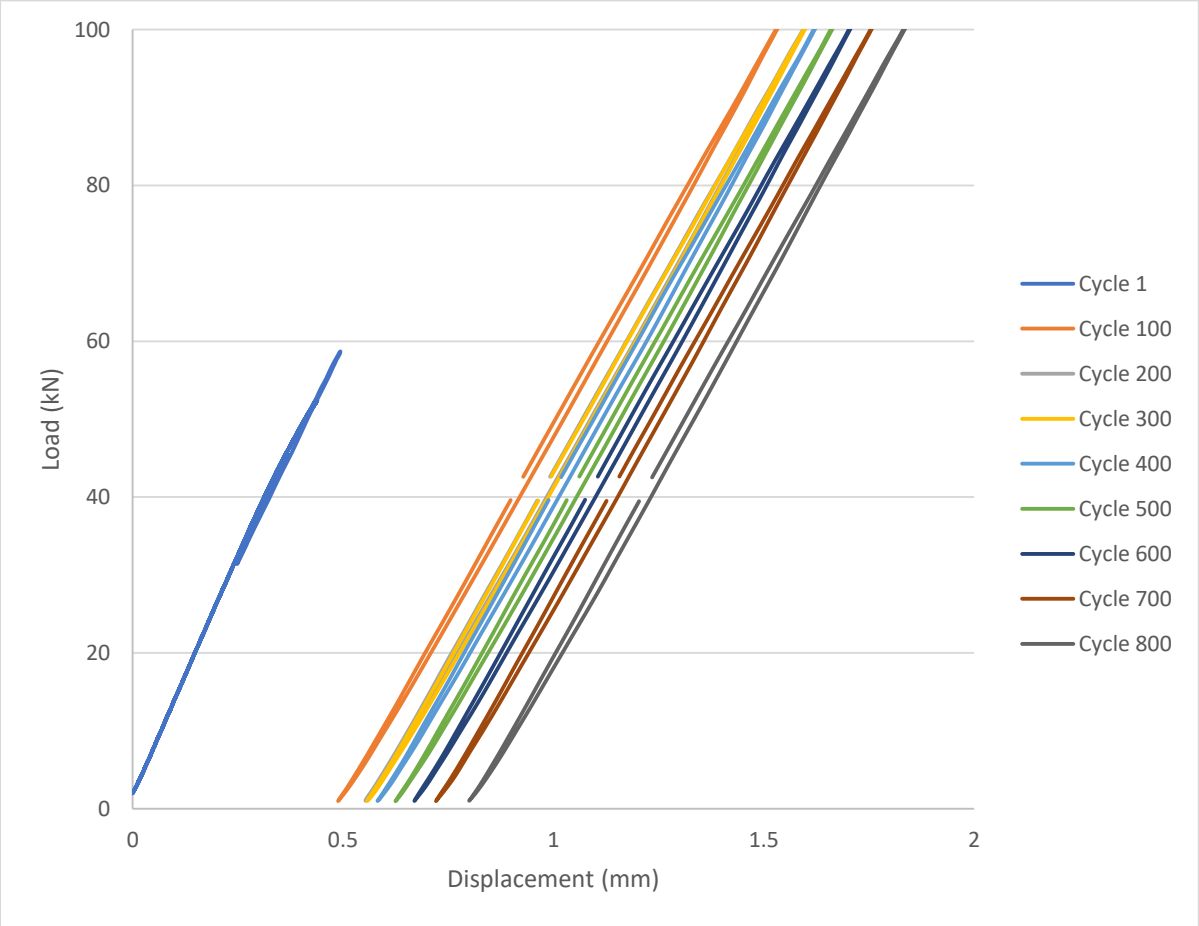

Figure 5.36: Cyclic loading of $100kN$ on 1-inch API threaded connection.

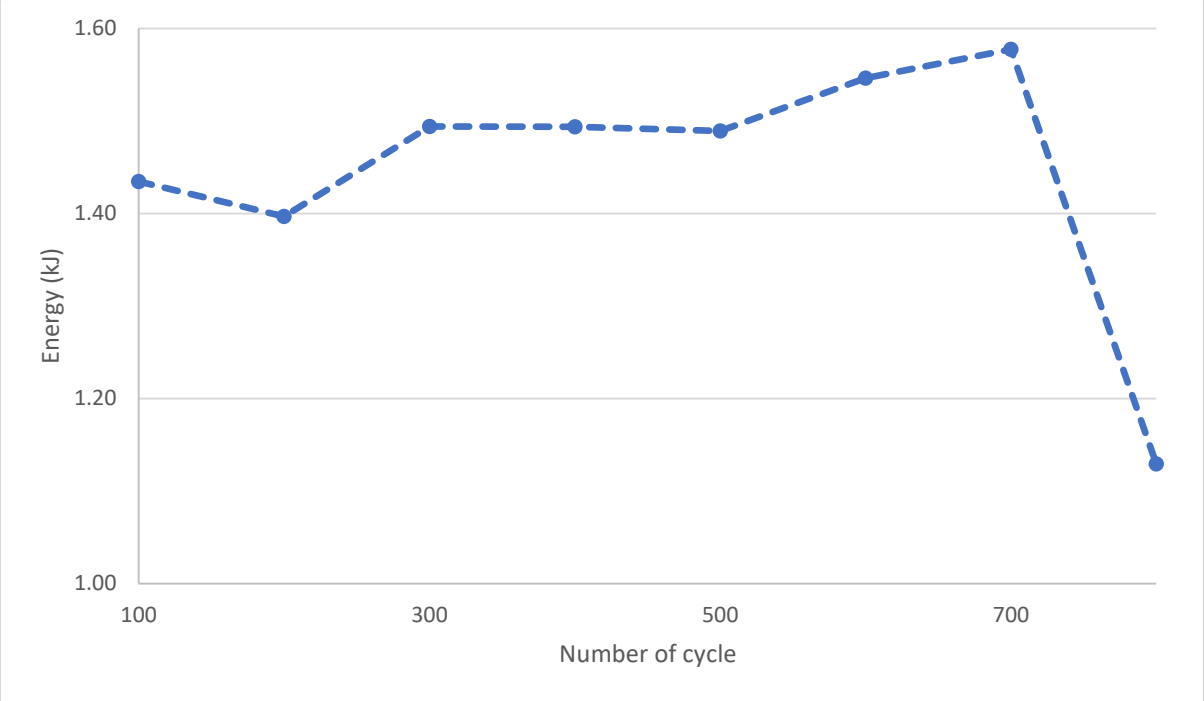

Figure 5.37: Energy dissipation in 1-inch threaded pipe connection during a cyclic test of 100kN.

5.9 Loss of stiffness

The other method is measuring loss of stiffness of material due to cyclic loading, it is established that material loss its stiffness due to cyclic load, using this method it can be analysed how much a material loss its stiffness and reaches it failure point. The way of measuring stiffness of material in this research was using cyclic loading and hysteresis loop in figure 5.36 from loading and displacement, the gradient of the hysteresis loop considers to be the material stiffness, after finding the gradient for each cycle they were plotted in figure 5.37. It can be seen from the graph the line flow a straight pattern until it reaches a sudden failure. This method is not very successful.

5.10 Summary and Conclusions

In this chapter, the experimental work of this research is presented. Both static and fatigue experiments are carried out. The test rigs that are developed during this research to perform the experiments are outlined.

Using the results of static torque tests, the coefficient of friction of the contacting threads is determined. The obtained value will be used as input in the finite element model described in next chapter. In addition, the strains measured during the static torque test, axial test will be used as a validation for this finite element model.

In total 20 fatigue test are carried out of which one axial tension fatigue test, 4 medium scale axial load tests and 20 small scale axial load tests. This amount of results provide a strong experimental basis for further analysis of different connection types. It is pointed out that the number of conducted experiments is similar to the number of testing done by previous researcher on the fatigue of threaded pipe connections found in literature. As shown in chapter 2 the results of 175 fatigue tests on threaded pipe connections were found in literature, where the most extensive study presents the results of 31 tests. Hence, this study provides important additional experimental data.

The results of the small-scale tests show that a local modification of the threaded connection's geometry or contact conditions can have an important influence on the total connection's fatigue life. As a consequence, the idea introduced in chapter 2 that a connection's stiffness change can improve its fatigue life is hereby confirmed.

Several measurement techniques are used to detect fatigue damage during the performed tests. During the medium scale, several techniques are used to detect fatigue damage in threaded connections. The measurements are used to distinguish between the crack initiation and propagation and are confirmed by the beach mark lines that are observed in fracture surface. The ratio of crack propagation life to total life corresponds well with values reported in literature.

Detailed analysis of the fracture surfaces shows that the fatigue cracks initiated at the root of the LET of the pin. This corresponds to documented failure cases and published results of the laboratory test. In addition, this is the location where the highest stress concentration is reported to occur. After initiation, a crack propagates gradually over a large segment of the circumference, forming a long shallow crack. When the crack penetrates the wall of the pin, the crack rapidly increases in size along two crack fronts.

In this chapter, the experimentally obtained fatigue data is compared to standardized fatigue assessment techniques and to the results from the finite element model. It is also shown that the obtained experimental results to standard fatigue curve show that standard curves are either too conservative or not accurate enough to predict the exact fatigue behaviour of different connection designs.

The general concept of using a connection's thread load distribution as a measure for its fatigue life is shown to be inaccurate. The main reason for this is that the load distribution is mainly defined by the distribution of axial stresses over the connection.

The make-up introduces important hoop stresses that contributed to the local stresses and equivalent plastic strain around the root of the LET and that consequently affects the connection's fatigue life. To account for this multiaxiality, a damage evaluation law is used.

This model combines information about the local multiaxial stress distribution at the thread root of the LET of the pin obtained from the finite element model with experimentally obtained damage parameters. With this damage evolution law, the experimentally observed trends can be explained. It is shown that creating a more uniform load distribution can be beneficial if the equivalent stress range and equivalent plastic range at the LET remain limited and if the value of triaxiality function R_V is increased.

References

- Assanelli, A.P., Xu, Q., Benedetto, F., Johnson, D.H. and Dvorkin, E.N., 1997. Numerical/experimental analysis of an API 8-round connection. *Journal of energy resources technology*, *119*(2), pp.81-88.
- Boiler, A.S.M.E. and Code, P.V., 2010. Section VIII-Rules for Construction of Pressure Vessels. *Division I*.
- Boiler, A.S.M.E., 2007. Pressure vessel code. *Sec VIII Div2 (2007 Edition), ASME Publication*.
- Boyer, H.E. ed., 1985. *Atlas of fatigue curves*. Asm International.
- Brennan, F.P., 1992. *Fatigue and fracture mechanics analysis of threaded connections* (Doctoral dissertation, University of London).
- British Standards Institution, 1999. *Guide on methods for assessing the acceptability of flaws in metallic structures*. British Standard Institution.
- BS7608, B.S., 1993. Code of practice for fatigue design and assessment of steel structures. *British Standards Institution*.
- BSi, B.S., 2005. 7910: Guide on methods for assessing the acceptability of flaws in metallic structures. *British Standards Institute*.
- Buchalet, C.B. and Bamford, W.H., 1976. Stress intensity factor solutions for continuous surface flaws in reactor pressure vessels. In *Mechanics of crack growth*. ASTM International.
- Bul, A.P.I., 1999. 5C3. *Bulletin on Formulas and Calculations for Casing, Tubing, Drill Pipe, and Line*.
- Cai, C.Q. and Shin, C.S., 2005. A normalized area-compliance method for monitoring surface crack development in a cylindrical rod. *International journal of fatigue*, *27*(7), pp.801-809.
- Clinedinst, W.O., 1965. Strength of Threaded Joints for Steel Pipe. *Journal of Engineering for Industry*, *87*(2), pp.125-134.
- Clinedinst, W.O., 1976. Joint strength formulas for API threaded Line Pipe. *API Circular PS-1533*.
- Dale, B.A., 1988. An experimental investigation of fatigue-crack growth in drillstring tubulars. *SPE drilling engineering*, *3*(04), pp.356-362.
- El Haddad, M.H., Dowling, N.E., Topper, T.H. and Smith, K.N., 1980. J integral applications for short fatigue cracks at notches. *International Journal of Fracture*, *16*(1), pp.15-30.
- Forman, R.G., Shivakumar, V., Cardinal, J.W., Williams, L.C. and McKeighan, P.C., 2005. Fatigue crack growth database for damage tolerance analysis.
- Knight, M.J., Brennan, F.P. and Dover, W.D., 2004. Effect of residual stress on ACFM crack measurements in drill collar threaded connections. *Ndt & E International*, *37*(5), pp.337-343.
- Kocak, M., Webster, S., Janosch, J.J., Ainsworth, R.A. and Koerset, R., 2008. FITNET Fitness-for-Service (FFS) Procedure. *Revision MK8*, *1*.
- Korin, I. and Ipiña, J.P., 2010. Controlled residual stresses introduction to improve fatigue resistance of rotary shouldered connections used in oil drilling

industry. *International Journal of Pressure Vessels and Piping*, *87*(12), pp.696-703.

- Lam, P.S., Sindelar, R.L., Duncan, A.J. and Adams, T.M., 2009. Literature survey of gaseous hydrogen effects on the mechanical properties of carbon and low alloy steels. *Journal of pressure vessel technology*, *131*(4), p.041408.
- Lihavainen, V.M., 2007. A novel approachfor assessing the fatigue strength of ultrasonic impact treated welded structures. *Acta Universitatis Lappeenrantaensis*.
- Liu, J. and Bowen, P., 2003. DC potential drop calibration in matrix-cladded Ti MMC specimens with a corner notch. *International journal of fatigue*, *25*(7), pp.671-676.
- Majzoobi, G.H., Farrahi, G.H., Hardy, S.J., Pipelzadeh, M.K. and Habibi, N., 2005. Experimental results and finite-element predictions of the effect of nut geometry, washer and Teflon tape on the fatigue life of bolts. *Fatigue & fracture of engineering materials & structures*, *28*(6), pp.557-564.
- Peterson, R.E., 1959. Notch sensitivity. *Metal fatigue*, pp.293-306.
- Raghava, G., Mithun, I.K., Gandhi, P., Vaze, K.K., Bhate, S.R. and Bhattacharya, A., 2005. Application of beach marking technique to the study of fatigue crack growth in steel plate specimens subjected to tensile loads. *Journal of Structural Engineering*, *32*(3), pp.229-232.
- Santus, C., 2008. Fretting fatigue of aluminum alloy in contact with steel in oil drill pipe connections, modeling to interpret test results. *International Journal of Fatigue*, *30*(4), pp.677-688.
- Schneider, W.P., 1982. Casing and tubing connection stresses. *Journal of Petroleum Technology*, *34*(08), pp.1-851.
- Shigley, J.E., 2011. *Shigley's mechanical engineering design*. Tata McGraw-Hill Education.
- Spec, A.P.I., 2008. 5B Specification for Threading. *Gauging and Thread Inspection of Casing, Tubing, and Line Pipe Threads*.
- Stavrovský, V., Papuga, J. and Růžička, M., 2010. Multiaxial approach for local elastic stress analysis. *Procedia Engineering*, *2*(1), pp.1721-1729.
- Susmel, L. and Taylor, D., 2011. The Theory of Critical Distances to estimate lifetime of notched components subjected to variable amplitude uniaxial fatigue loading. *International Journal of Fatigue*, *33*(7), pp.900-911.
- Taylor, D., 1999. Geometrical effects in fatigue: a unifying theoretical model. *International Journal of Fatigue*, *21*(5), pp.413-420.
- Van Wittenberghe, J., 2011. *Experimental analysis and modelling of the fatigue behaviour of threaded pipe connections* (Doctoral dissertation, Ghent University).
- Walker, K., 1970. The effect of stress ratio during crack propagation and fatigue for 2024-T3 and 7075-T6 aluminum. In *Effects of environment and complex load history on fatigue life*. ASTM International.

- Weiner, P.D. and Sewell, F.D., 1967. New Technology for Improved Tubular Connection Performance. *Journal of Petroleum Technology*, *19*(03), pp.337-343.
- Yuan, G., Yao, Z., Han, J. and Wang, Q., 2004. Stress distribution of oil tubing thread connection during make and break process. *Engineering Failure Analysis*, *11*(4), pp.537-545.
- Zhang, L. and Thomas, B.G., 2003, November. Inclusions in continuous casting of steel. In *XXIV National Steelmaking Symposium, Morelia, Mich, Mexico* (Vol. 26, p. 28).

Chapter 6 Finite Element Model

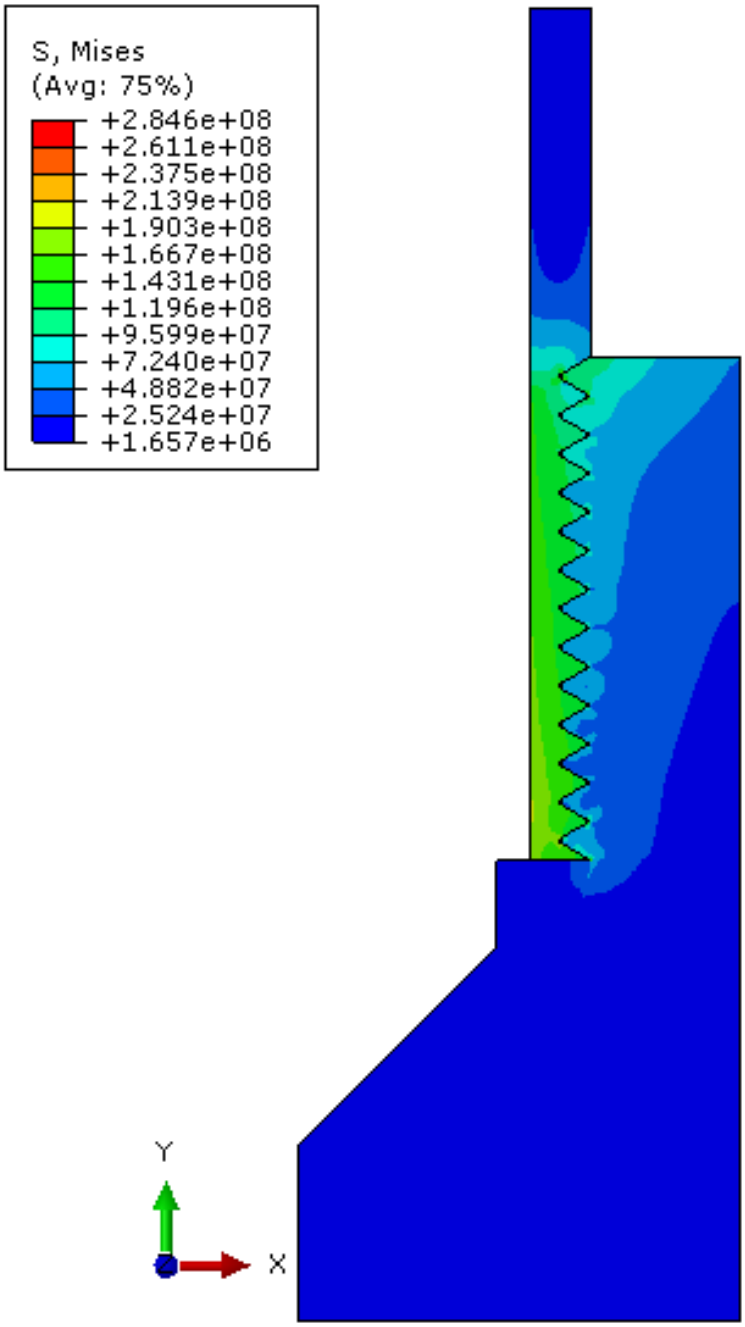

6.1 Summary

To understand further the experimental results obtained in the previous chapter, a 2D axisymmetric finite model is developed. This numerical model is constructed in a parametric way so that different connection types can be efficiently modelled.

In this chapter, the details of this finite element model are provided. First the modelling strategy is defined, followed by a description of the model mesh and its applied non-linearities. To illustrate the use of the model a detailed analysis is presented of standard 1" inch API Line Pipe Connection. Afterward, a comparison is given between the 2D axisymmetric model and full 3D model. Finally, the model is validated by comparing results of the simulations with experimental results described in chapter 5.

6.2 Background and literature review

6.2.1 Fracture mechanics and fatigue crack growth models

Fatigue Crack Growth (FCG) models are empirical models generally based on fracture mechanics developed to describe data from experiments by empirical curve fitting to a function of the form (Beden, 2009):

$$\frac{da}{dN} = f(\Delta K, R) \qquad (6.1)$$

Irwin (1958) introduced the stress intensity factor (SIF) K for static fracture analysis (see Eq.6.2), after his analysis of the stress field around the crack tip in 1957 (Irwin, 1967):

$$K = F\sigma\sqrt{\pi a} \qquad (6.2)$$

Where a is the crack length and F is the geometry factor which depends on the relative crack length $= \frac{a}{b}$.

Paris (1961) employed a simple empirical form of equation (6.1) to apply linear elastic fracture mechanics (LEFM) to fatigue. The Paris' Law describes fatigue crack growth rate, $\frac{da}{dN}$, and is today the most common equation to use for opening mode FCG analysis, appearing as:

$$\frac{da}{dN} = C_P(\Delta K_I)^{m_p} \qquad (6.3)$$

Where the range of stress intensity ΔK is taken as:

$$\Delta K_I = F\Delta S\sqrt{\pi a} \qquad (6.4)$$

Where C_P and m_p are constants which depend on the material, frequency of the cycles and the environment, and ΔS is the stress range. This model is further reviewed in section 6.3

6.2.2 Fatigue rate curve

The fatigue rate curve is a $\frac{da}{dN}$ versus ΔK curve as shown in figure 6.1. The curve is often divided into three regions; as shown.

In region I is the early development of the fatigue crack is represented, where the growth rate is in the order $10^{-6} mm/cycle$ or below. This region is very sensitive to micro structure features like grain size, the mean stress within the applied load range, the environment and the operating temperature (Beden, 2009). The most important feature in this region is the FCG threshold, ΔK_{th}. This is the limit for the propagation of fatigue cracks start. For SIF ranges below the ΔK_{th} crack growth will usually not occur (Dowling, 1993).

Region II is the intermediate zone for growth rates in the order of 10^{-6} to $10^{-3} \frac{mm}{cycle}$. In this region the crack growth is stable, the data is following a power equation and the plastic zone in front of the crack tip is large compared to the mean grain size (Beden, 2009). Since the data obeys a power equation, the fit will be linear on a log-log plot (Figure 6.1) and the use of LEFM eq.6.3 is applicable. For region II the mean stress has the highest influence on the results, but this influence is small compared with region I.

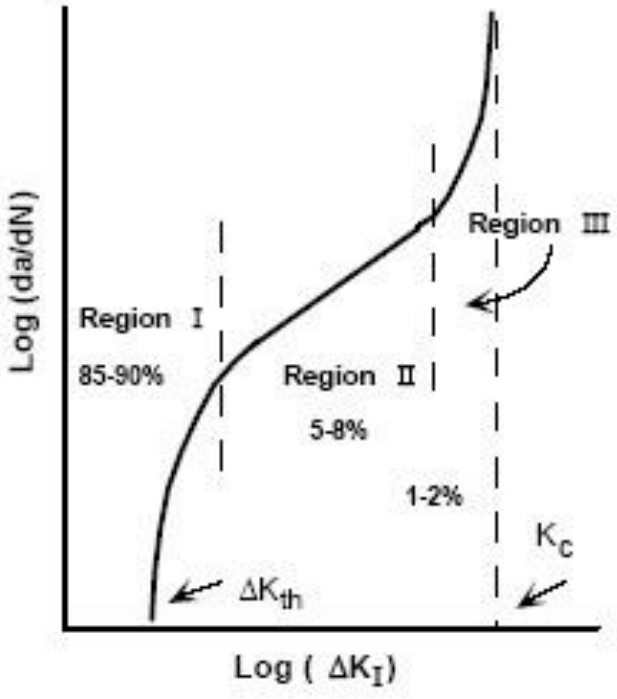

Figure 6.1: Fatigue rate curve.

The last region, III, starts where the curve (figure 6.1) shows an accelerating rate usually in the order $10^{-3} mm/cycle$ and above. This is a high crack growth rate region caused by the rapid unstable growth prior to final failure. The curve approaches in this region an asymptote corresponding to fracture toughness, K_c, for the material.

The nonlinear properties cannot be ignored in this region due to the present of large scale yielding. For this region LEFM cannot be used for the data in this region, instead nonlinear fracture mechanics should be applied. Analyzing FCG for this region is very complex and as the FCG rates are high and little fatigue life $(1-2\%)$ involved. As a result, life prediction for this region are ignored.

6.2.3 Review of fatigue crack growth models

Engineering components are rarely exposed to constant amplitude loading, but rather variable amplitude. To decrease calculation time and simplify the always the variable amplitude loading may be modified and simplified in order to use constant amplitude models with fewer parameters. In FCG models the parameters are often empirical.

6.2.3.1 Paris Model

The FCG model most commonly used in fatigue analysis today is the power law introduced by Paris and Erdogan (1961), also known as the Paris Law equation 6.3. The model is simple in use and only needs two curve fitting parameters to be determined. In the descriptions of data in region II (figure 6.1) The Paris Law is widely used, but region I and region III cannot be sufficiently described by this model. Other limitations of the Paris law are that it does not account for the effect of stress ratio, but the results do depend upon the material. Most importantly Paris law is intended for pure model I loading. Paris' law can be modified for application to mixed mode loading by the use of equivalent *SIF*, further described in section 2.4.

In the common used standard BS7910:2005 (British Standards Institution, 1999) and "Wellhead Fatigue Analysis Method" by DNV Paris' Law is suggested for fatigue analysis. For obtaining correct results from Paris model is it important to collect the fatigue rate data from the related stress ratio.

6.2.3.2 Walker Model

Walker (1970) modified the Paris law to include the effect of stress ratio, R. This model gives the growth rate as:

$$\frac{da}{dN} = C_W(\overline{\Delta K})^{m_w} = C_W\left(\frac{\Delta K}{(1-R)^{1-\gamma_w}}\right)^{m_w} \qquad (6.5)$$

$$\Delta K = K_{max}(1-R)$$

These equation shows:

$$\frac{da}{dN} = C_W\left[\frac{K_{max}(1-R)}{(1-R)^{1-\gamma_W}}\right]^{m_w} = C_w[K_{max}(1-R)^{\gamma_m}]^{m_w}$$

where the constant C_W and m_w are similar to the constants in Paris model (equation (6.3)) C_P and m_P. The parameter $\overline{\Delta K}$ is an equivalent zero to tension stress intensity that causes the same growth rate as the actual K_{max}, R combination. The third curve

fitting parameter, γ_w, is a constant for the material. This parameter may be obtained from data of various R values by linear regression or by trial and error. It is possible that there is no value to be found for γ_w, then the Walker model cannot be valid. If $\gamma_w = 1$ then $\overline{\Delta K}$ equals ΔK and the stress ratio has no effect on the crack growth rate.

6.2.3.3 Forman model

When using the SIF approach, the critical value arises with be an instability of the crack growth (region III, figure 6.1). Neither Paris or Walker's models take this into account. The Forman expression is given by the following relationship:

$$\frac{da}{dN} = \frac{C_F(\Delta K)^{m_y}}{(1-R)K_c - \Delta k} = \frac{C_F(\Delta K)^{m_y}}{(1-R)(K_c - K_{max})} \qquad (6.6)$$

where K_C is the fracture toughness. The use of this constant is necessary to model cracks with high growth rates. Also from the Forman model the relationship between K_{max}, K_c and $\frac{da}{dN}$ show that as the maximum SIF approaches the fracture toughness, the crack growth tends to infinity. With this the Forman equation can be used to represent data for both region II and region III (figure 6.1). If crack growth data for various stress ratios are available, these can be used to compute the quantity Q in equation (6.7) for each data point.

$$Q = \frac{da}{dN}[(1-R)K_c - \Delta K] \qquad (6.7)$$

If the different combinations of ΔK and R all fall together on a straight line on a log-log plot of Q and ΔK, the Forman equation is assumed to be successful and may be used (Dowling,1993).

6.2.3.4 XFEM crack growth

A preliminary study has been performed under the title "Modelling fatigue crack growth using XFEM in ABAQUS 6.10" (Vethe, 2012) to examine the principle of the XFEM simulation.

A variety of techniques are used to calculate the mixed mode stress intensity factor by the XFEM. Literature review performed by Paris (2011) and Belytschko (2009) identified the advantages and disadvtanges of the different calculation techniques. The most common technique according to their prior studies is the use of the domain form of interaction integrals extracted from J-integrals. This method has high accuracy for different crack conditions when used together with a suitable mesh (Pais, 2011).

Required are the domain form of the mode interaction integral and the conversion of the line integral to an area integral. The J-integral is used to find the energy release rate while the interaction integral is used to obtained the mixed-mode stress intensity factor.

6.2.3.4.1 Theory of Interaction Integral

Prior to obtaining the integration integral the J-integrals need to be established. On the basis of the relationship between the *J*-integral, stress intensity factors and the effective Young's modulus, E_{eff}, the energy released rate G for a two-dimensional mixed-mode crack may be expressed as (Pais, 2011). Static what mode I and II refer to:

$$G = J = \frac{K_I^2}{E_{eff}} + \frac{K_{II}^2}{E_{eff}} \qquad (6.8)$$

Where:

$$E_{eff} = \begin{Bmatrix} E & Plane\ stress \\ \dfrac{E}{1-v^2} & Plane\ strain \end{Bmatrix} \qquad (6.9)$$

Where E is Young's modulus and v is Poisson's ratio. Further for a crack counter Γ are the J-integral specified as (Pais, 2011):

$$J = \int_{\Gamma} \left(W n_1 - \sigma_{jk} n_i \frac{\partial u_k}{\partial x_1} \right) d\Gamma \qquad (6.10)$$

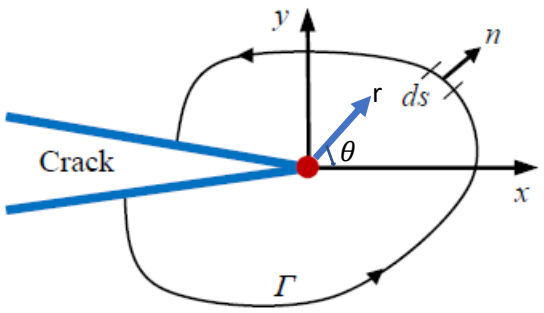

Figure A: Definition of J integral around the crack tip.

Where W is the strain energy density, σ is stress, u is displacement and n_1 is nominal to the counter Γ. To ease the implementation to a finite element code equation 6.10 should be rewritten by introducing the Dirac delta to the first term of the integral.

$$J = \int_{\Gamma} \left(W \delta_{1i} - \sigma_{jk} \frac{\partial u_k}{\partial x_1} \right)_i n_i d\Gamma \qquad (6.11)$$

6.2.4 Crack growth direction

The 1-direction of the crack propagation is established to be a function of mixed-mode stress intensity factors at the crack tip. There are several different criteria to choose the growth direction. Some of the most widely used mixed mode criteria are: the maximum tangential stress criterion, the maximum energy release rate criterion, the zero-shear criterion ($K_{II} = 0$) and maximum circumferential stress criterion.

6.2.4.1 The maximum tangential stress criterion (MTS)

With this criterion are the deflection angle of the crack growth defined to perpendicular to the maximum tangential stress at the crack tip. This criterion is based on the work of Erdogan and Sih (1963) and are given by:

$$\hat{\theta} = cos^{-1}\left(\frac{3K_{II}^2 + \sqrt{K_I^4 + 8K_I^2K_{II}^2}}{K_I^2 + 9K_{II}^2}\right) \qquad (6.12)$$

Where $\hat{\theta}$ is the and with respect to the crack original plane. If mode II SIF (K_{II}) is positive, the propagation angle is negative and opposite. The maximum tangential stress $\sigma_{\theta m}$ are described by the following relationship (Barry, 1992).

$$\sigma_{\theta m} = \frac{1}{\sqrt{2\pi r}} cos^2\frac{\theta_m}{2}\left[K_I cos\frac{\theta_m}{2} - 3K_{II} sin\frac{\theta_m}{2}\right] \qquad (6.13)$$

One important remark with this criterion is that the crack will not propagate in its own plane (expect for pure mode I loading) but in respect to the original plane (Barry, 1992).

6.2.4.2 The maximum energy release rate criterion (MERR)

The MERR criterion is based on the work of Hussain et al. (Hussain, 1974) the criterion assume that the crack propagates in the direction which maximizes the energy release rate.

6.2.4.3 The zero K_{II} criterion ($K_{II} = 0$)

The essence of the $K_{II} = 0$ criterion is to let the mode II SIF dissipate in shear mode for microscopic crack extensions.

6.2.4.4 The maximum circumferential stress criterion (MCS)

The MCS criterion is defined as the angle θ_c, given by the following relationship:

$$\theta_c = -arccos^{-1}\left(\frac{3K_{II}^2 + \sqrt{K_I^4 + 8K_I^2K_{II}^2}}{K_I^2 + 9K_{II}^2}\right) \qquad (6.14)$$

This is a simple and a widely used in the literature for XFEM crack growth, but as this is not an option in the ABAQUS software, is this not considered as an alternative for the FCG simulation in this thesis.

6.2.5 Crack growth magnitude

To calculate the magnitude of the increment at each iteration for constant amplitude loading are two method established in the literature (Pais, 2011). This first methods

assumes that for all the given iterations will a constant crack growth increment occur. The second method assumes that a FCG law may be used to find the amount of growth for the corresponding iteration (i.e. Paris law (6.3)). While for variable amplitude loading, the methods adopted for constant amplitude loading are no longer valid and the amount of growth need to be calculated separately for each cycle.

For both cases, the SIF ranges can be defined by the maximum and minimum SIF for each mode within each cycle:

$$\Delta K_I = K_{I,max} - K_{I,min} \tag{6.15}$$

$$\Delta K_{II} = K_{II,max} - K_{II,min} \tag{6.16}$$

In order to determine the FCG for mixed mode loading by Paris law an equivalent stress intensity factor is required. To calculate the equivalent SIF are several different models proposed.

Tanaka (1974) proposed a relationship for the equivalent SIF based on curve fitting data. The is given as:

$$\Delta K_{eq} = \sqrt[4]{\Delta K_I^4 + 8\Delta K_{II}^4} \tag{6.17}$$

A relationship based on the energy release rate is the equivalent SIF defined as (Pais, 2011):

$$\Delta K_{eq} = \sqrt{\Delta K_I^2 + 8\Delta K_{II}^2} \tag{6.18}$$

From the maximum circumferential stress criterion are relationship is the following expressing given as (Pais, 2011):

$$\Delta K_{eq} = \frac{1}{2}\cos\left(\frac{\theta}{2}\right)[\Delta K_I(1 + cos\theta) - 3\Delta K_{II} sin\theta] \tag{6.19}$$

The modified Paris law is given as:

$$\frac{da}{dN} = C_P\left(\Delta K_{eq}\right)^{m_p} \tag{6.20}$$

By integrating eq (6.20) are a function to determine number of cycle N needed for crack to propagate from initial crack a_0 to a crack length a:

$$N(a) = \frac{1}{C_p}\int_{a_0}^{a}\left(\frac{1}{\Delta K_{eq}}\right)^{m_p} da \qquad (for\ a \geq a_0) \tag{6.21}$$

6.3 Modelling Strategy

To simulate the influence of material, contact and geometrical properties on the connection's behaviour, using ABAQUS 6.14. The input data consist of the connection's geometric, material and contact properties together with loading

conditions (Figure 6.2). The data is used as an input to ABAQUS. Specific parameters related to the numerical analysis such as meshing strategy and element type are included in the software. The choice of the mesh parameters is based on the mesh optimization study presented in later sections.

Based on the input data, the model geometry is constructed with the necessary material data, load and boundary conditions. Second stage file is run by ABAQUS where the finite element is carried out.

The 2D axisymmetric elastic-plastic model will be modelled. It will be used for stress based fatigue assessment by means of the peak stress approach and for a comparison with experimental work. The second and third models are both based on a linear elastic material model, in order to be used for fatigue assessment by FCG methods. One is also a 2D axisymmetric model, which was created by modifying the first model and the other is a 3D half model.

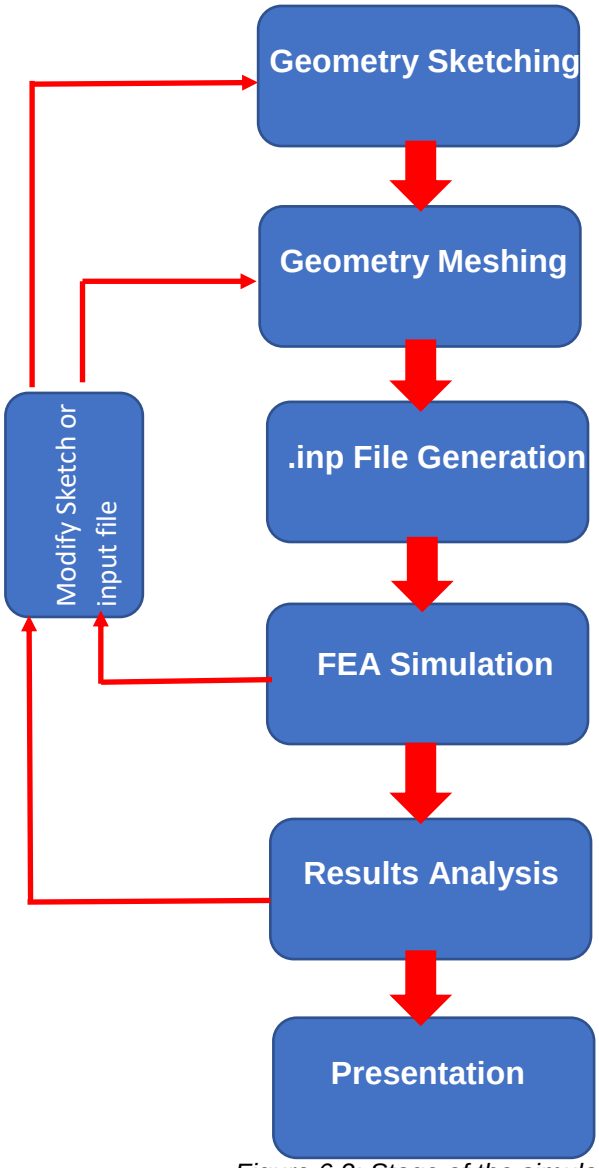

Figure 6.2: Stage of the simulation.

6.4 Finite element model

6.4.1 Model geometry

In analogy to the models found in literature and described in chapter 2, a 2D axisymmetric geometry is used to model the threaded connections. Although this is widely accepted method, it is originally based on comparisons with photo-elastic models under simple loading conditions and assuming fully elastic behaviour of the connection. To justify the choice of the 2D approach, a comparison is made with a full 3D model in section 5 of this chapter.

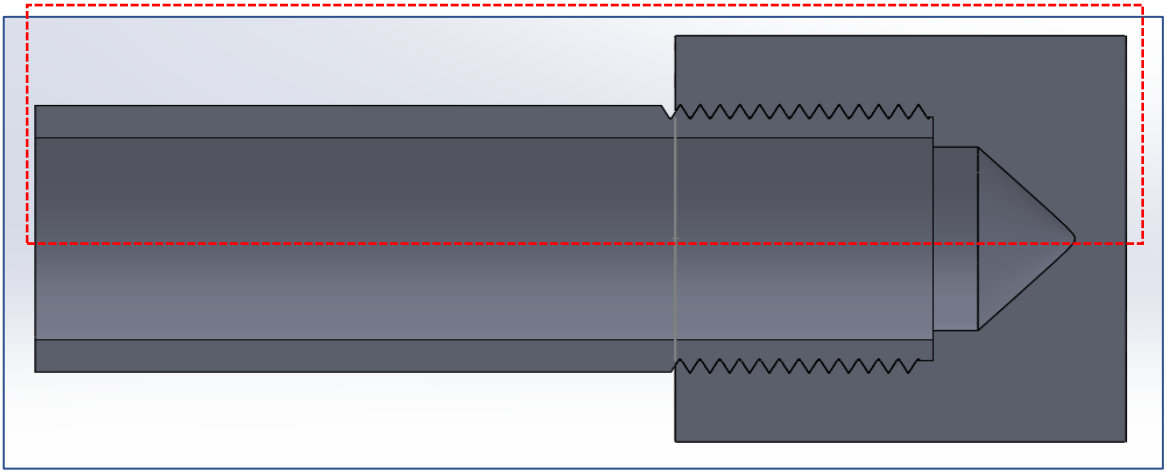

Figure 6.3: Section view of an API Line Pipe connection.

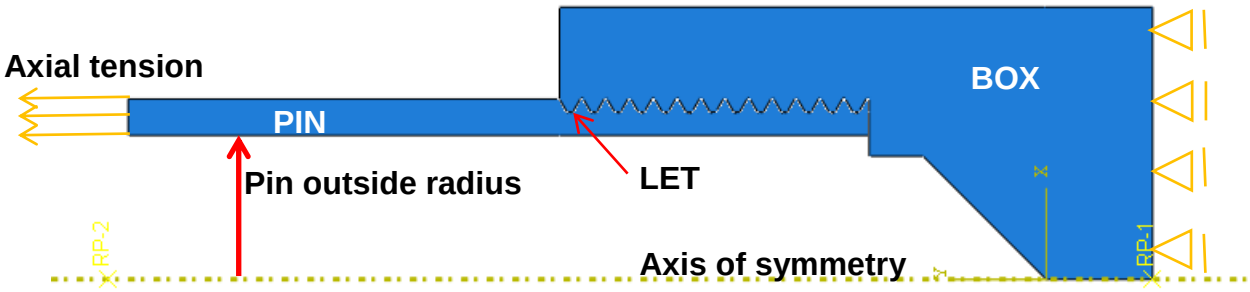

Figure 6.4: 2D axisymmetric model of an API Line Pipe connection.

The parametric model is optimized to simulate API Line Pipe connections as shown schematically in figure 6.3 and confirmations derived from this standard connection type. In addition, other types such as BSPT connection will be shown later.

Next to the use of axisymmetry, a plane of symmetry is assumed at the coupling's centre of the threaded and coupled API Line Pipe connection (see boundary conditions in figure 6.4). Hence the model comprises only the region inside the red dashed line in figure 6.3. The resulting axisymmetric model is schematically shown in figure 6.4 and consists of a separate pin and box part. The unthreaded pipe body of the pin is

sufficiently long (150 mm for the $1''$ API Line Pipe connection model) to eliminate boundary effects when an external tensile stress is applied at its free end.

The geometry of the pin and box are constructed using a limited number of parameters so that different connection sizes and modifications can be easily simulated. To do this, the construction of the global pin and box geometry is separated from the construction of the connection's threads.

After the global connection geometry is constructed, the threads are introduced. The thread shape is defined in figure 6.5 and is based on a triangular thread shape with a fully developed thread height H and pitch length P. The thread angle of the API Line Pipe connection is 60°, but this value can be altered to model other thread types. The thread crest and root are truncated over a certain truncation height respectively t_c and t_r.

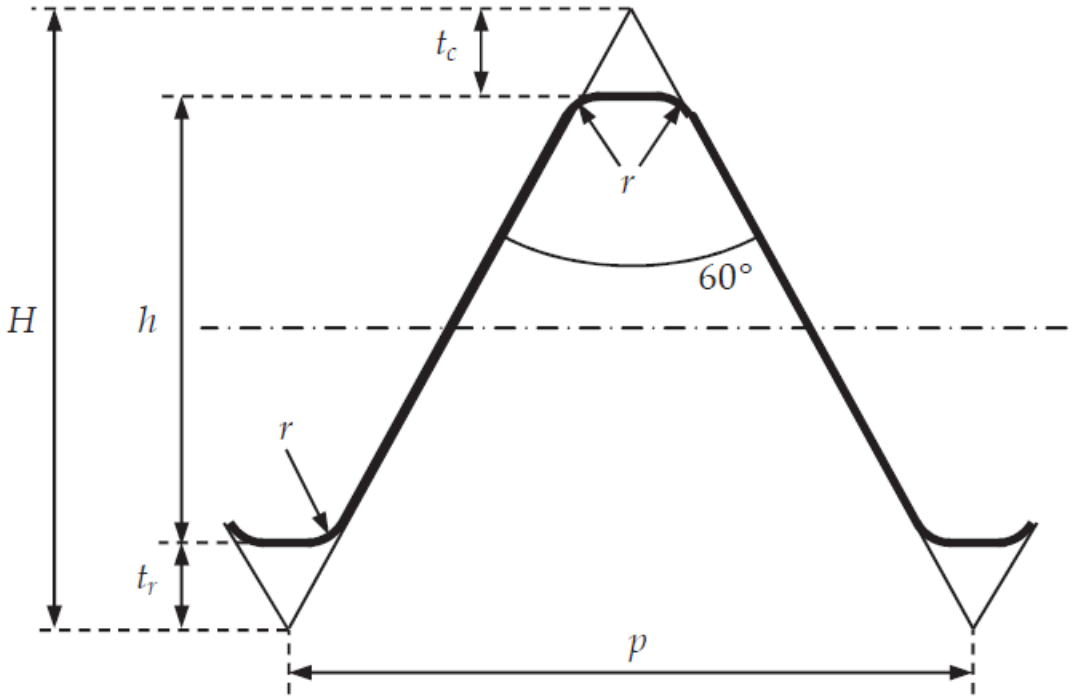

Figure 6.5: Construction of the threads.

In addition, a fillet radius r is used since a sharp edge would result in a stress singularity in the model and in practice a thread cutting tool has a certain small radius. It is also noted that by increasing this radius to the appropriate values, round thread shapes can be modelled. For the standard API Line Pipe geometry, a fillet radius of $r = 0.05\ mm$ is applied.

6.4.2 Model Non-linearities

To include the necessary non-linear behaviour in the finite element model elastic-plastic material behaviour and elaborate contact interactions are introduced.

6.4.2.1 Material properties

Non-linear material behaviour is provided by the use of a multilinear elastic-plastic material model with isotropic hardening. The material data used in this study is either based on the experimentally determined stress-strain behaviour of the pipeline steel (determined by tensile testing as described in chapter 5) or on the minimum specified material properties from the applicable standards.

6.4.2.2 Contact definition and make-up

The contact between the pin and box threads is defined by a node to surface interaction and allows for finite sliding. Being the most rigid part of the connection, the box threads are defined as the master surface and the pin threads as the slave pair. The effect of friction is included by the use of a coulomb friction model with an isotropic coefficient of friction.

Abaqus/Standard using a general contact algorithm where it can treat initial overclosures as interference fits. Contact algorithm uses a shrink-fit technique to gradually resolve the interference distance over the first step of the analysis (if multiple load increments are used for the first step) as shown in figure 6.6, such that the fraction of the interference resolved up to and including a particular increment corresponds approximately to the fraction of the step completed. After the interference is resolved, stresses and strains are generated. Gradually resolving interference over several increments accounts for cases in which a nonlinear response occurs for “interference-fit loading.” Between contacting pairs in the option the interference is resolved in a single increment. It is generally recommended that one does not apply other loads while the interference fit is being resolved.

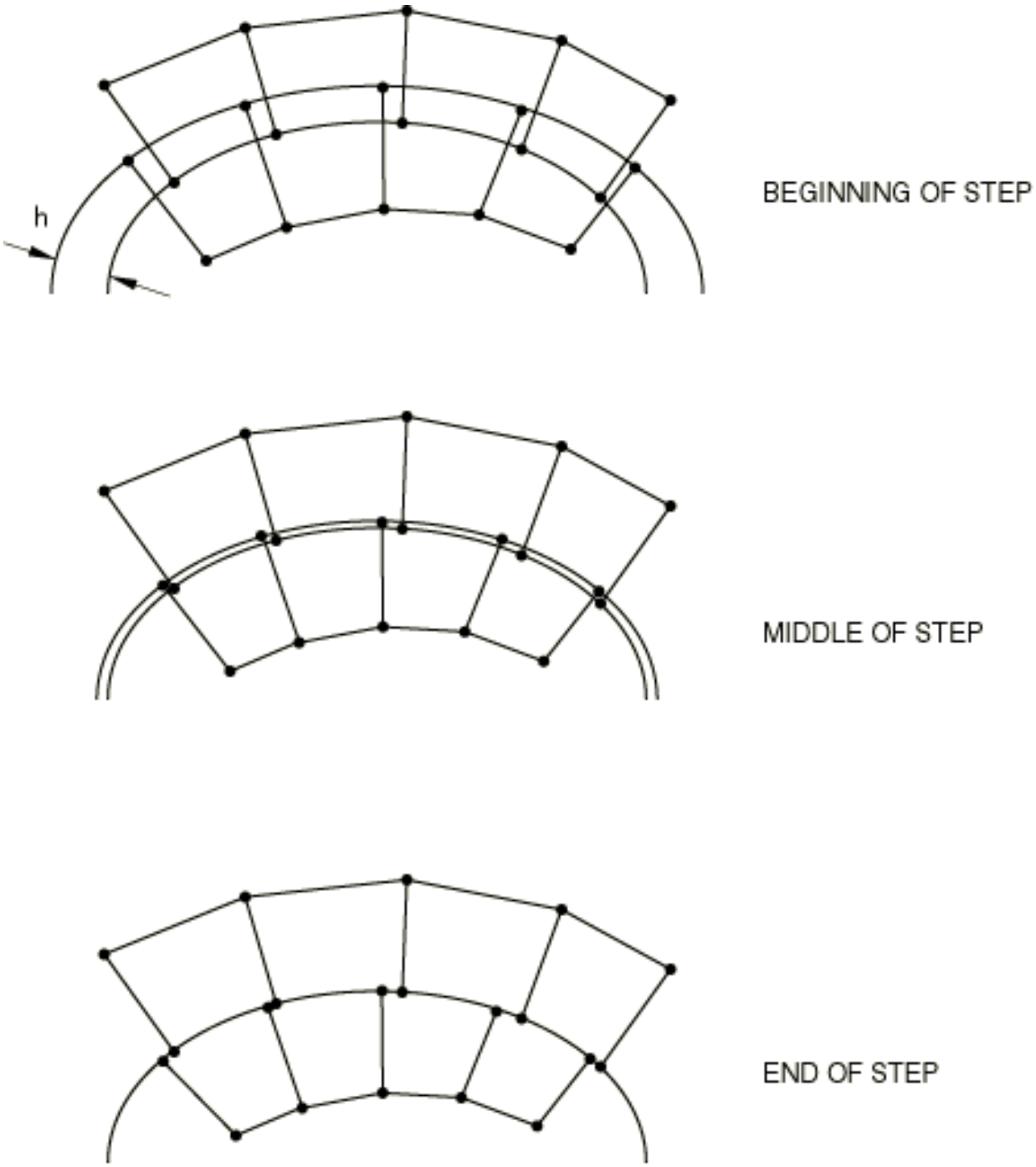

Figure 6.6: Shrink fit simulation in ABAQUS.

Since a 2D axisymmetric model is used, the make-up turns cannot be modelled by rotation. For this reason, a certain interference or radial overlap between pin and box is provided in the model, which corresponds to the number of make-up turns by Eq.(5.5). This is shown schematically in figure 6.7. The thread surface is then brought into contact using the interference fit option in ABAQUS.

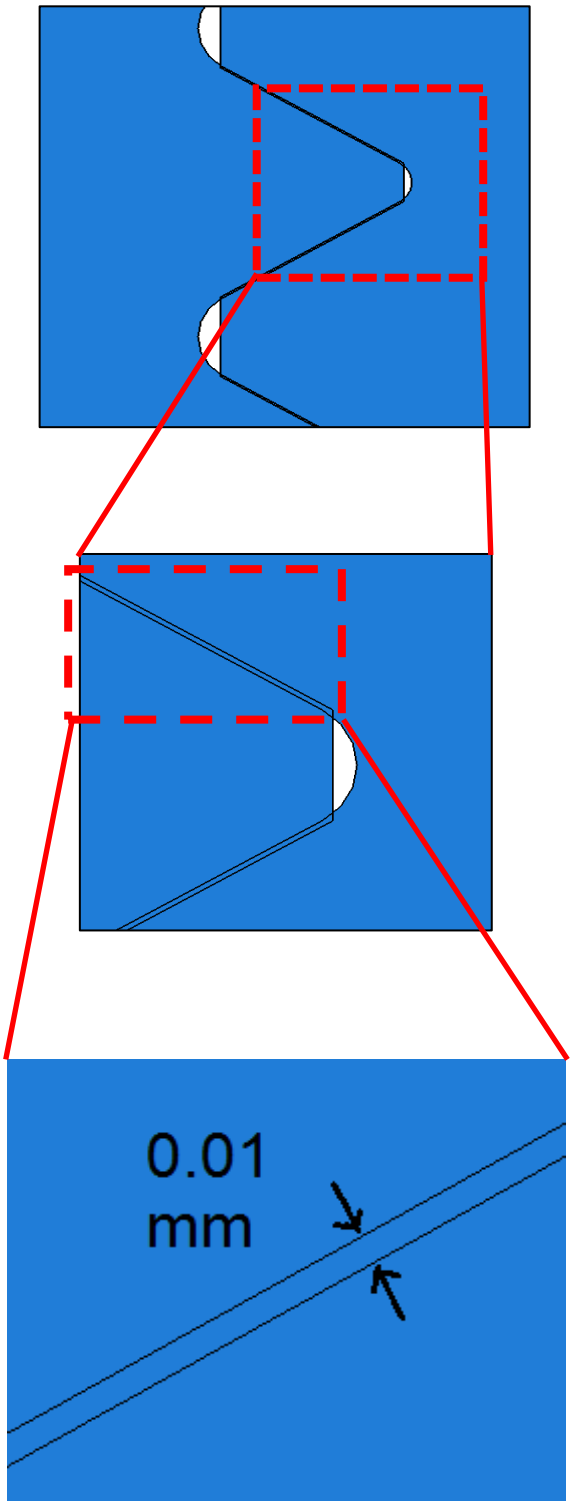

Figure 6.7: Radial overlap to model make-up.

Different ways of modelling the make-up processes were developed over the last 20 years. Also with the development of more advanced FE software more accurate ways of modelling make-up processes were proposed. Earlier method was based on applying thermos loads to a strip of thermo-element (Baragetti et al, 2002 and 2004),

pre-tensions (Salihu, 2011), and gap-elements (Santus, 2009). Recently, a new method was developed for modelling of the assembly process of drilling riser made of aluminum and steel by Santus et al (2009).

During the assembly, a torque is applied to the connection, after the mating surfaces are fully connected. Since the surfaces are not able to penetrate each other contact pressure arises. By interference an amount of penetration is implied should, if the mating surfaces not block each other. According to Santus et al (2009) two kinds of interference are caused between the male and female part of the connection during assembly of pin and box of drilling riser. Referring to Fig 6.8 those interferences are:

- a radial interference at the root I_r, thread flanks, and the conical thread-free portion I_c;
- an axial interference at the shoulder stop face obtained by imposed rotation during assembly after initial contact at the shoulder stop face I_s;

The radial interference is controlled by geometrical tolerances, which are prescribed in standards for the respective connection type. During assembly, the radial interference changes by imposing an extra rotation after the so-called hand-tight situation is achieved. This is due to the conical shape of the connection (Santus, 2009). In the literature, this effect is often compared to two wedges being forces into each other (Van Wittenberghe, 2011).

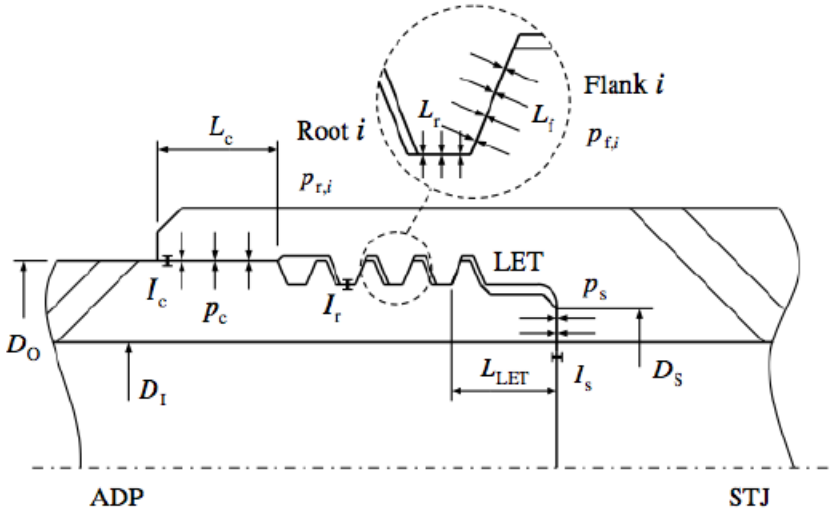

Figure 6.8: Sketch of a drilling riser connection with interferences and contact pressure taken from Santus et al (2009).

In order to ensure at the mating surface's when the connection is cyclically loaded, a certain torsional strength T_s of the connection is needed. During assembly, the interference between the mating surfaces cause a contact pressure, which generates a force normal to the contact surfaces. Since the normal forces are applied away from the connection's symmetry axis, a torque is generated. By integration of all torque contributions the connection's torsional strength is obtained from the friction term contribution and a negative helix term T_h, which does not need to be considered in this case.

$$T_s = f_s T_1 - T_h \tag{6.22}$$

Where T_1 is defined as the friction torque corresponding to a coefficient of friction f_s of 1. In order to calculate T_1 the individual torque contributions at all contact surfaces are summed up. For this purpose, the contact pressures at the location of interference are integrated over the contact surfaces ($p_c, p_{r,i}, p_{f,i}, p_s$). From Fig 6.8:

$$T_1 = p_c \pi D_0 L_c \frac{D_0}{2} + p_s \frac{\pi}{4}(D_S^2 - D_I^2)\frac{D_S + D_I}{2} + \sum_{i=1}^{n_r} p_{r,i} \pi D_0 L_r \frac{D_0}{2} + \sum_{i=1}^{n_f} p_{f,i} \pi D_0 L_f \frac{D_0}{2} \tag{6.23}$$

where the contact pressures are p_c at the conical thread-free portion, $p_{r,i}$ at the thread root i, $p_{f,i}$ at the thread flank i, p_s at the shoulder stop face. D_0 is the outer diameter of the male part, D_i as inner diameter of the male part, D_S as outer diameter at the end of the shoulder stop face, L_c is the contact length at the conical thread-free portion, L_r is the contact length at the thread roots, L_f is the contact length at the thread flank, n_r is the number of engaged thread root sections, and n_f are the number of engaged thread flanks. This formula Eq 6.23 has been established for riser connection without a taper, such as the one presented in figure 6.8. For other connections with taper, lengths and diameters at the respective thread should be used.

Since the API line pipe connection analysed in this thesis has truncated threads, there is no interference at the thread roots. Moreover, due to the in prescribed clearance API 5B between the male and female part along the thread-free surfaces the equation is further simplified. The terms related to the contact pressure at the conical thread-free portion p_c and the contact pressure at the shoulders p_s can therefore be neglected. With 24 thread flanks being in the contact the equation reduces to:

$$T_1 = \sum_{i=1}^{24} p_{f,i}\, \pi D_0 L_f \frac{D_0}{2} \tag{6.24}$$

T_1 is the friction torque corresponding to a coefficient of friction of 1. The actual torsional strength T_s can be calculated according to equation 6.22 for a given coefficient of friction f_s. The advantage of this method is, that the torsional strength T_s, via equation 6.22 and 6.23 linearly relates to the interference at the contact surfaces. This allows a simulation of the connection's make-up torque by iteratively the interference increasing until the torsional strength T_s equals the aimed make-up moment M_{up}.

6.4.3 Make-up process of the 1" API line pipe connection

In this section, the previously introduced method shall be applied to simulate the make-up process of the 2D axisymmetric FE model of the 1" API Line Pipe connection. In order to find the friction torque corresponding to a coefficient of friction f_s of 1 for the 1" API Line Pipe connection, an initial 0.01 mm radial interference was taken between the pin and box, similar to the final interference in figure 6.7, in the 2D FE model. The contact surfaces are then brought into contact by using the interference for option of Abaqus, which gradually removes the penetration of mating nodes on the contact surfaces, before the analysis is started. This introduces contact pressure along the 6 elements of each thread flank. Subsequently, a first estimate for the friction torque

corresponding to a coefficient of friction of 1, T_1 is obtained by integration of the averaged contact pressure distribution according to equation 6.24.

According to Santus et al. (2009) the linearity between interferences and contact pressure only holds as long as the local stress does not exceed the yielding limit of the material anywhere in the structure, and all the mating surfaces remain closed after imposing the interference (Santus, 2009) From the FE results it follows that for such a small interference this assumption holds well, since there is only a small plastic zone at the thread root of the LET. It is hence possible to relate the friction torque corresponding to a coefficient of friction of 1, T_1 directly to the applied interference in the radial direction I_c by the following equation.

$$T_1 = C_1 I_c \tag{6.25}$$

where C_1 is a correction factor that can be found by imposing a chosen interference and calculating the friction torque corresponding to a coefficient of friction of 1, T_1 from the FE results. Originally, I_c was defined Santus et al. (2009) as the interference at the conical thread-free portion as shown in figure 6.8 However, since there is no interference in the thread-free portion I_c is used as radial interference in this thesis.

By applying an initial interference in radial direction of pin and box of $I_c = 0.01\ mm$, a friction torque corresponding to a coefficient of friction of 1, T_1 of $0.3546\ kNm$ was found from the FE results. From E.q 6.25 a correction factor in radial direction C_1 of $35.46\ kNm/mm$ is obtained.

During assembly, a certain make-up torque M_{up} is applied, which has to be balanced by the torsional strength of the connection T_s. Based on tabulated values of M_{up} for the $1''$ API Line Pipe connection it is hence possible to calculate the interference in radial direction I_c from equation 6.22 and 6.25 with the previously obtained correction factor C_1. The interference corresponding to the aimed make-up torque M_{up} is then implemented in the FE model. As follow:

$$M_{up} = T_s = f_s T_1 = f_s C_1 I_c \tag{6.26}$$

API RP 5C1- specifies a maximum make-up torque of 190 Nm and an optimal make-up torque of 152 Nm for the $1''$ API line pipe connection. In order to find the required friction torque corresponding to a coefficient of the friction of 1, T_1 different sources have been checked for published coefficient of friction f_S between mating threads. All papers found stated a value f_s 0.08 (Baragetti, 2002. Baragetti, 2004, Ferjani, 2011).

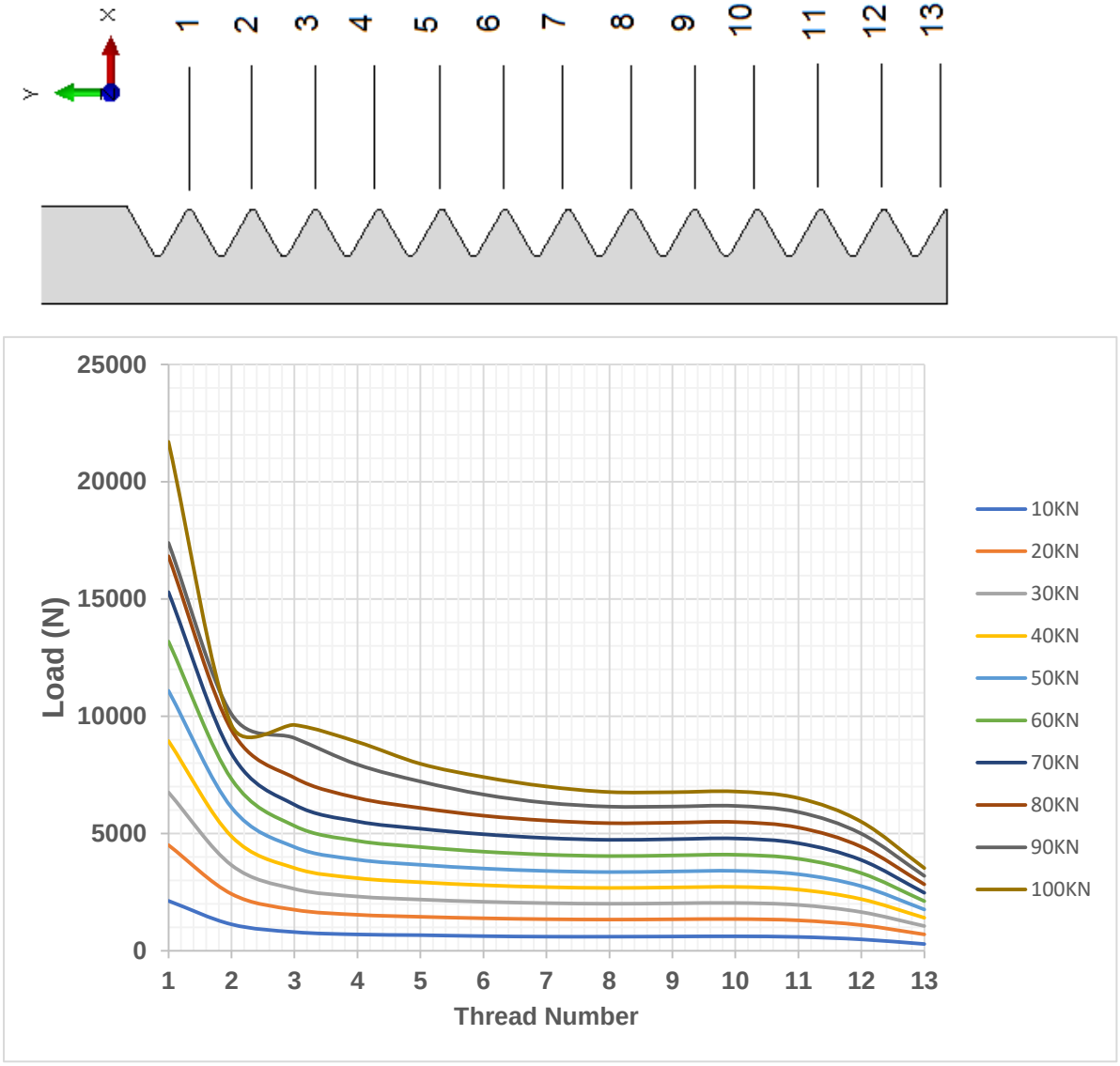

Figure 6.9: Load distribution on different thread for male connection.

Based on the optimal make-up moment $M_{up} = 152\ Nm$ and a coefficient of friction $f_s = 0.08$ the first estimate of the correction factor C_1 was calculated and implemented in the model for a required interference of 0.054 mm. After a second simulation, the contact pressure distribution was extracted again, averaged (see figure 6.9) and integrated over thread flanks.

From the equation 6.24 a friction torque corresponding to a coefficient of friction of 1, T_1 of $1.69\ kNm$ was calculated, which corresponds to a make-up moment M_{up} of 135 Nm for 1 inch pipe, which applied to the model. This is in fact a lower than the optimal make-up moment of 152 Nm. The reason for the deviation from the aimed make-up moment is the severe plasticity at the thread roots. Consequently, the linear relation does not hold anymore. This does not imply that an error was made in the computation, only that the relation between the friction torque corresponding to a coefficient of friction 1, T_1 and the applied interference in radial direction I_c is not linear. It is therefore

assumed that the achieved make-up moment is within the specified make-up moment interval for the 1" API line pipe connection.

6.5 Mesh Details

6.5.1 Mesh optimization study

To mesh the geometric model, CAX4R elements are used (see figure 6.10. These are 4-node axisymmetric quadrilateral element with reduced integration. In order to determine the optimal mesh size of the threaded connection model, a mesh optimization study is carried out on the $1''$ API Line Pipe geometry.

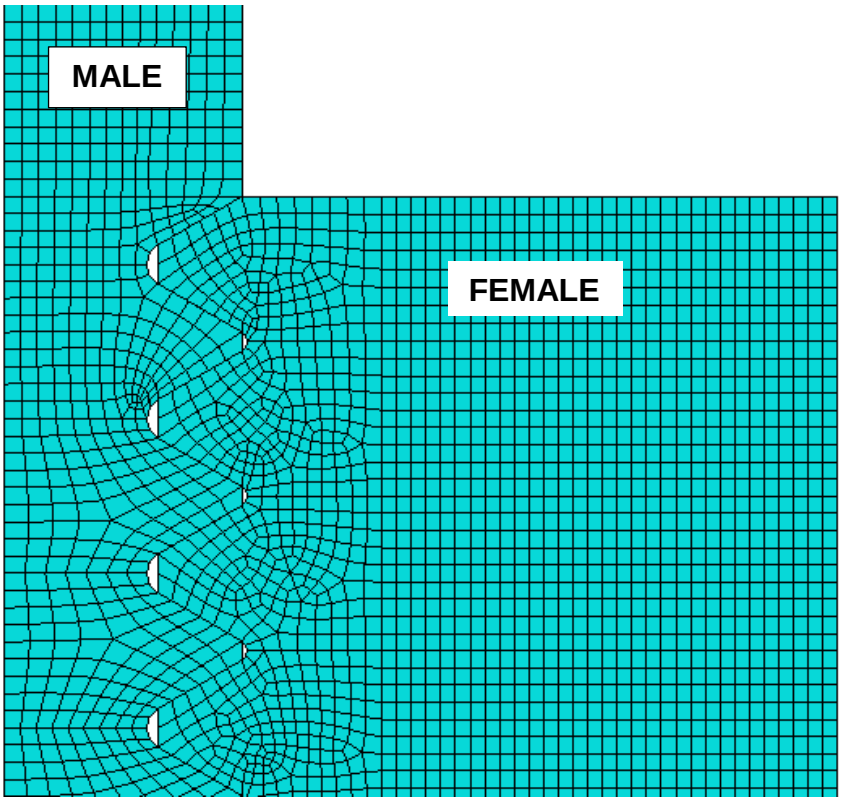

Figure 6.10: CAX4R four node element to mesh the model.

The complete model mesh is defined by 3 parameters as shown in figure 6.11. The global seed size defines the basic size of the mesh in the pin and the box.

Since the stress distribution around the thread surfaces is to be studied in detail, a smaller local seed size is used for the threads of the box and the last thread region of the pin. Because the pin threads are the slave surface of the contact pair they require a finer mesh than the box threads. Additionally, because it is known from the experiments that fatigue cracks initiate at the thread root of the pin, the smallest elements are used at that location. The resulting mesh of the pin threads is defined by three additional parameters. Both the thread crest and thread root have their own seed size. The thread flanks have a specific number of element using biased seeding, which means the element size reduces linearly from crest to root. A bias ratio of five is used,

which is the ratio between the size of the largest element at the crest and the smallest element at the root.

During the mesh optimization study, all three parameters are changed to see the influence on the stress field and the resulting calculation time. The simulations are carried out on a central server system which is a cluster of quad-core CPU's. Six simulations from the mesh optimization study shown in Figure 6.14; they are arranged by increasing number of elements in the model. The coarsest and finest meshes are illustrated respectively in figure 6.12. The first model contains 1542 element and is analysed in 30s, while the latter consists of 58469 elements and takes over 23 minutes to calculate. The relation between number of elements and calculation time is approximately linear.

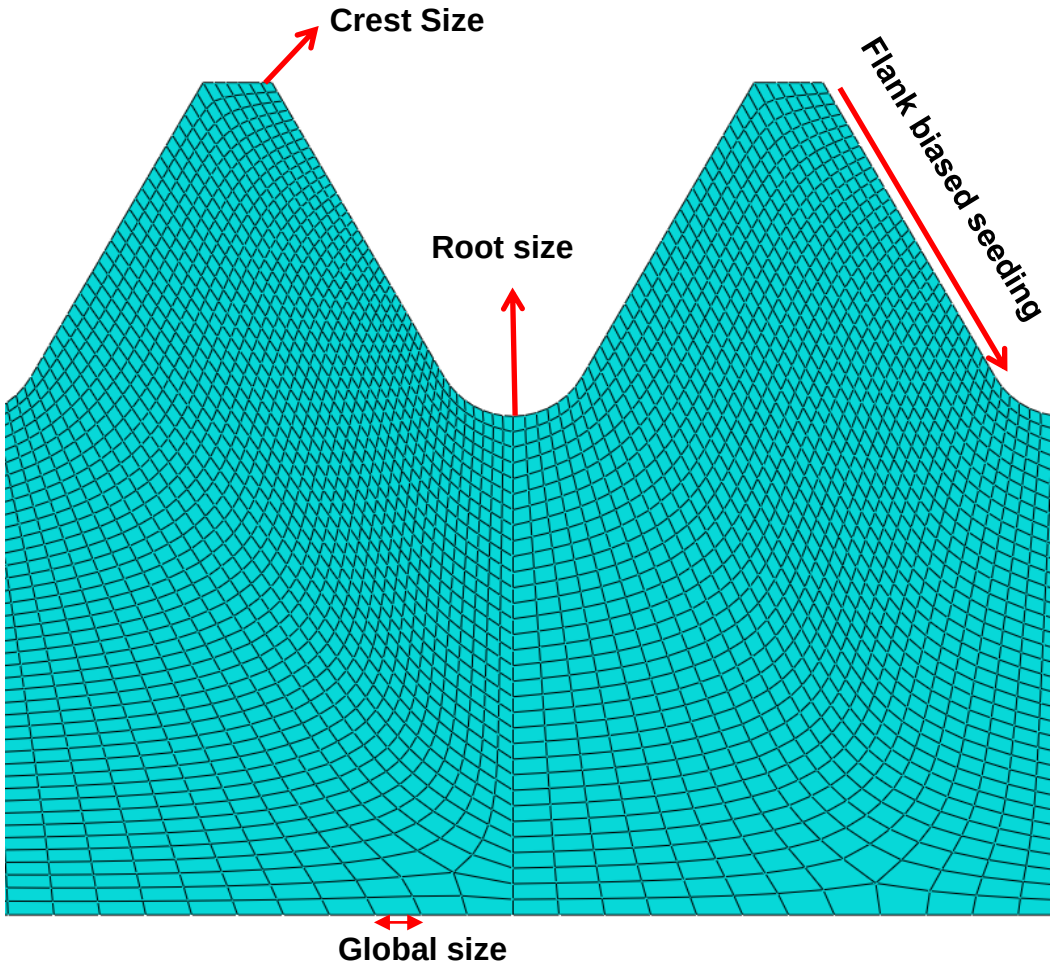

Figure 6.11: Mesh Parameter.

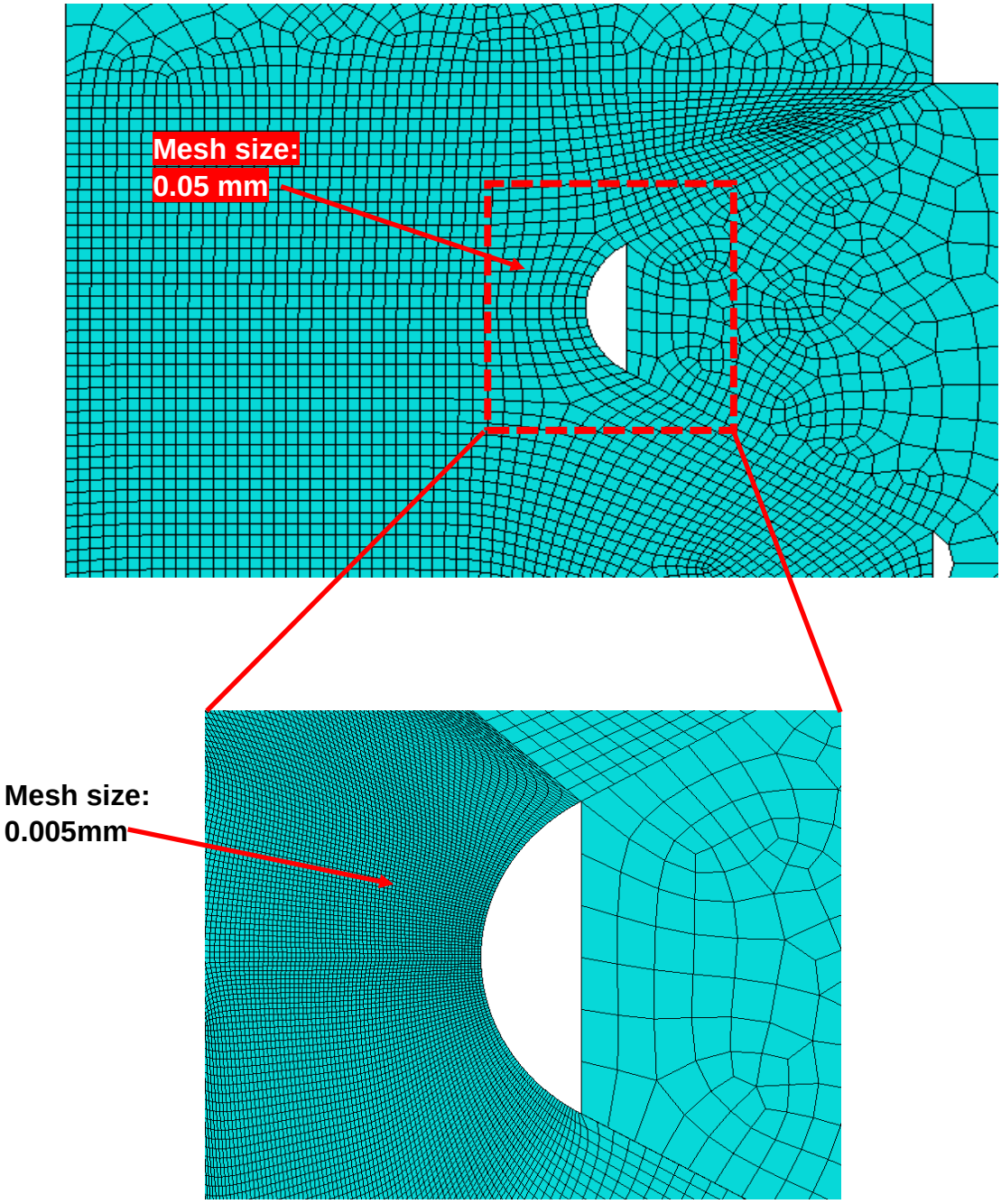

Figure 6.12: Mesh density.

To evaluate to obtained accuracy of the stress field around the LET of the pin, the von Mises stress as a function of the radial distance from the LET is plotted for 5 different meshes in figure 6.14. The three mesh configurations with the global mesh size of 5, 3 and 1 mm are compared with the finest mesh of Figure 6.13. The mesh configuration selected for this study represented in figure 6.13b corresponds to a calculation time of 4 min.

XFEM is intended to be a mesh independent method, but this is not true when used in Abaqus. In order to get accurate results, the mesh size has to be below 3% of the crack size (Vethe, 2012). With a coarse mesh the calculated crack propagation direction becomes too large and the crack will propagate in an oscillating pattern until the crack has grown until the mesh size is below 3% of crack size.

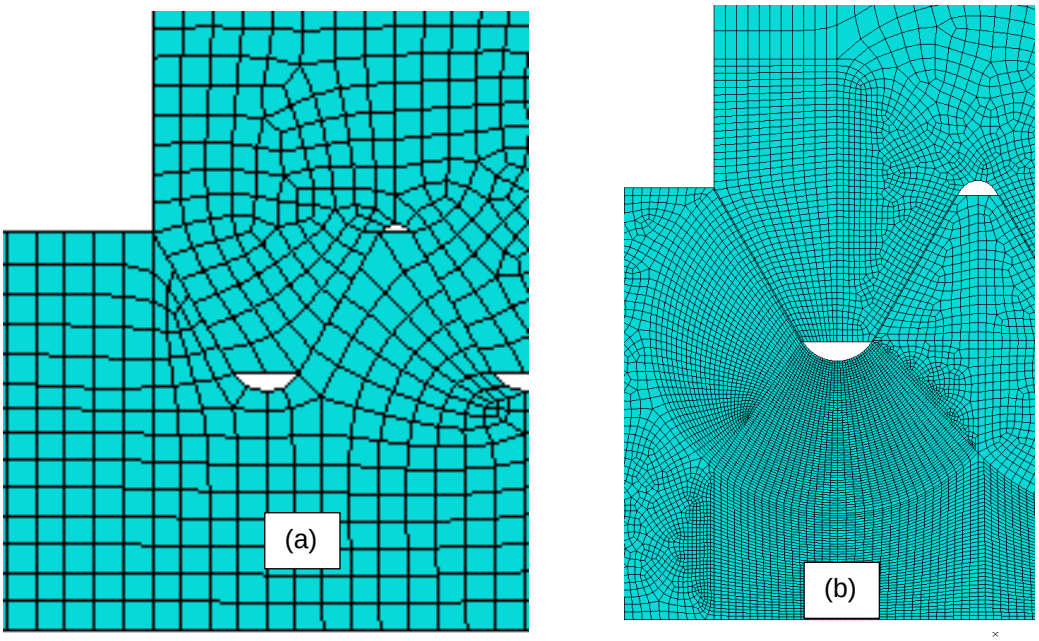

Figure 6.13: Coarse mesh with global size of 5 mm; b) fine mesh with root element size of 0.001 mm.

Figure 6.13a and b shows the difference between two mesh, in the finite element simulation. Two most important steps were (i) to define the right contact between the surface in order to friction correctly between the metal-to-metal surfaces and (ii) the choice of meshing. Given that there is no guide or definition about using the right amount of mesh or how many elements apply to the model.

The mesh at the thread root was progressively refined and made finer covering a range of mesh density seeding in a series of two-dimensional axisymmetric models. The boundary conditions and loads were kept the same for each of the simulations.

As it can be seen in figure 6.14 the traditional way is to run the model with different mesh until the stress result reaches a constant and stable value. Starting with a large element then reducing its size will not make any difference after once it reaches stability reaches (fig 6.14).

Since it was observed during the experiment in chapter five the LET is the failure location therefore for a better simulation a smaller element is chosen for the LET as shown in figure 6.13b.

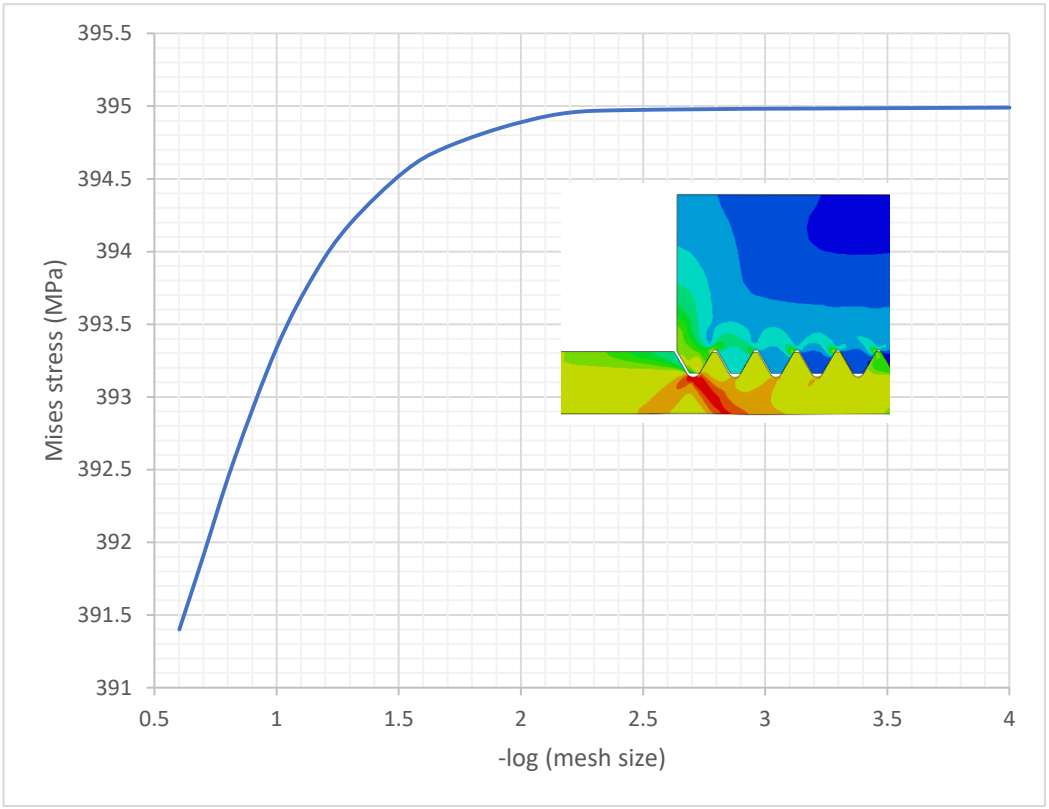

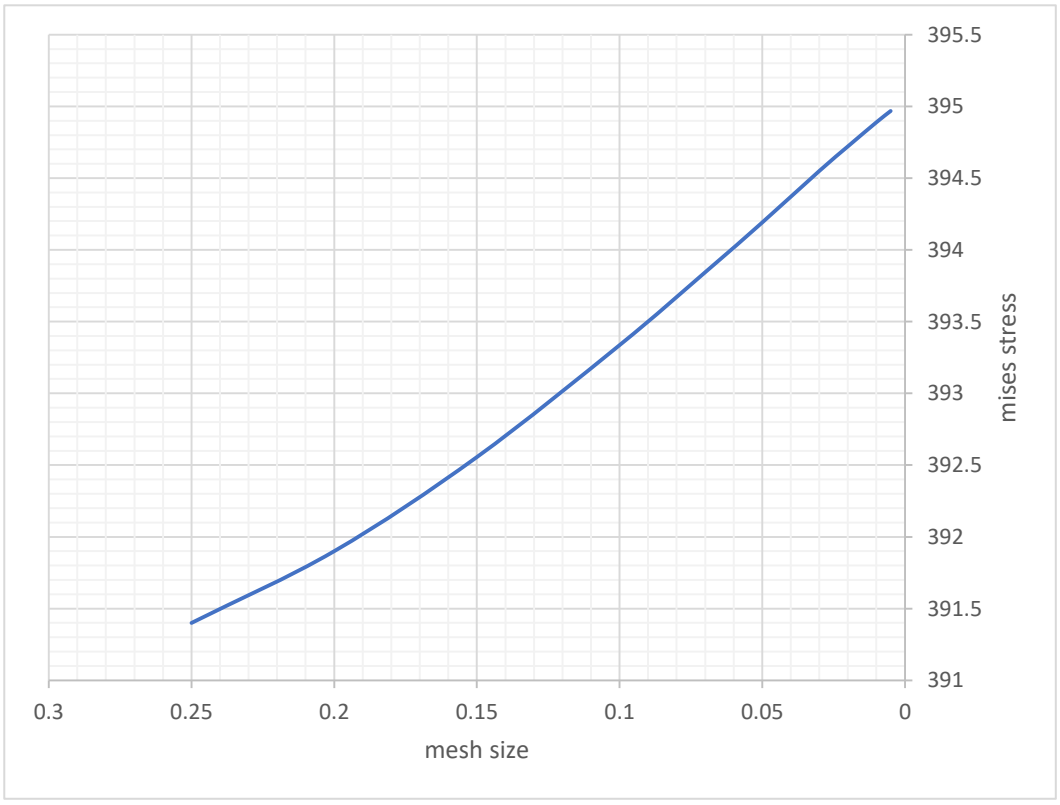

Figure 6.14: Mesh stability of stress field (von Mises values) around the LET for different meshes.

6.5.2 Model mesh

The optimization model mesh of the 1" API line pipe connection is shown in figure 6.15. it consists of 19871 elements of which 14223 are pin elements and 5760 box elements.

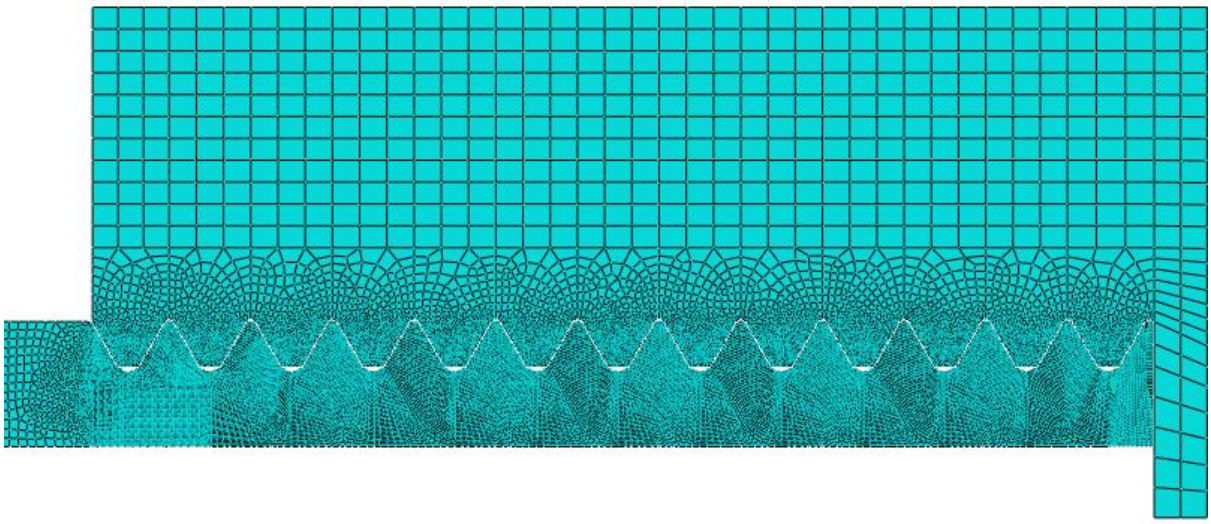

Figure 6.15: 1" API Line Pipe model mesh.

Table 6.1: Rules for determining mesh parameter.

Global seed size	Pin WT/6
Local seed size	Global/ 5
Pin thread crest seed	Global/20
Pin thread root seed	Global/100
Number of element of pin flanks	35

6.6 Analysis of a 1" and 4.5" API Line Pipe Connection

To illustrate the finite element analysis results of standard 1" API Line Pipe connection presented. The elastic-plastic material model adopted, for figure 6.16, is based on the minimum properties of API Grade B steel as specified by API 5L (2000) the material uses a Young's modulus of 208 GPa and a Poisson's ratio of 0.3. The material's yield strength is 241 MPa and the ultimate tensile stress is 521 MPa. The corresponding elongation is 23%. A coefficient of friction $\mu = 0.12$ is used for contact between the threads.

The analysis is carried out in two consecutive steps. In the first step the make-up of the connection is simulated. Unless mentioned otherwise, an effective number of 1 make-up turn is used throughout the simulations on the 1" connection. This value lies within the range of the API specifications (A.P.I., 1996. 5B) and is closed to the value

of 0.8 effective make-up turns measured in the torque tests. During the second step an additional uniform axial tensile stress is applied, as illustrated in figure 6.16. in the following paragraphs the resulting stress state and load distribution are discussed.

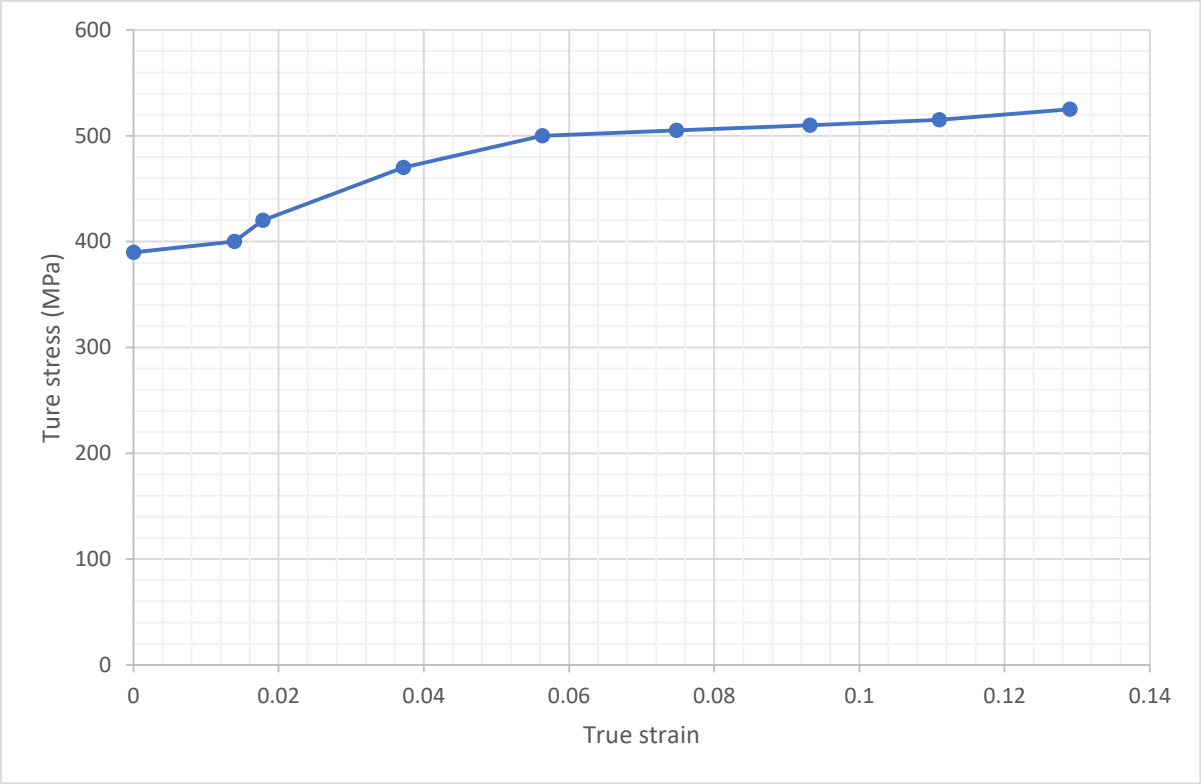

Figure 6.16: Multilinear elastic-plastic material model based on the minimum properties of API Grade B steel.

In order to account for local yielding during make-up and cyclic loading an isotropic hardening rule was used and for modelling elastic-plastic material model based on the minimum properties of API grade B steel, as recommended by DNV-RP-C203 and applied by (Veritas, 2010).

6.6.1 Stresses

The von Mises equivalent stress distribution for both calculated steps is shown in figure 6.17. Note that the stresses in the pin over the length of the engaged threads are very high and exceed the material's yield strength even in the make-up stage, which correspond to the observations made during the three consecutive make-up tests described in chapter 5. In addition, this is in agreement with plastic deformation of the engaged threads of an API round connection during make-up. Dvorkin and Toscano (2003) that an elastic-plastic material response is necessary to model behaviour observed. Showed that when the axial load is applied, the highest stress concentration appears at the root of the last engaged thread of the pin (indicate by the arrow in figure 6.17.b).

To analysis the stress more in detail, the different stress components for the make-up stage and the made-up connection with additional axial load of $100\ kN$ are shown respectively in figure 6.18 and figure 6.19.

From figure 6.18.c it can be seen that the high von Mises stress during make-up is mainly the result of the acting hoop stress. The hoop stress in the pin has a negative sign, which indicates a compressive stress while the hoop stress in the box is positive, being a tensile stress. This is because during make-up the pin is forced to move the box. Hence at the engaged threads the pin is compressed in a uniform way, while the box is expanded. Due to its large wall thickness, the box is a more rigid part than the pin, and the amplitude of the hoop stress in the pin is higher than in the box. It can be seen that the compressive hoop stress in the pin decreases when moving further away from the engaged threads.

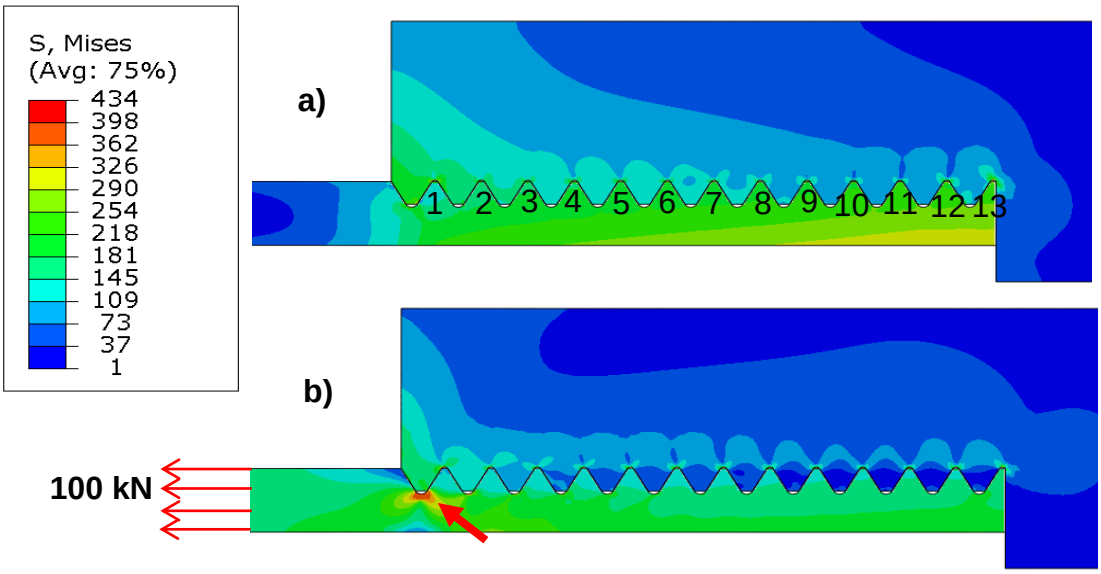

Figure 6.17: Von Mises stress distribution a) at make-up; b) with an external axial stress of $100kN$.

From figure 6.18.b and d it can be seen that the radial and shear stress are low, apart from some local effect around the LET of the pin.

The axial stress is given in figure 6.18.a. in the thread region of the pin. The axial stress changes from a compressive stress at the inside wall of the pin to a tensile stress at the outside. This is the consequence of bending of the pin due to make-up deformation. A similar bending situation appears at the box recess region where the axial stress changes from bending tensile at the outside wall to compressive near the inside diameter. Important to note is that at the LET of the pin an axial tensile stress appears over the wall thickness of the pin even though no external axial stress is applied. This is caused by the bending of the box recess, causing a local axial tensile stress situation at the LET of the pin.

The stress situation after application of the external axial load of $100\ kN$ is presented in figure 6.19. from figure 6.19.b and it is clear that the radial and shear stress remain low.

Since a uniform axial tensile stress is applied over the wall at the free end a pin, the axial stress distribution is changed as can be seen in figure 6.19.a. the axial stress in the pin reduces over the engaged threads of the pin from left to right because the axial load is transferred by the engaged threads to the box. Accordingly, the axial stress in the box increases from left to right over the engaged threads. In the pin the axial stress causes high stress concentrations around the root of the LET.

The maximum axial stress act at the LET of the pin is 624 MPa. This correspond to a stress concentration factor of 3.97 relative to applied axial tensile stress load of $100\ kN$. A similar stress concentration factor of 3.7 was calculated by Shoji and Sawa (2010) for metric bolts which have a comparable triangular thread angle of 60°.

Due to the applied axial stress, the hoop stress is partly affected as illustrated in figure 6.19.c. although the main hoop stress is still compressive in the pin and tensile in the box. The high axial stress at the LET and thread runout reduces the hoop stress due to diameter contractions under tension the Poisson effect.

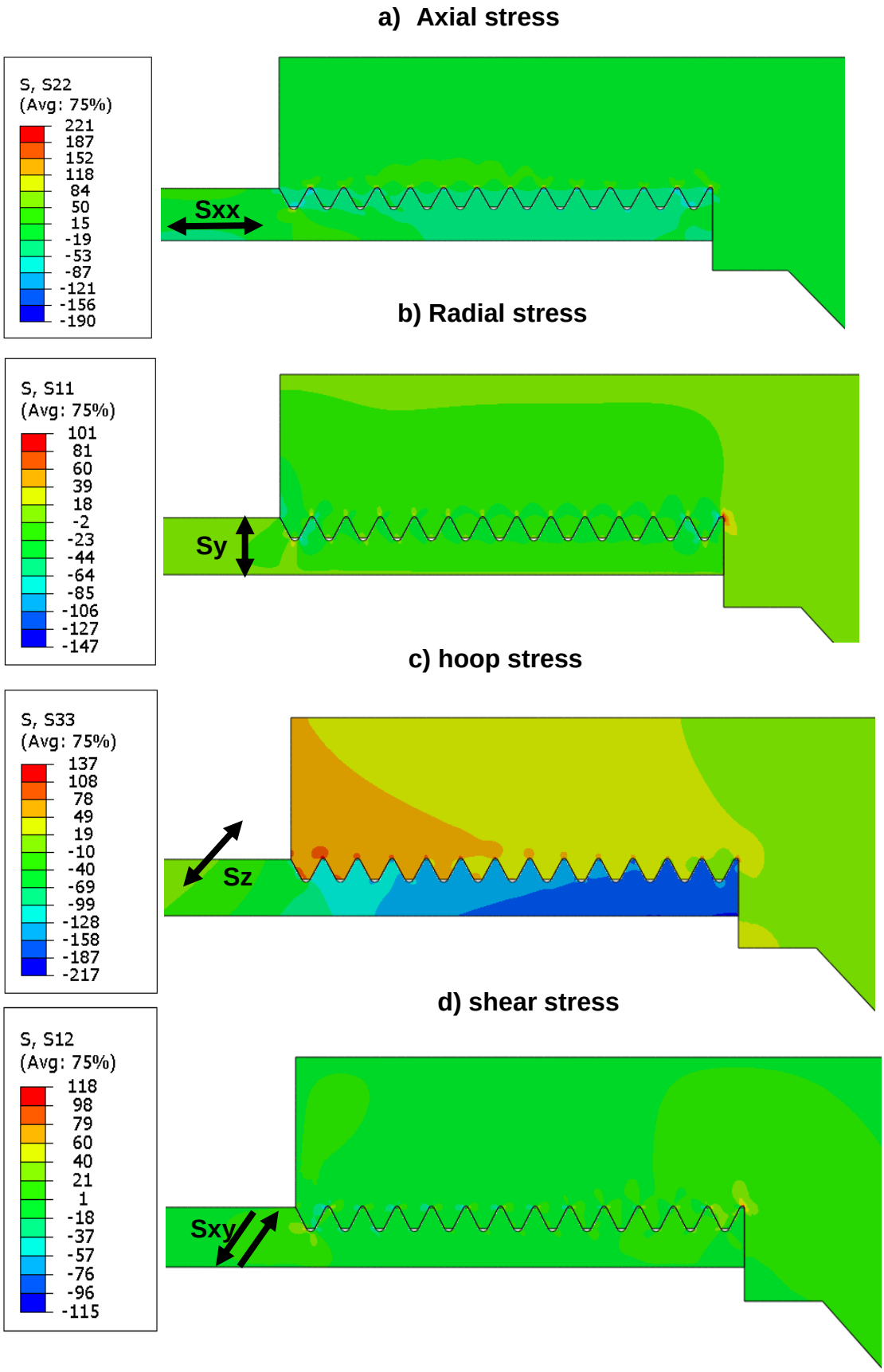

Figure 6.18: Stress components in a made-up connection.

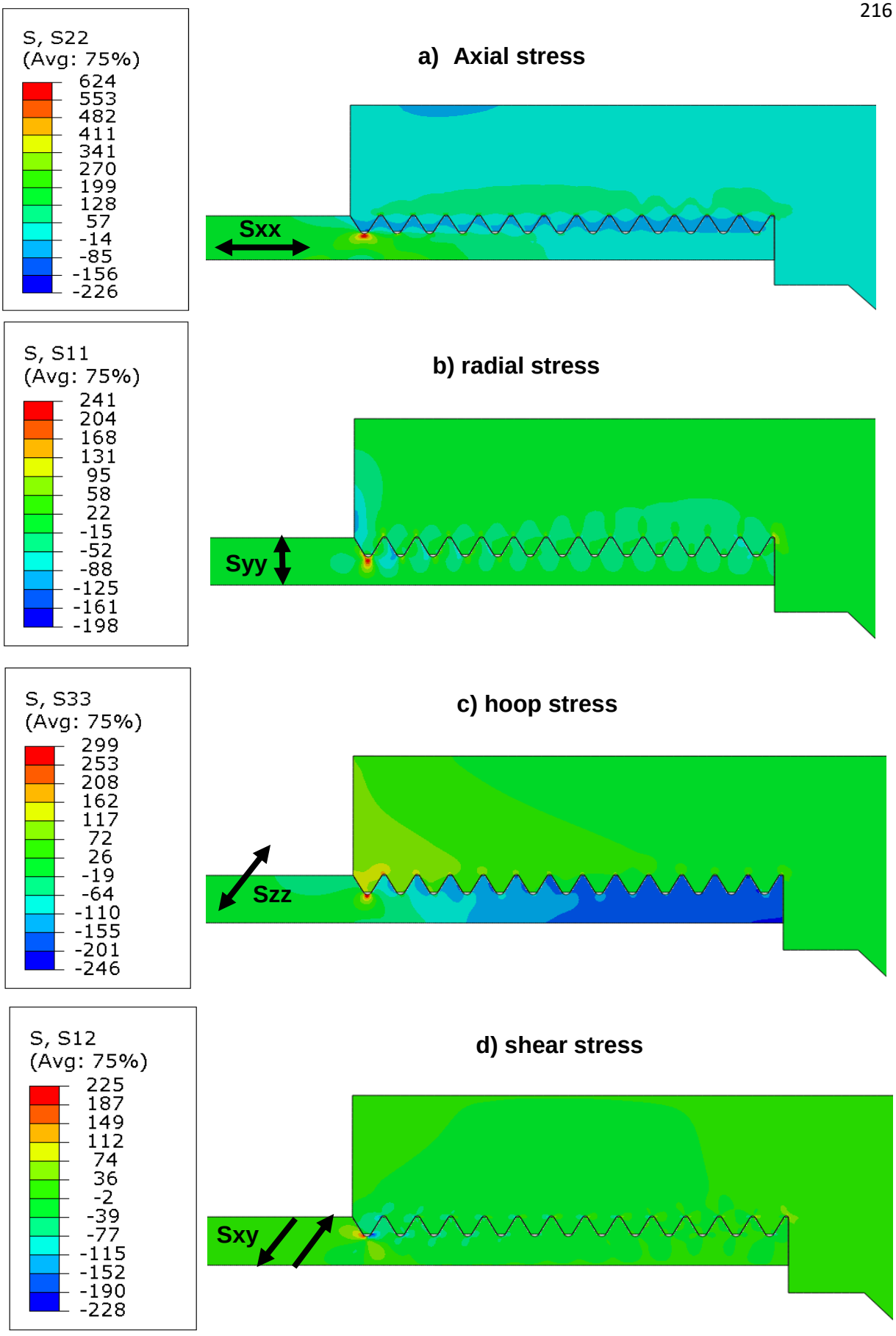

Figure 6.19: Stress component in a make-up connection with additional axial tensile stress of 100 kN.

6.6.2 Plasticity at thread root

As known from the local strain approach described in chapter 2, the local strain range is determining factor for a component fatigue life. The highest equivalent plastic strain ε_p appears at the root of the LET of the pin. This is shown in figure 6.20 for both make-up as for the connection with an additional axial tensile stress of 100 MPa. After make-up, the equivalent plastic strain reaches 0.7%. With the additional axial tensile stress of 100 MPa, ε_p increases to 2% and when the stress is increased to $100\,kN$ the maximum ε_p values is 9.6%. These values are in the same order of magnitude as the values obtained by Dvorkin and Toscano (2003) in their analysis of an API Round connection.

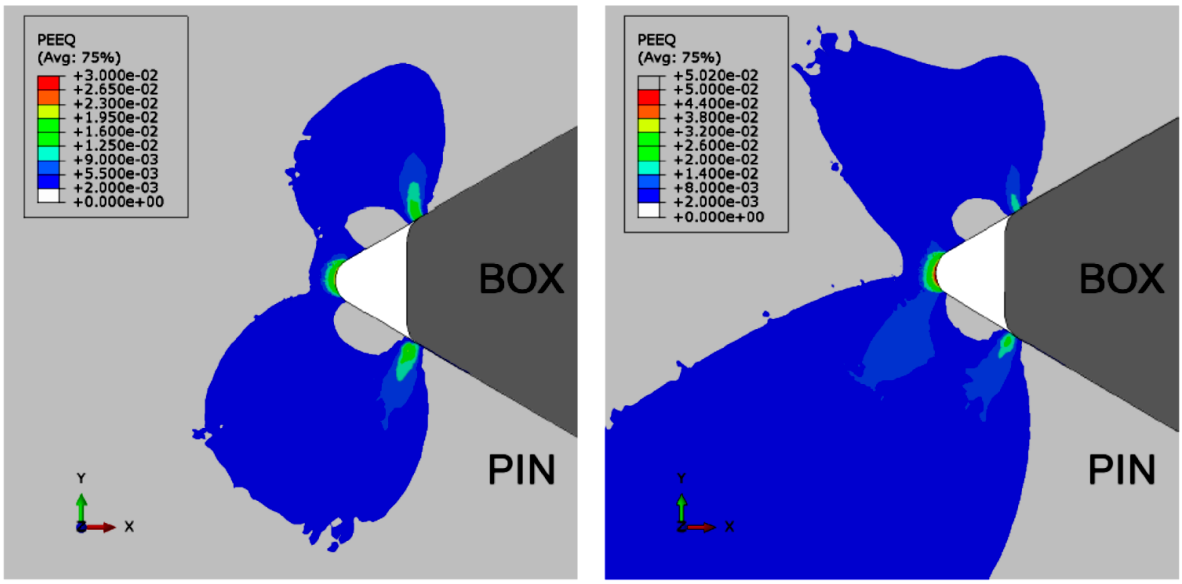

(a) Equivalent plastic strain at the root of the LET due to the make-up process.

(b) Equivalent plastic strain at the root of the LET due the make-up process and a tensile load of $100kN$.

Figure 6.20: Axial stress results of the 2D axisymmetric elastic model of the 1" API Line Pipe connection.

As expected the maximum stress can be found at the root of the LET. The von Mises stress reach 446 MPa and 558 MPa after the make-up process. Since yield stress of 294 MPa is exceed significantly, a distinct plastic zone, with a maximum equivalent plastic strain of 2.74% is introduced at the root of the LET. This value rises to approximately 5.02% by applying a nominal tensile stress of 150 MPa, after the make-up process was finished. Both strain fields are presented in figure 6.20a and 6.20b. the equivalent plastic strain is about 50% lower after make-up process and applied tensile stress.

The complete axial stress and equivalent plastic strain distribution along the anticipated crack growth path after make-up process and a tensile stress of 150 MPa.

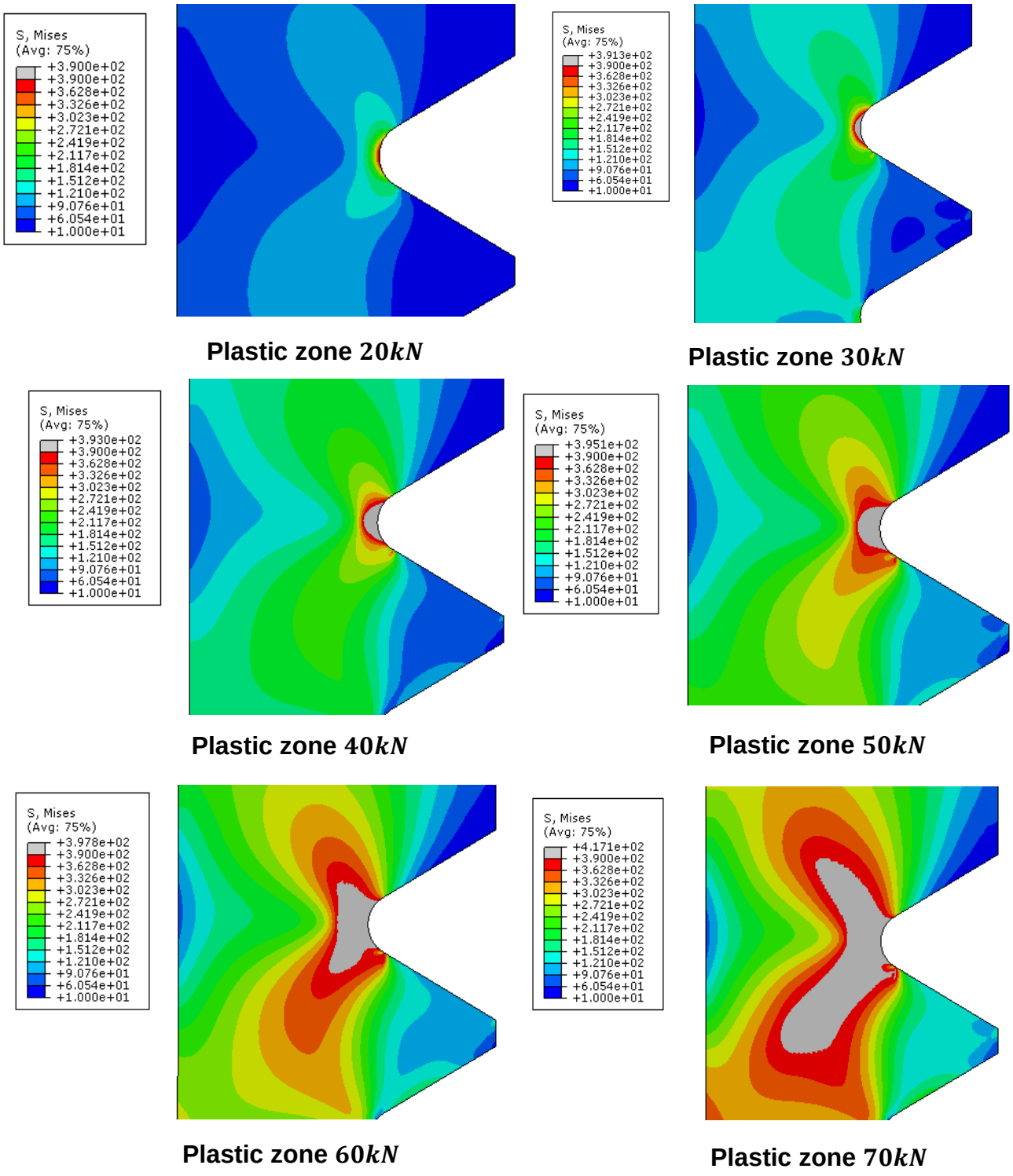

Figure 6.21: Development of the plastic zone without make-up.

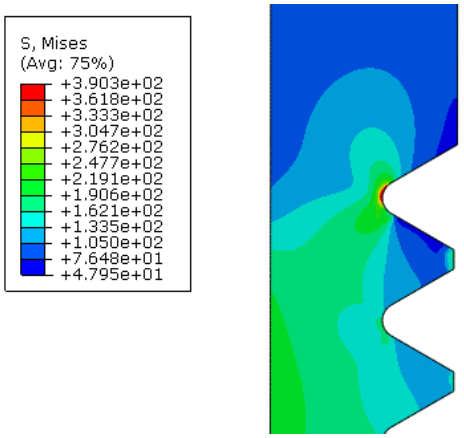

No Plastic zone $20kN$

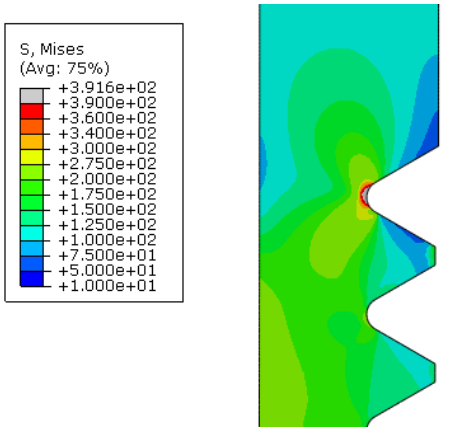

Plastic zone $30kN$

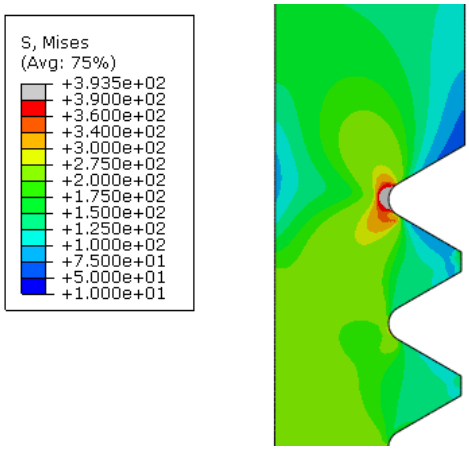

Plastic zone $40kN$

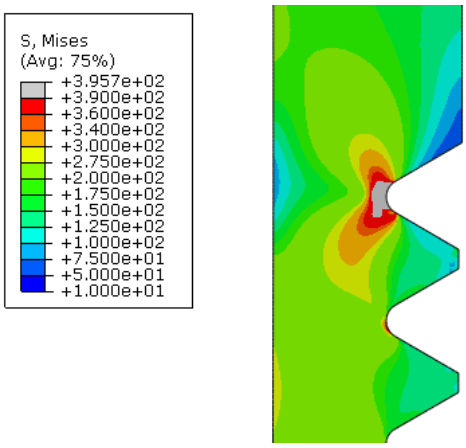

Plastic zone $50kN$

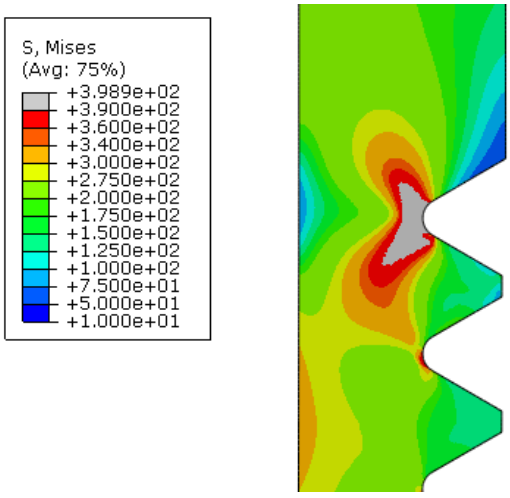

Plastic zone $60kN$

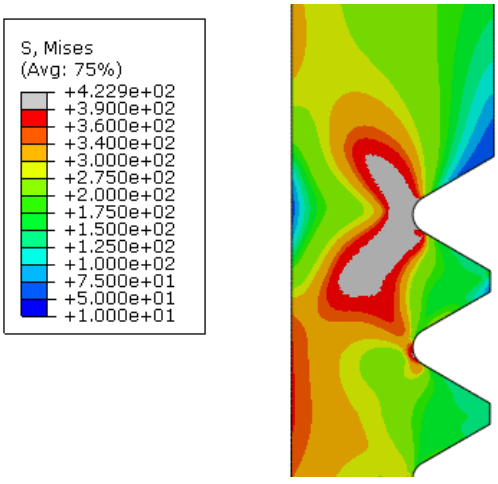

Plastic zone $70kN$

Figure 6.22: Development of plastic zone with make-up

6.6.3 Separation

As described in section chapter 5, the applied axial load is transferred by contact forces acting on the threads. Due to the triangular thread profile, these contact forces have an important radial component, the so-called separation force. When the applied axial tensile stress exceeds a certain value, the separation force will cause a sliding of the threads and an opening will be created between the thread stab flanks as in figure 6.22. It can be seen that this opening remains limited in value up to an axial tensile stress of 125 MPa. Afterwards, an important opening increase can be observed. A similar thread opening behaviour was obtained by Assanelli et al. (1997) for an API Round connection. Yet, the opening appearing between the thread flanks is highly undesirable since a fluid inside the pipe can find its way out through the created helical path, for increased loads the thread sliding causes thread jump-out and under dynamic loading conditions the sliding can initiate fretting fatigue cracks (Santus, 2008).

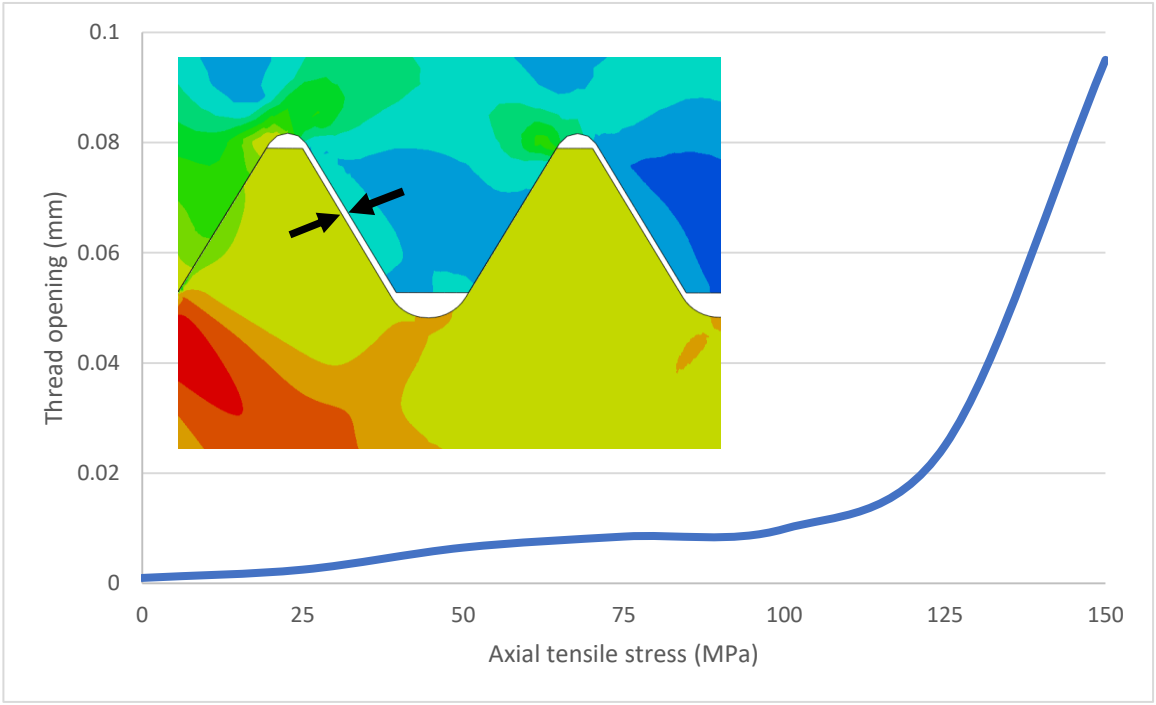

Figure 6.22: Thread opening as a function of the applied axial stress.

As mentioned in chapter 2 a wide variety of values for the coefficient of friction (COF, μ) are used, ranging from 0.02 to 0.20 and beyond. Although simulations showed that the value used does not affect the loading distribution over threads, it has an important influence on the thread opening as can be seen in figure 6.22. The opening at an external gross axial tensile stress of 150 MPa varies from 0.03 mm when $\mu = 0.16$ to 0.41 mm for the frictionless situation ($\mu = 0$). This illustrated the importance of accurate knowledge of the COF to perform accurate finite element simulation.

When the maximum stress during the cyclic loading of a fatigue test exceeds the limits stress, the thread sliding can cause fretting damage at the contact surface. During all

experiments in the medium scale axial loading setup, the limiting stress (for $\mu = 0.12$) is exceeded and it was observed that the thread grease at the engaged threads coloured black, which is an indication of fretting corrosion. The appearance of fretting fatigue in threaded connections is studied more in detail by Santus (2008) but is not further investigated in this work. During all subsequent simulation, the COF equal 0.12 since this value is employed during the first torque test described.

6.6.4 Load distribution

It is clear from figure 6.23 that an increase of the axial load is transferred from pin to box by the LET of the pin. Hence, the stress concentration at the last engaged thread of the pin is caused by the non-uniform distribution of the axial load over the adjoining threads. This load distribution with no make-up torque is shown in figure 6.24.

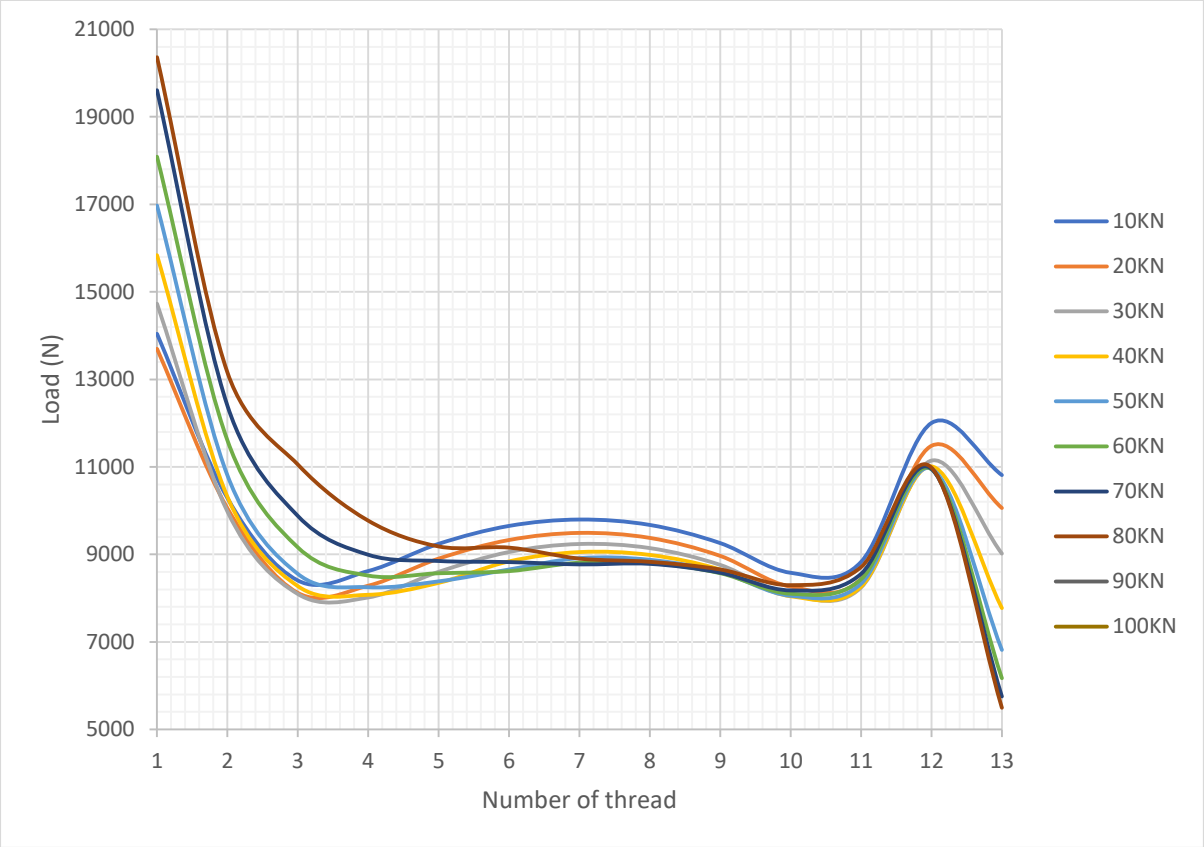

Figure 6.23: Relative thread load distribution; thread numbering as in figure 6.17.

In figure 6.23, the relative thread load as a percentage of the total axial load is given for each engaged pin thread. The threads are numbered from 1 to 13 according to figure 6.17 with thread number 1 being the LET of the pin. From figure 6.23 it can be seen that when an external tensile stress load of $100\ kN$ is applied, the LET carries 47% of the total load. This is highly undesirable since it means almost half the load is divided over twelve engaged threads. When the external stress increased to 150 MPa, the LET starts to bend, transmitting part of its load to the other threads. Furthermore, at this applied stress, separation of the thread load flanks has occurred, eliminating the compressive load on thread 1. This way the load carried by the LET is reduced to 36% of the total load.

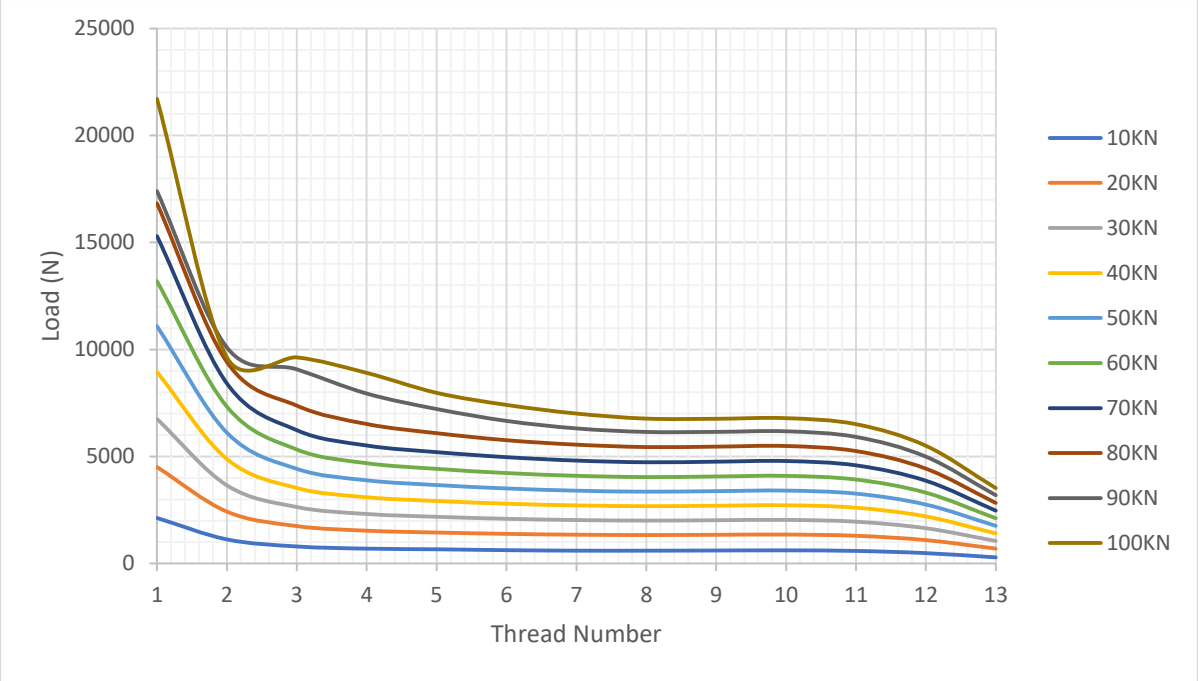

Figure 6.25: Relative thread load distribution with no ma-up; thread numbering as in figure 6.17.

6.7 2D Axisymmetric vs 3D Modelling

6.7.1 3D Model details

The use of 2D axisymmetric models instead of full 3D models is widely accepted in literature and has the advantage of shorter calculation times. Still, the majority of the experimental tests performed in this study are carried out under axial loading test. Since MacDonald and Deans (1995) showed that an axisymmetric approach is only valid when the wall thickness to diameter ratio is sufficiently small, it is important to check the validity of using 2D axisymmetric models to represent a bending load case.

Since the standard 1" API Line Pipe connection has a larger wall thickness to diameter ratio than the standard 4.5" API Line Pipe connection, the 1" configuration is evaluated both by the 2D axisymmetric model and a full 3D model. The 3D model is constructed by revolving the 2D axisymmetric geometry, so the exact thread helix is neglected see Figure 6.26. Nonetheless, both models use the same elaborated contact definitions, with a coefficient of friction of 0.12 and a multilinear elastic-plastic material model based on the results of tensile testing of the 1" specimen material, as shown in figure 6.25. Hence, both models include the necessary non-linearities for accurate modelling of a threaded pipe connection. For both models, a plane of symmetry is introduced at the center of the box. The 2D axisymmetric model is meshed according to the mesh parameters mentioned earlier, but the 3D model has a coarser mesh to reduce the model's calculation time.

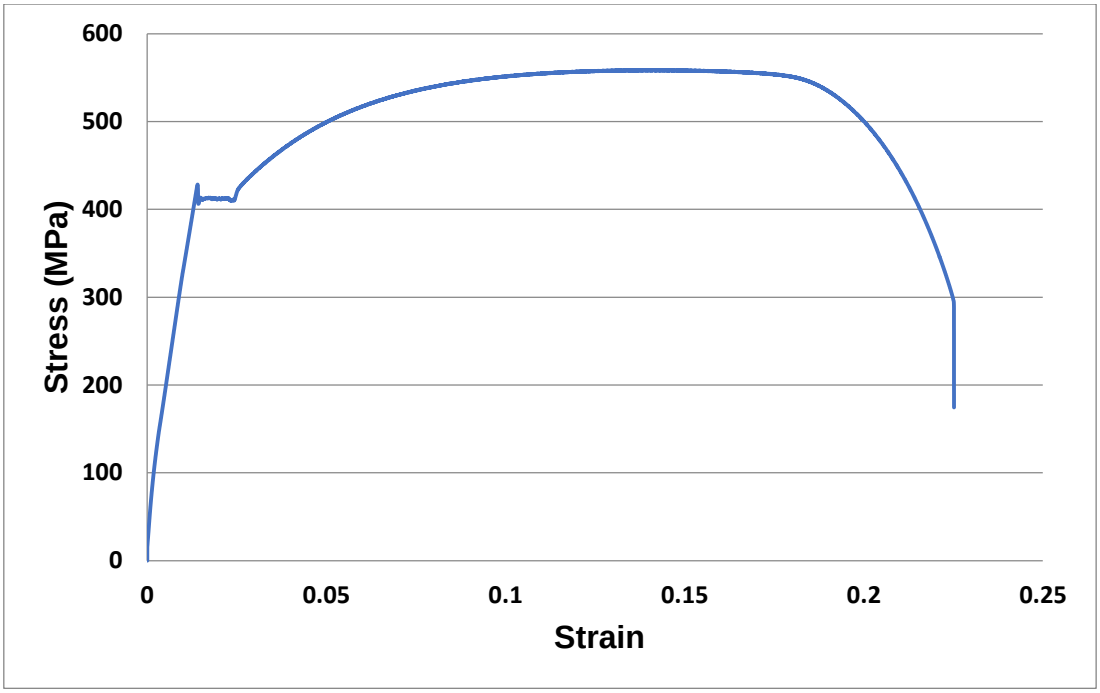

Figure 6.25: Average stress-strain curve based on tensile test results of ten 5.5" API Grade B steel tubes.

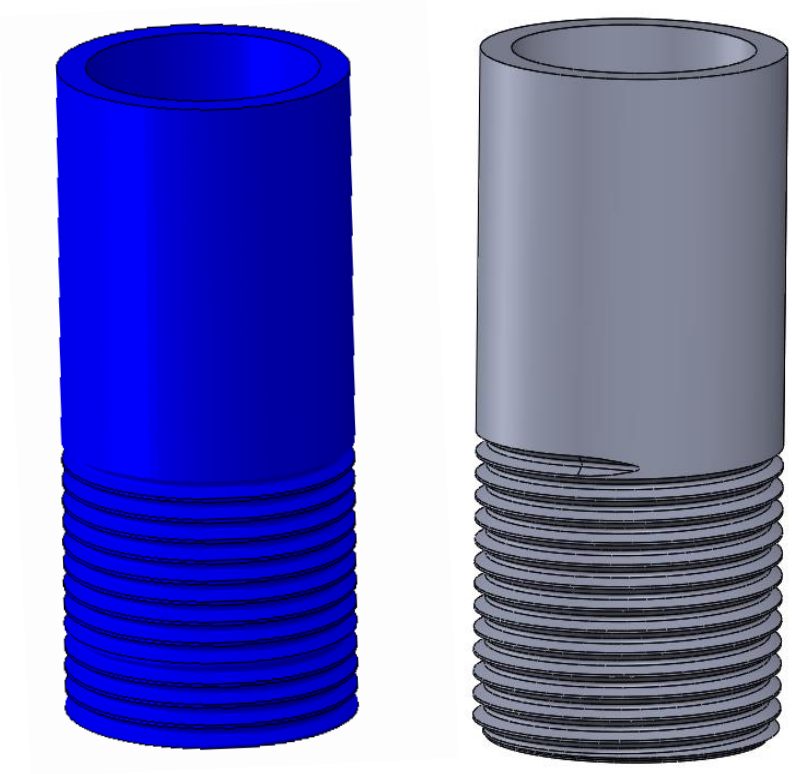

Figure 6.26: On the left ABAQUS revolving no helix, on the right using Solidworks with helix included.

6.7.2 Make-up

In figure 6.27 the resulting von Mises stress distribution for both the 3D and 2D axisymmetric model are given for the make-up coupling without any additional load, the boundary condition kept the same both for 2D and 3D. Note that there is a very good correspondence between both stress fields. As a comparison, the von Mises stress of all nodes along the inside wall of the pin and the outside wall of the box is plotted for the 2D axisymmetric and the 3D model in figure 6.27. The x-distance is measured along the x-axis, with $x = 0$ the plane of symmetry at the centre of the box. Along the outside wall of the box, the stress increases from the first to last engaged threads. Further along the x-axis, the box stress decreases again. The pin stress along the engaged threads is nearly constant, as the stress value reach the material's yield strength and plastic deformation occur during make-up. Further along the x-axis, the pin stresses become zero.

It can be seen that difference between the stress along the pin for both models is negligible (root mean square RMS deviation = 4.1 MPa or 0.8% of the maximum appearing von Mises stress). The resulting stresses in the box deviate a little more between the models (RMS deviation = 13.6 MPa), but still a good agreement can be observed. This difference is explained by the coarser mesh in the 3D model of the box that had a seed size of 2.0 mm compared of 0.6 mm for axisymmetric model.

From these observations, it may be concluded that the 2D axisymmetric model is a good approximation for the 3D threaded coupling in the make-up situation as shown previously by Zhong (2007).

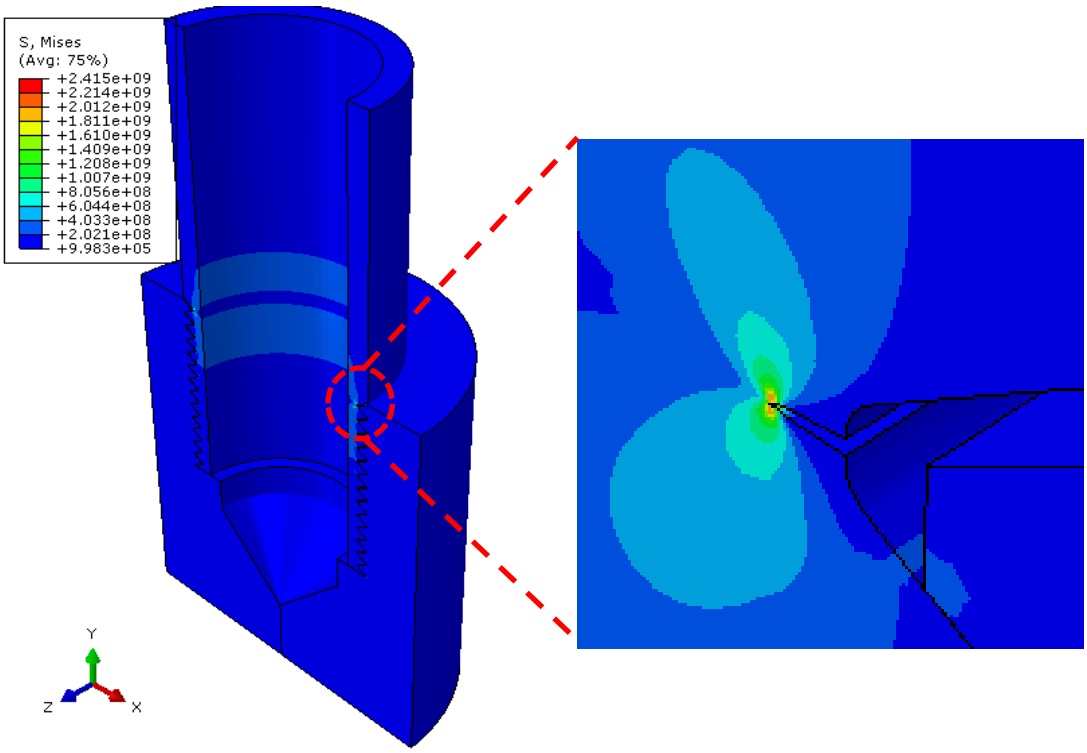

Figure 6.27: Von Mises stress in 3D model.

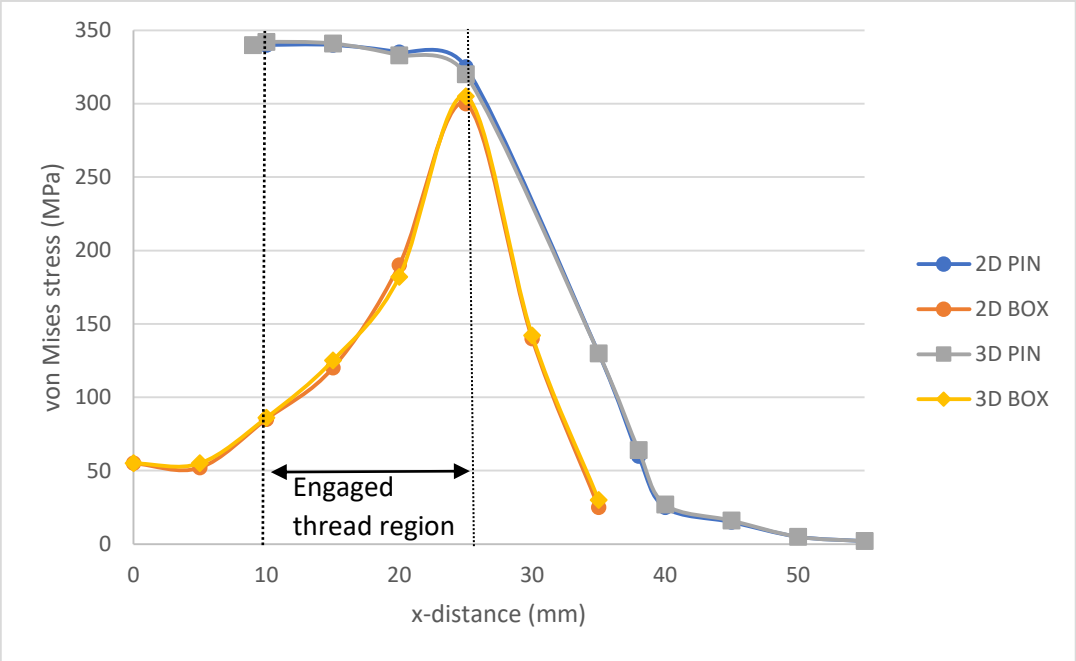

Figure 6.28: Von Mises stress along the inside pin wall and outside box wall after make-up.

6.8 Model validation

In this section, the finite element model is validated by comparing the experimental results of the static tests described in chapter 5 with the corresponding results of the 2D axisymmetric finite element program.

6.8.1 Make-up Validation

To validate the modelling of the make-up stage, the strains measured on the made-up connection are compared with the modelled strain values. As described in chapter 5 the effective number of the 0.80 make-up turns taking into account the necessary rotation for the settlement of the connection during the experiments is used in the models.

The resulting axial hoop and shear strain are respectively shown in figures 6.29, 6.30 and 6.31. The points in the graphs are the values measured by the strain gauges (SG) and the lines are the simulated strain along the inside wall of the pin and the outside wall of the box. The gauge length of the strain gauges is 3 mm. Hence, the measured values are the mean strains over that length. A good qualitative and quantitative correlation can be observed. Since the box is the most rigid part of the threaded connection, the magnitude of the strains in the box is generally smaller than the magnitude of the pin strains. The maximum axial strain values appear around the location of the LET at the inside wall of the pin. Similar to the hoop stress situation described hoop strains in the pin are compressive and tensile in the box. It is also

confirmed that the shear strains remain limited indicating a near alignment with principal direction. The overall correspondence is good. The root mean square deviation (RMS) between all measured and modelled strains is $78\ \mu\varepsilon$. Compared to results found in literature, previously described in chapter 2, the measurements from the make-up tests of Yuan et al (2004, 2006) carried out on API Round Non-Upset Tubing T&C threaded connections.

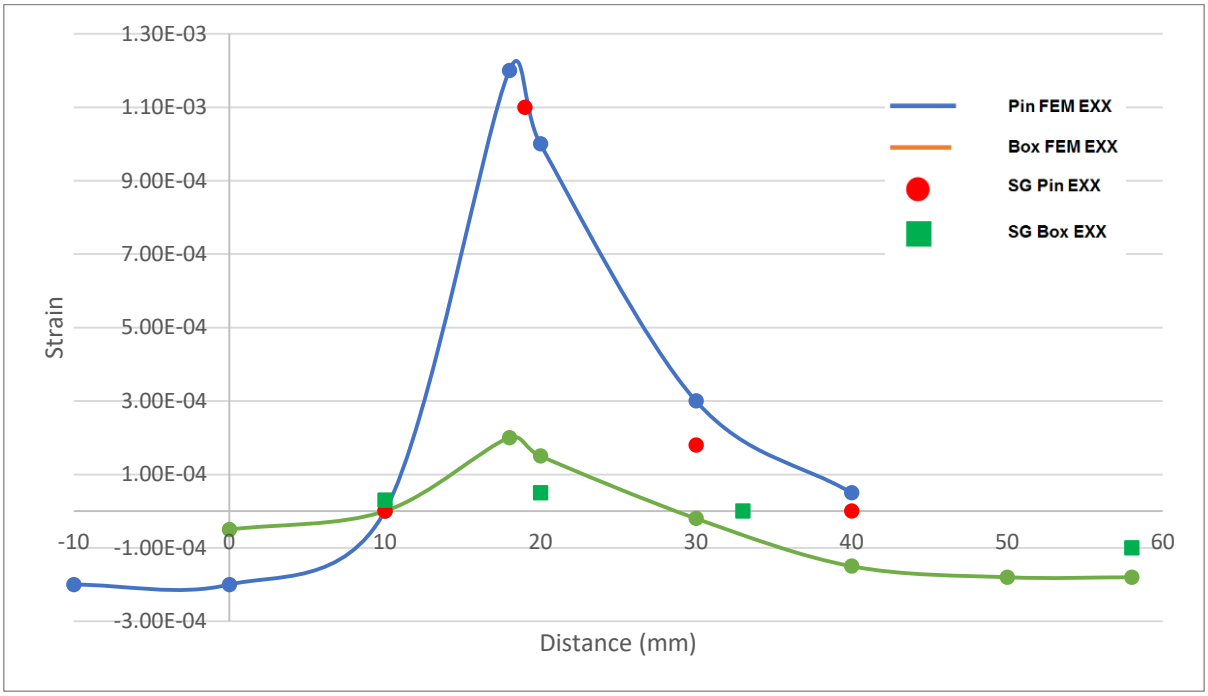

Figure 6.29: Experimental vs simulated axial strain values due to make-up.

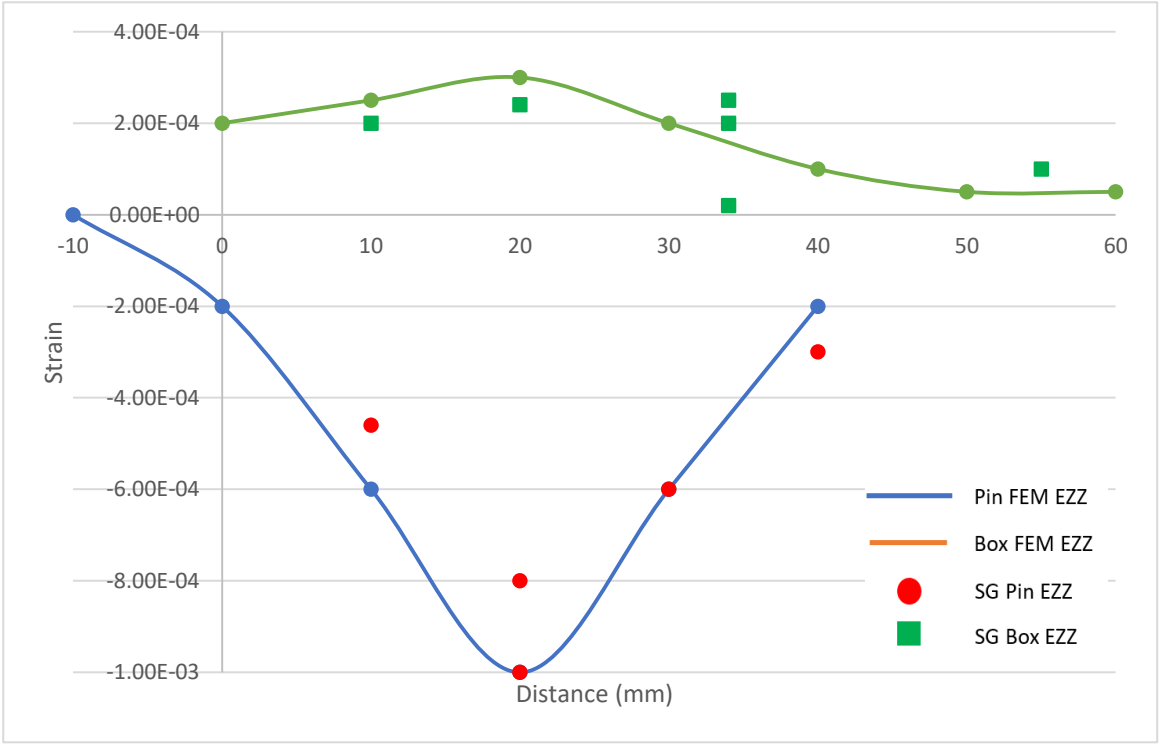

Figure 6.30: Experimental vs simulated hoop strain values due to make-up.

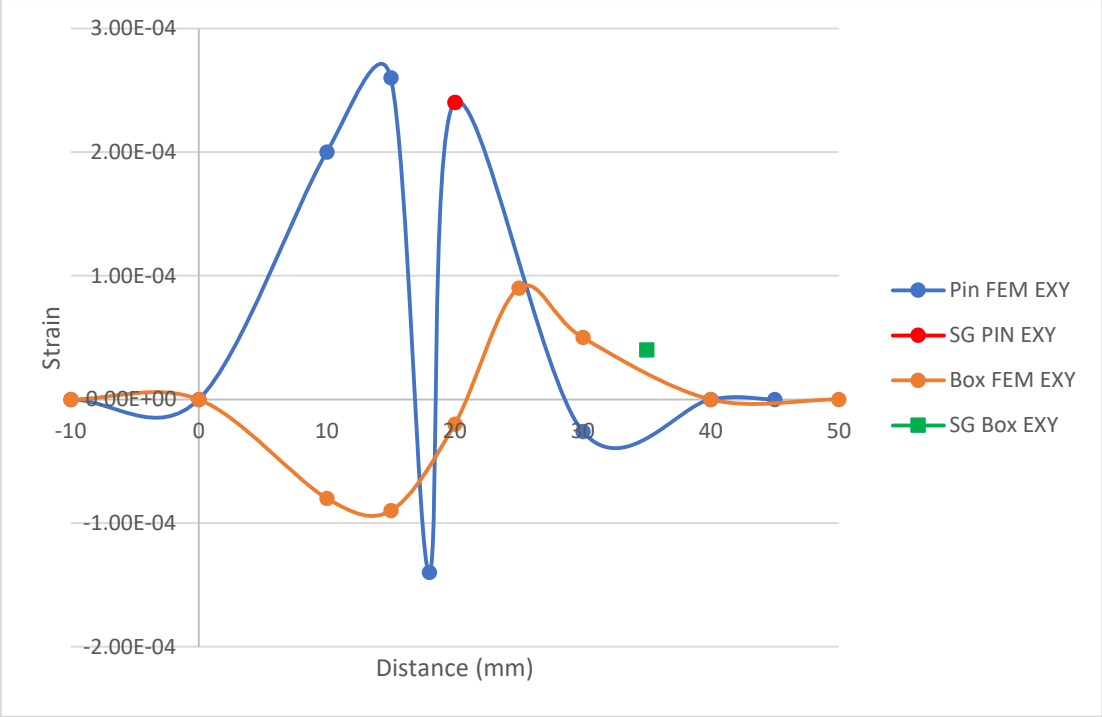

Figure 6.31: Experimental vs simulated shear strain values due to make-up.

6.8.2 Axial tension validation

During the axial tensions test described in chapter 5, a uniform axial tensile load is applied to a 4.5" API Line Pipe connection. Hence, an axisymmetric load is created. The strains measured during this test serve to validate the 2D axisymmetric model with a uniform axial load. In figures 6.32-34 the strain is compared for uniform axial tensile stress load of $100\ kN$. The strains apply to the made-up situation.

Strain gauge 1 and 3 on the pin (as given in figure 5.8) failed during the test, hence for these location no measured strain values is given.

For all strain components, the results obtained by the finite element model are in good agreement with the measured strains, due to the failure in strain gauge, all the data were not recorded during the experiment. The RMS deviation is $84\ \mu\varepsilon$, which is comparable to the deviation obtained for the connection make-up validation test. Consequently, the model is validated for the axisymmetric load cases of the make-up and axial tensile loading.

Compared to the strain measurements of the premium shouldered connection subjected to an axial load of Dvorkin et al. (1996) the strains measured in this study show similar trends. However, the torque shoulder of the premium connection effects the strain distribution.

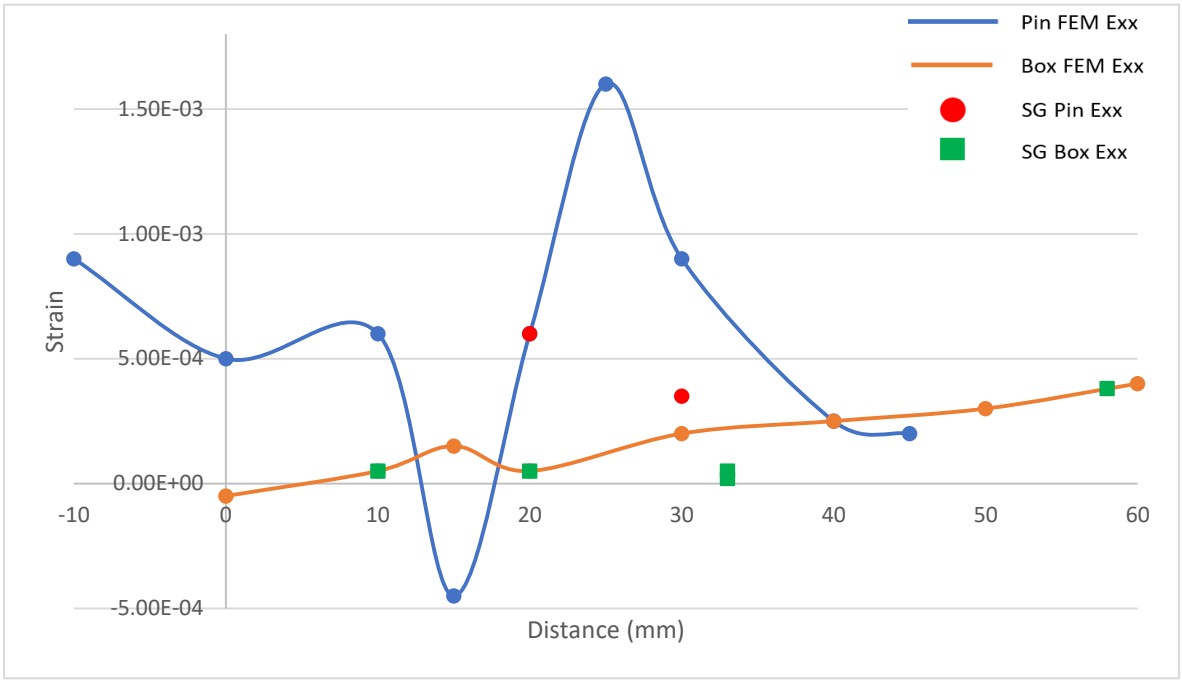

Figure 6.32: Experimental vs simulated axial strain values due to an axial tensile stress load of $100\ kN$.

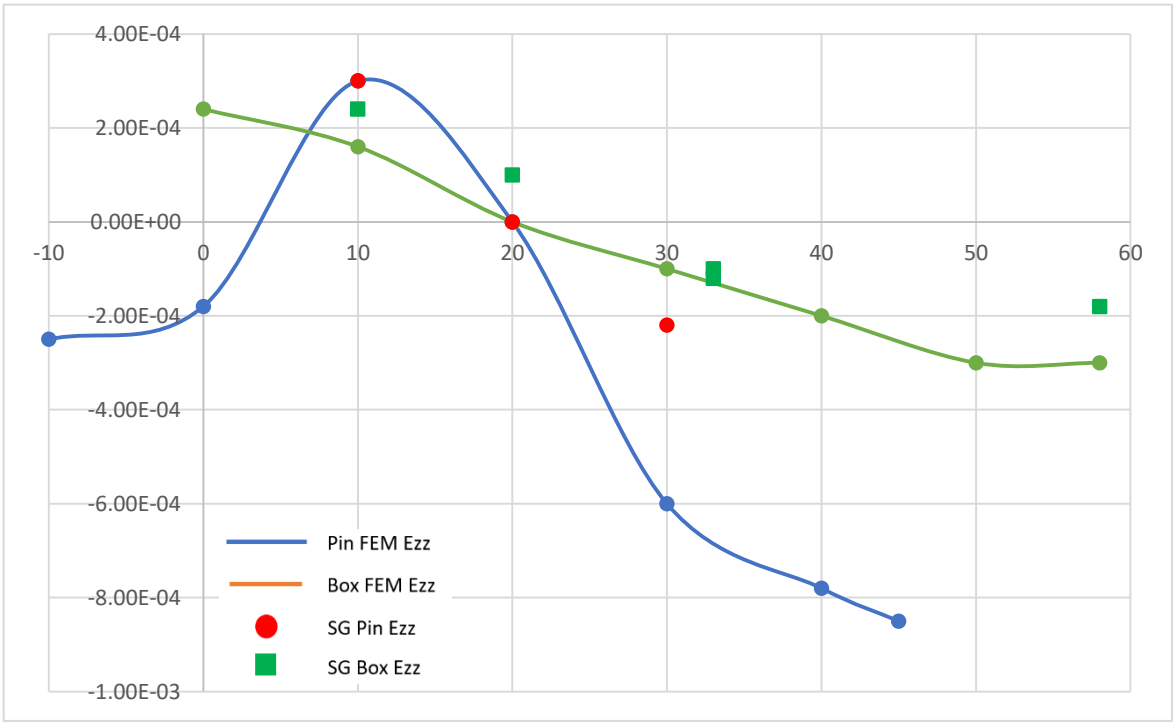

Figure 6.33: Experimental vs simulated hoop strain values due to axial tensile stress load of $100\ kN$.

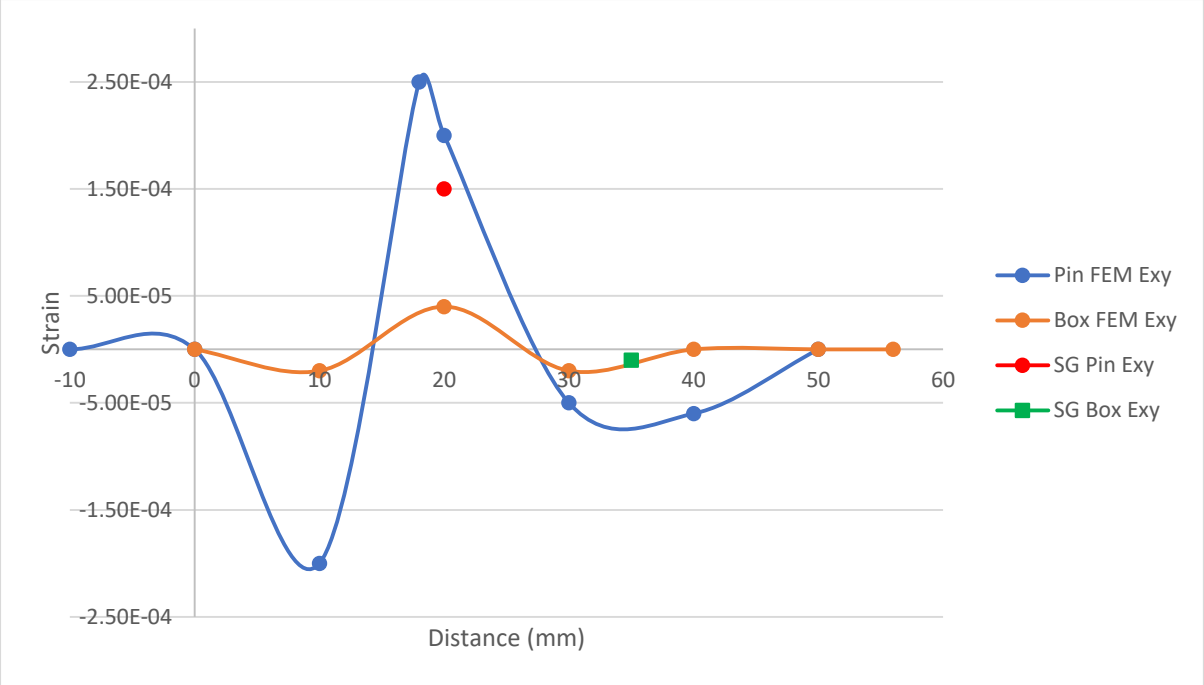

Figure 6.34: Experimental vs modelled shear strain values due to an axial tensile stress load of $100\ kN$.

6.8.3 Conventional FEM model

For modelling crack propagation by mean of conventional FEM, which is also called the re-meshing technique approach, the crack should be modelled using an embedded line. This is called a “seam” in ABAQUS, lying at an estimated location of an initial crack. In order to model sharp crack propagation based on conventional FEM technique two steps are important. The first step is capturing a singularity at crack the tip. For a sharp crack the stress field becomes singular at the crack tip. Including the singularity at the crack tip for a small-strain analysis improves the accuracy of the J-integral, Stress Intensity Factors (SIFs) and in general the stress and strain fields calculations. The second step is refining the mesh for each crack propagation increment. The re-meshing technique enables a further propagation of the growing crack.

The partitioning of the geometry was defined by the circular lines centered at the crack tip. The partitions facilitate the generation of a focused mesh. The crack tip was meshed using a ring of collapsed quadratic quadrilateral elements, which are generally used to obtain a mesh singularity at the crack tip. Specification of the mid-side node parameter and the crack-tip element degeneracy allows different singularity types to be defined. In the present study, a value of 0.25 was used for the mid-side parameter as illustrated in figure 6.35. This definition moved the mid-side nodes on the element side adjoining the collapsed edge to the ¼ points of the element. At the crack tip, the element side were collapsed with single-node-type degenerate element control. These setting combine to create a $1/\sqrt{r}$ singularity in strain. The circular partition areas were meshed using the “swept meshing” technique, which allows the mesh to be regular

and focused. This inclusion of the seam and singularity definition serve to create automatically collapsed element with correct connectivity definitions.

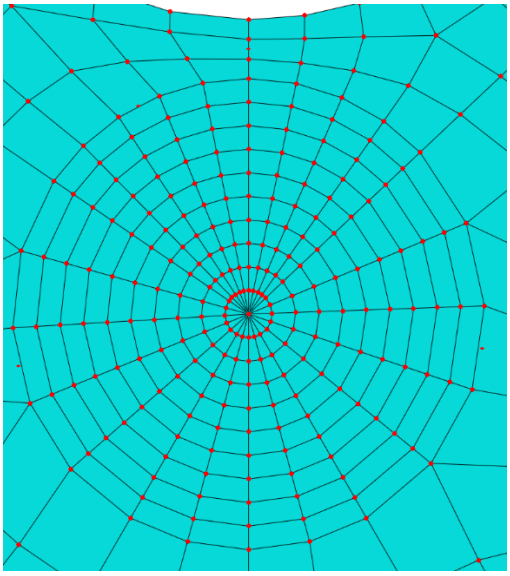

Figure 6.35: Focused mesh around crack tip along with the contour integral circular ring.

The “single node” degeneracy method was used for the elements at the crack tip. In this approach, the collapsed element edges are defined by repeating nodes in the element connectivity. After each increment of crack propagation, the mode I (K_I) and mode II (K_{II}) SIFs were extracted using the domain from an interaction integral method, which available in ABAQUS. This approach is based on a path independent J-integral which is also mesh independent. All the elements within the crack front and one layer of element outside the crack front were used to determine the first counter integral. In computing the additional counter integrals, ABAQUS automatically adds a single layer of elements to the group of elements that were used to calculate the previous counter integral. These steps are available in ABAQUS for modelling stationary cracks. In order to propagate the crack a script was written using Python programming language written by the researcher in conjunction with ABAQUS solver. It means that the pre-posted processing were carried out using Python code and the ABAQUS solver was used to solve the model for each individual crack propagation step.

6.8.5 XFEM model

Modelling stationary cracks using conventional FEM needs the geometry of cracked body to be matched with the mesh. Therefore, modelling crack propagation using mesh refinement techniques are really cumbersome, especially in 3D and complex models. As elaborated in chapter 2, XFEM decreases inadequacy associated with re-meshing of the crack tip. The XFEM technique is an extended version of FEM approach. It allows local enrichment functions to be easily incorporated into a FE approximation. For the purpose of fracture mechanics analysis, the enrichment functions typically consist of the near-tip asymptotic functions that capture the singularity around the crack tip and a discontinuous function that represents the jump in displacement across the crack line (in the case of 2D) as explained in beginning.

There are a lot of studies, which are aimed to implement the XFEM feature in conjunction with conventional FE software. For instance, Giner et al. (2008) have carried out a two-dimensional implementation of XFEM within the ABAQUS software by means of user element subroutine. Since after ABAQUS 6.9 the XFEM feature has been added by developers, in this study this capability was used to model the 2D crack propagation by means of XFEM approach. However, there are some limitations that should be overcome by using Python programming techniques. One major restriction is extracting the SIFs at the crack tip for a 2D stationary crack. The implemented XFEM feature in ABAQUS does not provide the function of extracting J-integral or SIF. Therefore, after modelling a cracked specimen based on the stress and displacement fields at the crack tip, a Python script was written to extract the original form of the J-integral for a line contour surrounding the crack tip and SIFs subsequently. However, after releasing ABAQUS 6.11 there is an alternative way to extract J-integral and SIFs by means of counter integral crack function.

Some limitation of modelling discontinuities, such as cracks, as an enriched feature (XFEM) in ABAQUS, which are reported by their developers, can be stated as:

- An enriched element cannot be intersected by more than one crack.
- A crack is not allowed to turn more than 90° in one increment during an analysis.
- Only asymptotic crack-tip fields in an isotropic elastic material are considered for a stationary crack.
- Adaptive re-meshing is not supported.

Nevertheless, these are not the only limitations. In general, XFEM approach is developed to be a mesh refinement independent method, while this not the reality with the implementation in ABAQUS. It was found that the mesh should be refined at crack tip to capture real stress and strain field around it. The same fact has also been realized by Vethe (2012). He found that to achieve an accurate results the mesh size at crack tip has to be at least below 3% the crack size. By refining the mesh at area of interest the results were shown to be accurate.

6.8.6 Crack propagation direction

The direction of the crack propagation can be determined as function of the stress and strain fields at the crack tip. There are several criteria that can be chosen to calculate crack propagation direction. Some of the most widely used mixed mode criteria are: Maximum Tangential Stress Criterion (MTS), the Maximum Energy Release Rate criterion (MERR), the zero K_{II} criterion ($K_{II} = 0$) criterion.

6.8.7 Maximum Tangential Stress (MTS)

Based on this criterion, the crack propagation angle is defined to be perpendicular to the maximum tangential stress at the crack tip (Erdogan and Sih, 1963). The crack tip stress field for a homogeneous, isotropic linear elastic material is given by:

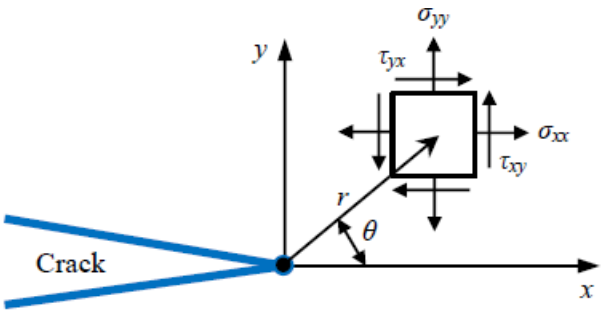

Figure B: Crack tip stress field.

$$\sigma_{\theta\theta} = \frac{1}{\sqrt{2\pi r}} cos\frac{\theta}{2}\left[K_I cos^2\frac{\theta}{2} - \frac{3}{2}K_{II} sin\theta\right] \qquad (6.27)$$

$$\tau_{r\theta} = \frac{1}{\sqrt[2]{2\pi r}} cos\frac{\theta}{2}[K_{II} sin\theta - K_{II}(3cos\theta - 1)] \qquad (6.28)$$

Where r and θ are polar coordinates at the crack tip in a plane orthogonal to the crack face. The direction of crack propagation then can be obtained using either the condition ${\partial\sigma_{\theta\theta}}/{\partial\theta} = 0$ or $\tau_{r\theta} = 0$, i.e.,

$$K_I sin\theta_p + K_{II}\left(3cos\theta_p - 1\right) = 0 \qquad (6.29)$$

$$\theta_p = arccos\left[\frac{3K_{II}^2 + \sqrt{K_I^4 + 8K_I^2 K_{II}^2}}{K_I^2 + 9K_{II}^2}\right] \qquad (6.30)$$

Where the crack propagation angle θ_p is measured with respect to the crack plane, i.e., $\theta_p = 0$ represents the crack propagation in a "straight ahead" direction and $\theta_p \leq 0\ if\ K_{II} \geq 0$, while $\theta_p \geq 0\ if\ K_{II} \leq 0$.

6.8.8 Maximum energy release rate (MERR)

By considering a crack segment of length l kinking out the plane of the crack at an angle θ_p. When l is infinitesimally small compared with all other lengths (including the length of the original crack), the SIFs, K_I^k and K_{II}^k at the tip of the crack can be expressed as linear combination of K_I and K_{II} (Hayashi and Nemat-Nasser, 1981). The existing SIFs prior to kinking for the original crack are:

$$K_I^k = \left(\frac{4}{3+cos^2\theta}\right)\left(\frac{1-{\theta}/{\pi}}{1-{\theta}/{\pi}}\right)^{\frac{\theta}{2\pi}}\left(K_I cos\theta + \frac{3}{2}K_{II} sin\theta\right) \qquad (6.31)$$

$$K_{II}^k = \left(\frac{4}{3+cos^2\theta}\right)\left(\frac{1-{\theta}/{\pi}}{1-{\theta}/{\pi}}\right)^{\frac{\theta}{2\pi}}\left(K_{II} cos\theta + \frac{3}{2}K_{II} sin\theta\right) \qquad (6.32)$$

For the crack segment the relation between energy release rate (G^k) and SIFs at small crack tip can be written as:

$$G^k = \frac{1}{E}\left[\left(K_I^k\right)^2 + (K_{II}^k)^2\right] \qquad (6.33)$$

The MERR criterion postulate that the original crack initially propagates in the direction the maximizes G^k. Finding G^k will establish for the general mixed mode case the duality which is the basis of the fracture mechanics: the equivalence in viewing fracture initiation from either a global energy balance or a local stress intensity point of view.

6.8.9 Criterion of local symmetry (zero K_{II})

This criterion simply postulates that a crack initially propagates in the direction that makes $K_{II} = 0$, which proposed by Cotterell and Rice (1980). Implementation within a FE model involves the extension of a infinitesimally small crack from the crack-tip, whose direction is varied to attain a minimum for $K_{II} = 0$. Hayashi and Nemat (1981) have provided a series of direction-dependent coefficients C_{ij}. At the crack tip, the stress intensity factors for different direction can be expressed as:

$$K_I^k = C_{11}K_I + C_{12}K_{II} \tag{6.34}$$

$$K_{II}^k = C_{21}K_I + C_{22}K_{II} \tag{6.35}$$

As mentioned, the $K_{II} = 0$ criterion postulates that a crack will propagate in the direction that makes $K_{II}^k = 0$. However, it was observed that the variation in mode II SIF, K_{II}, with infinitesimally small crack direction is approximately linear over a wide range of angles. This linearity has been utilised in an improved algorithm in ABAQUS for finding the optimum deflection angle. Therefore equation 6.6 can be used to find the next crack propagation angle, in which leads to minimum value of K_{II}. In some loading conditions, which are not possible to reach $K_{II} = 0$, therefore ABAQUS searches for minimum value of K_{II}.

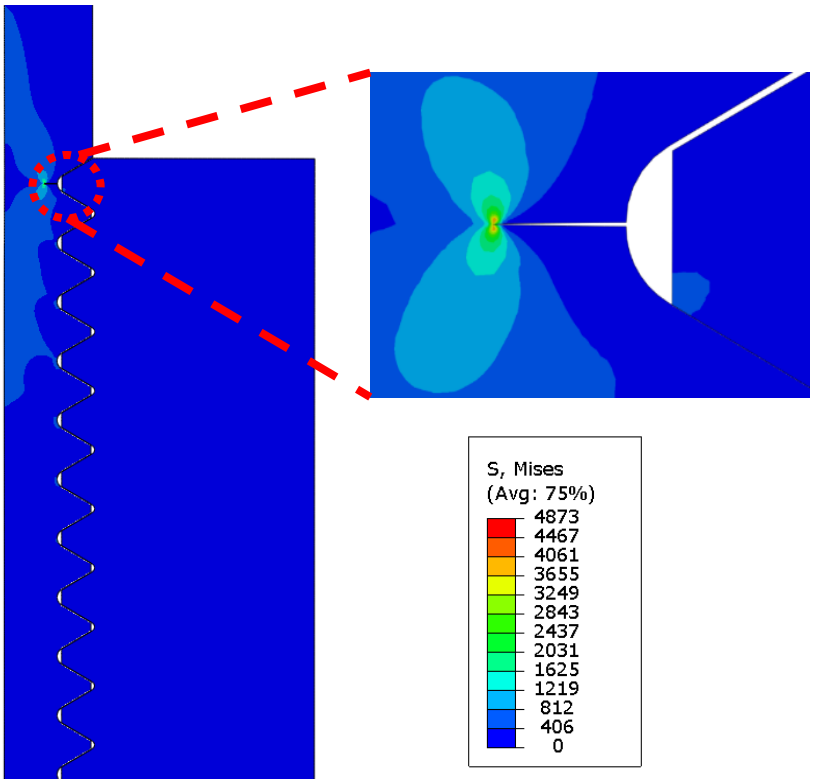

Figure 6.36: Crack simulating using J-Integral methods.

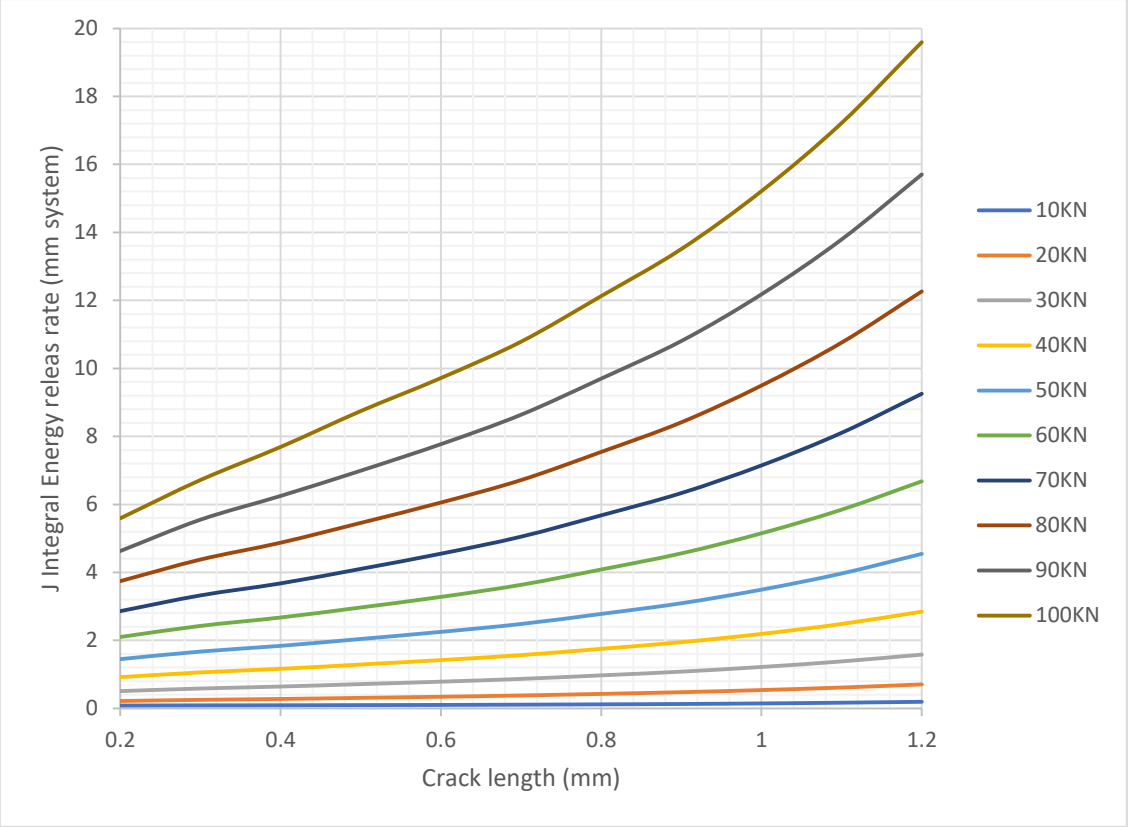

Figure 6.37: Energy release vs crack propagation length.

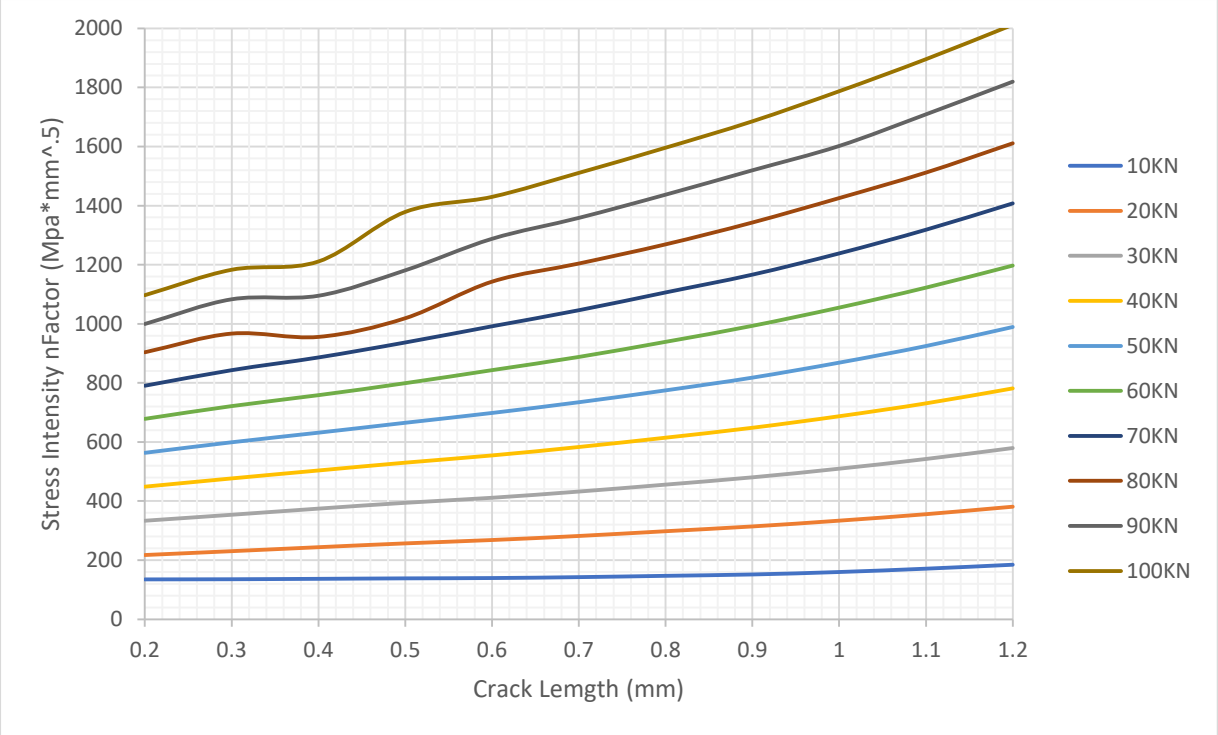

Figure 6.38: Stress intensity factor vs crack propagation.

The analysis is performed according to the procedure described earlier. In order to get accurate results, the mesh is divided into many partitions, the section around the crack has a mesh size of 3% of the initial crack.

The initiation of the crack was located in the area with highest stress. The knowledge about the location of fatigue crack initiation and propagation is inadequate. The initiation is often located where the highest stress concentration occurs; at the root of the last threads with full connection. In the analysis, an initial crack 0.5 mm was initiated at the root of the last thread on the pin. This is close to where the highest stress occurred in the static analysis without crack.

As the highest stress occurs a little lower than where the crack was initiated, the crack propagates in the direction of the highest stress. The limited analysis with an initial crack of 0.1 mm follows the same path as the initial crack of 0.5 mm except it starts to change direction at a crack length of 0.3 mm.

The simulation obtained a crack path as expected, and the crack propagated in the direction of the highest stress. These results show that the required accuracy of the initial crack location is low as long as it is close to the highest stress.

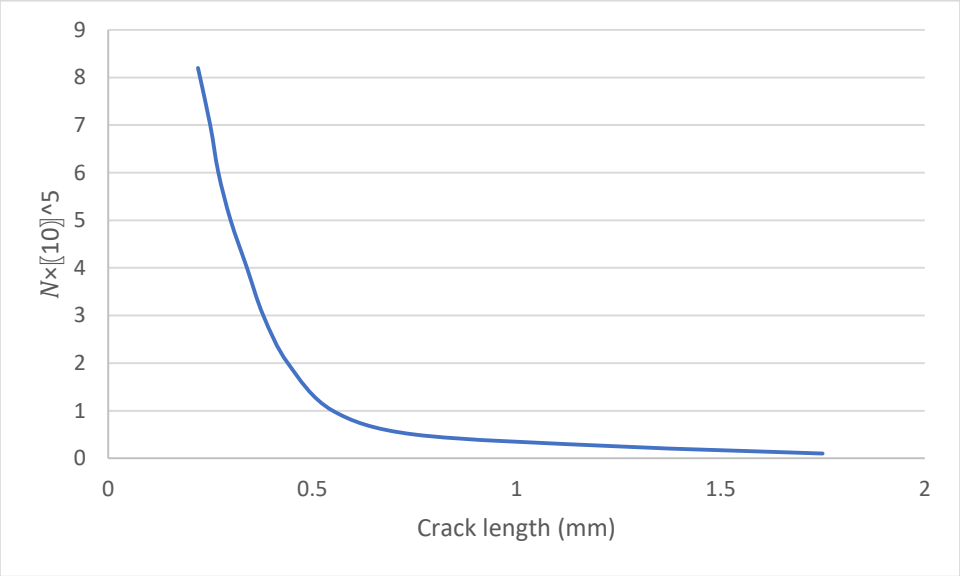

Figure 6.39: Number of elapsed cycle per crack growth increment of a crack with initial crack depth $a_i = 0.1\ mm$ and nominal stress amplitude $S_a = 10\ MPa$.

The stress intensity factor increases exponentially with increasing crack depth a. The stress intensity factor range at the deepest point A are therefore underestimated during the late crack growth. But as can be seen from the plot of elapsed number of cycles per increment of figure 6.39, this behaviour is not relevant for the estimated lifetime, since most of the lifetime is spend in the early stage of the crack growth.

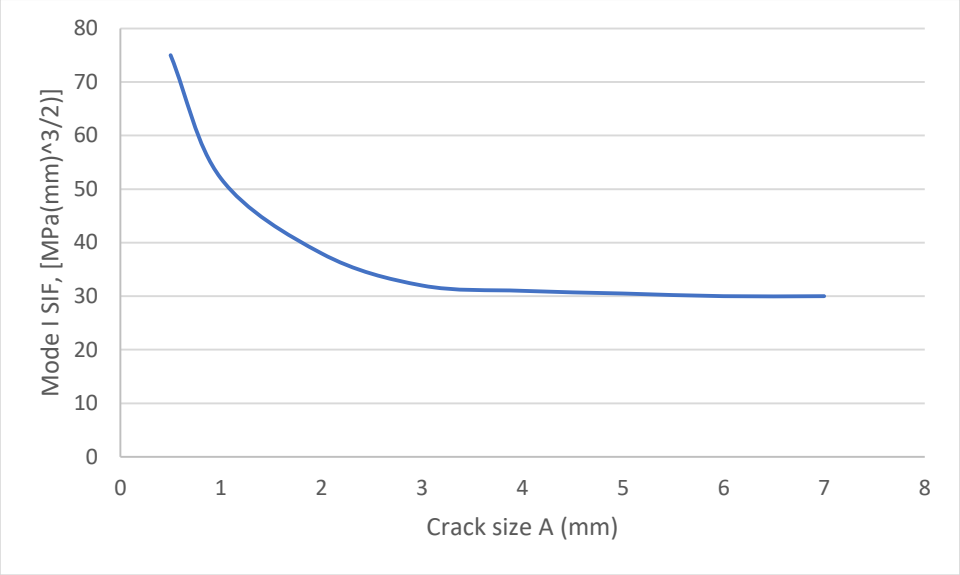

Figure 6.40: SIF mode I vs crack size.

The graph of the SIFs 6.40 shows decreasing SIFs as the stress also decrease and the stabilize. The simulation show that the combination of the applied stress and geometrical stress cause SIFs above the threshold value for cracks up to $a = 0.70\ mm$.

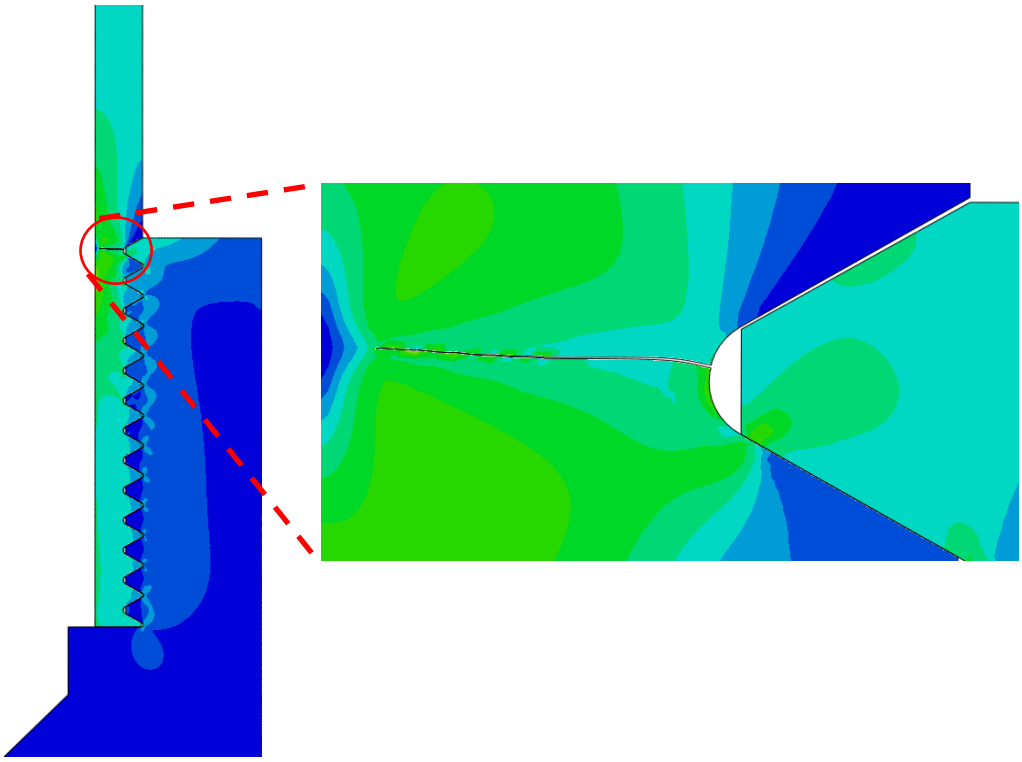

Figure 6.41: Crack initiation and propagation in LET.

The simulation obtained a crack path as expected, and the crack propagated in the direction of the highest stress. The results show that the required accuracy of the initial crack location is low as long as it is close to the highest stress.

6.9 Summary and Conclusion

2D axisymmetric model geometry of a threaded connection created to perform a detailed stress analysis based on a number of geometrical parameters. The model mesh is automatically generated and elaborate contact behaviour is included. Next to this, the necessity of using elastic-plastic material properties is shown by the appearance of plastic deformation during the make-up stage.

To validate the 2D model, a comparison is made with a full 3D model. As also found in literature, the stress state resulting from make-up for both models is as good as identical. In addition, a comparison is made between a 3D model and a 2D axisymmetric model with an equivalent uniform axial tensile stress. It is shown that also for these load case, the stress states around the engaged threads are similar.

Furthermore, the validity of the model is proven experimentally. This is done be comparing simulated strain values with strain gauge measurements for four different load case: make-up, axial tension, bending and internal pressure. For all load case the difference between the measured and modelled strains are small.

In previous work the validity of 2D axisymmetric models was always assumed. These assumptions were based on the results of photo-elastic scale model under simple linear elastic load case. In this chapter, however, the validity of these assumptions is rigorously proven and extended to real elastic-plastic material behaviour and non-linear connect properties. Hence, a fully validated model is presented that is suitable of modelling a wide variety of load cases.

Following trends are observed when considering the contact conditions and thread properties.

- The coefficient of friction between the threads of pin and box has an important influence on the thread opening, but does not affect the load distribution.
- The thread opening can be decreased by applying a higher number of make-up turns, but this introduces an increased loading of the LET of the pin.
- The relative thread load on the LET of the pin of an axially loaded connection can be reduced by using a thread with smaller pitch length. The more flexible thread transfers the load better overall engaged threads, but also tends to create an increased thread opening.
- Both the relative load on the LET and the thread opening can be reduced when a positive taper difference is applied between the pin and box threads.
- The stress concentration factor of different thread types are compared. As could be expected, the thread root radius has an important influence on the

resulting stress distribution, the buttress thread shape creating the lowest stress concentration.

The stiffness ratio between pin and box can be changed by altering their dimensions and the load distribution can be influenced. To obtained a reduced relative thread load at the LET of the pin and the following finding were supported by FE study.

- A local box stiffness reduction can be used. For example, the stiffness gradient or bevelled groove design result in a slightly improved load distribution.
- A more significant reduction of the thread load can be obtained by reducing the box recess length. This also causes a limited increase in the thread opening.
- By applying relative stiffness reduction of the box, the thread load can also be reduced. This can either be done by decreasing the box wall or increasing the thickness of the pin wall. The thread opening however, increases for a box wall reduction, but deceases for a pin wall increase.
- Reducing the engaged thread length can significantly increase the load at the LET, while having more than 7 engaged threads does not improve this value any more. Furthermore, the thread opening can be reduced by having 8 engaged threads, which is identified to be the optimum pin length.

Hence, it can be concluded that important changes in thread load distribution can be obtained by changing globally or locally the pin and box geometry dimensions.

As stated in section 2.2.3 of chapter 2, the pressure sealing of premium connections can be provided by metal-to-metal seals instead of using sealing threads. Hence, the value of thread opening becomes less important. When optimizing a connection, it might be appropriate to combine several design features. The thread shape can be optimized to obtained a low stress concentration factor and reduce the local strains at the thread roots; the connection geometry and make-up conditions can be optimized to improve the load distribution over the threads and the resulting local stresses and strain at the threads; metal-to-metal seals can be added to ensure appropriate leak resistance.

References

- API, R., 1999. 5C1 “Recommended Practice for Care and Use of Casing and Tubing”.
- Assanelli, A.P., Xu, Q., Benedetto, F., Johnson, D.H. and Dvorkin, E.N., 1997. Numerical/experimental analysis of an API 8-round connection. *Journal of energy resources technology*, *119*(2), pp.81-88.
- Baragetti, S. and Terranova, A., 2004. Effects of over-torque on stress relief in conical threaded connections. *Journal of Mechanical design*, *126*(2), pp.351-358.
- Baragetti, S., 2002. Effects of taper variation on conical threaded connections load distribution. *Journal of Mechanical Design*, *124*(2), pp.320-329.
- Barry, N.W., Raghu, N.S. and Gexin, S., 1992. Rock fracture mechanics principles design and applications.
- Beden, S.M., Abdullah, S. and Ariffin, A.K., 2009. Review of fatigue crack propagation models for metallic components. *European Journal of Scientific Research*, *28*(3), pp.364-397.
- Belytschko, T., Gracie, R. and Ventura, G., 2009. A review of extended/generalized finite element methods for material modeling.*Modelling and Simulation in Materials Science and Engineering*, *17*(4), p.043001.
- British Standards Institution, 1999. *Guide on methods for assessing the acceptability of flaws in metallic structures*. British Standard Institution.
- Dowling, N.E., 1993. *Mechanical behavior of materials: engineering methods for deformation, fracture, and fatigue*. Prentice hall.
- Dvorkin, E.N. and Toscano, R.G., 2003. Finite element models in the steel industry: Part II: Analyses of tubular products performance. *Computers & Structures*, *81*(8), pp.575-594.
- Dvorkin, E.N., Assanelli, A.P. and Toscano, R.G., 1996. Performance of the QMITC element in two-dimensional elasto-plastic analyses. *Computers & Structures*, *58*(6), pp.1099-1129.
- Erdogan, F. and Sih, G.C., 1963. On the crack extension in plates under plane loading and transverse shear. *Journal of basic engineering*, *85*(4), pp.519-525.
- Ferjani, M., Averbuch, D. and Constantinescu, A., 2011. A computational approach for the fatigue design of threaded connections. *International Journal of Fatigue*, *33*(4), pp.610-623.
- Giner, E., Sukumar, N., Denia, F.D. and Fuenmayor, F.J., 2008. Extended finite element method for fretting fatigue crack propagation. *International Journal of Solids and Structures*, *45*(22), pp.5675-5687.
- Guangjie, Y., Zhenqiang, Y., Qinghua, W. and Zhentong, T., 2006. Numerical and experimental distribution of temperature and stress fields in API round threaded connection. *Engineering Failure Analysis*, *13*(8), pp.1275-1284.
- Hussain, M.A., Pu, S.L. and Underwood, J., 1974, January. Strain energy release rate for a crack under combined mode I and mode II. In *Fracture*

Analysis: Proceedings of the 1973 National Symposium on Fracture Mechanics, Part II. ASTM International.

- Macdonald, K.A. and Deans, W.F., 1995. Stress analysis of drillstring threaded connections using the finite element method. *Engineering Failure Analysis*, *2*(1), pp.1-30.
- Pais, M.J., 2011. *Variable amplitude fatigue analysis using surrogate models and exact XFEM reanalysis*. University of Florida.
- Paris, P.C., Gomez, M.P. and Anderson, W.E., 1961. A rational analytic theory of fatigue. *The trend in engineering*, *13*(1), pp.9-14.
- Salihu, B.M., 2011. Stress analysis of drillstring threaded connections.
- Santus, C., 2008. Fretting fatigue of aluminum alloy in contact with steel in oil drill pipe connections, modeling to interpret test results. *International Journal of Fatigue*, *30*(4), pp.677-688.
- Santus, C., Bertini, L., Beghini, M., Merlo, A. and Baryshnikov, A., 2009. Torsional strength comparison between two assembling techniques for aluminium drill pipe to steel tool joint connection. *International Journal of Pressure Vessels and Piping*, *86*(2), pp.177-186.
- Shoji, Y. and Sawa, T., 2010, January. Stress concentration at the ROOT of bolt thread. In *ASME 2010 Pressure Vessels and Piping Division/K-PVP Conference* (pp. 427-432). American Society of Mechanical Engineers.
- Specification, A.P.I., 1996. 5B, Specification for Threading, Gauging and Thread Inspection of Casing, Tubing and Line Pipe Threads (US Customary Units). *American Petroleum Institute*.
- Specification, A.P.I., 2000. 5L, 2000,". *Specification for line pipe*, *42*.
- Tanaka, K., 1974. Fatigue crack propagation from a crack inclined to the cyclic tensile axis. *Engineering Fracture Mechanics*, *6*(3), pp.493-507.
- Van Wittenberghe, J., 2011. *Experimental analysis and modelling of the fatigue behaviour of threaded pipe connections* (Doctoral dissertation, Ghent University).
- Veritas, D.N., 2010. Fatigue design of offshore steel structures. *No. DNV-RP-C203*.
- Vethe, S., 2012. Numerical Simulation of Fatigue Crack Growth.
- Vethe, S., 2012. Numerical Simulation of Fatigue Crack Growth.
- Westergaard, H.M., 1997. Bearing pressures and cracks. *SPIE MILESTONE SERIES MS*, *137*, pp.18-22.
- Williams, M.L., 1997. On the stress distribution at the base of a stationary crack.
- Yuan, G., Yao, Z., Han, J. and Wang, Q., 2004. Stress distribution of oil tubing thread connection during make and break process. *Engineering Failure Analysis*, *11*(4), pp.537-545.
- Zhong, A., 2007, May. Thread Connection Response to Critical Pressures. In *Abaqus Users' Conference, Paris, France* (pp. 690-706).

Chapter 7 Conclusions and Future Research

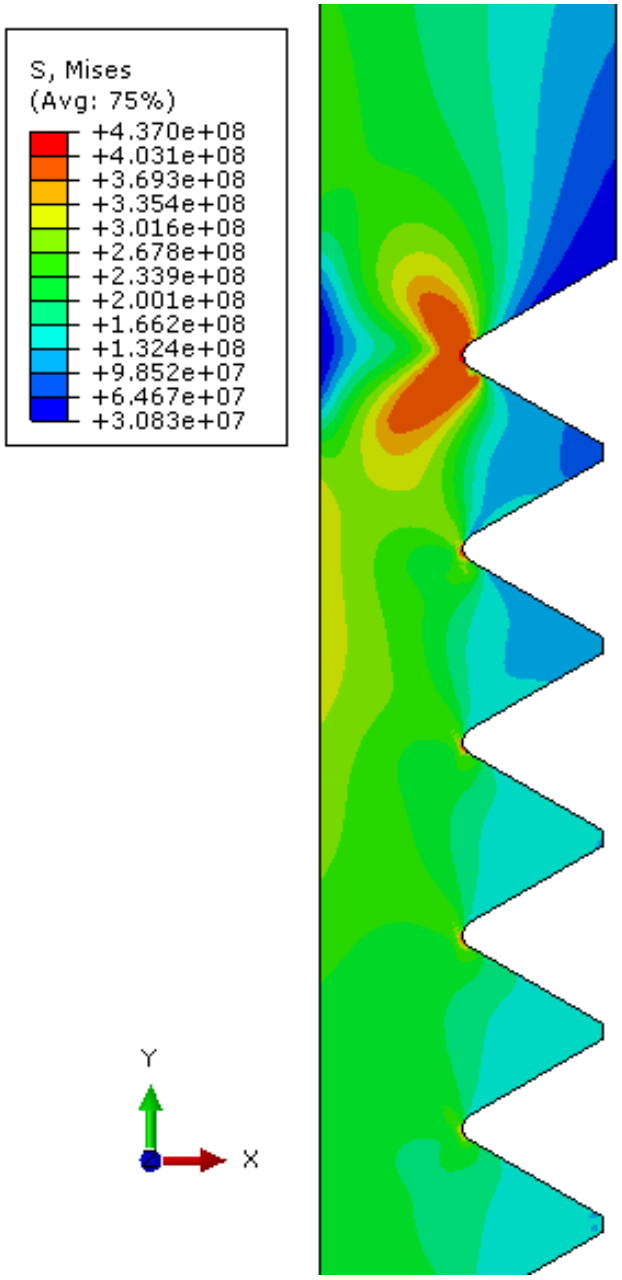

7.1 General Conclusions

7.1.1 Summary

The purpose of this research is to provide a better understanding of how the fatigue mechanisms of threaded pipe connections work and to analysis and study of different design features on a connection's fatigue life.

In the literature as shown and discussed in chapter 2 the experimental data available is limited. Experimental data published is generally comprise experiment on a single connection type. Results from different studies cannot be used for a detailed fatigue analyses to compare the designs as there is no uniformity in testing setup, loading conditions and damage detection techniques exists. Furthermore, current design curves in codes and standards lead to overly conservative or inaccurate results.

The API Line Pipe connection used as a reference in this study. Few modifications and design features are applied to this connection type. In order to evaluate the influence of connection properties and design features on the threaded connection's fatigue behaviour a finite element model is developed. Besides, an experimental test program is carried out, comprising 20 fatigue test, to create an extensive experimental database. The results from the simulations and the experiments are combined in a multiaxial fatigue analysis and the observed trends are explained. Based on these main results, guidelines for future development of fatigue resistant premium threaded connections are formulated.

7.1.2 Methodology used in this work

7.1.2.1 Finite element modelling

In this study, a parametric 2D axisymmetric finite element model is developed. It is important that elaborate contact conditions and the correct value of the coefficient of friction between the threads in contact are included. The use of elastic-plastic material behaviour is of utmost importance, as plastic deformation can already appear during the make-up stage. The required material properties are obtained by tensile testing and the coefficient of friction is derived from the results of a torques test.

Compared to full 3D models, the 2D axisymmetric approach has the advantage of a much shorter calculation time, without significant loss in accuracy. 2D axisymmetric and 3D model is shown by a comparison of the stresses during make-up and also a comparison between a 2D axisymmetric model and 3D model with an equivalent uniform axial tensile stress. The validity of the model is proven experimentally by comparing simulated strain values with strain gauge measurements for different load cases: make-up and axial tensions. For all load cases, the differences between the measured and modelled strains are negligible.

7.1.2.2 Experimental testing

7.1.2.2.1 Test setup

In this work both static and fatigue tests have been carried out in setups that were either newly designed or adapted existing setups. The static tests used for model validation comprise torque tests and axial tension test. Fatigue tests on threaded pipe connections are carried out in two setups, axial tension for small and medium scale. The majority of tests is carried on small scale 1" specimens. The medium scale tests are conducted on 4.5" specimens.

7.1.2.2.2 Measurement techniques

During the experiments, attention is paid to elaborate instrumentation. As until present no direct online monitoring technique exists for crack sizing in threaded pipe connection, due to lack of equipment no technique has been applied to monitor crack propagation indirectly. During the small-scale test, crack was detected as a sudden failure. During the medium scale test, more elaborated techniques are applied to detect fatigue damage. However, any technique of measurement is only suitable for use in laboratory conditions.

The measurements are used to distinguish between crack initiation and propagation and are confirmed by the beach mark lines that are observed in fracture surface. The crack opening measurement gives the most accurate results.

7.1.3 Main Results

7.1.3.1 Trends in fatigue life

Using thread load distribution technique as a measure for analysing fatigue life is proven to be inaccurate since the load distribution is related to the axial stresses over the connection. Analysis of fatigue life for threaded pipe connection is determined by local multiaxial stress and strain at the root of the LET. The axial load distribution results are not the only local condition, but they are also affected by other stress and strain components such as the hoop stress introduced during make-up, which can additionally be effected by a changed connection stiffness.

Using a damage evolution law, the multiaxiality at the thread root is accounted for. This model combines data from the simulations with experimentally obtained damage parameters and is able to explain the experimentally observed trends. It is shown that creating a more uniform load distribution can be beneficial if the equivalent stress range and equivalent plastic strain range at the LET remain limited.

A range of design features and modifications, used in patented fatigue resistant threaded connections, are evaluated and compared using the damage evolution law. Their effectiveness to improve a connection’s fatigue life is investigated.

Positive feature of improving fatigue life

The new finding and contribution to the knowledge explained in the following stpes:

Make-up: application of sufficient number of make-up turns can significantly reduce the local dynamic stress and strain range at the root of the LET. Although this increases the thread load, this is positive for the connection's fatigue life.

Thread type: applying a thread type with a low stress concentration factor will reduce the local stresses at the thread root and consequently improve the connection's fatigue life.

Thread pitch: reducing the thread pitch length (or increasing the number of threads per inch) increases the fatigue life due to a thread reduction and reduction of local plastic strain range at the last engaged thread.

Male and female wall thickness: changing the relative stiffness of the male and female by altering their wall thickness can be used to obtain a more uniform load distribution which can result in an improved fatigue life. However, when the stiffness of the female becomes too small relative to the male stiffness, the local strain range at the LET root will increase, and the positive effect is reduced.

Female recess: the box recess length can be reduced to improve the thread load and strain range at the LET and to obtain a higher fatigue life. In addition, applying a chamfer to the female recess can also deliver a slight fatigue life improvement.

Negative feature of improving fatigue life

Male engaged thread length: increasing the male engaged thread length to more than 7 reduces the thread opening, but does not affect the fatigue life.

7.1.3.2 Fatigue crack growth

The contribution of the crack propagation life to the total fatigue life of the connection ranges from 2% for a high total life ($N > 100{,}000$ cycles) up to 25% for a lower total life.

In the root of the LET of the male is where fatigue crack is developing, this is the location where the highest local stress and strain are calculated in finite element model. After the first stage which is the crack initiation, the second stage begin where a crack propagates gradually over a large segment of the circumference, forming a long shallow crack. When the crack penetrates the wall of the pin, the crack rapidly increases in size along two crack fronts.

The observed crack shapes, visualised by the beach mark lines, do not have a semi-elliptical shape as is commonly used in fracture mechanics. However, the ASME BPVC recommends an approach where a crack is considered to be an annular flaw. Consequently, this approach is able to accurately predict the fatigue crack growth.

7.1.4 Guidelines for fatigue resistant connection designs

As the multiaxial stress distribution and strain range around the last engaged thread of the male are affected by the connection geometry, the thread type as well as the make-up conditions, it might be appropriate to combine several design features when optimizing a connection. A multiaxial fatigue analysis technique, such as the damage evolution law, should be used to quantify the effect on the fatigue life of the new design. The new finding and contribution to knowledge is explained in the following steps.

- The thread shape can be optimized to obtain a low stress concentration factor and reduce the local strains at the thread roots. The API Buttress thread can be used as a starting point, since this thread type shows a lowest stress concentration factor.
- An important factor to taken into account is the thread pitch. A shorter pitch length can be beneficial for the fatigue life.
- The connection global geometry in combination with the make-up conditions can be optimized to improve the load distribution over the threads and resulting local stresses and strains at the threads
- Metal-to-metal seals can be added to ensure appropriate leak resistance when sealing is not provided by the threads.
- Thread lubricant or compounds can be used in practice, but these can affect the coefficient of friction in the connecting threads. In order to obtain reliable predictions, the correct friction value should be used in the finite element analysis.

7.2 Recommendation for future research

7.2.1 Connection design optimization

Using the damage evolution law, it become possible to optimize a connection design for fatigue purposes. Next to the considered features, more advanced thread types can be included. In addition, the effect of torque shoulders and sealing surface can be studied. More advance multiaxial fatigue models have been developed during the last years and might be applied to threaded pipe connections. A detailed comparison can be made of these models with the experimental results in order to select the most reliable and best applicable technique.

The parametric finite element program can be constructed in such a way that advanced optimization, using special algorithms, is possible. When such an optimization algorithm would be implemented, a series of simulations has to be carried out. Each connection geometry, generated by such an algorithm, would be based on the resulting fatigue lives of the previous geometries, calculated by the damage evolution law. The usefulness of such techniques is already shown by Ekh and Schon

(2008) in their analysis of bolted lap joints and by Han and Yamazaki (2004) in the shape optimization technique could be the genetic algorithm, as used by Kradinov et al. (2007) for optimizing bolted lap joints.

7.2.2 Experiments and measurement techniques

For experimental validation of the modelling results, the resonant bending fatigue setup can be used to test full scale connections. To monitor fatigue crack growth, the dynamic 3D optical displacement measurement system and advanced model analysis can be used. However, there are still indirect crack growth measurement systems. The development of an online crack limited to laboratory conditions, remains an important challenge.

7.2.3 Additional load case

Low cycle fatigue behaviour of threaded joint is of importance in relation to the seismic performance of piping systems. As recently pointed out by Ryu et al. (2011), threaded connections are often used in the uncoupled secondary systems (e.g. fire extinguishing piping) and the seismic performance of these components is hardly documented. Additional load case can be considered. For example, in casing drilling applications, the connection's fatigue properties are of importance during the drill insulation. Afterwards, the connection's response to internal and external pressure and static loads becomes predominant. These load case can be incorporated in the finite element simulations.

References

- Ekh, J. and Schön, J., 2008. Finite element modeling and optimization of load transfer in multi-fastener joints using structural elements. *Composite Structures*, *82*(2), pp.245-256.
- Han*, J. and Yamazaki, K., 2004. A novel technique of shape optimization for the contact parts of bolt–nut fastening structures. *Engineering Optimization*, *36*(6), pp.691-703.
- Kradinov, V., Madenci, E. and Ambur, D.R., 2007. Application of genetic algorithm for optimum design of bolted composite lap joints. *Composite structures*, *77*(2), pp.148-159.
- Ryu, Y., Behrouzi, A., Melesse, T. and Matzen, V.C., 2011, January. Inelastic behavior of threaded piping connections: reconciliation of experimental and analytic results. In *ASME 2011 Pressure Vessels and Piping Conference* (pp. 357-362). American Society of Mechanical Engineers.

Appendix A

$$S_a = 848.7 \times N^{-0.2233}$$

$$S_a = 848.7 \times 1221250^{-0.2233} = 37.12$$

$$S_a = 848.7 \times 653193^{-0.2233} = 42.68$$

$$S_a = 848.7 \times 225763^{-0.2233} = 54.11$$

$$S_a = 848.7 \times 107975^{-0.2233} = 63.8$$

$$S_a = 848.7 \times 61886^{-0.2233} = 72.24$$

$$S_a = 848.7 \times 39518^{-0.2233} = 79.85$$

$$S_a = 848.7 \times 22125^{-0.2233} = 90.89$$

$$S_a = 848.7 \times 12968^{-0.2233} = 102.41$$

$$S_a = 848.7 \times 10012^{-0.2233} = 108.50$$

Part 2

$$N = 2.95 \times 10^6 . \Delta\sigma_{eq}^{-1.26} . R_V^{4.12}$$

$$\frac{N}{\Delta\sigma_{eq}^{-1.26}} = \frac{2.95 \times 10^6 \times \Delta\sigma_{eq}^{-1.26} \times R_V^{4.12}}{\Delta\sigma_{eq}^{-1.26}}$$

$$N \times \Delta\sigma_{eq}^{-1.26} = 2.95 \times 10^6 . R_V^{4.12}$$

$$\Delta\sigma_{eq} = \sqrt[1.26]{\frac{2.95 \times 10^6 \times R_V^{4.12}}{N}}$$

Appendix B

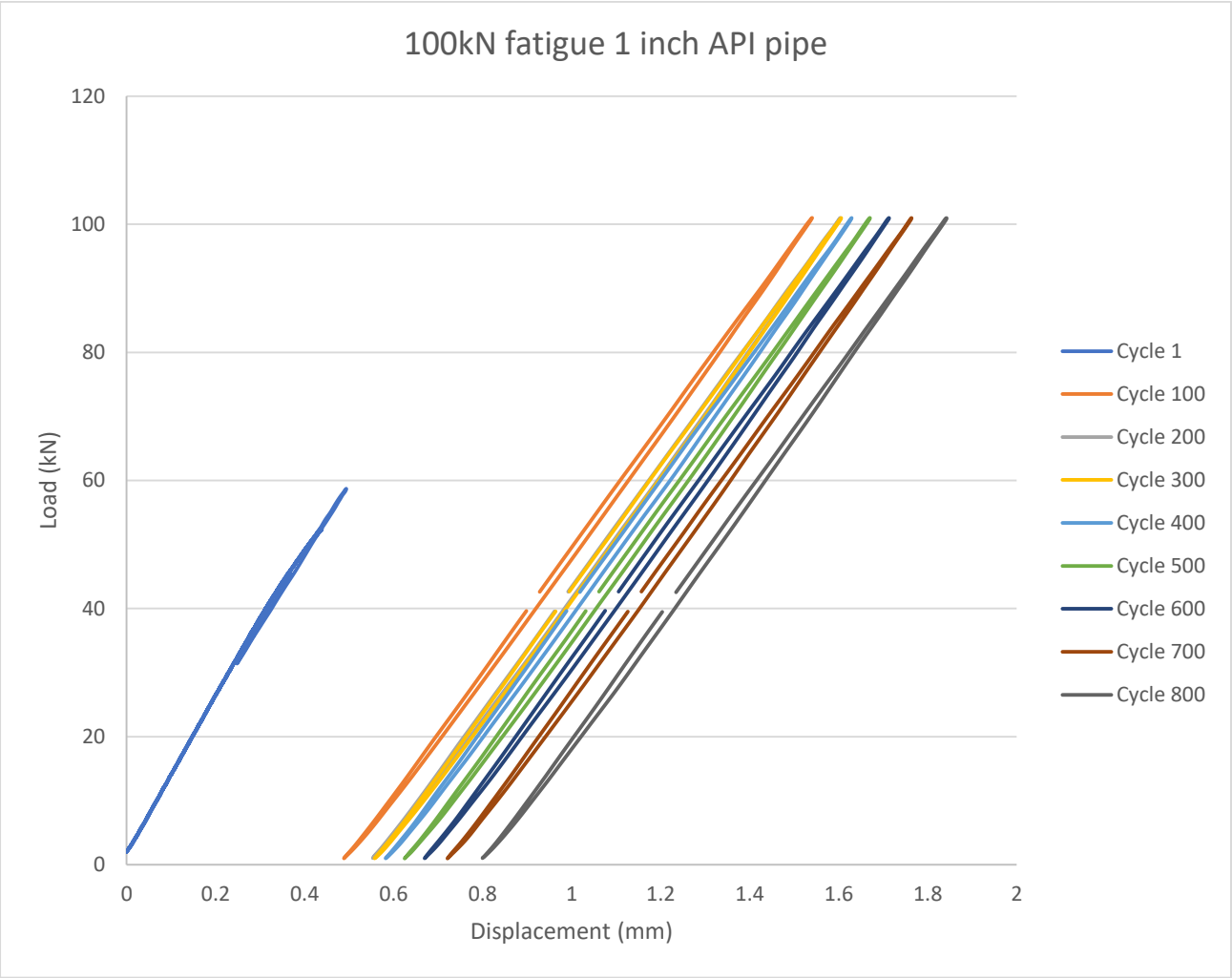

Figure 6.42: Cyclic loading at $100kN$.

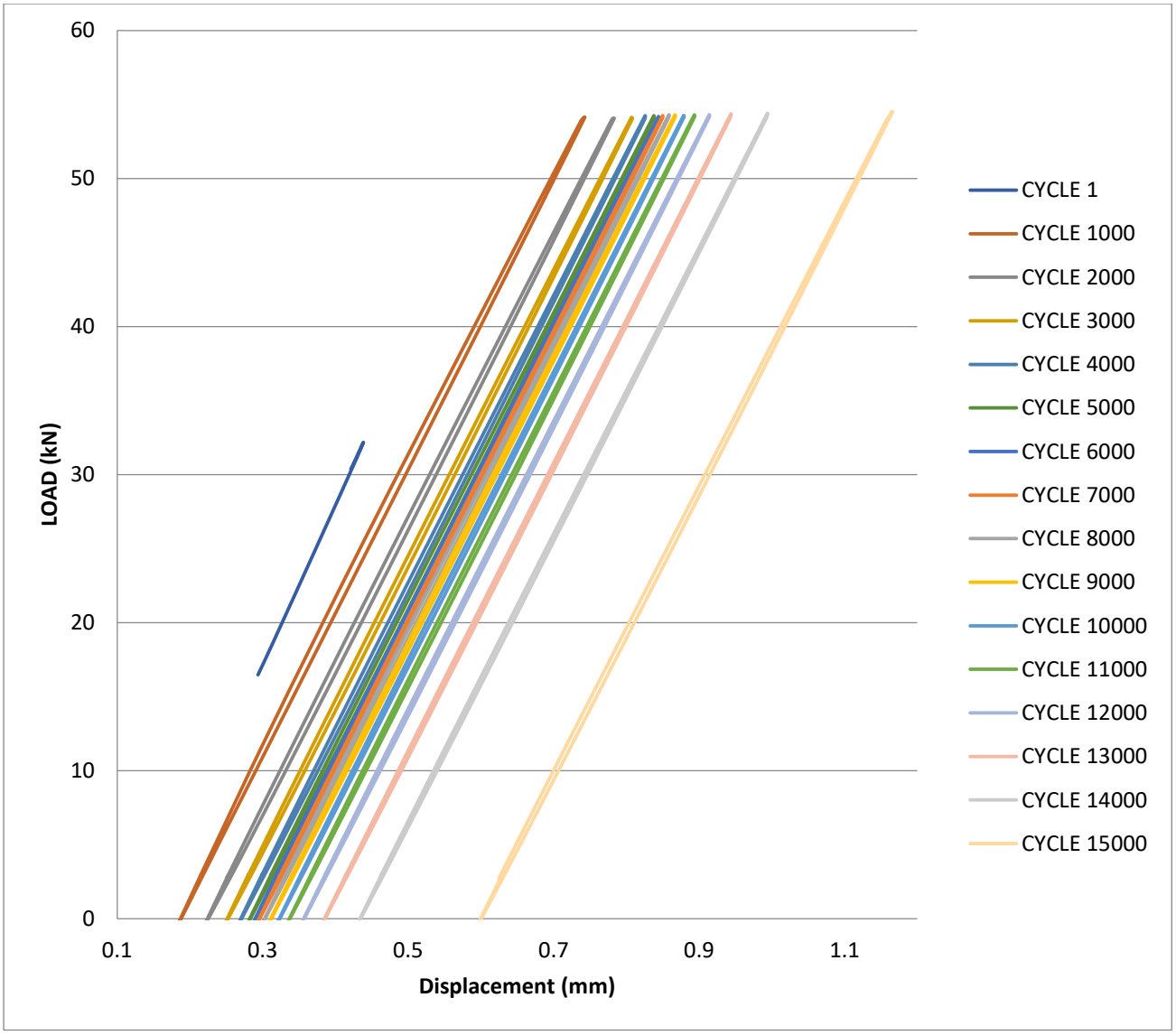

Figure 6.43: Cyclic loading at $60kN$.

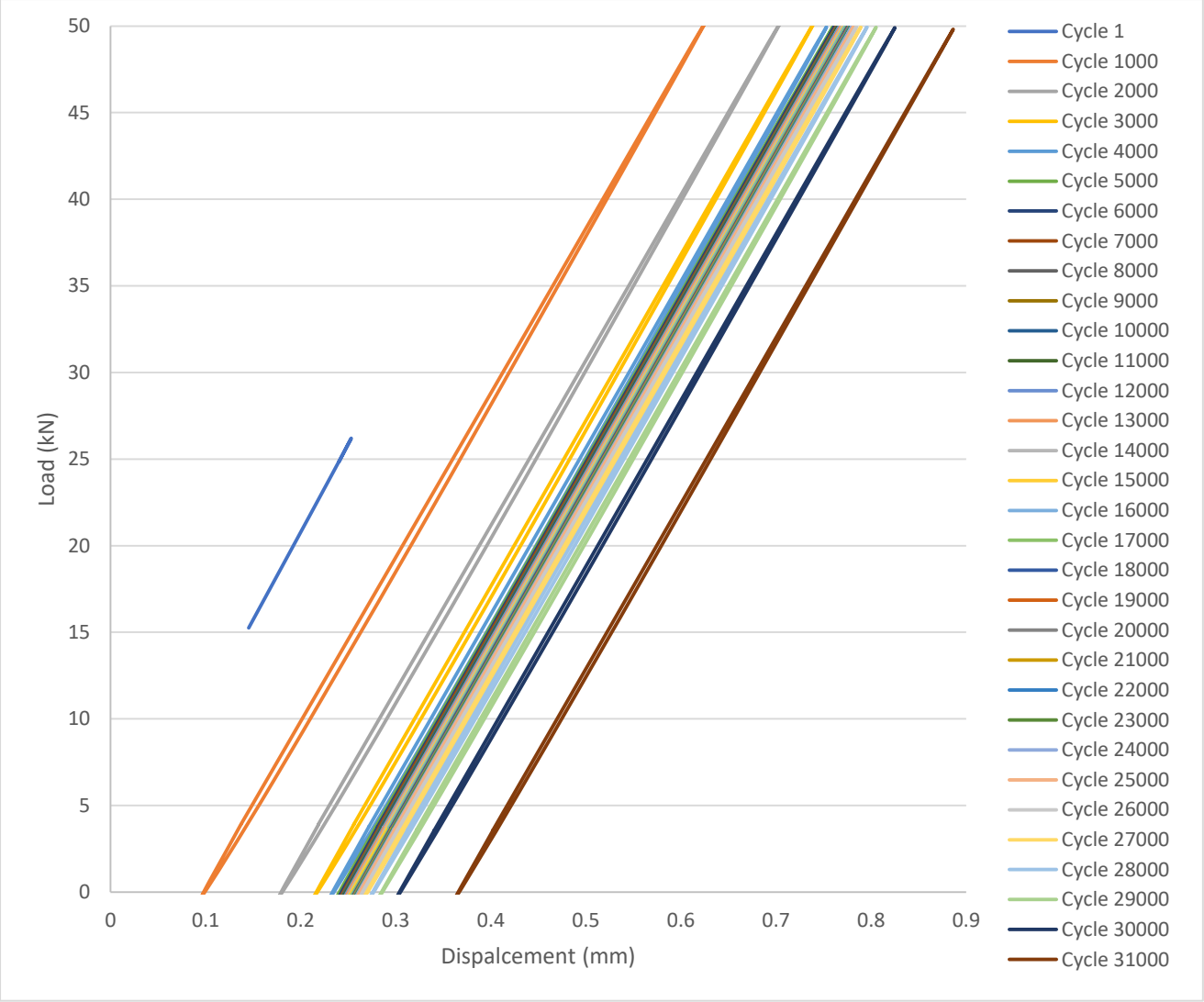

Figure 6.44: Cyclic loading at $50kN$.

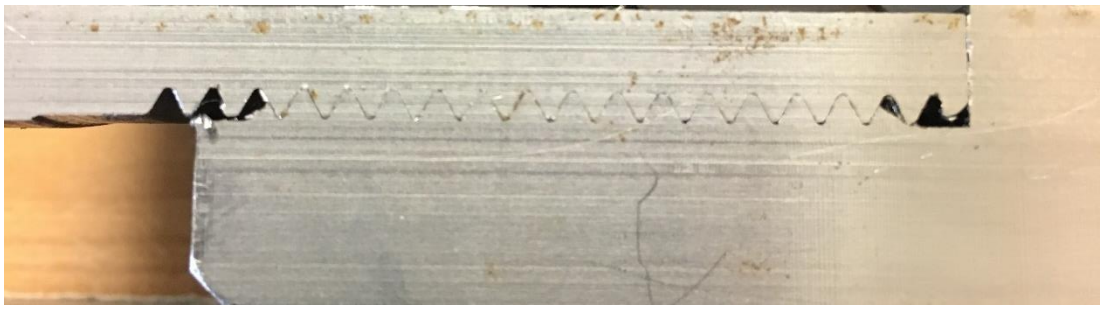

Figure 6.55: British thread (BSPT)

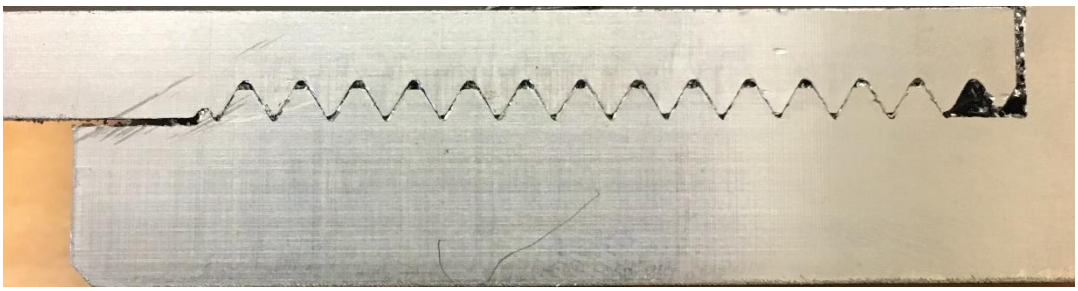

Figure 6.56: API thread.